

A Study on Deformation Mechanisms in Perfect and Twinned Cu Nanowires by Atomistic Simulations

By

P. ROHITH

(Enrolment No : ENGG 02 2014 05 016)

**Indira Gandhi Centre for Atomic Research
Kalpakkam- 603 102, India**

*A thesis submitted to the
Board of Studies in Engineering Sciences*

*In partial fulfillment of requirements
for the Degree of*

DOCTOR OF PHILOSOPHY

of

HOMI BHABHA NATIONAL INSTITUTE



JUNE, 2020



Homi Bhabha National Institute
(A university established under Section 3 of the UGC Act. 1956)
Indira Gandhi Centre for Atomic Research
Kalpakkam – 603 102 Tamil Nadu, India



Dr. V.S. Srinivasan,
Associate Professor, HBNI,
Head, LIMS, SIRD, SQRMG, IGCAR

Date: 06.03.2021

Certificate from Guide

This is certify that **Mr. P. Rohith**, who had submitted thesis entitled “**A Study on Deformation Mechanisms in Perfect and Twinned Cu Nanowires by Atomistic Simulations**”, has incorporated all the relevant corrections suggested by both the reviewers. The final revised thesis has been bound and submitted to HBNI for the award of Degree of Doctor of Philosophy.

V.S. Srinivasan

(Dr. V.S. Srinivasan)
Guide & Convener

HOMI BHABHA NATIONAL INSTITUTE

Recommendations of the Viva Voce Committee

As members of the Viva Voce Committee, we certify that we have read the dissertation prepared by **P. Rohith** entitled "**A Study on Deformation Mechanisms in Perfect and Twinned Cu Nanowires by Atomistic Simulations**" and recommend that it may be accepted as fulfilling the thesis requirement for the award of Degree of Doctor of Philosophy.

Chairman : Dr. B.K. Panigrahi *B.K. Panigrahi* Date: 02/03/2021

Guide & Convener : Dr. V.S. Srinivasan *V.S. Srinivasan* Date: 02-03-2021

Member : Dr. S. Murugan *S. Murugan* Date: 02.03.2021

Member : Dr. R. Divakar *R. Divakar* Date: 02-03-2021

Member : Dr. Anand Krishna Kanjarla *Anand* Date: 02-03-2021

Tech. Advisor : Dr. G. Sainath *G. Sainath* Date: 02/03/2021

Final approval and acceptance of this thesis is contingent upon the candidate's submission of the final copies of the thesis to HBNI.

I hereby certify that I have read this thesis prepared under my direction and recommend that it may be accepted as fulfilling the thesis requirement.

Date: 02-03-2021

Place: IGCAR, Kalpakkam

V.S. Srinivasan

Guide

Dr. V.S. Srinivasan

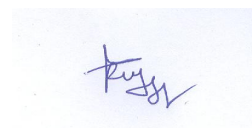
STATEMENT BY AUTHOR

This dissertation has been submitted in partial fulfillment of requirements for an advanced degree at Homi Bhabha National Institute (HBNI) and is deposited in the Library to be made available to borrowers under rules of the HBNI.

Brief quotations from this dissertation are allowable without special permission, provided that accurate acknowledgement of source is made. Requests for permission for extended quotation from or reproduction of this manuscript in whole or in part may be granted by the Competent Authority of HBNI when in his or her judgment the proposed use of the material is in the interests of scholarship. In all other instances, however, permission must be obtained from the author.

Date:

Place: Kalpakkam



(P. Rohith)

DECLARATION

I, hereby declare that the investigation presented in the thesis has been carried out by me. The work is original and has not been submitted earlier as a whole or in part for a degree /diploma at this or any other Institution /University.

A small, square, light blue stamp containing a handwritten signature in blue ink. The signature appears to be 'P. Rohith'.

(P. Rohith)

LIST OF PUBLICATIONS ARISING FROM THE THESIS

Peer reviewed journals

1. Role of axial twin boundaries on deformation mechanisms in Cu nanopillars, **P. Rohith**, G. Sainath, Sunil Goyal, A. Nagesha, and V.S. Srinivasan, *Philosophical Magazine* **2020**, 100, 529-550. DOI: [10.1080/14786435.2019.1695163](https://doi.org/10.1080/14786435.2019.1695163).
2. Effect of size, temperature and strain rate on dislocation density and deformation mechanisms in Cu nanowires, **P. Rohith**, G. Sainath, and V.S. Srinivasan, *Physica B: Condensed Matter*, **2019**, 561, 136-140. DOI: [10.1016/j.physb.2019.03.003](https://doi.org/10.1016/j.physb.2019.03.003).
3. Effect of orientation and mode of loading on deformation behaviour of Cu nanowires, **P. Rohith**, G. Sainath, and B.K. Choudhary, *Computational Condensed Matter* **2018**, 17, e00330. DOI:[10.1016/j.cocom.2018.e00330](https://doi.org/10.1016/j.cocom.2018.e00330).
4. Double reorientation in <110> Cu nanowires, **P. Rohith**, G. Sainath, and B.K. Choudhary, *Philosophical Magazine letters* **2017**, 97, 408-416. DOI:[10.1080/09500839.2017.1390618](https://doi.org/10.1080/09500839.2017.1390618).
5. Size dependent deformation behaviour and dislocation mechanisms in Cu nanowires, G. Sainath, **P. Rohith**, and B.K. Choudhary, *Philosophical Magazine* **2017**, 97, 2632-2657. DOI:[10.1080/14786435.2017.1347300](https://doi.org/10.1080/14786435.2017.1347300). [This work has been chosen as the cover page figure of the journal.]
6. Fatigue deformation of polycrystalline Cu using molecular dynamics simulations, G. Sainath, **P. Rohith**, and B.K. Choudhary, *Transaction of Indian Institute of Metals* **2016**, 69, 489-493. DOI:[10.1007/s12666-015-0823-2](https://doi.org/10.1007/s12666-015-0823-2).

Edited Book Chapter

1. Molecular dynamics simulations study on the grain size dependence of deformation and failure behavior of polycrystalline Cu, **P. Rohith**, G. Sainath, and B.K. Choudhary, Structural Integrity Assessment, Lecture Notes in Mechanical Engineering, Chapter 20, (2020) Springer, Singapore. DOI:[10.1007/978-981-13-8767-8_21](https://doi.org/10.1007/978-981-13-8767-8_21).

Communicated/Manuscripts under preparation

1. **P. Rohith**, G. Sainath, and V.S. Srinivasan, Effect of shape on mechanical properties and deformation behaviour of Cu nanowires: An atomistic simulations study (*Communicated*).
2. **P. Rohith**, G. Sainath, and V.S. Srinivasan, Influence of twin boundary position on yield strength of Cu nanopillars (*Manuscript under preparation*).

Conference/Symposium

1. Molecular dynamics simulations study on the grain size dependence of deformation and failure behavior of polycrystalline Cu, **P. Rohith**, G. Sainath, B.K. Choudhary, Second International Conference On Structural Integrity (ICONS2018), December 14-17 **2018**, IIT Madras, India.
2. Tension-compression asymmetry in the strength of Cu nanowires using molecular dynamics simulations, **P. Rohith**, G. Sainath, B.K. Choudhary, Research Scholar Meet on Material Science and Engineering of Nuclear Materials (RSM-MSENM 2018), May 7-9 **2018**, IGCAR, Kalpakkam, India.
3. Dependence of equilibrium stacking fault width on thickness of Cu thin films : A molecular dynamics study, **P. Rohith**, G. Sainath, B.K. Choudhary, DAE Solid State Physics Symposium (DAE-SSPS 2016), December 26-30 **2016**, KIIT, Bhubaneswar, India. DOI: [10.1063/1.4980520](https://doi.org/10.1063/1.4980520)

Presentations

1. Deformation behaviour and dislocation mechanisms in Cu nanowires, **P. Rohith**, G. Sainath, B.K. Choudhary, Current Advances in Materials and Processing- CAMP, IIM Kalpakkam Chapter, February 20-21, **2018**, IGCAR, Kalpakkam, India.

Publications not part of thesis

1. Molecular dynamics simulation studies on the influence of aspect ratio on tensile deformation and failure behaviour of <100> copper nanowires, **P. Rohith**, G. Sainath, B.K. Choudhary, Computational Materials Science **2017**, 138, 34-41. (Part of M.Sc. Thesis) DOI: [10.1016/j.commatsci.2017.06.019](https://doi.org/10.1016/j.commatsci.2017.06.019)
2. Size dependent deformation and failure behaviour of Cu nanowires, **P. Rohith**, G. Sainath, B.K. Choudhary, Conference on Emerging Materials (CEMAT), July 18- 19, (**2016**), IISC-Bangalore. (Part of M.Sc. Thesis)



(**P. Rohith**)

To my family

ACKNOWLEDGEMENTS

First and foremost, I take this opportunity to express my deep regards and sincere gratitude to my guide **Dr. V.S. Srinivasan** for his guidance and constant encouragement during project work. This project would not have been possible without his help and the valuable guidance. I would like to extend my hearty gratitude to **Dr. B.K. Choudhary** for his patient supervision, guidance and encouragement.

Besides my guide, I would like to thank the doctoral committee members for extremely useful and valuable suggestions during the course of this work. I am thankful to **Dr. A. Nagesha, Dr. R. Divakar, Dr. Anish Kumar** and **Dr. G. Sasikala** for the ease of administrative works and suggestions.

My heartfelt thanks to my technology adviser, **Dr. G. Sainath**, who has played a crucial role in shaping the Ph.D. theme, manuscripts and the final thesis. Special thanks to him for helping me to write and compile the software/codes as well as his patience while teaching me how to run these codes using remote terminals. I am wholeheartedly indebted to him for assisting me in technical aspects and providing me moral support during my hard times.

I would also like to convey my sincere thanks to **Dr. J. Christopher** for useful discussion related to technical as well as societal aspects during the course of this study. I also earnestly appreciate the support and encouragement from all the members of deformation and damage modelling section (**DDMS**) and fatigue studies section (**FSS**).

I would like to thank the support rendered by **Dr. Shaju K. Albert**, Director, MMG, and **Dr. A.K. Bhaduri**, Director, IGCAR for providing me this opportunity to utilize IGCAR resources, and work in a challenging environment. Also, I would like to appreciate IGCAR for providing a comfortable stay at JRF enclave, Kalpakkam. Special thanks also to my friends, who made my life at enclave memorable. I would like to express my love and gratitude to my beloved family for their understanding and endless love. Last but not least, I would like to extend my hearty gratitude to all the people who encouraged and helped me during this study.

SUMMARY

Metallic nanowires exhibit remarkable electrical, optical, thermal and mechanical properties due to limited defects, finite size, and high surface to volume ratio. The fundamental understanding of mechanical properties and associated deformation mechanisms improves the durability and reliability of the nanowires. MD simulations have become an effective tool for evaluating material properties. The present thesis focuses on understanding the mechanical behaviour of single crystalline, twinned and polycrystalline Cu nanowires under the influence of orientation, mode of loading (tension/compression), nanowire size, cross sectional shape, and the presence of twin and grain boundaries using MD simulations.

Simulation results indicate that, under compression, deformation in the orientations close to $\langle 100 \rangle$ corner on a standard stereographic triangle is dominated by deformation twinning, while the remaining orientations (ex: $\langle 110 \rangle$) deform by dislocation slip. On the other hand, twinning is dominated in all the nanowires under tension, which results in tension-compression asymmetry in deformation mechanisms for the orientations close to $\langle 110 \rangle$ and $\langle 111 \rangle$. This asymmetry in deformation mechanisms has been explained based on the parameter α_M , defined as the ratio of Schmid factors of leading and trailing partial dislocations. Further, Cu nanowires exhibit tension-compression asymmetry in yield stress, which has been attributed to the differences in Schmid factor value for leading partial dislocations under tension and compression.

MD simulation results indicated that Young's modulus is insensitive to nanowire shape. However, both yield stress and strain to failure are sensitive to nanowire shape and size. Yielding in $\langle 100 \rangle$ Cu occurs through the nucleation of Shockley partials. Following yielding, plastic deformation in small size $\langle 100 \rangle$ Cu nanowires occurs through partial dislocation slip at all strains, while in large size Cu nanowires, slip of extended dislocations has been observed at high strains in addition to slip of partial dislocations. Interestingly, formation of pentagonal atomic chains has been observed in small size nanowires with size ≤ 1.446 nm. Further, average dislocation length, different dislocation-dislocation interactions resulting in various dislocation locks, annihilation of stacking faults, and size dependent dislocation surface interactions have been observed. Results also indicate that the variations in dislocation density as

a function of strain exhibit two stages: (i) dislocation exhaustion at small strains followed by (ii) dislocation starvation at high strains. However, with decreasing size and increasing strain rate/temperature, rate of dislocation exhaustion increases. Tensile deformation of $\langle 110 \rangle$ Cu nanowire indicated the double reorientation from $\langle 110 \rangle$ to $\langle 100 \rangle$, and to $\langle 112 \rangle$ axis. This occurrence of double reorientation and associated high ductility is restricted to low nanowire length. For nanowires with large length, reorientation process does not occur due to the activation and interaction of multiple twin systems.

Simulation results also indicate that under both tension and compression, yield strength increases with decreasing TB spacing and is always higher than that of perfect nanopillars. Under compression, deformation in perfect and nanopillars with twin boundaries (twinned nanopillars) proceeds by slip of extended dislocations. In twinned nanopillars, an extensive cross-slip through both Friedel-Escaig (FE) and Fleischer mechanisms has been observed in compression. However, deformation in perfect nanopillars occurs by partial slip/twinning, while in twinned nanopillars, it proceeds by the slip of extended dislocations under tension. This extended dislocation activity is facilitated by stair-rod formation and its dissociation on twin boundary. Similar to compressive loading, the extended dislocations under tensile loading also exhibit cross-slip activity in twinned nanopillars. However, under tension, cross-slip activity occurs only through FI mechanism, but not through FE mechanism. Also, simulation results shows that yield strength increases with increasing twin boundary distance from nanopillar surface.

MD simulation results reaffirmed inverse Hall-Petch relation as a function of grain size in polycrystalline Cu. Tensile deformation is dominated through partial dislocations and deformation twinning. Formation of fivefold twin has been observed due to interaction of multiple twin systems. Similarly, fatigue simulation results indicated that the deformation is dominated by partial dislocations. Cyclic stress-strain behaviour is characterized by initial softening up to 3rd cycle followed by hardening till the end of 10th cycle. Initial softening followed by hardening has been inversely correlated with dislocation density. Extensive grain growth during deformation has been observed under both tensile and fatigue loadings. Under tension, for nanowires of grain size up to 3.61 nm, failure has been observed by shear along the slip planes, while, grain boundary failure has been observed in nanowire with a grain size of 5.42 nm. Irrespective of the grain size, all nanowires under tension exhibit similar ductility indicating that ductility is insensitive to grain size.

Contents

SUMMARY	viii
LIST OF FIGURES	xxv
LIST OF TABLES	xxvi
1 Introduction	1
1.1 Theory of plastic deformation	1
1.2 Metallic nanowires/nanopillars	4
1.3 Mechanics of materials	7
1.3.1 Dislocation slip in FCC systems	7
1.3.2 Stacking sequence, stacking fault and Shockley partials in FCC systems	9
1.3.3 Twinning in FCC systems	12
1.3.4 Schmid factor	12
1.3.5 Generalized stacking fault energy (GSFE)	14
1.4 Literature review on deformation behaviour of FCC nanowires	16
1.4.1 Orientation dependent deformation behaviour	18
1.4.2 Effect of nanowire/nanopillar size	22
1.4.3 Influence of twin boundaries on deformation behaviour	30
1.5 Objective and thesis outline	36
2 Atomistic simulation methods and pre- and post-processing techniques	40
2.1 Molecular dynamics simulations	41
2.1.1 Inter-atomic potentials	42
2.1.2 Integration algorithms	50
2.1.3 Boundary conditions	52

2.2	LAMMPS for molecular dynamics simulations	55
2.3	Pre-processing	56
2.4	Loading procedure	58
2.4.1	Procedure I:	58
2.4.2	Procedure II:	59
2.5	Post-Processing	61
2.5.1	Coordination number (CN)	62
2.5.2	Common neighbor analysis (CNA)	62
2.5.3	Central symmetry parameter (CSP)	65
2.5.4	AtomEye	66
2.5.5	Dislocation extraction algorithm (DXA)	67
3	Orientation dependent deformation behaviour of Cu nanowires under compression and tension	69
3.1	Introduction	69
3.2	MD simulation details	71
3.3	Results	72
3.3.1	Deformation behaviour under compression	72
3.3.2	Deformation behaviour under tension	75
3.3.3	Stress-strain behaviour	77
3.4	Discussion	80
3.4.1	Orientation and loading mode dependent deformation mechanisms	80
3.4.2	Tension-compression asymmetry in yield stress	83
3.5	Conclusions	85
4	Effect of shape and size on the deformation behaviour of Cu nanowires	87
4.1	Introduction	87
4.2	MD simulation details	88
4.3	Size effects in <100> Cu nanowires	91
4.3.1	Stress-strain behaviour	91
4.3.2	Yield stress and dislocation nucleation	93
4.3.3	Deformation mechanisms	95

4.3.4	Variations in dislocation density	97
4.3.5	Average length of dislocations	102
4.3.6	Dislocation-defect interactions	103
4.3.7	Ductility and failure behaviour	108
4.4	Size effects in $\langle 110 \rangle$ Cu nanowires and double reorientation	110
4.4.1	Size effects	110
4.4.2	Double reorientation	111
4.4.3	Stress-strain behaviour	116
4.5	Influence of nanowire cross section/shape	117
4.5.1	Nanowires of different shape having different surface area to volume ratio	118
4.5.2	Nanowires of different shapes having same surface area to volume ratio	120
4.5.3	Deformation mechanisms in different shapes	122
4.6	Conclusions	125
5	Role of axial twin boundaries on the deformation mechanisms in Cu nanopillars	129
5.1	Introduction	129
5.2	Computational details	130
5.3	Effect of twin boundary spacing	131
5.3.1	Stress-strain behaviour	131
5.3.2	Deformation mechanisms in perfect $\langle 112 \rangle$ Cu nanopillars	134
5.3.3	Deformation mechanisms in twinned $\langle 112 \rangle$ Cu nanopillars under compressive loading	134
5.3.4	Deformation mechanisms in twinned $\langle 112 \rangle$ Cu nanopillars under tensile loading	137
5.3.5	Yield stress in twinned nanopillars	141
5.3.6	Deformation mechanisms and cross-slip	143
5.4	Influence of twin boundary position	146
5.4.1	Stress-strain behaviour	146
5.4.2	Yield strength dependence on twin boundary position	148
5.5	Conclusions	149
6	Deformation behaviour of polycrystalline Cu under monotonic and cyclic load-	

ing	151
6.1 Introduction	151
6.2 Computational details	152
6.3 Results	153
6.3.1 Deformation behaviour under monotonic loading	153
6.3.2 Deformation behaviour under cyclic loading	158
6.4 Conclusions	162
7 Conclusions and future studies	165
7.1 Conclusions	165
7.2 Future studies	169

List of Figures

1.1	a) The schematic diagram illustrating the formation of slip bands during the deformation. Slip bands (a, b, c, d, e) occurs through sliding of elementary portions of material over one another. b). Optical micrograph of deformed polycrystalline Pb representing that deformation occurs through slip. c). Optical micrograph of deformed polycrystalline Cu representing that deformation occurs through twinning. These figures have been taken from Ewing and Rosenhain [1].	2
1.2	The variations in the ratio of surface area to volume, as a function of cubic nanoparticle diameter.	4
1.3	Cu nanowires used as fillers in stretchable electronics. (a) Top view OF SEM image of Cu nanowire network coated on glass. The inset shows a homogeneously dispersed Cu nanowire ink. (b). SEM image of Cu nanowire sizes. These figures has been taken from the reference [18].	5
1.4	A and B Cu nanowire ink dispersed on polyethylene terephthalate (PET) substrate with a Meyer rod to form a thin, uniform film . C) Highly flexible Cu films: A bent Cu nanowire film in a closed electrical circuit connected with a battery pack and a LED [21].	6
1.5	The schematic illustration of region (hatched) within a slip plane has been displaced relative to the other. Burgers vector, b represents the magnitude and direction of the displacement.	8
1.6	The schematic illustration of slip systems in FCC crystals. Four $\{111\}$ slip planes with three $\langle 110 \rangle$ slip directions lying on the slip planes constitute the 12 slip systems in FCC crystals.	9
1.7	The atomic arrangement in close packed manner for FCC and HCP structures. Arrangement of A and B layer of atoms is common in both FCC and HCP systems. However, the third layer (either A or C) is different for FCC and HCP systems. This figure has been taken from Ref. [34].	10
1.8	a) The atomic arrangement in FCC system (normal to $\{111\}$ plane). The possible slip path are through either glide of dislocation, b_1 or sequential glide of b_2 and b_3 . b) The disassociation of perfect to Shockley partials with associated stacking fault.	11

1.9	Twinning in FCC systems. Twinning occurs on $\{111\}$ planes along $\langle 112 \rangle$ directions. The shaded region indicates the instantaneous atomic positions during deformation. The atomic displacement has been indicated by arrow symbols along the twin directions [36].	13
1.10	Schematic illustration of calculation of shear stress in a single crystalline cylindrical specimen under tensile force	14
1.11	a). Atomic transition during glide of 111 plane along $\langle 112 \rangle$ direction. b). GSFE curve during the atomic transition in FCC crystals. Displacements C, C' and A corresponds to the lattice position shown in a.	15
1.12	Snapshots illustrating the operating deformation mechanisms in $\langle 001 \rangle$ Al nanopillar under compression. a) glide of partial dislocations and associated stacking faults , b) formation of nano-twins and c) twins. These figures has been taken from Ref. [42]	17
1.13	The atomic configuration of $\langle 112 \rangle$ Al nanopillar under compression. a) Full dislocations nucleate separately along the $(\bar{1}\bar{1}\bar{1})$ and $(1\bar{1}\bar{1})$ slip planes, and b) full dislocations interacting with each other.	17
1.14	The atomic snapshots of phase transformation of Au nanowires from FCC lattice to BCT lattice. These figures has been taken from Ref. [47]	18
1.15	Deformation behaviour of $\langle 110 \rangle$ Au nanopillars under compression and tension [38]. a) TEM images and MD simulations showing the nucleation of dislocation loops and subsequent slip under compression [38]. b) The sequential TEM images revealing the domination of twinning under tension [38]. The orange arrows in (b) show the slip steps, while the yellow arrow show half dislocation loops.	20
1.16	The atomic snapshots of $\langle 110 \rangle$ Cu nanowires under tension[27]. The operating deformation mechanism, deformation twinning reorients Cu nanowires from $\langle 110 \rangle$ to $\langle 100 \rangle$ orientation.	21
1.17	Deformation behaviour in Cu nanowires [28]. In Cu $\langle 111 \rangle$ nanowires, deformation proceeds through a) slip through perfect/full dislocations under compression [40], and b) slip through partial dislocations under tension. c) under similar tensile conditions, deformation through twinning in $\langle 110 \rangle$ Cu nanowires.	22
1.18	Compressive yield stress of Cu(100) pillars with varying sample diameters in the range 90 nm to 1700 nm. Also, change in operating deformation morphology with varying size. Different deformation regimes has been indicated with differently colored bars [56]. The insets represents the compressed Cu pillars	23
1.19	Sample size dependence of two deformation mechanisms: Slip through partial dislocations and full dislocations. Relative contribution of both deformation mechanisms for pure Cu nanowires at various sizes. The transition can be seen at $D = 150$ nm [50].	25
1.20	Pseudo-elasticity in single crystalline Cu nanowires [22].	26

1.21	Operating deformations of FCC metallic nanowires under different axial loading conditions. In partial slip region: $\tau_1 < \tau_2$ and $\tau_1 < 1$. In full slip region, $\tau_2 < \tau_1$, and $\tau_2 < 1$. In twin region: $\tau_1 > 1$ and $\tau_2 > 1$. Open symbols represents the loading conditions of $\langle 100 \rangle$ tension, $\langle 110 \rangle$ compression and $\langle 111 \rangle$ compression. Filled symbols represents the loading condition of $\langle 100 \rangle$ compression, $\langle 110 \rangle$ tension and $\langle 111 \rangle$ tension[28].	28
1.22	Size effect on the tensile yield strength of pentagonal, rhombic, cated-rhombic silver nanowires[73].	29
1.23	Influence of cross-sectional geometry on deformation behaviour of $\langle 110 \rangle$ Ag nanowires. a). Cross-sectional geometry of Ag nanowires. b) Reoriented $\langle 001 \rangle$ Ag nanowire with 110 and 001 Ag nanowires. c) Countour map explaining transition of deformation from twinning to dislocation slip for varying cross-sectional Open black squares refers to twinning-dominated mode, and open red circles indicates that deformation dominated by dislocation slip[74].	29
1.24	Shape dependent strengthening behaviour in twinned nanowires. Nanowires with a) square b) circular shaped nanowires. c) yield strength variation with twin boundary spacing for circular and square shaped nanowires [81].	30
1.25	Mechanical behaviour of Cu nanowires. a) yield strength variation with twin boundary spacing for nanowires of different lengths. b) ductile to brittle transition with increasing twin boundary spacing [83].	31
1.26	Operating deformation mechanisms in twinned Au nanowires [89]. a) Model twinned nanowires with orthogonal and slanted twin boundaries. deformation proceeded through b) discrete twin boundary -dislocation interactions in longitudinally twinned nanopillars, and c) de-twinning in slanted twin boundaries [89].	32
1.27	a) A model nanocrystalline copper with an average grain diameter of 5.2 nm. Grain boundary atoms are colored blue, while stacking fault atoms are colored red. b) true stress-strain behaviour of nanocrystalline Cu for different grain sizes/diameter. c) variations of flow stress and yield stress with grain size [96].	34
1.28	Operating deformation twinning process. a) Glide of partial dislocation enclosing stacking fault in the interior of grain. b) twin growth by a single lattice plane. c) before straining and d) after 18.1% applied strain. The plastic deformation induced extensive grain growth. The average grain size is 6 nm [97]. Two coarsened and elongated grains are marked with asterisks. All atoms are colored according to CNA. Green colored atoms represent pure FCC Ni, while red colored atoms represents stacking fault atoms and ash colored atoms represent grain boundary atoms.	34
1.29	Statistical distribution explaining the operating deformation mechanism as a function of grain size d for nanocrystalline Pt [98]. At larger grains, deformation through full dislocations denoted by square symbol. For $6 < d < 10$ nm partial dislocations enclosing stacking faults denoted by dots were observed, and for $d < 6$ nm, the grain boundaries dominate the plasticity, indicated by black triangles.	35

2.1	Flowchart explaining the molecular dynamics (MD) simulation methodology	42
2.2	LJ potential illustrating the attractive and repulsive terms	45
2.3	A model three dimensional system with periodic boundary conditions along three directions. Red colored region represents the original simulation cell and all blue colored cells are the exact replicas of red colored simulation cell.	53
2.4	Boundary conditions applied for generating different models. a) Bulk material model, b) thin film model, c) nanowire model d) nanopillar model.	55
2.5	a) Tinkercad, an open source online platform for modeling nanowire shapes [127]. b) A model polycrystal nanowire prepared using Voronoi algorithm from AtomEye software[129, 131]	57
2.6	Testing procedure I: The original dimensions of simulation cell represented by dotted lines as L_x , L_y , and L_z . The instantaneous simulation cell dimensions during loading is shown by continuous line $L(t)_x$, $L(t)_y$, and $L(t)_z$.	59
2.7	Procedure II: Bottom end of nanowires has been hold constant and the top end has been elongated at a constant velocity. Velocity profile vs position in correspondence to the simulation cell.	60
2.8	CNA for a) FCC b) HCP, and c-d) BCC systems with different indexes according to Honeycutt and Anderson [141].	63
2.9	A model nanowires visualized using CNA parameter. The blue color atoms represents the perfect FCC atoms, cyan color atoms represents HCP atoms (both stacking faults in FCC and twin boundaries), while the red color atoms indicate the free surfaces and dislocation core.	64
2.10	Colored opposite pairs in a) FCC, and b) BCC structures.	66
2.11	DXA methodology illustrating the interface mesh sweeping the dislocation line. While the Burgers circuit is being advanced in a step-wise fashion, triangle by triangle, a continuous line representation of the dislocation defect is produced.	68
3.1	Standard stereographic triangle with various crystallographic orientations chosen in the present study. Cu nanowires with these orientations have been subjected to tensile and compressive loading.	70
3.2	Atomic snapshots displaying (a) nucleation of a Shockley partial, (b) glide of twinning partial and nano-twin, (c-d) twin growth (e) reoriented nanowire, and (f) the slip of extended dislocation in the reoriented nanowire during the compressive deformation of $\langle 100 \rangle$ Cu nanowires. In Figure (d), the partial dislocations are shown as green lines as obtained in OVITO [130], while the remaining figures are obtained using AtomEye. The atoms are colored according to the common neighbor analysis (CNA). The blue color atoms represents the FCC and the red color atoms indicate the surfaces and dislocation core.	73

3.3	Atomic snapshots displaying the compressive deformation of $\langle 111 \rangle$ Cu nanowires as a function of strain. The deformation by the slip of extended dislocations along with stacking fault tetrahedron and many point defects can be seen in (b), (c) and (d). Figure (d) is the OVITO [130] output of Figure (c), where partial dislocations are shown as green lines, the stair-rod dislocations enclosing the stacking fault tetrahedron are shown in magenta lines. The atoms are colored according to the common neighbor analysis (CNA).	74
3.4	Atomic snapshots displaying the compressive deformation of $\langle 214 \rangle$ Cu nanowires as a function of strain. The deformation proceeds through the glide of extended dislocations. The atoms are colored according to the common neighbor analysis (CNA).	75
3.5	The atomic snapshots displaying the tensile deformation of $\langle 110 \rangle$ Cu nanowires as a function of strain. Deformation proceeds through twinning followed by reorientation to $\langle 100 \rangle$ axial direction.	76
3.6	The atomic snapshots during the tensile deformation of $\langle 214 \rangle$ Cu nanowires as a function of strain. Deformation proceeds through twinning mechanism followed by reorientation to high index $\langle hkl \rangle$ direction. The final failure occurs by sliding along the twin boundaries.	77
3.7	Atomic snapshots presenting the deformation and failure behaviour of $\langle 100 \rangle$ and $\langle 102 \rangle$ Cu nanowires under tensile loading. The twin-twin interactions and the twin boundary sliding disrupting the reorientation process can be seen in both the orientations.	78
3.8	The stress-strain behaviour of Cu nanowires deforming by (a) twinning and (b) full dislocation slip under compressive loading of different orientations at 10 K.	79
3.9	The stress-strain behaviour of Cu nanowires deforming by twinning (a) with reorientation and (b) without reorientation under tensile loading at 10 K.	79
3.10	The variation of yield stress with respect to orientation presented on the standard stereographic triangle under (a) compressive loading, and (b) tensile loading of Cu nanowires. The yield stress values are in GPa.	80
3.11	The standard stereographic triangle showing two different regions, one with $\alpha_M > 1$ (red color) and other with $\alpha_M < 1$ (light blue) under (a) compressive loading and (b) tensile loading. The black solid line between red and blue colors represent a boundary with $\alpha_M = 1$. The parameter, α_M is defined as the ratio of Schmid factors of leading and trailing partial dislocations.	82
3.12	The values of (a) yield stress asymmetry (b) Schmid factor asymmetry shown on the standard stereographic triangle for different orientations of Cu nanowires. Yield stress asymmetry is defined as the ratio of yield stress in tension to that in compression (T/C), while the Schmid factor asymmetry is defined as the ratio of leading partial Schmid factor in compression to that in tension (C/T).	84

4.1	Square shaped nanowires of fixed length of 21.69 nm with varying square cross-sections width (d) of 10.48 nm. The cross-sections width (d) of nanowires has been varied in the range 0.723-43.38 nm.	89
4.2	The nanowires cross-section shapes considered in the present study. (a) Triangular, (b) square, (c) pentagonal, (d) hexagonal, and (e) circular, with their corresponding side surfaces.	90
4.3	Stress-strain curves for $\langle 100 \rangle$ Cu nanowires with constant length of 21.69 nm at different cross section width (d) in the range 0.723-43.38 nm at 10 K. For clarity of elastic deformation, the magnified figure at small strains is shown in inset.	92
4.4	The variation of Young's modulus as a function of cross section width (d) for $\langle 100 \rangle$ Cu nanowires at 10 K.	92
4.5	Variation of yield strength as a function of cross section width (d) for $\langle 100 \rangle$ Cu nanowires at 10 K. For comparison, the results from other MD simulations on $\langle 100 \rangle$ Cu nanowires [164, 165] are superimposed.	93
4.6	The variation of initial stress as a function of cross section width (d) for $\langle 100 \rangle$ Cu nanowires at 10 K.	94
4.7	Yielding by the nucleation of $1/6\langle 112 \rangle$ Shockley partial dislocations in $\langle 100 \rangle$ Cu nanowires of different cross section width (d) in the range 0.723-43.38 nm at 10 K. (a) d = 0.723 nm (b) d = 1.446 nm (c) d = 2.169 nm (d) d = 3.615 nm (e) d = 10.845 nm (f) d = 43.380 nm. With increasing size, the increase in defect nucleation sites can be seen. The blue color atoms represent the stacking faults and the red color atoms indicate the surfaces and dislocation core. The perfect FCC atoms were removed for clarity.	95
4.8	Deformation behaviour in small size $\langle 100 \rangle$ Cu nanowires with cross section width (d) = 3.615 nm under tensile loading. The deformation occurring by slip of partial dislocations can be seen at all strains. The blue color atoms represent the stacking faults and the red color atoms indicate the surfaces and dislocation core. The perfect FCC atoms were removed for clarity.	96
4.9	Deformation behaviour in large size $\langle 100 \rangle$ Cu nanowires with cross section width (d) = 20.69 nm under tensile loading. In addition to partial dislocation slip at small strains, deformation dominated by slip of extended dislocations can be seen at high strains. The white arrow indicates the extended dislocations. The blue color atoms represent the stacking faults and the red color atoms indicate the surfaces and dislocation core. The perfect FCC atoms were removed for clarity.	97
4.10	Variation of dislocation density, dislocation microstructure and flow stress as a function of strain for Cu nanowire with d = 21.69 nm under tensile loading at 10 K. In the inset snapshots, the green color lines show the $1/6\langle 112 \rangle$ Shockley partial dislocations and the magenta lines represent the L-C dislocations having Burgers vector $1/6\langle 110 \rangle$. The thick black dots represent the point defects. The snapshots of the nanowire shown in inset figures were obtained in OVITO [130].	98

4.11	(a) Variations in dislocation density as a function of strain (or time) for nanowires of different size deformed at a constant strain rate of $1 \times 10^9 \text{ s}^{-1}$ and temperature of 10 K. (b) The variations in rate of dislocation exhaustion with respect to nanowire size.	100
4.12	(a) Variations in dislocation density as a function of strain (or time) at different temperatures for a nanowire of size (d) = 10.85 nm deformed at a constant strain rate of $1 \times 10^9 \text{ s}^{-1}$. (b) The variations in dislocation exhaustion rates as a function of temperature.	101
4.13	(a) Variations in dislocation density as a function of strain at different strain rates for a nanowire of size (d) = 10.85 nm deformed at 10 K. (b) The variations in dislocation exhaustion rate as a function of strain rates.	102
4.14	The variation of average length of dislocations as a function of strain in $\langle 100 \rangle$ Cu nanowires with different cross section width.	103
4.15	Dislocation-stacking fault interactions leading to annihilation of stacking faults in Cu nanowire with d = 20.69 nm. The green color lines show $1/6 \langle 112 \rangle$ Shockley partial dislocations and black lines display $1/3 \langle 110 \rangle$ stair-rod dislocations.	104
4.16	The interaction of a leading partial dislocation with the surface in large size nanowires. The annihilation of leading partial at the surface gives rise to the nucleation of a new trailing partial dislocation.	105
4.17	Interaction of a leading partial dislocation with surface in small size nanowires. The partial dislocation reflects multiple times from the nanowire surface.	106
4.18	Dislocation-dislocation interactions leading to the formation of L-C lock at acute junction and Hirth lock at obtuse junction of $\{111\}$ planes in $\langle 100 \rangle$ Cu nanowires. The green lines indicate Shockley partials, magenta color lines represent L-C dislocations and blue color lines show Hirth dislocation.	107
4.19	The interaction of Shockley partial dislocation with L-C dislocation leading to the formation of Frank partial. The green lines indicate Shockley partials, magenta color lines represent L-C dislocations and cyan color lines show Frank partials.	108
4.20	Variation of strain to failure or ductility as a function of cross section width (d) for $\langle 100 \rangle$ Cu nanowires at 10 K.	109
4.21	Failure behaviour in (a) the smallest size (d = 0.723 nm) (b) intermediate size (d = 10.845 nm) (c) large size (d = 21.69 nm) $\langle 100 \rangle$ Cu nanowire during tensile deformation at 10 K. The formation of pentagonal atomic chain in the necking region of the smallest size nanowire can be seen in a.	110
4.22	The double or sequential reorientation of $\langle 110 \rangle$ Cu nanowire of cross section width (d) and length (l) = 7.15 nm (aspect ratio 1) under tensile loading. The double reorientation changes the cross section shape from square to rhombus and then rhombus to parallelogram. The atoms are colored according to their coordination number.	112

4.23	Detailed deformation mechanisms responsible for double reorientation from $\langle 110 \rangle$ tensile axis to $\langle 100 \rangle$ axis and then $\langle 100 \rangle$ axis to $\langle 112 \rangle$ axis in Cu nanowire. The blue color represents the FCC atoms, cyan color atoms represent the stacking faults and twin boundaries and the red color atoms indicate the surfaces and dislocation core. The atoms color has been assigned according the common neighbor analysis (CNA).	113
4.24	Absence of reorientation during the tensile deformation of $\langle 110 \rangle$ Cu nanowire of cross section width (d) = 7.15 nm and length (l) = 14.3 nm (aspect ratio 2). The blue color represents the FCC atoms, cyan color atoms represent the stacking faults and twin boundaries and the red color atoms indicate the surfaces and dislocation core. The atoms color has been assigned according the common neighbor analysis (CNA).	115
4.25	Stress-strain behaviour of $\langle 110 \rangle$ Cu nanowire with constant cross section width (d) = 7.15 nm and different length (l) of 7.15 nm (aspect ratio = 1) and 14.31 nm (aspect ratio = 2). Nanowire undergoing double reorientation (aspect ratio = 1) show three elastic peaks (shown by arrows) separated by twin growth regimes.	117
4.26	A method showing the inscription all the shapes within the circular shape. In the first scenario, the size for different shapes is chosen in such a way that all shapes can be inscribed in circular nanowire of radius 'r'. $a_T, a_S, a_P,$ and a_H represents the side length of triangular, square, pentagonal and hexagonal shaped nanowires.	118
4.27	Stress-strain behaviour of $\langle 100 \rangle$ Cu nanowires of different shape in Scenario-1, where each shape has a different surface area to volume ratio. The stress-strain behaviour till strain of 20 % has been shown in inset for better clarity.	119
4.28	Variation of yield strength along with surface area to volume ratio for different nanowire shapes in Scenario-1.	120
4.29	Stress-strain behaviour of $\langle 100 \rangle$ Cu nanowires of different shape in Scenario-2, where all the shapes have same surface area to volume ratio. The stress-strain behaviour till strain of 20 % has been shown in inset for better clarity.	121
4.30	Variation of yield strength and potential energy for different nanowire shapes in Scenario-2.	122
4.31	The dislocation nucleation during the yielding/beginning of plastic deformation in nanowires of different shapes. This nucleation mechanism remains the same for both scenarios. The white arrows indicates the direction of dislocation motion. The nucleation occurs from the intersection of two different side surfaces.	123
4.32	The deformation mechanisms observed in nanowires of different shapes, each shown at different strain value. The yellow arrows indicate the direction of twin boundaries movement. The white arrows indicate the direction of glide of Shockley partial dislocations on $\{111\}$ planes.	123

4.33	The schematic showing the orientation of initial (top row) and twinned side surfaces for (a) triangular, (b) square and, (c) hexagonal shaped nanowires. In pentagonal and circular nanowires, even though the deformation twinning has been observed, but we are not able to identify the new surface orientations due to high roughness.	124
4.34	The final failure behaviour of nanowires of different shapes. The encircled regions indicate the initiation of necking and black arrows shows failed region.	125
5.1	The model system of (a) perfect Cu nanopillar and twinned Cu nanopillars with (b) one (c) two (d) three and, (e) four, equidistant twins. The double Thompson tetrahedron illustrating the slip planes and directions is shown in (f). The crystallographic orientation and twin boundary spacing has been shown for clarity. The cross-section width (d) of all the nanowires is 10 nm. In (a)-(e), The front surfaces are removed and the atoms are colored according to the common neighbor analysis (CNA).	131
5.2	The atomic configuration of twinned nanopillar with varied twin boundary position. Twin boundary position has been modified by changing twin distance (x) from surface in the range 1 nm to 5 nm (For instance, $x = 3$ nm as shown in the present Figure). The atoms are colored according to the common neighbor analysis (CNA). The blue color atoms indicate the pure FCC Cu atoms, while cyan color atoms indicate the twin boundary atoms and the red color atoms represent surface atoms.	132
5.3	The stress-strain curves of $\langle 112 \rangle$ Cu nanopillars with and without axial twin boundaries under (a) tension (b) compression.	132
5.4	The variation of yield strength as a function of twin boundary spacing (TBS) under (a) tensile (b) compressive loading. For reference, the yield strength of perfect nanopillar has been represented as a horizontal line.	133
5.5	Variation of yield strength asymmetry in twinned nanopillar of different twin boundary spacings. For comparison, the yield strength asymmetry of perfect nanopillar has been shown as a horizontal line. Here, the yield strength asymmetry is defined as the ratio of yield stress in tension (σ_{yt}) to that in compression (σ_{yc}).	134
5.6	The deformation behaviour under the compressive loading of twinned Cu nanopillars at different strains. The glide of an extended dislocation (ED) undergoing slip transmission through multiple twin boundaries can be seen. This process involves the constriction of an extended dislocation followed by cross-slip. The atoms are colored according to the common neighbor analysis (CNA). The blue color atoms represents the FCC and the red color atoms indicate the surfaces and dislocation core.	135

5.7	The deformation behaviour under the compressive loading of twinned Cu nanopillars (a-d). Here, the extended dislocation cross-slips to the twin boundary plane by forming an intermediate stair-rod dislocation. The purple color surface represents the stacking fault and twin boundary. The green color lines indicate the Shockley partial dislocations and the magenta color line represents stair-rod dislocation.	136
5.8	The atomic configurations displaying the deformation behaviour of twinned Cu nanopillars under tensile loading. The two leading partials (LP) (a-b) interacts at the twin boundary and results in the formation of a stair-rod dislocation (b). The stair-rod dislocation (SRD) again dissociates into two trailing partials (c), which glide on the same plane as that of the leading partials but in opposite direction. The sequential glide of leading and trailing partials enclosing the stacking fault makes the deformation to proceed by extended dislocations (ED) (d). The purple color surface represents the stacking fault and twin boundary. The green color lines indicate the Shockley partial dislocations and the magenta color line represents a stair-rod dislocation.	137
5.9	The deformation mechanism under the tensile loading of twinned Cu nanopillars. The leading partial impeded by the twin boundary can be seen in (a). This partial dislocation cross-slips to the next grain leaving behind a Hirth stair-rod dislocation at the twin boundary (b). The Hirth dislocation again dissociates into two partials, which results the deformation in the nanopillar to proceed by extended dislocations (c). The perfect and surface atoms are removed for clarity. The red color atoms represents the HCP atoms (stacking fault and twin boundaries). The green color lines indicate Shockley partials and yellow color line shows Hirth stair-rod.	138
5.10	The dislocation activity at the twin boundary resulting in the formation of well organized dislocation network. The bottom line figure shows the top view of the nanopillar. For clarity, the dislocation network without the stacking fault atoms are shown in inset figures.	139
5.11	The atomic snapshots displaying the deformation behaviour of twinned $\langle 112 \rangle$ Cu nanopillars under tensile loading. The deformation behaviour in nanopillar with (a) two twins and, (b) three twins. The atoms are colored according to the common neighbor analysis (CNA). The blue color atoms represents the FCC and the red color atoms indicate the surfaces and dislocation core.	140
5.12	(a) Comparison of yield stress in twinned and twin free nanopillars with size equal to twin boundary spacing. (b) Comparison of yield stress in twinned nanopillars with that reported in other studies from the literature [83, 84, 88, 89]. For comparison, the yield stress of perfect nanopillar of size 10 nm has also been shown.	142
5.13	The schematic view showing a sequence of events in (a) Friedel-Escaig (FE) [191, 192, 193], and (b) Fleischer mechanism [194] of cross-slip. In FE mechanism, the constriction of two partials in the initial glide plane followed by re-dissociation into the cross-slip plane can be seen. In Fleischer mechanism, the leading partial and stacking fault fold over from initial glide plane to cross-slip plane, by leaving a stair-rod dislocation at the intersection.	144

5.14	(a) Cu thin film of thickness "t" oriented in [1-11], [110] and [1-1-2] axial directions containing a $1/2\langle 110 \rangle$ edge dislocation on [1-11] plane. (b) Variation of stacking fault width as a function of thin film thickness in Cu. The horizontal line shows the stacking fault width in thin film of infinite thickness.	146
5.15	(a) The stress-strain behaviour of $\langle 112 \rangle$ longitudinally twinned Cu nanopillars of single twin, with twin boundary located at with different distances (x) from the surface. (b) The variations of yield strength of twinned nanopillar of single twin as a function of twin boundary distance at various nanopillar sizes and orientation. For comparison, the yield strength of perfect nanopillar has been represented as a straight line.	147
5.16	(a,b) The atomic configurations displaying the nucleation of $1/6\langle 112 \rangle$ Shockley partial (SP) dislocations in twinned Cu nanopillars with single twin under tensile loading. The nucleation in all twinned nanopillars occurs at free surface which is far away from the twin boundary. (c) The variations of repulsive force and the yield strength of twinned nanopillars with single twin, as a function of twin boundary distance (l-x). The perfect and surface atoms were removed for better clarity. The red color atoms represents the HCP atoms (stacking fault and twin boundaries). The green color lines indicate $1/6\langle 112 \rangle$ Shockley partial (SP) dislocations.	149
6.1	The model polycrystalline Cu with a average grain size of 5.4 nm after the equilibration. The front surfaces of model system has been removed and the atoms are colored according to the common neighbor analysis (CNA)	153
6.2	Stress-strain curves for polycrystalline Cu nanowires ($10.84 \times 10.84 \times 21.69$ nm) with different average grain size in the range of 1.54-5.42 nm at 10 K. . . .	154
6.3	a The variation of yield stress and flow stress at 10% strain as a function of grain size for polycrystalline Cu nanowire at 10 K. b Yield stress variation with the inverse square root of grain size ($d^{-1/2}$) in $nm^{-1/2}$ exhibiting inverse Hall-Petch (IHP) relation.	155
6.4	Deformation behaviour of polycrystalline Cu nanowire with grain size of 3.61 nm under tensile loading. The deformation through the slip of partial dislocations can be seen at all strains. The blue color atoms represent FCC atoms, cyan color atoms represent the stacking faults and the red color atoms indicate the surfaces, grain boundaries and dislocation cores. The solid (green, white, yellow and ash) curves represent the trace of initial grain boundaries, while the dashed curves represent the traces of instantaneous grain boundaries.	156
6.5	The fivefold deformation twin observed during tensile deformation of polycrystalline Cu nanowire with a grain size of 2.16 nm. The blue color atoms represent the perfect FCC atoms, the cyan color atoms represent the twin boundaries and the red color atoms represent the grain boundary.	157
6.6	The fivefold deformation twin observed during tensile deformation of polycrystalline Cu nanowire with a grain size of 2.16 nm. The blue color atoms represent the perfect FCC atoms, the cyan color atoms represent the twin boundaries and the red color atoms represent the grain boundary.	158

6.7	a The monotonic and the cyclic stress-strain behaviour of polycrystalline Cu. The peak cyclic stress response in tension and compression with number of cycles is shown in (b)	159
6.8	The atomic snapshots showing plastic deformation at a strain level of 3 % for a 1st, b 5th and c 10th cycles. The front surface was removed for clarity. The atoms were colored according to the CNA. The red atoms represent the grain boundaries, dislocation cores and surface atoms. Blue atoms represent perfect FCC atoms and cyan atoms represent HCP atoms.	160
6.9	The percentage of disordered atoms as a function of time during cyclic deformation. The disordered atoms include the grain boundary atoms, surfaces and the dislocation core atoms. Each 100 ps is equivalent to one cycle as shown by vertical grids.	161
6.10	The variations of a dislocation density and b the percentage of stacking fault atoms as a function of time during cyclic deformation. Each 100 ps is equivalent to one cycle shown by vertical grids	162

List of Tables

1.1	Some of the important milestones in the theory of plastic deformation.	3
1.2	Schmid factors for leading m_L and trailing m_T partial dislocations under tension and compression for different orientations of various FCC systems.	23
2.1	Material properties of Cu predicted by the Mishin and co-workers [108] EAM potential in comparison with experimental data.	49
3.1	The nanowire orientations along with their side surfaces.	71
3.2	Schmid factor values for leading (m_L) and trailing (m_T) partial dislocations for some of the orientations of Cu nanowires along with the predicted and observed deformation mechanisms. The ratio of leading partial Schmid factor (m_L) to trailing partial Schmid factor (m_T) has been presented as α_M	83
4.1	The Schmid factors (m) for leading and trailing partial dislocations under the tensile loading of $\langle 110 \rangle$, $\langle 100 \rangle$ and $\langle 112 \rangle$ orientations.	116
4.2	The nanowire size and surface area to volume ratio of different shapes in Scenario-1 and Scenario-II. In scenario-I, the nanowire size has been chosen in such a way that all shapes can be inscribed in circular shape as shown in Figure 4.26. In scenario-II, nanowire size has been chosen in such a way that all the shapes have same surface area to volume ratio.	118

Contents

SUMMARY	viii
LIST OF FIGURES	xxv
LIST OF TABLES	xxvi
1 Introduction	1
1.1 Theory of plastic deformation	1
1.2 Metallic nanowires/nanopillars	4
1.3 Mechanics of materials	7
1.3.1 Dislocation slip in FCC systems	7
1.3.2 Stacking sequence, stacking fault and Shockley partials in FCC systems	9
1.3.3 Twinning in FCC systems	12
1.3.4 Schmid factor	12
1.3.5 Generalized stacking fault energy (GSFE)	14
1.4 Literature review on deformation behaviour of FCC nanowires	16
1.4.1 Orientation dependent deformation behaviour	18
1.4.2 Effect of nanowire/nanopillar size	22
1.4.3 Influence of twin boundaries on deformation behaviour	30
1.5 Objective and thesis outline	36
2 Atomistic simulation methods and pre- and post-processing techniques	40
2.1 Molecular dynamics simulations	41
2.1.1 Inter-atomic potentials	42
2.1.2 Integration algorithms	50
2.1.3 Boundary conditions	52

2.2	LAMMPS for molecular dynamics simulations	55
2.3	Pre-processing	56
2.4	Loading procedure	58
2.4.1	Procedure I:	58
2.4.2	Procedure II:	59
2.5	Post-Processing	61
2.5.1	Coordination number (CN)	62
2.5.2	Common neighbor analysis (CNA)	62
2.5.3	Central symmetry parameter (CSP)	65
2.5.4	AtomEye	66
2.5.5	Dislocation extraction algorithm (DXA)	67
3	Orientation dependent deformation behaviour of Cu nanowires under compression and tension	69
3.1	Introduction	69
3.2	MD simulation details	71
3.3	Results	72
3.3.1	Deformation behaviour under compression	72
3.3.2	Deformation behaviour under tension	75
3.3.3	Stress-strain behaviour	77
3.4	Discussion	80
3.4.1	Orientation and loading mode dependent deformation mechanisms	80
3.4.2	Tension-compression asymmetry in yield stress	83
3.5	Conclusions	85
4	Effect of shape and size on the deformation behaviour of Cu nanowires	87
4.1	Introduction	87
4.2	MD simulation details	88
4.3	Size effects in <100> Cu nanowires	91
4.3.1	Stress-strain behaviour	91
4.3.2	Yield stress and dislocation nucleation	93
4.3.3	Deformation mechanisms	95

4.3.4	Variations in dislocation density	97
4.3.5	Average length of dislocations	102
4.3.6	Dislocation-defect interactions	103
4.3.7	Ductility and failure behaviour	108
4.4	Size effects in $\langle 110 \rangle$ Cu nanowires and double reorientation	110
4.4.1	Size effects	110
4.4.2	Double reorientation	111
4.4.3	Stress-strain behaviour	116
4.5	Influence of nanowire cross section/shape	117
4.5.1	Nanowires of different shape having different surface area to volume ratio	118
4.5.2	Nanowires of different shapes having same surface area to volume ratio	120
4.5.3	Deformation mechanisms in different shapes	122
4.6	Conclusions	125
5	Role of axial twin boundaries on the deformation mechanisms in Cu nanopillars	129
5.1	Introduction	129
5.2	Computational details	130
5.3	Effect of twin boundary spacing	131
5.3.1	Stress-strain behaviour	131
5.3.2	Deformation mechanisms in perfect $\langle 112 \rangle$ Cu nanopillars	134
5.3.3	Deformation mechanisms in twinned $\langle 112 \rangle$ Cu nanopillars under compressive loading	134
5.3.4	Deformation mechanisms in twinned $\langle 112 \rangle$ Cu nanopillars under tensile loading	137
5.3.5	Yield stress in twinned nanopillars	141
5.3.6	Deformation mechanisms and cross-slip	143
5.4	Influence of twin boundary position	146
5.4.1	Stress-strain behaviour	146
5.4.2	Yield strength dependence on twin boundary position	148
5.5	Conclusions	149
6	Deformation behaviour of polycrystalline Cu under monotonic and cyclic load-	

ing	151
6.1 Introduction	151
6.2 Computational details	152
6.3 Results	153
6.3.1 Deformation behaviour under monotonic loading	153
6.3.2 Deformation behaviour under cyclic loading	158
6.4 Conclusions	162
7 Conclusions and future studies	165
7.1 Conclusions	165
7.2 Future studies	169

List of Figures

1.1	a) The schematic diagram illustrating the formation of slip bands during the deformation. Slip bands (a, b, c, d, e) occurs through sliding of elementary portions of material over one another. b). Optical micrograph of deformed polycrystalline Pb representing that deformation occurs through slip. c). Optical micrograph of deformed polycrystalline Cu representing that deformation occurs through twinning. These figures have been taken from Ewing and Rosenhain [1].	2
1.2	The variations in the ratio of surface area to volume, as a function of cubic nanoparticle diameter.	4
1.3	Cu nanowires used as fillers in stretchable electronics. (a) Top view OF SEM image of Cu nanowire network coated on glass. The inset shows a homogeneously dispersed Cu nanowire ink. (b). SEM image of Cu nanowire sizes. These figures has been taken from the reference [18].	5
1.4	A and B Cu nanowire ink dispersed on polyethylene terephthalate (PET) substrate with a Meyer rod to form a thin, uniform film . C) Highly flexible Cu films: A bent Cu nanowire film in a closed electrical circuit connected with a battery pack and a LED [21].	6
1.5	The schematic illustration of region (hatched) within a slip plane has been displaced relative to the other. Burgers vector, b represents the magnitude and direction of the displacement.	8
1.6	The schematic illustration of slip systems in FCC crystals. Four $\{111\}$ slip planes with three $\langle 110 \rangle$ slip directions lying on the slip planes constitute the 12 slip systems in FCC crystals.	9
1.7	The atomic arrangement in close packed manner for FCC and HCP structures. Arrangement of A and B layer of atoms is common in both FCC and HCP systems. However, the third layer (either A or C) is different for FCC and HCP systems. This figure has been taken from Ref. [34].	10
1.8	a) The atomic arrangement in FCC system (normal to $\{111\}$ plane). The possible slip path are through either glide of dislocation, b_1 or sequential glide of b_2 and b_3 . b) The disassociation of perfect to Shockley partials with associated stacking fault.	11

1.9	Twinning in FCC systems. Twinning occurs on $\{111\}$ planes along $\langle 112 \rangle$ directions. The shaded region indicates the instantaneous atomic positions during deformation. The atomic displacement has been indicated by arrow symbols along the twin directions [36].	13
1.10	Schematic illustration of calculation of shear stress in a single crystalline cylindrical specimen under tensile force	14
1.11	a). Atomic transition during glide of 111 plane along $\langle 112 \rangle$ direction. b). GSFE curve during the atomic transition in FCC crystals. Displacements C, C' and A corresponds to the lattice position shown in a.	15
1.12	Snapshots illustrating the operating deformation mechanisms in $\langle 001 \rangle$ Al nanopillar under compression. a) glide of partial dislocations and associated stacking faults , b) formation of nano-twins and c) twins. These figures has been taken from Ref. [42]	17
1.13	The atomic configuration of $\langle 112 \rangle$ Al nanopillar under compression. a) Full dislocations nucleate separately along the $(\bar{1}\bar{1}\bar{1})$ and $(1\bar{1}\bar{1})$ slip planes, and b) full dislocations interacting with each other.	17
1.14	The atomic snapshots of phase transformation of Au nanowires from FCC lattice to BCT lattice. These figures has been taken from Ref. [47]	18
1.15	Deformation behaviour of $\langle 110 \rangle$ Au nanopillars under compression and tension [38]. a) TEM images and MD simulations showing the nucleation of dislocation loops and subsequent slip under compression [38]. b) The sequential TEM images revealing the domination of twinning under tension [38]. The orange arrows in (b) show the slip steps, while the yellow arrow show half dislocation loops.	20
1.16	The atomic snapshots of $\langle 110 \rangle$ Cu nanowires under tension [27]. The operating deformation mechanism, deformation twinning reorients Cu nanowires from $\langle 110 \rangle$ to $\langle 100 \rangle$ orientation.	21
1.17	Deformation behaviour in Cu nanowires [28]. In Cu $\langle 111 \rangle$ nanowires, deformation proceeds through a) slip through perfect/full dislocations under compression [40], and b) slip through partial dislocations under tension. c) under similar tensile conditions, deformation through twinning in $\langle 110 \rangle$ Cu nanowires.	22
1.18	Compressive yield stress of Cu(100) pillars with varying sample diameters in the range 90 nm to 1700 nm. Also, change in operating deformation morphology with varying size. Different deformation regimes has been indicated with differently colored bars [56]. The insets represents the compressed Cu pillars	23
1.19	Sample size dependence of two deformation mechanisms: Slip through partial dislocations and full dislocations. Relative contribution of both deformation mechanisms for pure Cu nanowires at various sizes. The transition can be seen at $D = 150$ nm [50].	25
1.20	Pseudo-elasticity in single crystalline Cu nanowires [22].	26

1.21	Operating defromations of FCC metallic nanowires under different axial loading conditions. In partial slip region: $\tau_1 < \tau_2$ and $\tau_1 < 1$. In full slip region, $\tau_2 < \tau_1$, and $\tau_2 < 1$. In twin region: $\tau_1 > 1$ and $\tau_2 > 1$. Open symbols represents the loading conditions of $\langle 100 \rangle$ tension, $\langle 110 \rangle$ compression and $\langle 111 \rangle$ compression. Filled symbols represents the loading condition of $\langle 100 \rangle$ compression, $\langle 110 \rangle$ tension and $\langle 111 \rangle$ tension[28].	28
1.22	Size effect on the tensile yield strength of pentagonal, rhombic, cated-rhombic silver nanowires[73].	29
1.23	Influence of cross-scetional geometry on deformation behaviour of $\langle 110 \rangle$ Ag nanowires. a). Cross-scetional geometry of Ag nanowires. b) Reoriented $\langle 001 \rangle$ Ag nanowire with 110 and 001 Ag nanowires. c) Countour map explaining transition of deformation from twinning to dislocation slip for varying cross-sectional Open black squares refers to twinning-dominated mode, and open red circles indicates that deformation dominated by dislocation slip[74].	29
1.24	Shape dependent strengthening behaviour in twinned nanowires. Nanowires with a) square b) circular shaped nanowires. c) yield strength variation with twin boundary spacing for circular and square shaped nanowires [81].	30
1.25	Mechanical behaviour of Cu nanowires. a) yield strength variation with twin boundary spacing for nanowires of different lengths. b) ductile to brittle transition with increasing twin boundary spacing [83].	31
1.26	Operating deformation mechanisms in twinned Au nanowires [89]. a) Model twinned nanowires with orthogonal and slanted twin boundaries. deformation proceeded through b) discrete twin boundary -dislocation interactions in longitudinally twinned nanopillars, and c) de-twinning in slanted twin boundaries [89].	32
1.27	a) A model nanocrystalline copper with an average grain diameter of 5.2 nm. Grain boundary atoms are colored blue, while stacking fault atoms are colored red. b) true stress-strain behaviour of nanocrystalline Cu for different grain sizes/diameter. c) variations of flow stress and yield stress with grain size [96].	34
1.28	Operating deformation twinning process. a) Glide of partial dislocation enclosing stacking fault in the interior of grain. b) twin growth by a single lattice plane. c) before straining and d) after 18.1% applied strain. The plastic deformation induced extensive grain growth. The average grain size is 6 nm [97]. Two coarsened and elongated grains are marked with asterisks. All atoms are colored according to CNA. Green colored atoms represent pure FCC Ni, while red colored atoms represents stacking fault atoms and ash colored atoms represent grain boundary atoms.	34
1.29	Statistical distribution explaining the operating deformation mechanism as a function of grain size d for nanocrystalline Pt [98]. At larger grains, deformation through full dislocations denoted by square symbol. For $6 < d < 10$ nm partial dislocations enclosing stacking faults denoted by dots were observed, and for $d < 6$ nm, the grain boundaries dominate the plasticity, indicated by black triangles.	35

2.1	Flowchart explaining the molecular dynamics (MD) simulation methodology	42
2.2	LJ potential illustrating the attractive and repulsive terms	45
2.3	A model three dimensional system with periodic boundary conditions along three directions. Red colored region represents the original simulation cell and all blue colored cells are the exact replicas of red colored simulation cell.	53
2.4	Boundary conditions applied for generating different models. a) Bulk material model, b) thin film model, c) nanowire model d) nanopillar model.	55
2.5	a) Tinkercad, an open source online platform for modeling nanowire shapes [127]. b) A model polycrystal nanowire prepared using Voronoi algorithm from AtomEye software[129, 131]	57
2.6	Testing procedure I: The original dimensions of simulation cell represented by dotted lines as L_x , L_y , and L_z . The instantaneous simulation cell dimensions during loading is shown by continuous line $L(t)_x$, $L(t)_y$, and $L(t)_z$	59
2.7	Procedure II: Bottom end of nanowires has been hold constant and the top end has been elongated at a constant velocity. Velocity profile vs position in correspondence to the simulation cell.	60
2.8	CNA for a) FCC b) HCP, and c-d) BCC systems with different indexes according to Honeycutt and Anderson [141].	63
2.9	A model nanowires visualized using CNA parameter. The blue color atoms represents the perfect FCC atoms, cyan color atoms represents HCP atoms (both stacking faults in FCC and twin boundaries), while the red color atoms indicate the free surfaces and dislocation core.	64
2.10	Colored opposite pairs in a) FCC, and b) BCC structures.	66
2.11	DXA methodology illustrating the interface mesh sweeping the dislocation line. While the Burgers circuit is being advanced in a step-wise fashion, triangle by triangle, a continuous line representation of the dislocation defect is produced.	68
3.1	Standard stereographic triangle with various crystallographic orientations chosen in the present study. Cu nanowires with these orientations have been subjected to tensile and compressive loading.	70
3.2	Atomic snapshots displaying (a) nucleation of a Shockley partial, (b) glide of twinning partial and nano-twin, (c-d) twin growth (e) reoriented nanowire, and (f) the slip of extended dislocation in the reoriented nanowire during the compressive deformation of $\langle 100 \rangle$ Cu nanowires. In Figure (d), the partial dislocations are shown as green lines as obtained in OVITO [130], while the remaining figures are obtained using AtomEye. The atoms are colored according to the common neighbor analysis (CNA). The blue color atoms represents the FCC and the red color atoms indicate the surfaces and dislocation core.	73

3.3	Atomic snapshots displaying the compressive deformation of $\langle 111 \rangle$ Cu nanowires as a function of strain. The deformation by the slip of extended dislocations along with stacking fault tetrahedron and many point defects can be seen in (b), (c) and (d). Figure (d) is the OVITO [130] output of Figure (c), where partial dislocations are shown as green lines, the stair-rod dislocations enclosing the stacking fault tetrahedron are shown in magenta lines. The atoms are colored according to the common neighbor analysis (CNA).	74
3.4	Atomic snapshots displaying the compressive deformation of $\langle 214 \rangle$ Cu nanowires as a function of strain. The deformation proceeds through the glide of extended dislocations. The atoms are colored according to the common neighbor analysis (CNA).	75
3.5	The atomic snapshots displaying the tensile deformation of $\langle 110 \rangle$ Cu nanowires as a function of strain. Deformation proceeds through twinning followed by reorientation to $\langle 100 \rangle$ axial direction.	76
3.6	The atomic snapshots during the tensile deformation of $\langle 214 \rangle$ Cu nanowires as a function of strain. Deformation proceeds through twinning mechanism followed by reorientation to high index $\langle hkl \rangle$ direction. The final failure occurs by sliding along the twin boundaries.	77
3.7	Atomic snapshots presenting the deformation and failure behaviour of $\langle 100 \rangle$ and $\langle 102 \rangle$ Cu nanowires under tensile loading. The twin-twin interactions and the twin boundary sliding disrupting the reorientation process can be seen in both the orientations.	78
3.8	The stress-strain behaviour of Cu nanowires deforming by (a) twinning and (b) full dislocation slip under compressive loading of different orientations at 10 K.	79
3.9	The stress-strain behaviour of Cu nanowires deforming by twinning (a) with reorientation and (b) without reorientation under tensile loading at 10 K.	79
3.10	The variation of yield stress with respect to orientation presented on the standard stereographic triangle under (a) compressive loading, and (b) tensile loading of Cu nanowires. The yield stress values are in GPa.	80
3.11	The standard stereographic triangle showing two different regions, one with $\alpha_M > 1$ (red color) and other with $\alpha_M < 1$ (light blue) under (a) compressive loading and (b) tensile loading. The black solid line between red and blue colors represent a boundary with $\alpha_M = 1$. The parameter, α_M is defined as the ratio of Schmid factors of leading and trailing partial dislocations.	82
3.12	The values of (a) yield stress asymmetry (b) Schmid factor asymmetry shown on the standard stereographic triangle for different orientations of Cu nanowires. Yield stress asymmetry is defined as the ratio of yield stress in tension to that in compression (T/C), while the Schmid factor asymmetry is defined as the ratio of leading partial Schmid factor in compression to that in tension (C/T).	84

4.1	Square shaped nanowires of fixed length of 21.69 nm with varying square cross-sections width (d) of 10.48 nm. The cross-sections width (d) of nanowires has been varied in the range 0.723-43.38 nm.	89
4.2	The nanowires cross-section shapes considered in the present study. (a) Triangular, (b) square, (c) pentagonal, (d) hexagonal, and (e) circular, with their corresponding side surfaces.	90
4.3	Stress-strain curves for $\langle 100 \rangle$ Cu nanowires with constant length of 21.69 nm at different cross section width (d) in the range 0.723-43.38 nm at 10 K. For clarity of elastic deformation, the magnified figure at small strains is shown in inset.	92
4.4	The variation of Young's modulus as a function of cross section width (d) for $\langle 100 \rangle$ Cu nanowires at 10 K.	92
4.5	Variation of yield strength as a function of cross section width (d) for $\langle 100 \rangle$ Cu nanowires at 10 K. For comparison, the results from other MD simulations on $\langle 100 \rangle$ Cu nanowires [164, 165] are superimposed.	93
4.6	The variation of initial stress as a function of cross section width (d) for $\langle 100 \rangle$ Cu nanowires at 10 K.	94
4.7	Yielding by the nucleation of $1/6\langle 112 \rangle$ Shockley partial dislocations in $\langle 100 \rangle$ Cu nanowires of different cross section width (d) in the range 0.723-43.38 nm at 10 K. (a) d = 0.723 nm (b) d = 1.446 nm (c) d = 2.169 nm (d) d = 3.615 nm (e) d = 10.845 nm (f) d = 43.380 nm. With increasing size, the increase in defect nucleation sites can be seen. The blue color atoms represent the stacking faults and the red color atoms indicate the surfaces and dislocation core. The perfect FCC atoms were removed for clarity.	95
4.8	Deformation behaviour in small size $\langle 100 \rangle$ Cu nanowires with cross section width (d) = 3.615 nm under tensile loading. The deformation occurring by slip of partial dislocations can be seen at all strains. The blue color atoms represent the stacking faults and the red color atoms indicate the surfaces and dislocation core. The perfect FCC atoms were removed for clarity.	96
4.9	Deformation behaviour in large size $\langle 100 \rangle$ Cu nanowires with cross section width (d) = 20.69 nm under tensile loading. In addition to partial dislocation slip at small strains, deformation dominated by slip of extended dislocations can be seen at high strains. The white arrow indicates the extended dislocations. The blue color atoms represent the stacking faults and the red color atoms indicate the surfaces and dislocation core. The perfect FCC atoms were removed for clarity.	97
4.10	Variation of dislocation density, dislocation microstructure and flow stress as a function of strain for Cu nanowire with d = 21.69 nm under tensile loading at 10 K. In the inset snapshots, the green color lines show the $1/6\langle 112 \rangle$ Shockley partial dislocations and the magenta lines represent the L-C dislocations having Burgers vector $1/6\langle 110 \rangle$. The thick black dots represent the point defects. The snapshots of the nanowire shown in inset figures were obtained in OVITO [130].	98

4.11	(a) Variations in dislocation density as a function of strain (or time) for nanowires of different size deformed at a constant strain rate of $1 \times 10^9 \text{ s}^{-1}$ and temperature of 10 K. (b) The variations in rate of dislocation exhaustion with respect to nanowire size.	100
4.12	(a) Variations in dislocation density as a function of strain (or time) at different temperatures for a nanowire of size (d) = 10.85 nm deformed at a constant strain rate of $1 \times 10^9 \text{ s}^{-1}$. (b) The variations in dislocation exhaustion rates as a function of temperature.	101
4.13	(a) Variations in dislocation density as a function of strain at different strain rates for a nanowire of size (d) = 10.85 nm deformed at 10 K. (b) The variations in dislocation exhaustion rate as a function of strain rates.	102
4.14	The variation of average length of dislocations as a function of strain in $\langle 100 \rangle$ Cu nanowires with different cross section width.	103
4.15	Dislocation-stacking fault interactions leading to annihilation of stacking faults in Cu nanowire with d = 20.69 nm. The green color lines show $1/6 \langle 112 \rangle$ Shockley partial dislocations and black lines display $1/3 \langle 110 \rangle$ stair-rod dislocations.	104
4.16	The interaction of a leading partial dislocation with the surface in large size nanowires. The annihilation of leading partial at the surface gives rise to the nucleation of a new trailing partial dislocation.	105
4.17	Interaction of a leading partial dislocation with surface in small size nanowires. The partial dislocation reflects multiple times from the nanowire surface.	106
4.18	Dislocation-dislocation interactions leading to the formation of L-C lock at acute junction and Hirth lock at obtuse junction of $\{111\}$ planes in $\langle 100 \rangle$ Cu nanowires. The green lines indicate Shockley partials, magenta color lines represent L-C dislocations and blue color lines show Hirth dislocation.	107
4.19	The interaction of Shockley partial dislocation with L-C dislocation leading to the formation of Frank partial. The green lines indicate Shockley partials, magenta color lines represent L-C dislocations and cyan color lines show Frank partials.	108
4.20	Variation of strain to failure or ductility as a function of cross section width (d) for $\langle 100 \rangle$ Cu nanowires at 10 K.	109
4.21	Failure behaviour in (a) the smallest size (d = 0.723 nm) (b) intermediate size (d = 10.845 nm) (c) large size (d = 21.69 nm) $\langle 100 \rangle$ Cu nanowire during tensile deformation at 10 K. The formation of pentagonal atomic chain in the necking region of the smallest size nanowire can be seen in a.	110
4.22	The double or sequential reorientation of $\langle 110 \rangle$ Cu nanowire of cross section width (d) and length (l) = 7.15 nm (aspect ratio 1) under tensile loading. The double reorientation changes the cross section shape from square to rhombus and then rhombus to parallelogram. The atoms are colored according to their coordination number.	112

4.23	Detailed deformation mechanisms responsible for double reorientation from $\langle 110 \rangle$ tensile axis to $\langle 100 \rangle$ axis and then $\langle 100 \rangle$ axis to $\langle 112 \rangle$ axis in Cu nanowire. The blue color represents the FCC atoms, cyan color atoms represent the stacking faults and twin boundaries and the red color atoms indicate the surfaces and dislocation core. The atoms color has been assigned according the common neighbor analysis (CNA).	113
4.24	Absence of reorientation during the tensile deformation of $\langle 110 \rangle$ Cu nanowire of cross section width (d) = 7.15 nm and length (l) = 14.3 nm (aspect ratio 2). The blue color represents the FCC atoms, cyan color atoms represent the stacking faults and twin boundaries and the red color atoms indicate the surfaces and dislocation core. The atoms color has been assigned according the common neighbor analysis (CNA).	115
4.25	Stress-strain behaviour of $\langle 110 \rangle$ Cu nanowire with constant cross section width (d) = 7.15 nm and different length (l) of 7.15 nm (aspect ratio = 1) and 14.31 nm (aspect ratio = 2). Nanowire undergoing double reorientation (aspect ratio = 1) show three elastic peaks (shown by arrows) separated by twin growth regimes.	117
4.26	A method showing the inscription all the shapes within the circular shape. In the first scenario, the size for different shapes is chosen in such a way that all shapes can be inscribed in circular nanowire of radius 'r'. $a_T, a_S, a_P,$ and a_H represents the side length of triangular, square, pentagonal and hexagonal shaped nanowires.	118
4.27	Stress-strain behaviour of $\langle 100 \rangle$ Cu nanowires of different shape in Scenario-1, where each shape has a different surface area to volume ratio. The stress-strain behaviour till strain of 20 % has been shown in inset for better clarity.	119
4.28	Variation of yield strength along with surface area to volume ratio for different nanowire shapes in Scenario-1.	120
4.29	Stress-strain behaviour of $\langle 100 \rangle$ Cu nanowires of different shape in Scenario-2, where all the shapes have same surface area to volume ratio. The stress-strain behaviour till strain of 20 % has been shown in inset for better clarity.	121
4.30	Variation of yield strength and potential energy for different nanowire shapes in Scenario-2.	122
4.31	The dislocation nucleation during the yielding/beginning of plastic deformation in nanowires of different shapes. This nucleation mechanism remains the same for both scenarios. The white arrows indicates the direction of dislocation motion. The nucleation occurs from the intersection of two different side surfaces.	123
4.32	The deformation mechanisms observed in nanowires of different shapes, each shown at different strain value. The yellow arrows indicate the direction of twin boundaries movement. The white arrows indicate the direction of glide of Shockley partial dislocations on $\{111\}$ planes.	123

4.33	The schematic showing the orientation of initial (top row) and twinned side surfaces for (a) triangular, (b) square and, (c) hexagonal shaped nanowires. In pentagonal and circular nanowires, even though the deformation twinning has been observed, but we are not able to identify the new surface orientations due to high roughness.	124
4.34	The final failure behaviour of nanowires of different shapes. The encircled regions indicate the initiation of necking and black arrows shows failed region.	125
5.1	The model system of (a) perfect Cu nanopillar and twinned Cu nanopillars with (b) one (c) two (d) three and, (e) four, equidistant twins. The double Thompson tetrahedron illustrating the slip planes and directions is shown in (f). The crystallographic orientation and twin boundary spacing has been shown for clarity. The cross-section width (d) of all the nanowires is 10 nm. In (a)-(e), The front surfaces are removed and the atoms are colored according to the common neighbor analysis (CNA).	131
5.2	The atomic configuration of twinned nanopillar with varied twin boundary position. Twin boundary position has been modified by changing twin distance (x) from surface in the range 1 nm to 5 nm (For instance, $x = 3$ nm as shown in the present Figure). The atoms are colored according to the common neighbor analysis (CNA). The blue color atoms indicate the pure FCC Cu atoms, while cyan color atoms indicate the twin boundary atoms and the red color atoms represent surface atoms.	132
5.3	The stress-strain curves of $\langle 112 \rangle$ Cu nanopillars with and without axial twin boundaries under (a) tension (b) compression.	132
5.4	The variation of yield strength as a function of twin boundary spacing (TBS) under (a) tensile (b) compressive loading. For reference, the yield strength of perfect nanopillar has been represented as a horizontal line.	133
5.5	Variation of yield strength asymmetry in twinned nanopillar of different twin boundary spacings. For comparison, the yield strength asymmetry of perfect nanopillar has been shown as a horizontal line. Here, the yield strength asymmetry is defined as the ratio of yield stress in tension (σ_{yt}) to that in compression (σ_{yc}).	134
5.6	The deformation behaviour under the compressive loading of twinned Cu nanopillars at different strains. The glide of an extended dislocation (ED) undergoing slip transmission through multiple twin boundaries can be seen. This process involves the constriction of an extended dislocation followed by cross-slip. The atoms are colored according to the common neighbor analysis (CNA). The blue color atoms represents the FCC and the red color atoms indicate the surfaces and dislocation core.	135

5.7	The deformation behaviour under the compressive loading of twinned Cu nanopillars (a-d). Here, the extended dislocation cross-slips to the twin boundary plane by forming an intermediate stair-rod dislocation. The purple color surface represents the stacking fault and twin boundary. The green color lines indicate the Shockley partial dislocations and the magenta color line represents stair-rod dislocation.	136
5.8	The atomic configurations displaying the deformation behaviour of twinned Cu nanopillars under tensile loading. The two leading partials (LP) (a-b) interacts at the twin boundary and results in the formation of a stair-rod dislocation (b). The stair-rod dislocation (SRD) again dissociates into two trailing partials (c), which glide on the same plane as that of the leading partials but in opposite direction. The sequential glide of leading and trailing partials enclosing the stacking fault makes the deformation to proceed by extended dislocations (ED) (d). The purple color surface represents the stacking fault and twin boundary. The green color lines indicate the Shockley partial dislocations and the magenta color line represents a stair-rod dislocation.	137
5.9	The deformation mechanism under the tensile loading of twinned Cu nanopillars. The leading partial impeded by the twin boundary can be seen in (a). This partial dislocation cross-slips to the next grain leaving behind a Hirth stair-rod dislocation at the twin boundary (b). The Hirth dislocation again dissociates into two partials, which results the deformation in the nanopillar to proceed by extended dislocations (c). The perfect and surface atoms are removed for clarity. The red color atoms represents the HCP atoms (stacking fault and twin boundaries). The green color lines indicate Shockley partials and yellow color line shows Hirth stair-rod.	138
5.10	The dislocation activity at the twin boundary resulting in the formation of well organized dislocation network. The bottom line figure shows the top view of the nanopillar. For clarity, the dislocation network without the stacking fault atoms are shown in inset figures.	139
5.11	The atomic snapshots displaying the deformation behaviour of twinned $\langle 112 \rangle$ Cu nanopillars under tensile loading. The deformation behaviour in nanopillar with (a) two twins and, (b) three twins. The atoms are colored according to the common neighbor analysis (CNA). The blue color atoms represents the FCC and the red color atoms indicate the surfaces and dislocation core.	140
5.12	(a) Comparison of yield stress in twinned and twin free nanopillars with size equal to twin boundary spacing. (b) Comparison of yield stress in twinned nanopillars with that reported in other studies from the literature [83, 84, 88, 89]. For comparison, the yield stress of perfect nanopillar of size 10 nm has also been shown.	142
5.13	The schematic view showing a sequence of events in (a) Friedel-Escaig (FE) [191, 192, 193], and (b) Fleischer mechanism [194] of cross-slip. In FE mechanism, the constriction of two partials in the initial glide plane followed by re-dissociation into the cross-slip plane can be seen. In Fleischer mechanism, the leading partial and stacking fault fold over from initial glide plane to cross-slip plane, by leaving a stair-rod dislocation at the intersection.	144

5.14	(a) Cu thin film of thickness "t" oriented in [1-11], [110] and [1-1-2] axial directions containing a $1/2\langle 110 \rangle$ edge dislocation on [1-11] plane. (b) Variation of stacking fault width as a function of thin film thickness in Cu. The horizontal line shows the stacking fault width in thin film of infinite thickness.	146
5.15	(a) The stress-strain behaviour of $\langle 112 \rangle$ longitudinally twinned Cu nanopillars of single twin, with twin boundary located at with different distances (x) from the surface. (b) The variations of yield strength of twinned nanopillar of single twin as a function of twin boundary distance at various nanopillar sizes and orientation. For comparison, the yield strength of perfect nanopillar has been represented as a straight line.	147
5.16	(a,b) The atomic configurations displaying the nucleation of $1/6\langle 112 \rangle$ Shockley partial (SP) dislocations in twinned Cu nanopillars with single twin under tensile loading. The nucleation in all twinned nanopillars occurs at free surface which is far away from the twin boundary. (c) The variations of repulsive force and the yield strength of twinned nanopillars with single twin, as a function of twin boundary distance (l-x). The perfect and surface atoms were removed for better clarity. The red color atoms represents the HCP atoms (stacking fault and twin boundaries). The green color lines indicate $1/6\langle 112 \rangle$ Shockley partial (SP) dislocations.	149
6.1	The model polycrystalline Cu with a average grain size of 5.4 nm after the equilibration. The front surfaces of model system has been removed and the atoms are colored according to the common neighbor analysis (CNA)	153
6.2	Stress-strain curves for polycrystalline Cu nanowires ($10.84 \times 10.84 \times 21.69$ nm) with different average grain size in the range of 1.54-5.42 nm at 10 K. . . .	154
6.3	a The variation of yield stress and flow stress at 10% strain as a function of grain size for polycrystalline Cu nanowire at 10 K. b Yield stress variation with the inverse square root of grain size ($d^{-1/2}$) in $nm^{-1/2}$ exhibiting inverse Hall-Petch (IHP) relation.	155
6.4	Deformation behaviour of polycrystalline Cu nanowire with grain size of 3.61 nm under tensile loading. The deformation through the slip of partial dislocations can be seen at all strains. The blue color atoms represent FCC atoms, cyan color atoms represent the stacking faults and the red color atoms indicate the surfaces, grain boundaries and dislocation cores. The solid (green, white, yellow and ash) curves represent the trace of initial grain boundaries, while the dashed curves represent the traces of instantaneous grain boundaries.	156
6.5	The fivefold deformation twin observed during tensile deformation of polycrystalline Cu nanowire with a grain size of 2.16 nm. The blue color atoms represent the perfect FCC atoms, the cyan color atoms represent the twin boundaries and the red color atoms represent the grain boundary.	157
6.6	The fivefold deformation twin observed during tensile deformation of polycrystalline Cu nanowire with a grain size of 2.16 nm. The blue color atoms represent the perfect FCC atoms, the cyan color atoms represent the twin boundaries and the red color atoms represent the grain boundary.	158

6.7	a The monotonic and the cyclic stress-strain behaviour of polycrystalline Cu. The peak cyclic stress response in tension and compression with number of cycles is shown in (b)	159
6.8	The atomic snapshots showing plastic deformation at a strain level of 3 % for a 1st, b 5th and c 10th cycles. The front surface was removed for clarity. The atoms were colored according to the CNA. The red atoms represent the grain boundaries, dislocation cores and surface atoms. Blue atoms represent perfect FCC atoms and cyan atoms represent HCP atoms.	160
6.9	The percentage of disordered atoms as a function of time during cyclic deformation. The disordered atoms include the grain boundary atoms, surfaces and the dislocation core atoms. Each 100 ps is equivalent to one cycle as shown by vertical grids.	161
6.10	The variations of a dislocation density and b the percentage of stacking fault atoms as a function of time during cyclic deformation. Each 100 ps is equivalent to one cycle shown by vertical grids	162

List of Tables

1.1	Some of the important milestones in the theory of plastic deformation.	3
1.2	Schmid factors for leading m_L and trailing m_T partial dislocations under tension and compression for different orientations of various FCC systems.	23
2.1	Material properties of Cu predicted by the Mishin and co-workers [108] EAM potential in comparison with experimental data.	49
3.1	The nanowire orientations along with their side surfaces.	71
3.2	Schmid factor values for leading (m_L) and trailing (m_T) partial dislocations for some of the orientations of Cu nanowires along with the predicted and observed deformation mechanisms. The ratio of leading partial Schmid factor (m_L) to trailing partial Schmid factor (m_T) has been presented as α_M	83
4.1	The Schmid factors (m) for leading and trailing partial dislocations under the tensile loading of $\langle 110 \rangle$, $\langle 100 \rangle$ and $\langle 112 \rangle$ orientations.	116
4.2	The nanowire size and surface area to volume ratio of different shapes in Scenario-1 and Scenario-II. In scenario-I, the nanowire size has been chosen in such a way that all shapes can be inscribed in circular shape as shown in Figure 4.26. In scenario-II, nanowire size has been chosen in such a way that all the shapes have same surface area to volume ratio.	118

Chapter 7

Conclusions and future studies

In the present thesis, molecular dynamics simulations had been performed to understand the deformation behaviour of FCC single, and polycrystalline Cu nanowires under the influence of orientation, mode of loading (tension/compression), nanowire size, cross sectional shape, and presence of twin boundaries. Also, the deformation behaviour of polycrystalline Cu under monotonic and cyclic loading conditions has been investigated. The important findings of the present study are described in the following:

7.1 Conclusions

Influence of orientation and mode of loading: Molecular dynamics simulation results have been performed to understand the deformation mechanisms in Cu nanowires under the influence of crystallographic orientation and mode of loading. Under compression, orientations close to $\langle 100 \rangle$ corner of a standard stereographic triangle i.e. $\langle 100 \rangle$, $\langle 103 \rangle$ and $\langle 113 \rangle$ orientations deformed by twinning, while the remaining orientations through full dislocation slip. On the other hand, all orientations deformed by twinning mechanism under tension. Further, the orientations close to $\langle 110 \rangle$ and $\langle 111 \rangle$ corners exhibited asymmetry in deformation mechanisms in terms of full dislocation slip under compression and twinning under tension. The tension-compression asymmetry in deformation mechanisms has been explained based on the parameter α_M , defined as the ratio of Schmid factors for leading and trailing partial dislocations. For the nanowire orientations falling in the region with $\alpha_M > 1$, the deformation by

twinning is preferred, while full dislocation slip is observed for the orientations falling in the region with $\alpha_M < 1$. For the orientations falling on the boundary line with $\alpha_M = 1$, both the mechanisms are equally probable. However, the exception is being the $\langle 100 \rangle$, $\langle 103 \rangle$ and $\langle 113 \rangle$ orientations under tensile loading, where twinning has been observed under tension and compression.

It has also been observed that the Cu nanowires display tension-compression asymmetry in yield stress. The orientations close to $\langle 001 \rangle$ corner exhibit higher yield stress in tension than in compression, while higher yield stress in compression than in tension has been observed in orientations close to $\langle 110 \rangle$ and $\langle 111 \rangle$ corners. Interestingly, for the specific orientation of $\langle 102 \rangle$, the values of yield stress under tensile and compressive loading were found to be same, thus indicating the absence of yield stress asymmetry in $\langle 102 \rangle$ Cu nanowire. Irrespective of loading mode, the $\langle 111 \rangle$ oriented Cu nanowires displayed the highest yield stress among all the orientations investigated. The asymmetry in yield values has been attributed to the different Schmid factor values for leading partial dislocations under tension and compression.

Influence of size and shape: MD simulations have been performed to understand the influence of size and shape in $\langle 100 \rangle$ and $\langle 110 \rangle$ Cu nanowires. The yielding in all $\langle 100 \rangle$ Cu nanowires occurred by the nucleation of $1/6\langle 112 \rangle$ Shockley partial dislocations and the number of dislocations nucleated during yielding increased with increasing nanowire size. The plastic deformation in small size nanowires occurred mainly by slip of partial dislocations at all strains, while in large size nanowires, slip of partial dislocations at low strains followed by slip of extended dislocation at high strains were observed.

Young's modulus and yield strength values decreased rapidly in small size nanowires followed by gradual decrease approaching towards saturation at larger size. The size dependence of yield strength has been explained in terms of initial stress and the number of dislocations nucleated during yielding. The failure strain has been found to increase linearly with increase in nanowire size and this has been correlated with higher pre- and post-necking deformation in large size nanowires. Further, formation of pentagonal atomic chains has been observed in small size nanowires with $d \leq 1.446$ nm. During plastic deformation, $\langle 100 \rangle$ nanowires with $d \geq 3.615$ nm exhibited initial dislocation exhaustion at small strains followed by dislocation starvation at high strains. Further, the rate of dislocation exhaustion increases with decrease in nanowire size. On the other hand, the nanowires with $d < 3.615$ nm show mainly dislocation

starvation at all strains. The large size nanowires show lower exhaustion rates as compared to smaller ones, i.e., resident time of dislocations within the nanowire increases with increasing size. In a nanowire of particular size, the dislocation exhaustion rates increases with increasing temperature and strain rate. Correspondingly, the transition strain decreases with increasing temperature and decreasing strain rate. In large size $\langle 100 \rangle$ Cu nanowires, the leading partial annihilation at the surface gives rise to the nucleation of a new trailing partial dislocation, while in small size nanowires, it gives rises to multiple reflections from the nanowire surface.

In $\langle 110 \rangle$ Cu nanowires with aspect ratio ≤ 1 display double reorientation during tensile deformation. It has been observed that the original $\langle 110 \rangle$ as well as reoriented $\langle 100 \rangle$ and $\langle 112 \rangle$ Cu nanowires deform by twinning mechanism facilitating double reorientation from $\langle 110 \rangle$ to $\langle 100 \rangle$ and from $\langle 100 \rangle$ to $\langle 112 \rangle$ orientations. The deformation by twinning in $\langle 110 \rangle$ and $\langle 112 \rangle$ orientations has been explained using the Schmid factor analysis, while twinning in $\langle 100 \rangle$ orientation has been ascribed to the minimization of surface energy. The occurrence of double reorientation leads to high tensile ductility in $\langle 110 \rangle$ Cu nanowires with aspect ratio ≤ 1 . The reorientation process has not been observed in $\langle 110 \rangle$ Cu nanowires with aspect ratio higher than 1. The absence of reorientation in nanowires with high aspect ratio results from the activation of multiple twin systems facilitating twin-twin interactions leading to significantly lower tensile ductility.

Young's modulus is insensitive to the nanowire shape. The yield strength increases with increasing number of side surfaces. The triangular nanowire shows the lowest strength and ductility (failure strain), while the circular nanowire display highest strength combined with good ductility. In all nanowires, irrespective of their shape and surface area to volume ratio, the deformation is dominated by the slip through Shockley partial dislocations and deformation twinning. The deformation twinning changed the orientation of side surfaces at the twinned region, whose orientation is different for different shapes. Finally nanowires of all shapes fail in a ductile manner.

Influence of twin boundaries: The simulation results indicated that the presence of twin boundaries strengthens the nanopillars. The yield strength in longitudinally or axial twinned nanopillars increases with decreasing twin boundary spacing. This strengthening in twinned nanopillars has been attributed to both repulsive force offered by twin boundaries on dislocations and stress redistribution in individual twinned regions. Further, twin boundary positions

also influences the yield strength of nanopillars irrespective of the nanopillar size and crystallographic orientation, i.e., with increasing the distance (x) of twin boundary from the free surface, the yield strength of twinned nanopillars increases. This increase in yield strength is due to the variations in the repulsive force which in-turn varies with twin boundary position (x).

In addition to strength, the presence of twin boundaries also changes the operative deformation mechanisms as compared to perfect nanopillars. Under compressive loading, the deformation in $\langle 112 \rangle$ perfect as well as twinned nanopillars is dominated by the slip of extended dislocations. Further, the presence of twin boundaries under compressive loading introduces extensive cross-slip activity from one grain the other and also onto the twin boundary plane. This cross-slip activity under compressive loading occurs through two different mechanisms namely Friedel-Escaig mechanism and Fleischer mechanism. However, no cross-slip activity has been noticed in perfect nanopillars.

On the other hand, under tensile loading, the deformation in perfect nanopillars occurs by partial dislocation slip/twinning, which changes to extended dislocation activity following the introduction of twin boundaries. This change in twinned nanopillars is due to the formation and dissociation of a stair-rod dislocation on the twin boundary. This stair-rod dislocation, which forms through the interaction of two leading partials at the twin boundary, dissociates into two trailing partials gliding on the same plane as that of the leading partials, thus constituting an extended dislocation slip. This extended dislocations under tensile loading also exhibit cross-slip activity in twinned nanopillars. However, this cross-slip occurs only through Fleischer mechanism and no Friedel-Escaig mechanism of cross-slip has been observed under tensile loading. Further, the dislocation glide along the twin boundary has also been observed under tensile and compressive loading, despite zero resolved shear stress on the twin boundary plane.

Monotonic and cyclic loading of polycrystalline Cu: Simulation results had shown that the tensile stress-strain behaviour is characterized by the initial elastic deformation up to peak stress followed by a gradual decrease in flow stress until failure. While, the cyclic stress-strain behaviour is characterized by initial softening up to 3rd cycle followed by hardening till the end of 10th cycle. Further, results had confirmed that the variation of yield stress and flow stress follows the inverse Hall-Petch relation as a function of grain size in polycrystalline Cu.

The deformation behaviour under the tensile deformation is dominated by the glide of partial dislocations which nucleates mainly from the grain boundaries. Along with partial dislo-

cation mediated plasticity, deformation by twinning has also been observed. the fivefold twin formation occurs due to twinning on multiple and interacting twin systems, Similarly, deformation behaviour under cyclic loading is dominated by the glide of partial dislocations enclosing the stacking faults. During the cyclic deformation, the twin boundaries were found to be stable boundaries, while the remaining high angle grain boundaries were highly unstable. As a result, an extensive grain growth is observed during the cyclic deformation. Under both monotonic and cyclic loading, extensive grain growth resulting in the formation of large grains during the plastic deformation. under monotonic loading, for nanowires of grain size up to 3.61 nm, the failure occurs through the shear along the slip planes, while, grain boundary failure for a nanowire with a grain size of 5.42 nm. Irrespective of the grain size, all nanowires exhibit similar ductility (failure strain) indicating that ductility is insensitive to grain size under monotonic loading.

7.2 Future studies

Molecular dynamics simulations in this work provide a wealth of information regarding the deformation behaviour and dislocation mechanisms of FCC single, twinned and polycrystalline Cu nanowires. For simplicity, pure FCC Cu which has low stacking fault energy has been chosen in the present study. Modifying the stacking fault energy by manipulating/controlling the chemical composition may result in interesting deformation behaviour. Further, well known twin boundary has been introduced in the present study. Influence of other defect structures like high angle grain boundaries provides us valuable insights about the deformation behaviour of Cu nanowires/nanopillars. Consequently, there are a number of issues that are not addressed in this work that potentially play a strong role in structure-property correlation, which are certainly more complex:

- Pure FCC Cu has low stacking fault energy. Addition of Aluminum, which has high stacking fault energy modifies the overall stacking fault energy. Insights in deformation behaviour of Cu-Al/Al-Cu alloys will be very interesting.
- In the present investigation, deformation behaviour under monotonic loading (tension and compression), and cyclic loading (10 cycles) had been studied for polycrystalline

Cu for nanowire size of 10 nm. It can be extended to higher nanowire size, so that deformation mechanisms pertaining to the cross-over of Hall-Petch to Inverse Hall-Petch can be known in much detail.

- Defect interactions and deformation behaviour in nanowires/nanopillars with initial defects such as twist boundaries, kinked twin boundaries and other defect structures can be studied.
- The formation of point and line defects under irradiation alters the initial sub-structure of pure copper. The defect distributions and their interactions vary with the kind of irradiation environments and their fluence. It would be interesting to study the influence of irradiation defects on the yielding and post-yielding behaviour of pure FCC Cu with varying temperatures and strain rates during irradiation/post-irradiation conditions.
- In the present investigation, most of simulations had been performed at 10 K. For better understanding the influence of temperature, these simulations can be performed at room temperature and high temperatures.
- Comparison of deformation behaviour under monotonic and cyclic loading can be investigated.

SUMMARY

Metallic nanowires exhibit remarkable electrical, optical, thermal and mechanical properties due to limited defects, finite size, and high surface to volume ratio. The fundamental understanding of mechanical properties and associated deformation mechanisms improves the durability and reliability of the nanowires. MD simulations have become an effective tool for evaluating material properties. The present thesis focuses on understanding the mechanical behaviour of single crystalline, twinned and polycrystalline Cu nanowires under the influence of orientation, mode of loading (tension/compression), nanowire size, cross sectional shape, and the presence of twin and grain boundaries using MD simulations.

Simulation results indicate that, under compression, deformation in the orientations close to $\langle 100 \rangle$ corner on a standard stereographic triangle is dominated by deformation twinning, while the remaining orientations (ex: $\langle 110 \rangle$) deform by dislocation slip. On the other hand, twinning is dominated in all the nanowires under tension, which results in tension-compression asymmetry in deformation mechanisms for the orientations close to $\langle 110 \rangle$ and $\langle 111 \rangle$. This asymmetry in deformation mechanisms has been explained based on the parameter α_M , defined as the ratio of Schmid factors of leading and trailing partial dislocations. Further, Cu nanowires exhibit tension-compression asymmetry in yield stress, which has been attributed to the differences in Schmid factor value for leading partial dislocations under tension and compression.

MD simulation results indicated that Young's modulus is insensitive to nanowire shape. However, both yield stress and strain to failure are sensitive to nanowire shape and size. Yielding in $\langle 100 \rangle$ Cu occurs through the nucleation of Shockley partials. Following yielding, plastic deformation in small size $\langle 100 \rangle$ Cu nanowires occurs through partial dislocation slip at all strains, while in large size Cu nanowires, slip of extended dislocations has been observed at high strains in addition to slip of partial dislocations. Interestingly, formation of pentagonal atomic chains has been observed in small size nanowires with size ≤ 1.446 nm. Further, average dislocation length, different dislocation-dislocation interactions resulting in various dislocation locks, annihilation of stacking faults, and size dependent dislocation surface interactions have been observed. Results also indicate that the variations in dislocation density as

a function of strain exhibit two stages: (i) dislocation exhaustion at small strains followed by (ii) dislocation starvation at high strains. However, with decreasing size and increasing strain rate/temperature, rate of dislocation exhaustion increases. Tensile deformation of $\langle 110 \rangle$ Cu nanowire indicated the double reorientation from $\langle 110 \rangle$ to $\langle 100 \rangle$, and to $\langle 112 \rangle$ axis. This occurrence of double reorientation and associated high ductility is restricted to low nanowire length. For nanowires with large length, reorientation process does not occur due to the activation and interaction of multiple twin systems.

Simulation results also indicate that under both tension and compression, yield strength increases with decreasing TB spacing and is always higher than that of perfect nanopillars. Under compression, deformation in perfect and nanopillars with twin boundaries (twinned nanopillars) proceeds by slip of extended dislocations. In twinned nanopillars, an extensive cross-slip through both Friedel-Escaig (FE) and Fleischer mechanisms has been observed in compression. However, deformation in perfect nanopillars occurs by partial slip/twinning, while in twinned nanopillars, it proceeds by the slip of extended dislocations under tension. This extended dislocation activity is facilitated by stair-rod formation and its dissociation on twin boundary. Similar to compressive loading, the extended dislocations under tensile loading also exhibit cross-slip activity in twinned nanopillars. However, under tension, cross-slip activity occurs only through FI mechanism, but not through FE mechanism. Also, simulation results shows that yield strength increases with increasing twin boundary distance from nanopillar surface.

MD simulation results reaffirmed inverse Hall-Petch relation as a function of grain size in polycrystalline Cu. Tensile deformation is dominated through partial dislocations and deformation twinning. Formation of fivefold twin has been observed due to interaction of multiple twin systems. Similarly, fatigue simulation results indicated that the deformation is dominated by partial dislocations. Cyclic stress-strain behaviour is characterized by initial softening up to 3rd cycle followed by hardening till the end of 10th cycle. Initial softening followed by hardening has been inversely correlated with dislocation density. Extensive grain growth during deformation has been observed under both tensile and fatigue loadings. Under tension, for nanowires of grain size up to 3.61 nm, failure has been observed by shear along the slip planes, while, grain boundary failure has been observed in nanowire with a grain size of 5.42 nm. Irrespective of the grain size, all nanowires under tension exhibit similar ductility indicating that ductility is insensitive to grain size.

Chapter 1

Introduction

1.1 Theory of plastic deformation

When a material is subjected to an external force/load, the material undergoes deformation i.e., changes in shape or dimensions. This change in shape/dimension can be either reversible in "elastic deformation" or irreversible in "plastic deformation". Generally, for most metallic materials, as long as the external load does not exceed the elastic limit, the deformation is proportional to the load. In other words, the material follows Hooke's law, also stated as stress is proportional to strain. If the material experiences the load higher than its elastic limit, the material undergoes plastic deformation, where material does not follow Hooke's law. The plastic deformation results from both nucleation and motion of various defects and their synergistic reactions. These defects include point defects (vacancies), line defects (dislocations), twins, twin boundaries, grain boundaries etc.,

It is interesting to note that the plastic deformation in crystalline materials was first observed in the nineteenth century by Mugge (1898), and Ewing and Rosenhain (1900) [1]. They observed that plastic deformation of metals occurred through the formation of slip bands and can be seen on the surface of the lead (Pb). When Pb is strained beyond its elastic limits, the plastic deformation occurs through sliding of elementary (small) portions of material over one another. However, they had observed that plastic deformation occurs through twinning in copper. Finally, they had concluded that the plastic deformation occurs through two modes. One is through simple slip, where the movements of the crystalline elements are purely translatory,

and their orientation is preserved [1]. The other is through twinning, where relative rotation of group of atoms occurs. Both modes are often found in a single specimen of metal, and even in a single crystalline grain [1]. The schematic diagram of formation of slip bands under deformation along with the optical images illustrating the plastic deformation through slip in Pb, and through twinning in Cu has been shown in Figure 1.1 However, their interpretation of results was unclear as metals were not viewed as crystalline at that time.

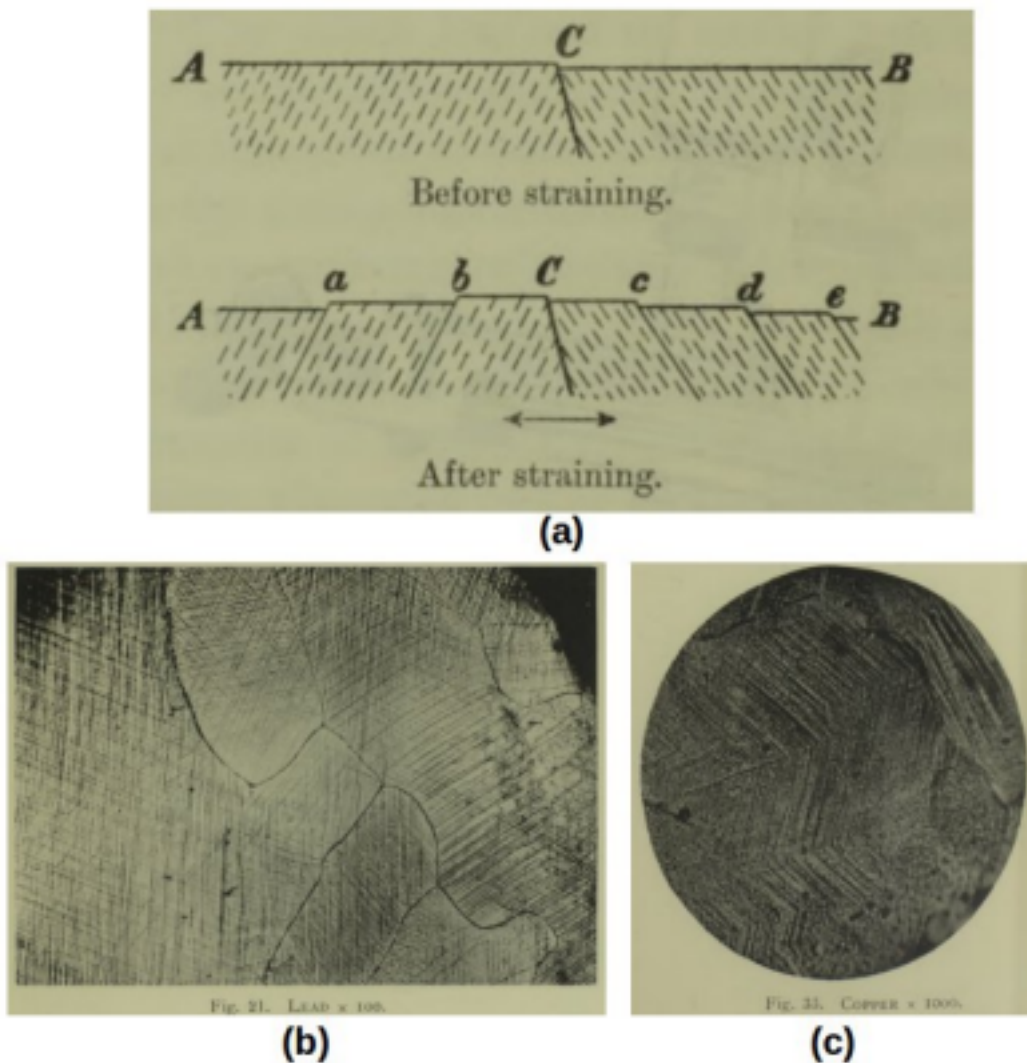


Figure 1.1: a) The schematic diagram illustrating the formation of slip bands during the deformation. Slip bands (a, b, c, d, e) occurs through sliding of elementary portions of material over one another. b). Optical micrograph of deformed polycrystalline Pb representing that deformation occurs through slip. c). Optical micrograph of deformed polycrystalline Cu representing that deformation occurs through twinning. These figures have been taken from Ewing and Rosenhain [1].

With the discovery of X-rays by W.C. Roentgen in 1895 [2], Von Laue had documented the diffraction pattern of copper sulfate crystals in 1912 [3]. Understanding that the atomic

structure of metals consists of atoms arranged in specific geometry, W. H. Bragg and W. L. Bragg determined the first crystalline structure in 1913 [4]. Following these discoveries, several researchers had established and confirmed many theories of plastic deformation successfully with the aid of X-rays. Some notable studies among them were the investigations of Taylor and his coworkers [5, 6]. Taylor and Elam had identified that the deformation in Al occurs on the family of octahedral {111} slip planes, and the slip directions as the particular $\langle 110 \rangle$ type directions lying in the {111} planes [5, 6]. Using tensile deformation of Zn single crystals, Schmid in 1924 suggested that, the plastic yield occurs on a slip system when the resolved shear stress reached a critical value, independent of the orientation of the tensile axis [7]. Further, Frenkel calculated the theoretical shear strength of a perfect crystal in 1926 and indicated that the theoretical shear strength required to slide an unit area is not less than about one-tenth of the the elastic shear modulus, a value which is higher by many orders of magnitude than the observed yield strength [8]. This discrepancy led to the discovery of concept of dislocation by Orowan[9], Polanyi [10], and Taylor[11] in 1934. Following the discovery of dislocations, many researchers have proposed various concepts of dislocations and plastic deformation. The time line of some of the important milestones have been tabulated below:

Table 1.1: Some of the important milestones in the theory of plastic deformation.

Year	Scientists	Milestone achievements
1926	Frenkel	Theoretical shear strength of ideal crystal
1934	Taylor, Polanyi and Orowan	Crystal dislocations
1939	Burgers J M	Curved and screw dislocation
1940	Burgers J M	Burgers vector
1940	Orowan	Orowan equation for plastic strain rate
1940	Peierls	Peierls (1940)- Nabarro (1947) stress
1948	Heidenreich and Shockley	Partial dislocations and dislocation reactions
1950	Peach and Koehler	Peach-Koehler force on dislocation
1950	Frank and Read	Frank-Read sources of dislocation multiplication
1956	Hirsch	TEM observation of dislocations
1950	Cockayne Ray and Whelan	TEM observation of partials dislocations

With the advances in experimental techniques, detailed understanding of plastic deformation and related concepts such as strain hardening, defect structures and their interactions, time dependent activated processes etc., has been studied in detail. The plastic deformation in bulk materials is well understood due to the efforts over the last century. However, in recent times, the nanomaterials are emerging as the next generation structural materials. In view of this, there is a need to understand the plastic deformation in nanowires/nanopillars.

1.2 Metallic nanowires/nanopillars

Nanowires are one dimensional structures with its lateral dimensions in the range of few nanometers. Due to finite size, nanowires/nanopillars possess high surface to volume ratio, high surface scattering of electrons and phonons, and low defect density [12]. In general, a surface area to volume ratio (SVR) of $> 10^7$ can be observed for nanomaterials, which is significantly higher than that for bulk materials. For instance, the SVR for a cubic nanoparticle of side length 1 nm can be calculated as 6×10^9 i.e., $6/a$, here, a is side length of cubic nanoparticle. The increase in surface area to volume ratio as a function of nanoparticle diameter/size has been shown in Figure 1.2.

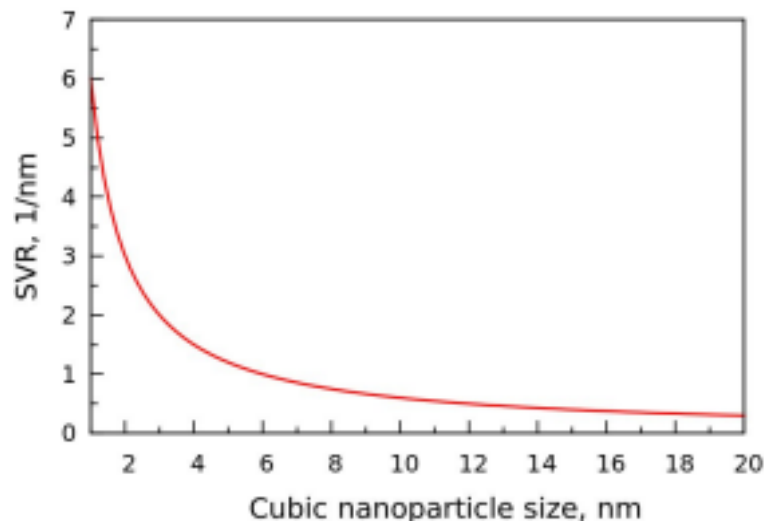


Figure 1.2: The variations in the ratio of surface area to volume, as a function of cubic nanoparticle diameter.

With decreasing the material dimensions to nanolevel, the number of surface atoms are comparable with that of interior atoms, which in turn produces the surface effects in nanowires/nanopillars. The surface effects associated with the nanowires/nanopillars offers remarkable electrical, op-

tical, thermal and mechanical properties than the bulk counterparts [13, 14]. These superior properties associated with nanowires/ nanopillars enables the design of novel and flexible NEMS/MEMS having potential applications in self-healing materials, nano-manipulators, energy storage, sensors, switches, etc. [15, 16]. Among all nanostructures, Cu nanowires, nanobelts, nanosprings and nano films have emerged as the promising next-generation conducting materials due to their excellent performance with high conductivity, high transmittance, mechanical flexibility, simple and inexpensive synthesis and cost-effectiveness [13, 14, 17, 18, 19, 20, 21].

For example, thermal interface materials(TIMs), are often employed to decrease the thermal resistance at the interface of jointed solid surfaces (between microprocessors and heat sinks), which enhances thermal transfer efficiency. As polymers have low intrinsic thermal conductivity, embedding high thermal conductive materials into polymer matrices significantly enhance the thermal conductivity, thermal stability, and mechanical strength. Cu nanowires, which have low percolation threshold and high thermal conductivity ($\approx 1\text{-}5 \text{ W m}^{-1} \text{ K}^{-1}$) are suitable materials [17]. In another field of stretchable electronics, where electronic circuits can be mounted/embedded on/in a stretchable substrate/matrix, enables devices to be deformed into arbitrary shapes without any loss of the performance and reliability of the devices. Due to superior electrical conductivity (only next to Ag), and high mechanical properties (stretchability), Cu nanowires have been chosen as excellent materials for stretchable electronics [18]. Cu nanowires coated in glass matrix has been shown in Figure 1.3.

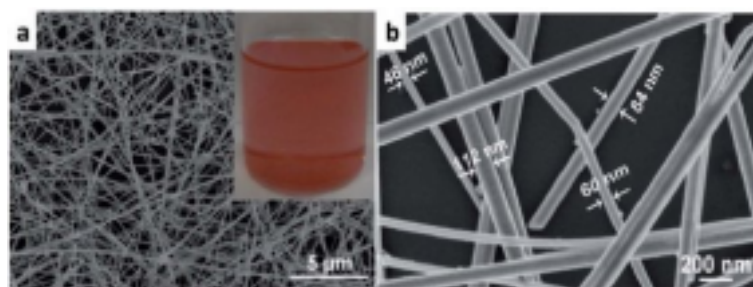


Figure 1.3: Cu nanowires used as fillers in stretchable electronics. (a) Top view OF SEM image of Cu nanowire network coated on glass. The inset shows a homogeneously dispersed Cu nanowire ink. (b). SEM image of Cu nanowire sizes. These figures has been taken from the reference [18].

For instance, Cu nanowires based transparent conducting films (TCF) have been identified as a promising materials [21]. These TCFs can be found in a wide array of products, including

the e-ink displays used in most brands of e-readers, as well as signature pads at the grocery stores. Cu nanowires based TCFs has been successfully fabricated by Meyer rod coating as a promising, scalable coating method as shown in Figure 1.4a-b by Rathmell and Wiley [21]. These Cu nanowire-based TCEs exhibited enhanced performance in terms of both transparency ($T = 85\%$) and conductivity ($R_s = 30 \Omega/sq$) to power display elements and lighting [21]. At the same time, Cu nanowire films exhibit high flexibility. Rathmell and Wiley [21] demonstrated that bent Cu films can easily carry enough current to power the LED, when they were positioned in a closed circuit with a battery pack and a LED (Figure 1.4c). This is due to the fact that well dispersed long and thin Cu nanowires on polyethylene terephthalate (PET) substrate can form a more effective electron percolation network with low nanowire number density [21]. Further, the high surface stresses make the Cu nanowires to display unique structural transformations and thermo-mechanical behaviour such as phase transformation, reorientation, shape memory effect, pseudo-elasticity and superplasticity [22, 23, 24, 25].

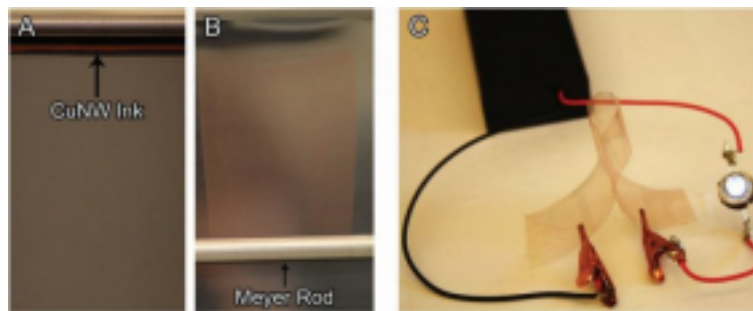


Figure 1.4: A and B Cu nanowire ink dispersed on polyethylene terephthalate (PET) substrate with a Meyer rod to form a thin, uniform film . C) Highly flexible Cu films: A bent Cu nanowire film in a closed electrical circuit connected with a battery pack and a LED [21].

The life, performance and reliability of such nanoscale devices critically depends on the mechanical behaviour of nanowires. The mechanical behaviour of nanowires differs significantly from their bulk counterparts due to confined size, limited defect density and high surface to volume ratio. Therefore, the general theories and models related to plastic deformation of bulk materials cannot be applicable directly to nanowires. As a result, the knowledge of mechanical properties and deformation behaviour also becomes important for tuning the mechanical, physical, chemical and other properties of nanowires such as reorientation, shape-memory, pseudo-elasticity, electronic conductivity and catalytic activity, which are sensitive to the applied strain [23, 26]. The present thesis focuses on the deformation behaviour of Cu nanowires/nanopillars

under the influence of various parameters such as crystallographic orientation, size, strain rate, and temperature and also the presence of twin boundaries.

1.3 Mechanics of materials

It is well known that, when the materials/nanowires experiences external load, which is higher than specified limiting load i.e., yield load, the plastic deformation initiates. Above yield load, the plastic deformation in face centered cubic (FCC) metallic nanowires proceeds mainly through slip or twin [27, 28, 29]. Further, the slip can occur by the glide of either full or partials dislocations, while the twinning occurs due to the motion of partials dislocations. In general, preferential activation of slip systems can be predicted through Schmid factor analysis [27, 28, 29]. Therefore, a brief introduction to the deformation concepts such as dislocation slip, twinning, twin boundaries, partial dislocations, and Schmid factor has been provided in this section.

1.3.1 Dislocation slip in FCC systems

The concept of dislocation was developed mathematically by Volterra in 1907 [30]. However, the mechanistic connection between dislocations and plastic deformation was not clearly recognized until the 1930's. In 1934, Orowan[9], Polanyi [10], and Taylor[11] postulated similar theories about edge dislocations, and suggested that plastic deformation through slip occurs at very low stresses than that of calculated theoretical stresses.

Dislocations, also known as line defects are the defect structures responsible for the phenomenon of slip, by which metals deform plastically. Slip can be considered as the shear between the planes of the crystal. However, the stress required for such shear process is very high (theoretically). As a result, slip between the planes does not occur spontaneously, but it occurs through the dislocations motion. In other words, dislocations can be viewed as the local lattice disturbance separating the slipped and un-slipped region of the material. The schematic illustration of the boundary between the slipped region and the un-slipped region, known as dislocations has been shown in Figure 1.5.

The direction and magnitude of the displacement is characterized by Burgers vector b .

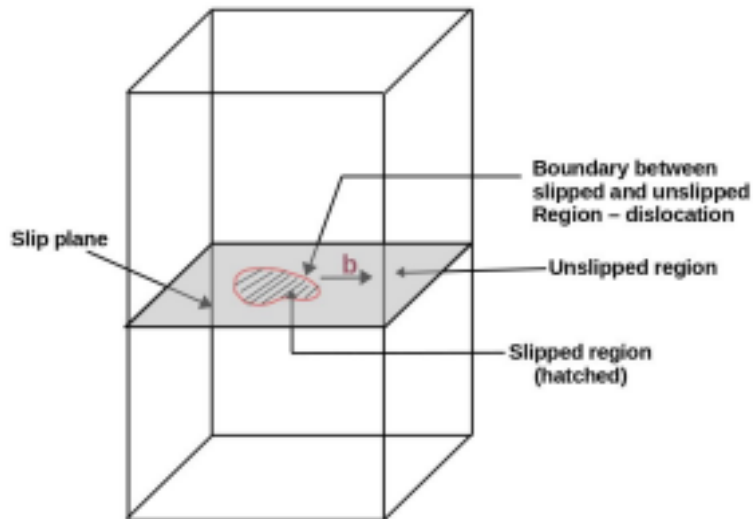


Figure 1.5: The schematic illustration of region (hatched) within a slip plane has been displaced relative to the other. Burgers vector, b represents the magnitude and direction of the displacement.

Burgers vector is a measure of both the distortion of the crystal lattice, and the shear associated with the dislocation. It also characterizes the energy and forces of the dislocation. The energy, and forces associated with dislocation varies with the relative orientation between Burgers vector and dislocation line vector. Accordingly, dislocations can be classified into a) the edge dislocation, where the Burgers vector is perpendicular to the dislocation line vector, b) the screw dislocation, where the Burgers vector is parallel to the dislocation line vector. A dislocation in which the Burgers vector is neither perpendicular nor parallel is a mixed dislocation. The systematic motion of dislocations, or slip occurs on slip plane along the slip directions. Generally, the slip plane is the plane of greatest atomic density and the slip direction is the closest packed direction within the slip plane. As the slip planes are greatest atomic density, they are also widely spaced planes in the crystal structure, which results in less resistance to slip. The slip plane along with slip direction constitutes a slip system. The slip plane with greatest atomic density in face centered cubic (FCC) systems are eight $\{111\}$ octahedral planes with a packing density of $2.31/(a^2)$, and slip direction is $\langle 110 \rangle$ directions with shortest atom to atom translation vector of $a/2\langle 110 \rangle$ [31]. However, the planes at opposite faces of an octahedron are parallel, as a result there are only four set of $\{111\}$ planes. As each plane contains three $\langle 110 \rangle$ directions, the FCC systems has 12 slip systems [32, 33]. The schematic representation of typical slip system in FCC lattice has been shown in Figure 1.6.

In FCC systems, the shortest translation vector is $a/2\langle 110 \rangle$, which is face diagonal, also

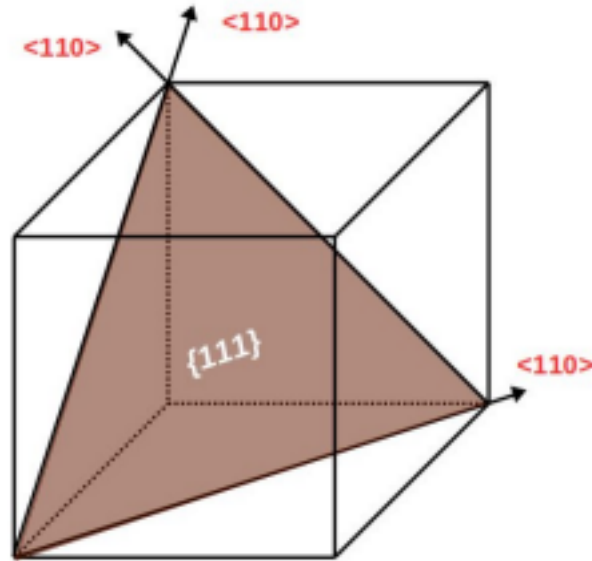


Figure 1.6: The schematic illustration of slip systems in FCC crystals. Four {111} slip planes with three $\langle 110 \rangle$ slip directions lying on the slip planes constitute the 12 slip systems in FCC crystals.

constitutes the Burgers vector of a full dislocations. The dislocation with the same lattice translation vector i.e., $a/2\langle 110 \rangle$, can also be known as perfect dislocations, because they produces an identical lattice translation in the stacking sequence. Dislocations whose Burgers vector are not regular lattice translation vectors are called as imperfect dislocations, as they cannot produce identical lattice translation.

1.3.2 Stacking sequence, stacking fault and Shockley partials in FCC systems

The face centered cubic and hexagonal close packed (HCP) structures both have a packing factor of 0.74, consists of closely packed planes of atoms, and have a coordination number of 12. However, the major difference between the FCC and HCP systems is the stacking sequence. The FCC layers cycle among the three equivalent shifted positions (A, B and c layers), whereas the HCP layers cycle between only two positions (A and B layers) [33]. As can be seen in the Figure 1.7, FCC structure contains three types of planes with altering ABCABCABC... sequence [31, 32, 33]. However, the stacking sequence of HCP system constitutes only two types of planes with ABABAB..... arrangement. In other words, the atoms of third layer are in exactly the same position as the atoms in the first layer. So, as the deformation in FCC systems

causes errors, or faults in stacking sequence, which exhibit HCP stacking sequence [31, 32, 33].

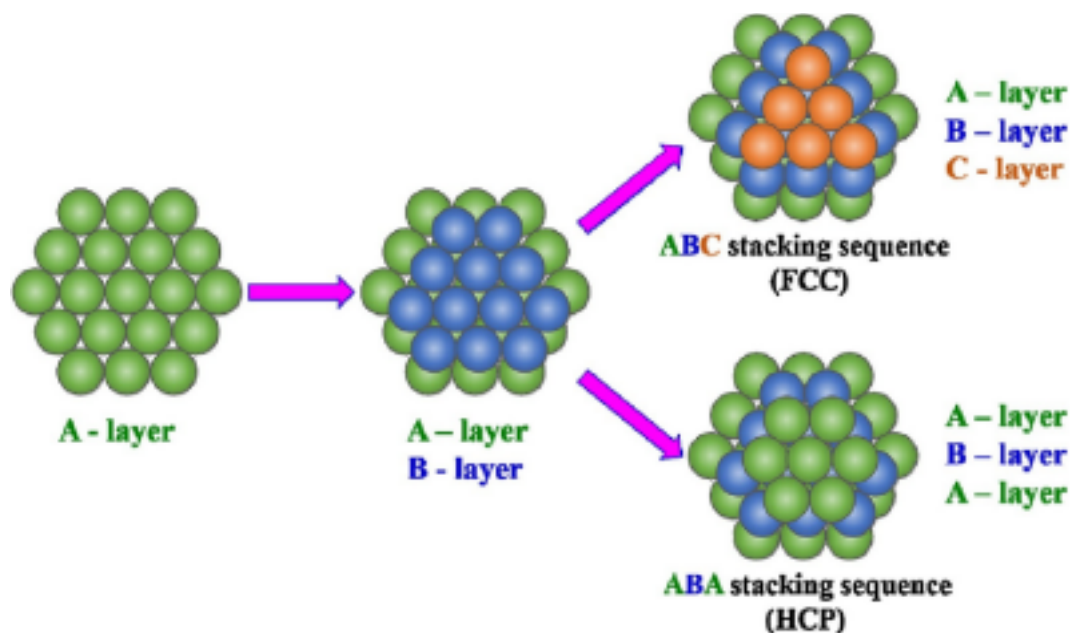


Figure 1.7: The atomic arrangement in close packed manner for FCC and HCP structures. Arrangement of A and B layer of atoms is common in both FCC and HCP systems. However, the third layer (either A or C) is different for FCC and HCP systems. This figure has been taken from Ref. [34].

The shortest lattice vector in close packed direction in FCC structures joins a cube corner atom to a neighboring face centre atom and defines the Burgers vector; one such slip vector $a/2\langle 10\bar{1} \rangle$ is shown as b_1 in Figure 1.8a. However, this straight line path of slip of B atoms, over A type of atomic sites has a high energy hill. Instead of this path, it is easy to achieve the same full slip in two sequential paths. First, the atoms move from B sites to C sites followed by C sites to B sites with Burgers vectors $b_2 = (a/6[2\bar{1}\bar{1}])$ and $b_3 = (a/6[11\bar{2}])$. Thus, one full slip can be accomplished in two successive passage of dislocations, b_2 and b_3 as shown in Figure 1.8b. It is evident from this slip that, during the glide of dislocation with Burgers vector b_2 , the atoms change their position from B to C, and a stacking fault in $\{111\}$ layers is produced with its sequence modified from ABCABC..... (represents FCC sequence) to ABC AC ABC..... (represents HCP sequence) as shown in Figure 1.8b. Further, it can be understood that the formation of stacking fault in FCC systems is equivalent to the formation of thin HCP region. The glide of dislocation with Burgers vector b_3 during the second part of the slip process restores the stacking sequence back to FCC system i.e., ABCABC..... as shown in Figure 1.8b. These dislocations with Burgers vector, b_2 and b_3 are known as Shockley partial

dislocations [35]. This theory describing the atomic movement during slip, has been reported by Heindenreich and Shockley [31, 32, 33]. They have pointed that for such dislocation to glide on $\{111\}$ plane, the unit dislocation must dissociate into two half dislocations according to the reaction:

$$\frac{a}{2} \langle 10\bar{1} \rangle \rightarrow \frac{a}{6} \langle 2\bar{1}\bar{1} \rangle + \frac{a}{6} \langle 11\bar{2} \rangle \quad (1.1)$$

This dislocation process is (i) algebraically correct, since the sum of the Burgers vector com-

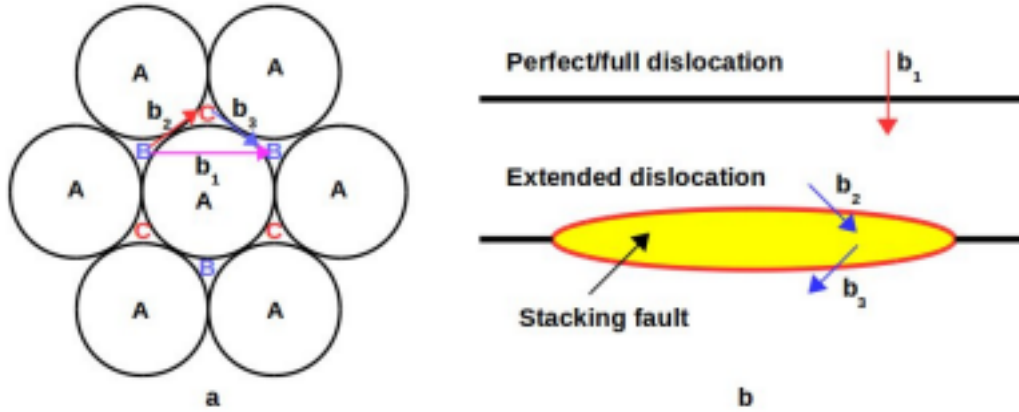


Figure 1.8: a) The atomic arrangement in FCC system (normal to $\{111\}$ plane). The possible slip paths are through either glide of dislocation, b_1 or sequential glide of b_2 and b_3 . b) The disassociation of perfect to Shockley partials with associated stacking fault.

ponents of the two partial dislocations are equal to the components of the Burgers vector of the unit dislocation, (ii) energetically favorable, since the sum of the strain energy values for the pair of partial dislocations is less than the strain energy value of the single full dislocation (the initial dislocation energy is proportional to b_1^2 ($a^2/2$) and the energy of the resultant partials is $b_2^2 + b_3^2 = a^2/3$). These partial dislocations, repel each other by a force, F . The associated stacking faulted region, which posses higher energy than the normal lattice, prevents the partials from separating too far. Thus, if γ is the energy per unit area of the fault, the force per unit area exerted on the dislocations by the fault is γ and the equilibrium separation, d is given by equating the repulsive force between the two Shockley partials, $\frac{Ga^2}{24\pi d}$, to the force exerted by the fault γ [31]. The equilibrium separation of two Shockley partial dislocations is then given by

$$d = \frac{Ga^2}{24\pi\gamma} \quad (1.2)$$

It can be seen that the width of the stacking fault ribbon is inversely proportional to the value of the stacking fault energy γ , and also depends on the value of the shear modulus G [31]. Fur-

ther, stacking fault width depends on many factors such as composition, stacking fault energy, temperature, surface energy and applied stress. Additionally, free surfaces in nanowires affects the equilibrium stacking fault width. Free surface exerts attractive forces on dislocation, since escape of dislocations from the crystal at the surface would reduce its strain energy [31, 32, 33]. The force exerted by a free surface would be approximately equal to the force which would be exerted in an infinite solid between the dislocation and one of the opposite sign located at the position of its image on the other side of the surface [31, 32, 33]. This image force is equal to

$$F = \frac{Gb^2}{4\pi(1-\nu)r} \quad (1.3)$$

here, ν is the Poisson's ratio and r is the distance from the surface.

1.3.3 Twinning in FCC systems

In addition to dislocation slip, the deformation in FCC metals occurs through another important mechanism i.e., deformation twinning. Ewing and Rosenhain (1990) had first observed the twinning mechanism in copper [1]. Twinning results when a portion of the crystal is oriented relative to the rest of the untwinned lattice in a definite, symmetrical manner. It can be seen that twinned portion of the crystal is a mirror image of the parent crystal, and the plane of symmetry between the twinned and untwinned portion is known as twinning plane, which is neither distorted nor rotated by the shearing process. The generalized twinning mechanism has been shown in the Figure 1.9. Under the application of shear stress, the atomic displacement on $\{111\}$ planes along the twinning direction can be seen in FCC systems. It is interesting to note that, both slip through Shockley partials and twin in FCC systems occurs on $\{111\}$ planes along $\langle 112 \rangle$ directions [31, 32, 33].

1.3.4 Schmid factor

A polycrystalline metal deforms plastically when its yield stress is attained. Similarly, slip in a single crystal too begins only after the applied stress on a slip plane has reached a certain minimum value [7]. In general, the crystal specimens are tested under tensile loading conditions. However, the plastic deformation in single crystals are not due to the tensile stresses but due to

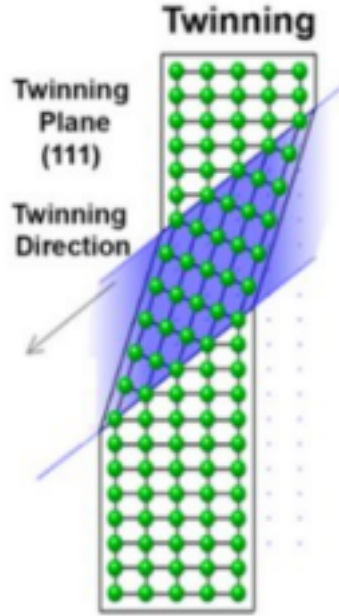


Figure 1.9: Twinning in FCC systems. Twinning occurs on $\{111\}$ planes along $\langle 112 \rangle$ directions. The shaded region indicates the instantaneous atomic positions during deformation. The atomic displacement has been indicated by arrow symbols along the twin directions [36].

the shear stress on definite slip systems. Hence, the resolved component of the applied stress on the operating slip plane and along the slip direction becomes important to cause deformation. For instance, consider a single crystalline cylindrical specimen under a tensile force F (Figure 1.10). The force that can initiate the plastic deformation is not due to the tensile force, but is the shear component of the applied tensile force on $\{111\}\langle 110 \rangle$ slip systems [27, 28, 31, 32, 33]. Hence, the tensile force must be resolved on $\{111\}$ planes along the $\langle 110 \rangle$ directions. The angle between the normal to the slip plane and the tensile axis be ϕ . The angle between the slip direction and the tensile axis is θ . If A is the cross-sectional area of the specimen, then, the area of the slip plane inclined at an angle ϕ is $A/\cos \phi$. The component of the axial force F acting along the slip direction is $F \cos \theta$ [31, 32, 33]. Hence, the resolved shear stress is given by,

$$\tau_{CRSS} = \frac{F \cos \theta}{A/\cos \phi} = \frac{F}{A}(\cos \theta \cos \phi) \quad (1.4)$$

The plastic deformation can be initiated only when this resolved shear stress exceeds or becomes critical, i.e., attains the value called critical resolved shear stress, or τ_{CRSS} [7]. Thus, the tensile stress at which slip starts in a crystal depends on the relative orientation of the stress

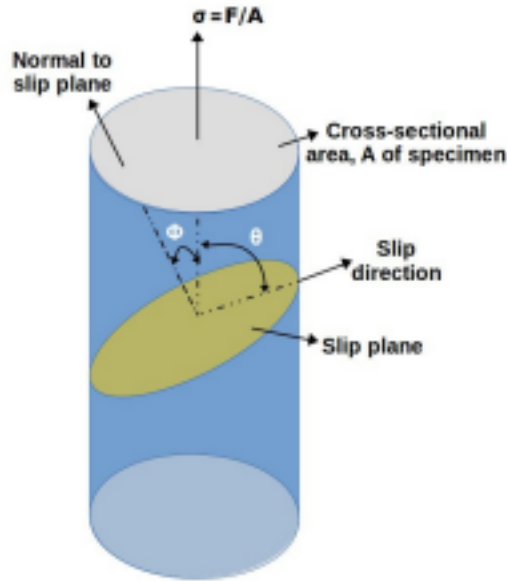


Figure 1.10: Schematic illustration of calculation of shear stress in a single crystalline cylindrical specimen under tensile force

axis with respect to the slip plane and the slip direction. It is evident from equation 1.4 that all slip systems in a crystal will not have the same resolved shear stress for a given tensile stress along an axis. Further, it can be seen that the resolved shear stress depends on the tensile axis. Hence, it can be noted that the plastic deformation in single crystalline sample depends on crystallographic orientation [27, 28].

As the applied tensile stress is increased from zero, the deformation will be initiated first on a particular slip system for which the resolved shear stress is maximum and thus, attains the critical value first. The term in parenthesis ($\cos \theta \cos \phi$) of equation is often known as Schmid factor, m . This equation also illustrates that the resolved shear stress of any slip system is proportional to its Schmid factor. The maximum resolved shear stress is obtained for a plane at 45° with the tensile axis, i.e., when $\theta = \phi = 45^\circ$, with a corresponding Schmid factor of $1/2$. For all other combinations of these two angles, the resolved shear stress is smaller than one-half [31, 32, 33].

1.3.5 Generalized stacking fault energy (GSFE)

Schmid factor enable us to determine the maximum probable slip system, which may activated upon reaching τ_{CRSS} . In FCC systems, generally 111 planes activate as they are most closely packed planes and widely spaced planes. Figure 1.11 shows that on any given 111 plane, as a

atom shift from position "C" to another "C" position (during slip), the energy associated with this atomic translation can be represented in the form of energy-displacement curve as shown in figure 1.11b. The energy-displacement curve also known as generalized stacking fault energy (GSFE). GSFE curve is the excessive energy per unit cross-sectional area of the shearing plane plotted as a function of the shearing displacement. As 111 planes glide past one another the energy per unit area of the slip plane increases to γ_{USF} and then decreases. For slip in some directions, such as the $\langle 112 \rangle$ directions in FCC crystals, some positions exist at which the lattice is stable, although the crystal is not in its bulk equilibrium structure. This stable configuration is known as the intrinsic stacking fault (ISF), with corresponding γ_{SF} energy as shown in figure 1.11b. Here, γ_{USF} is a measure of the energy barrier for the nucleation of a leading partial dislocation in a perfect crystal. The maximum slope of the GSFE curve between the position(C) and USF (position A) has the unit of stress, and is generally interpreted as the ideal shear strength of the crystal.

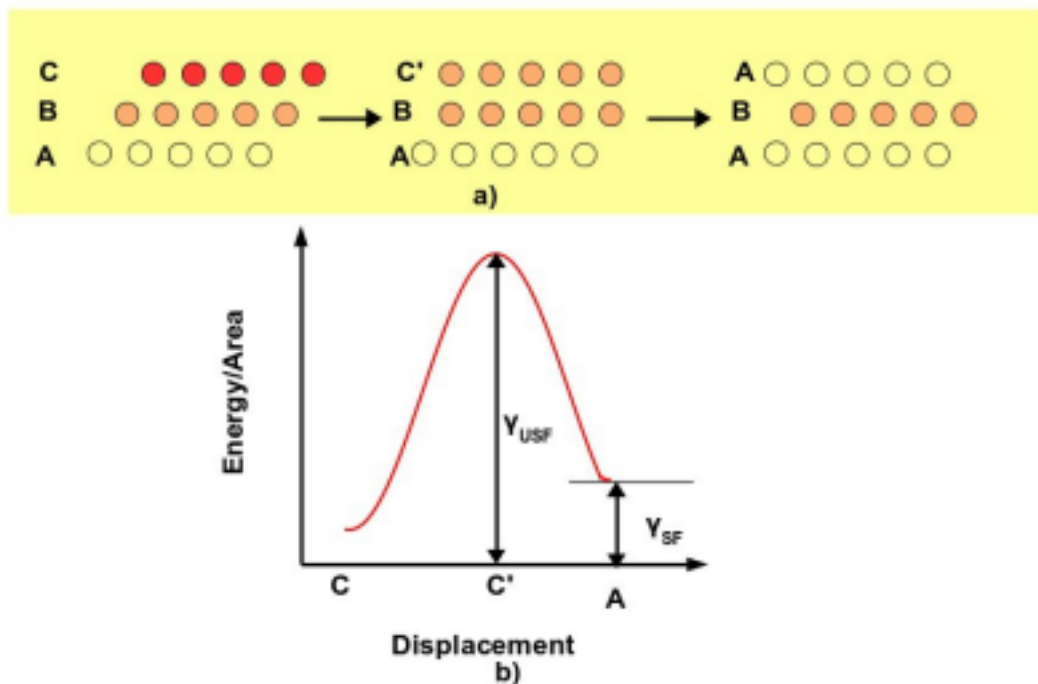


Figure 1.11: a). Atomic transition during glide of 111 plane along $\langle 112 \rangle$ direction. b). GSFE curve during the atomic transition in FCC crystals. Displacements C, C' and A corresponds to the lattice position shown in a.

1.4 Literature review on deformation behaviour of FCC nanowires

In view of mechanical properties, metallic nanowires are of great interest because they can withstand extremely large stresses and exhibit extensive ductility. Many small scale in situ mechanical testing as well as atomistic simulations have provided significant understanding of the deformation and failure mechanisms in FCC nanowires/nanopillars such as Au [27, 37, 38], Ag [39], Cu [27, 40], Pt [41], Al [42] and Ni [27, 43]. Both experimental observations and atomistic simulations have shown that the important mechanisms of plastic deformation in FCC metallic nanopillars /nanowires are slip through perfect and partial dislocations [27, 44, 45], deformation twinning [27, 46] and phase transformation [47]. The competition between these mechanisms is mainly influenced by the crystallographic orientation, size, shape and loading type (tension/compression) apart from the usual temperature and strain rate [28, 29, 48]. Except the sample size, all these factors influence the deformation behaviour even in bulk single crystals. A brief understanding of these deformation mechanisms has been explained in many reports with the help of molecular dynamics (MD) simulations as follows:

Xu et al. [42] investigated the deformation behaviour of $\langle 112 \rangle$ Al nanopillars under compression at 10 K for different orientations. They have shown that $\langle 001 \rangle$ orientated nanopillars, stacking faults bounded by partial dislocations and micro-twins are the main plastic deformation mechanisms, whereas full dislocations are responsible for the deformation in the $\langle 111 \rangle$, $\langle 112 \rangle$, and $\langle \bar{2}\bar{6}5 \rangle$ Al nanopillars. The deformation through partial dislocations and twinning in $\langle 001 \rangle$ Al nanopillars under compression has been shown in Figure 1.12. In general, the nucleation and glide of Shockley partial dislocations creates its associated stacking fault as shown in Figure 1.12a. The coplanar glide of Shockley partials results in the formation of nano-twins (Figure 1.12b). With further compressive deformation, these nano-twins grows along the length of the nanopillar (Figure 1.12c). The deformation in the $\langle 111 \rangle$, $\langle 112 \rangle$, and $\langle \bar{2}\bar{6}5 \rangle$ Al nanopillars is through full dislocations. As an example, the deformation in $\langle 112 \rangle$ Al nanopillars has been shown in Figure 1.13. These figures has been taken from Ref. [42] It can be seen from Figure 1.13 that, the deformation is dominated by full slip dislocations. It can be clearly seen for full dislocations that, the nucleation and glide of leading partial is immediately followed by the glide of trailing partial. On the other hand, the nucleation and glide of trailing partial cannot be observed in nanopillars/nanowires where the operative deformation

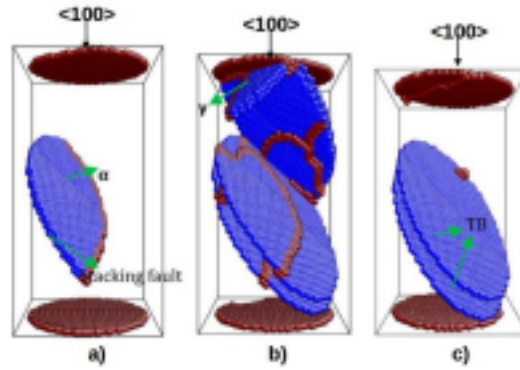


Figure 1.12: Snapshots illustrating the operating deformation mechanisms in $\langle 001 \rangle$ Al nanopillar under compression. a) glide of partial dislocations and associated stacking faults, b) formation of nano-twins and c) twins. These figures have been taken from Ref. [42]

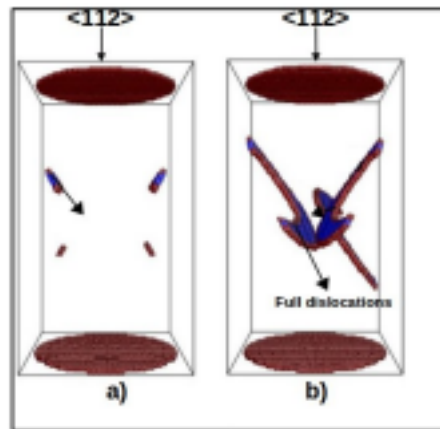


Figure 1.13: The atomic configuration of $\langle 112 \rangle$ Al nanopillar under compression. a) Full dislocations nucleate separately along the $(\bar{1}1\bar{1})$ and $(1\bar{1}\bar{1})$ slip planes, and b) full dislocations interacting with each other.

mechanism is through partial dislocation/twinning (Figure 1.12c).

Apart from dislocation slip and twinning, the deformation can also proceed by a phase transformation. Under specified conditions, surface stresses alone (without any external load) can induce phase transformation in some FCC metallic nanopillars/nanowires [47]. For example, Diao et al. [47] investigated the phase transformation of $\langle 100 \rangle$ Au nanowires. They have reported that tensile surface stress components along the length direction cause significant compressive stress-strain in the core of the wire, ultimately inducing a phase transformation from FCC structure to body-centered tetragonal (BCT) structure for Au nanowires with cross-sectional area less than 4 nm^2 [47]. The atomic configuration of Au nanowires illustrating the phase transformation of Au nanowires from FCC lattice to the BCT lattice has been shown

in the Figure 1.14. Figure 1.14 represents the dynamic progression of the phase transformation in Au nanowire. The phase transformation nucleates from the nanowire ends, progresses inwards. This phase transformation front shows the coordinated shift of the atoms from FCC

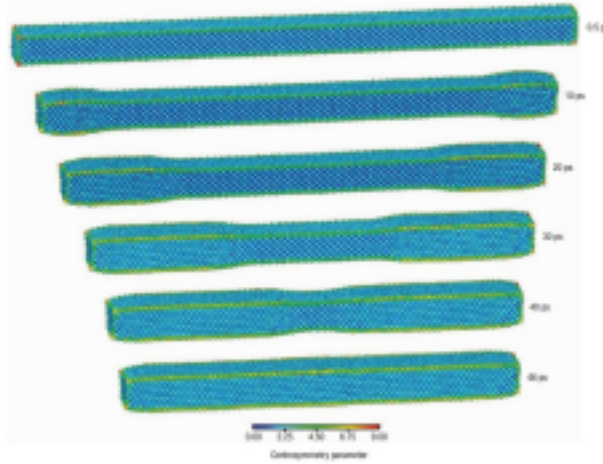


Figure 1.14: The atomic snapshots of phase transformation of Au nanowires from FCC lattice to BCT lattice. These figures have been taken from Ref. [47]

to the BCT. They have shown that the surface stress induced by nanowire size and $\langle 100 \rangle$ surfaces, is the driving force for the phase transformation.

1.4.1 Orientation dependent deformation behaviour

In single crystalline nanowires/nanopillars, crystallographic orientation plays an important role in determining the operating deformation mechanisms. Deformation through dislocation slip as well as deformation twinning has been observed in FCC nanowires of different orientations. For instance, Blewitt et al. [49] investigated the deformation behaviour of bulk Cu single crystals under tension at 4.2 K. They have observed the varying dominant deformation mechanisms for bulk single crystals of different crystallographic orientations [49]. In the region near $\langle 100 \rangle$, dislocation slip dominates the deformation behaviour. On the other hand, for single crystals with orientations close to $\langle 110 \rangle$ and $\langle 111 \rangle$, deformation occurs through twinning. Further, they mentioned that twinning occurs on $\{111\}$ plane along $\langle 112 \rangle$ direction [49].

As the single crystal size scales down to nano level, the topic of operating deformation of different single crystalline metallic nanowires seems interesting. For instance, Zheng et al. [37] investigated the orientation dependent deformation behaviour of Au nanocrystals using in-situ high resolution transmission electron microscope (HRTEM). They have observed

that dislocation slip is the operating deformation mechanism in $\langle 100 \rangle$ Au nanocrystals under tension, while deformation twinning is the dominated deformation mechanism in $\langle 110 \rangle$ nanocrystals. Likewise, Yue et al. [50, 51] performed in-situ TEM tensile testing to investigate the deformation behaviour of single crystalline $\langle 100 \rangle$ Cu nanowires. They have found that deformation in Cu nanowires is dominated by deformation twinning. Interestingly, along with crystallographic orientation, mode of loading (i.e., tension and compression) also influences the operating deformation behaviour [37, 38, 50, 51]. For instance, Lee et al. [38] have carried out both experimental investigations and MD simulations on $\langle 110 \rangle$ Au nanopillars under compression and tension. Both experimental investigations and MD simulations suggested that, under compressive loading of $\langle 110 \rangle$ Au nanopillars, deformation is dominated by slip through perfect dislocations with a Burgers vector of $1/2\langle 110 \rangle$ (Figure 1.15a,b). However, under tensile loading, $\langle 110 \rangle$ Au nanopillars deform by twinning (Figure 1.15c-e). Under tensile loading, initially a twin band had nucleated near the end grip region on one of the $\{111\}$ planes as shown in Figure 1.15d. With further deformation, this twin band progressively extend towards the other end of the nanopillar causing the crystallographic reorientation in the twinned region compared with that of un-twinned region (Figure 1.15d-e). From these results, it can be understood that the deformation behaviour of FCC nanopillars/nanowires depends on both mode of loading and crystallographic orientation.

In other reports, MD simulations alone have been employed to orientation and mode of loading dependent deformation mechanisms. For instance, Liang et al. [22] and Wu et al. [52] investigated the tensile deformation of $\langle 100 \rangle$ Cu nanowires using MD simulations. They have reported that the deformation behaviour in Cu nanowires is dominated by slip through partial dislocations and twinning. In another study, Park et al. [27] reported that, deformation in $\langle 110 \rangle$ Cu nanowires under tension is dominated by deformation twinning, which in turn results in complete reorientation of Cu nanowires from $\langle 110 \rangle$ to $\langle 100 \rangle$. The atomic configuration of $\langle 110 \rangle$ Cu nanowires illustrating the complete reorientation due to twinning has been shown in Figure 1.16. Under tensile loading, two twins nucleate at the opposite ends of nanowire. With deformation, the twin boundaries glides towards each other, and annihilate each other, resulting in a pristine, defect-free $\langle 100 \rangle$ nanowire [27].

Xu et al. [42] and Rabkin et al. [53] studied the orientation dependent deformation behaviour of Al nanopillars with varying crystallographic orientations under compression. The

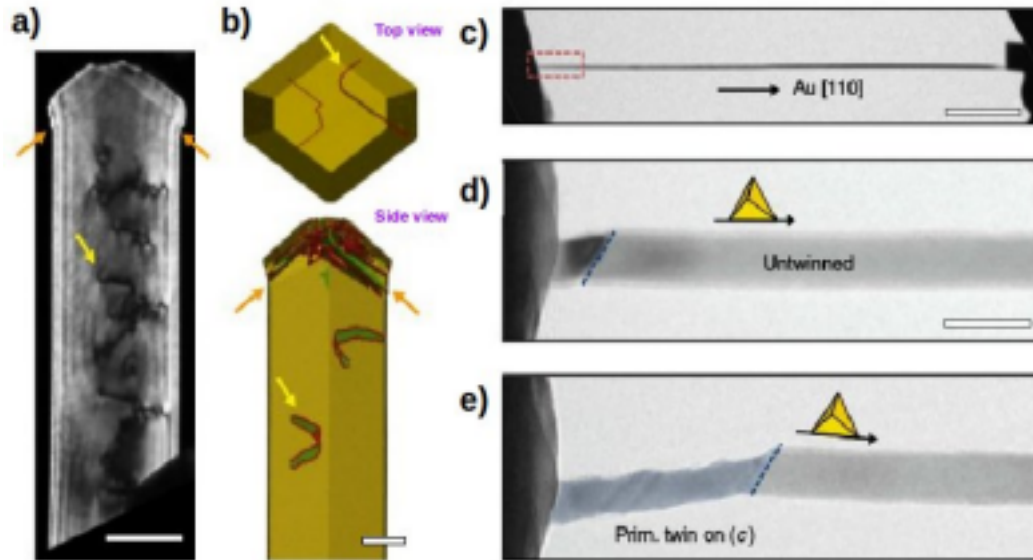


Figure 1.15: Deformation behaviour of $\langle 110 \rangle$ Au nanopillars under compression and tension [38]. a) TEM images and MD simulations showing the nucleation of dislocation loops and subsequent slip under compression [38]. b) The sequential TEM images revealing the domination of twinning under tension [38]. The orange arrows in (b) show the slip steps, while the yellow arrow show half dislocation loops.

leading Shockley partial dislocations are closely followed by trailing partials in Al nanopillars, when compressed along $\langle 110 \rangle$ and $\langle 111 \rangle$ resulting in the formation of full dislocations [42, 53]. This deformation behaviour for $\langle 110 \rangle$ and $\langle 111 \rangle$ nanopillars under compression [42, 53] is different from that under tension (i.e., through twinning/partial slip) [27, 37].

Weinberger and Cai [28] reviewed the influence of both orientation and mode of loading on various FCC metals. For instance, they have reported that the competition between slip through twinning and partial/extended/full dislocations depends on both orientation and mode of loading. They had shown that in Cu nanowires, deformation is dominated through slip by perfect/full dislocations in $\langle 111 \rangle$ nanowires under compression, but through partial dislocations under tension [28] as shown in Figure 1.17. The competition between the dominant deformation mechanisms has been attributed to the variations in magnitudes of Schmid factor [27, 28, 40]. Schmid factor is a measure of crystallographic possibility of observing either twinning or slip for a given combination of crystallographic orientation and stress state (i.e., tension and compression). The detailed description of Schmid factor has been presented in the previous section 1.3.4. The values of Schmid factor varies from 0.5 (which is a maximum) to 0.0 (indicating the zero probability of deformation). Schmid factors represent the maximum resolved shear stress factor for all possible slip/twin plane and slip/twin direction combinations.

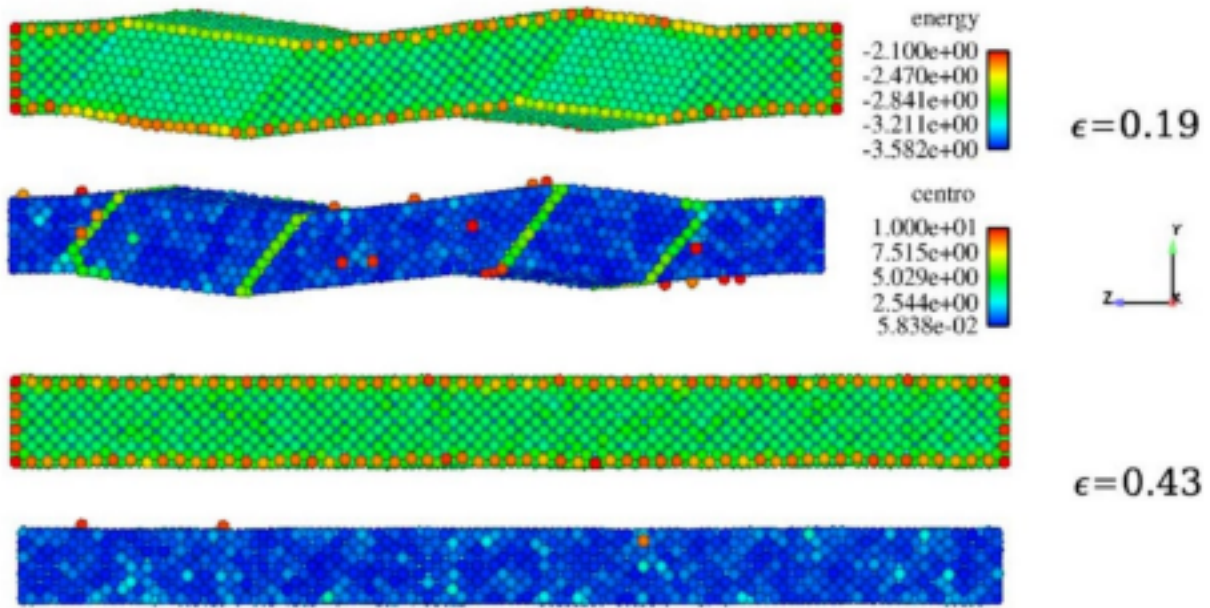


Figure 1.16: The atomic snapshots of $\langle 110 \rangle$ Cu nanowires under tension[27]. The operating deformation mechanism, deformation twinning reorients Cu nanowires from $\langle 110 \rangle$ to $\langle 100 \rangle$ orientation.

In general, Schmid factors will be purely geometric, and are independent of material properties. If the magnitude of Schmid factor of leading partial is higher than the trailing partial, then the deformation occurs through slip of partial dislocations or twinning [28]. On the contrary, if the value of Schmid factor of trailing partials is higher than the leading partials, nucleation of trailing partial immediately follows the leading partial, resulting in deformation dominated by the slip of full or extended dislocations [28]. The Schmid factor values for leading and trailing partials in different orientations of FCC nanopillars along with the reported mechanisms using experiments/simulations are presented in Table 1.2. It can be seen that the predicted mechanisms using the Schmid factor analysis are in good agreement with the reported mechanisms in Au and Al nanowires/nanopillars [37, 38, 40, 42] and other observations in Cu nanowires.

From the above mentioned studies, it can be understood that the orientation dependent deformation mechanisms under tension and compression have been investigated mainly in high symmetry $\langle 100 \rangle$, $\langle 110 \rangle$ and $\langle 111 \rangle$ crystallographic orientations, which constitutes the corners of a standard stereographic triangle. Along with variations in deformation mechanisms under stress-state (i.e., tension and compression), Weinberger and Cai [28], had also reported the variations in yield stress due to variations in stress-state. In view of this, understanding the deformation mechanisms over a wide range of orientations in FCC nanowires becomes important. Moreover, the variations of yield strength and strength asymmetry with respect

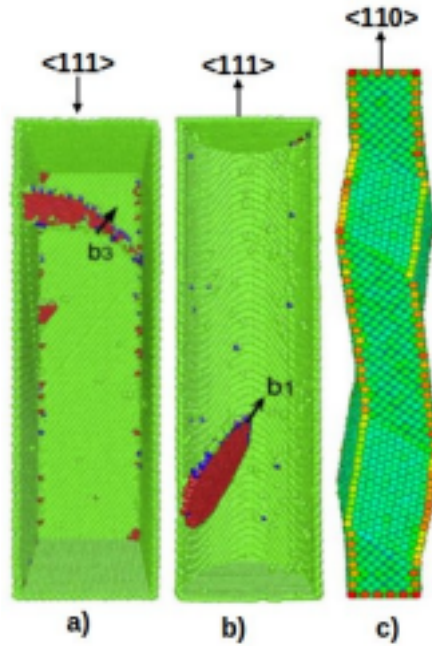


Figure 1.17: Deformation behaviour in Cu nanowires [28]. In Cu $\langle 111 \rangle$ nanowires, deformation proceeds through a) slip through perfect/full dislocations under compression [40], and b) slip through partial dislocations under tension. c) under similar tensile conditions, deformation through twinning in $\langle 110 \rangle$ Cu nanowires.

orientation have not been studied systematically. In order to address these multiple issues, we have performed MD simulations on tensile and compressive deformation of single crystalline FCC Cu nanowires of different orientations at a constant temperature of 10 K. Cu nanowires of thirteen (13) different crystallographic orientations distributed uniformly on the standard stereographic triangle have been chosen for this study.

1.4.2 Effect of nanowire/nanopillar size

As material size decreases from bulk to nano level, the surface to volume ratio increases, and also there is a decrease in defect density. As a result, nanowires/nanomaterials possess distinct physical and mechanical properties, which are size dependent in nature. For instance, the strength of FCC metallic nanowires increases with decreasing the sample size (i.e., smaller is stronger) and it is significantly higher than its bulk counterparts [50, 54]. The bulk Cu typically exhibits the maximum tensile strength of about 1 GPa, while experimental results have shown that the strength of single crystal Cu nanopillar (75 nm) could be as high as 7.0 GPa under tensile loading [55]. Similarly, with decreasing Cu nanopillar diameter from 1700 nm to 90 nm, Kiener and Minor [56] using in-situ compressive tests have shown an the increase in com-

Table 1.2: Schmid factors for leading m_L and trailing m_T partial dislocations under tension and compression for different orientations of various FCC systems.

Nanowire orientation	Loading type	m_L	m_T	Predicted mechanism	Reported mechanisms in literature
<100>	Tension	0.235	0.470	Full slip	Full slip (Au[37]), partial slip (Cu[22]) Twinning (Al[42])
	Compression	0.470	0.235	Twinning/partial slip	
<110>	Tension	0.470	0.235	Twinning/partial slip	Twinning (Au[37, 38], Cu[27]) Full slip (Au[38])
	Compression	0.235	0.470	Full slip	
<111>	Tension	0.310	0.155	Twinning/partial slip	Partial slip (Cu[40]) Full slip (Al[42], Cu[40])
	Compression	0.155	0.310	Full slip	

pressive yield strength (Figure 1.18). Further, they have shown that deformation mechanism too varies with varying pillar diameter (multiple slip systems to alternating slip, and finally to single slip). In view of these distinct properties, understanding effect of nanowire/nanopillar size on the deformation behaviour of nanowires has attracted a huge research attention in the scientific community.

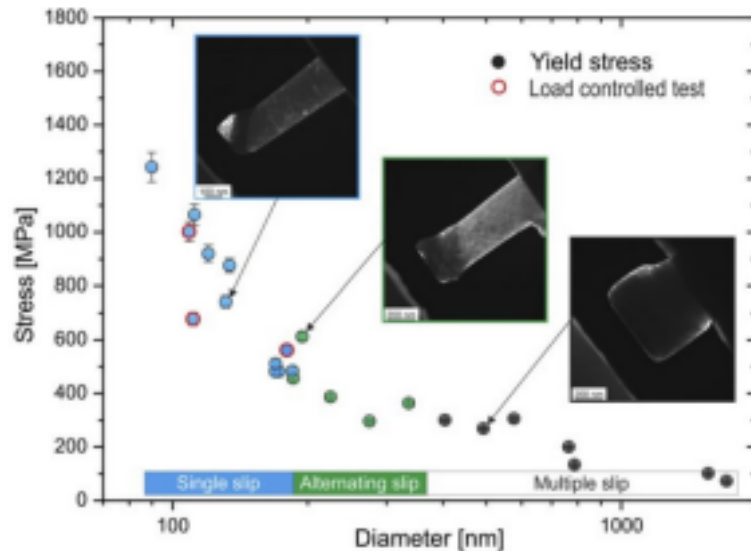


Figure 1.18: Compressive yield stress of Cu(100) pillars with varying sample diameters in the range 90 nm to 1700 nm. Also, change in operating deformation morphology with varying size. Different deformation regimes has been indicated with differently colored bars [56]. The insets represents the compressed Cu pillars

From the past decade, both the experimental investigations and atomistic simulations have shown that the nanowire/nanopillar size influences various material properties such as nucleation and character of dislocations [45, 50], deformation mechanisms [45, 50], defect inter-

actions [57, 58], failure behaviour [57, 58] and strength [54]. In order to explain the size-dependent strength in nanowires/nanopillars, various mechanisms such as source truncation, source exhaustion and dislocation starvation have been proposed [59, 60, 61]. These mechanisms originate from the microstructural parameters and dimensional constraints. The reduction in size transforms the double ended Frank-Read sources into single ended sources and leads to increased strength of nanowire by source truncation [62]. In addition, the lack of dislocation multiplication mechanisms at this length scale results in dislocation starvation and higher strength. Apart from yield strength, it has been demonstrated that the Young's modulus also exhibit the size dependence in FCC nanowires [63]. The surface-stress induced elasticity from the surface atoms and the non-linear elasticity of the nanowire core are responsible for this size dependence of Young's modulus [63].

In general, the operative deformation mechanisms depend mainly on the crystallographic orientation of the nanowire [28]. However, reported literature has suggested that the specimen size also influence deformation as well as failure behaviour of metallic nanowires. In general, the plastic deformation at room temperature is dominated by dislocation slip. However, twinning occurs only at specified conditions such as low temperatures, high strain rates, and availability of limited of slip systems. Along with these specified conditions, twinning is also favored in ultra thin dimensions. As the sample diameter decreases below certain size, the stress becomes so high that the deformation through twinning acts as a dominant mode of plastic deformation. Recently, Yue et al. [50] have obtained a quantitative results on plastic deformation of Cu nanowires with size ranging from 70 nm to 1000 nm. Figure 1.19 shows the relative contribution of partial dislocation mediated plasticity (including stacking faults and twins) and full dislocation slip to the total plastic deformation [50]. It can be seen that at relatively large nanowire diameters with $d > 150$ nm, the plastic deformation is dominated by full dislocations and the contribution of partial dislocations or stacking faults is minimal. On the contrary, in small nanowires with diameter less than 150 nm, the partial dislocation mediated plasticity including twinning is the dominant mode of deformation with total contribution as high as 90 %. This study clearly shows an evidence for the transition in plastic deformation from full dislocation slip to partial dislocation slip with decreasing size in single crystalline nanowires. A similar transition has been observed in different nanomaterials such as single crystalline nanowires [45], nanofilms [44] and nanoparticles [64]. Experimentally, the transition in deformation mechanisms has been investigated using in-situ transmission elec-

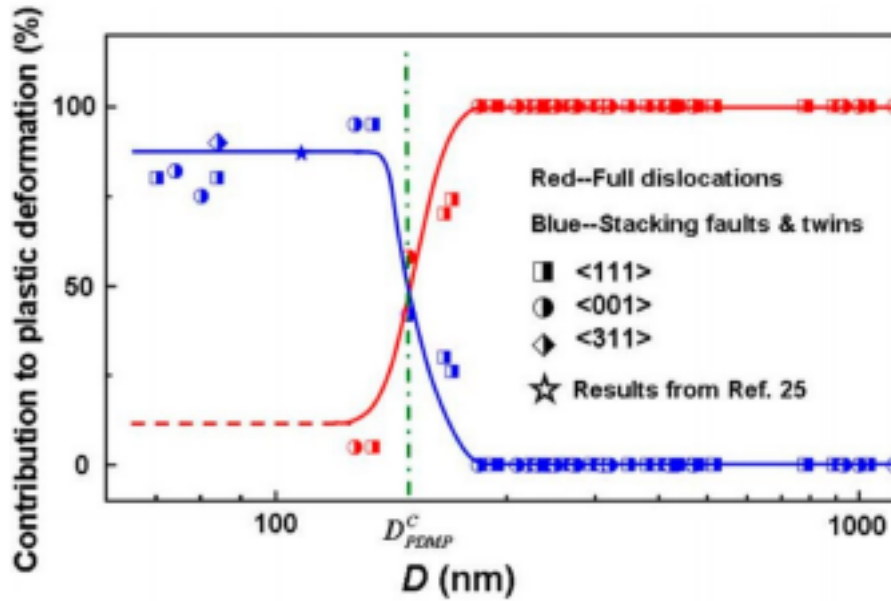


Figure 1.19: Sample size dependence of two deformation mechanisms: Slip through partial dislocations and full dislocations. Relative contribution of both deformation mechanisms for pure Cu nanowires at various sizes. The transition can be seen at $D = 150$ nm [50].

tron microscopy straining experiments in Au thin films and Ag nanowires with decreasing thin film thickness/nanowire size. For example, Oh et al. [44] had performed in-situ transmission electron microscopy straining experiments on 40, 60, 80 and 160 nm thick single crystalline Au films. They have observed that the deformation in thicker Au films is dominated by slip of perfect dislocations, while thinner films deform by the slip of partial dislocations [44]. Similar transition in operative deformation mechanism has been reported by Kong et al. [45] from their in situ deformation tests on Ag nanowires with size varying in the range 3-11 nm. They have reported that the plastic deformation dominated by slip of full dislocations has been observed in single crystalline Ag nanowires of 11 nm diameter, while nucleation and annihilation of stacking faults has been shown to govern plastic deformation of relatively small size nanowires of diameters in the range 5-8 nm [45]. With further decrease in nanowire diameter to 3 nm and less, plastic deformation accommodated by the relative slip between two adjacent $\{111\}$ planes without any dislocations has been reported [45].

Through MD simulations too, similar size dependent deformation behaviour has been reported. Interestingly, many reports suggest that when deformation occurs purely by twinning, it gives rise to reorientation [25], pseudoelasticity [23], shape memory [23, 65], super-elasticity and super-plasticity in nanowires of below certain critical size. For example, Liang and Zhou

[22] have shown the pseudoelastic behaviour in single crystalline Cu nanowires (Figure 1.20). They have observed the reversible lattice reorientations upon loading and unloading from original $\langle 110 \rangle / \{111\}$ nanowire with rhombic cross-sections to stretched $\langle 001 \rangle / \{001\}$ nanowire with square cross-sections for nanowires with size 1.76 to 3.39 nm, over the temperature range of 100 - 900 K. When deformation proceeds by twinning and the twin boundaries sweep across the nanowire length, the orientation of the nanowire changes and this phenomenon is known as reorientation. The reorientation mechanism has been observed in many FCC and BCC single crystalline metallic nanowires [23, 24, 66, 67], and also in inter-metallic alloy nanowires [68].

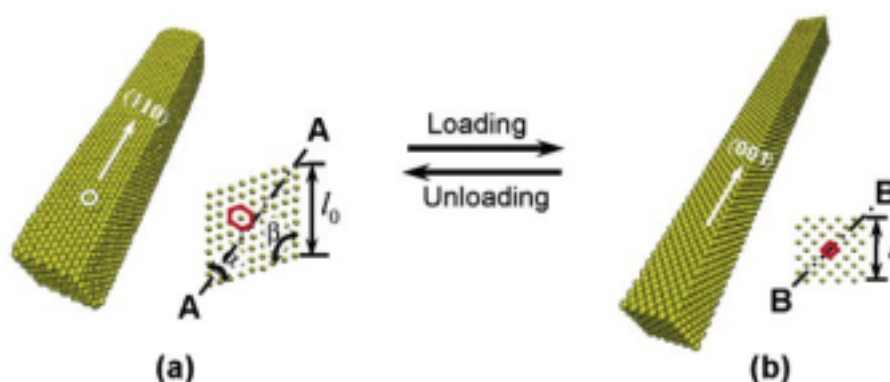


Figure 1.20: Pseudo-elasticity in single crystalline Cu nanowires [22].

Interestingly, this reorientation has not been observed when the nanowire undergoes deformation by slip of dislocations alone. For instance, Al nanowires does not show pseudoelastic behavior as seen for Cu nanowires [24]. This difference arises as the deformation proceeds through dislocation slip in Al nanowires rather than deformation twinning in Cu nanowires. The slip mechanism involving full dislocations causes the tensile deformation to be permanent and irreversible upon unloading. Consequently, no pseudoelasticity is possible in Al nanowires [24]. It is well known that metals with low stacking fault energy are more likely to deform through twinning. However, such twinning behaviour can be observed for high stacking fault energy of metals such as Ni. On the contrary, it has not been observed for Al (SF of Al \sim to Ni). To solve this issue, Liang and Zhou [24] have considered two scenarios following the nucleation of leading partials. In the first scenario, the nucleation of trailing partial is favored, which results in the formation of dislocation slip. In the second scenario, the nucleation of twin partial is favored, resulting in the formation of micro/nanotwin. From this, they have proposed energy based criteria with two energy ratios., namely, energy ratio of γ_{SF}/γ_{USF} , and γ_{USF}/γ_{UT} [24]. They have pointed out that metals with small γ_{SF}/γ_{USF} , and high γ_{USF}/γ_{UT}

results in the deformation favored by deformation twinning (such as Cu and Ni). The small values of γ_{SF}/γ_{USF} indicate higher barriers of the nucleation of the trailing partial and large γ_{USF}/γ_{UT} values indicate lower barriers for the nucleation of a twinning partial. This results in twin nucleation rather than slip [24]. On the otherhand, metals with high γ_{SF}/γ_{USF} , and small γ_{USF}/γ_{UT} results in the deformation dominated by dislocation slip[24].

Similarly, Weinberger and Cai [28] had modeled two-parameter criterion based on both the Schmid factor and the generalized stacking fault energies to understand whether twinning, partial slip or full slip dominates the deformation. In this model, they had considered three scenarios following nucleation of leading partial from the surface of the nanowire.

In the first case, another leading partial nucleating on a parallel plane, but not adjacent to the first slip plane. This leads to deformation dominated by partial slip, and then the critical stress can be estimated from the maximum slope of the GSFE curve from origin to USF, i.e., $\sigma_p^c = \gamma_{USF}/(b_p * S_{lead})$, where $\alpha \sim \pi$ is a geometric factor, b_p is the magnitude of the Burgers vector of partial dislocation, and S_{lead} is the Schmid factor of the leading partial.

In the second case, the trailing partial can nucleate on the same slip plane of the leading partial. This leads to full slip, and the critical stress can be estimated from the maximum slope of the GSFE curve between SF and USF (Figure 1.11)), i.e., $\sigma_f^c = (\gamma_{USF} - \gamma_{SF})/(b_p * S_{trail})$, where S_{trail} is the Schmid factor of the trailing partial.

In the third case, a leading partial can nucleate on the slip plane adjacent to the first leading partial. This leads to twinning, and its critical stress can be estimated as, $\sigma_t^c = (\gamma_{UT} - \gamma_{SF})/(b_p * S_{lead})$.

Among these three cases, any event with lowest critical stress is predicted to occur[28]. Further, they had mapped these three different cases as shown in Figure 1.21 based on two parameter as follows[28];

$$\tau_1 = \frac{\sigma_p^c}{\sigma_t^c} = \frac{\gamma_{USF}}{\gamma_{UT} - \gamma_{SF}} \quad (1.5)$$

$$\tau_2 = \frac{\sigma_f^c}{\sigma_t^c} = \frac{(\gamma_{USF} - \gamma_{SF})}{\gamma_{UT} - \gamma_{SF}} * \frac{S_{lead}}{S_{trail}} \quad (1.6)$$

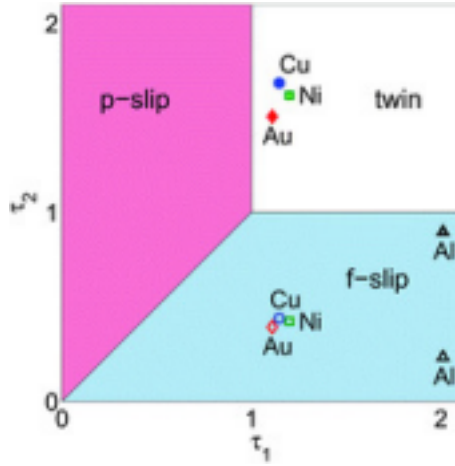


Figure 1.21: Operating deformations of FCC metallic nanowires under different axial loading conditions. In partial slip region: $\tau_1 < \tau_2$ and $\tau_1 < 1$. In full slip region, $\tau_2 < \tau_1$, and $\tau_2 < 1$. In twin region: $\tau_1 > 1$ and $\tau_2 > 1$. Open symbols represents the loading conditions of $\langle 100 \rangle$ tension, $\langle 110 \rangle$ compression and $\langle 111 \rangle$ compression. Filled symbols represents the loading condition of $\langle 100 \rangle$ compression, $\langle 110 \rangle$ tension and $\langle 111 \rangle$ tension[28].

Interestingly, if the dimension of the nanowire deforming by slip is of few atomic spacings, then interesting atomic chains such as linear, pentagonal, single shell, multi-shell and other peculiar structures have been reported in the necking region [65, 69, 70, 71, 72].

In another study, Leach et al. [73] had studied the mechanical behaviour of Ag nanowires with varying size (1 to 25 nm) and shape (rhombic, truncated rhombic, and pentagon). Leach et al. [73] has considered $\langle 110 \rangle$ axially oriented Ag nanowires with rhombic and truncated-rhombic cross-sections, as representatives of top-down fabrication, while pentagonal Ag nanowires represents a bottom-up fabrication route. In general, nanowire has been prepared from bulk material in top-down fabrication, while nanowire grown through chemical or molecular assembly constitutes a bottom-up fabrication. They have shown that both shape and size influences the yield strength of silver nanowires as shown in Figure 1.22. In other words, yield strength decreases with increase in nanowire cross-section. Further, pentagonal nanowires exhibit higher yield strength than rhombic, and truncated-rhombic silver nanowires [73]. They have also shown the variations in operating deformation mechanisms for different cross-sections. In particular, they have reported that twinning is operated in rhombic Ag nanowires which elongated more than 40 % before failure. While, deformation through partial dislocations is dominant in truncated-rhombic Ag nanowires [73].

Similarly, Yin et al. [74] had experimentally and through MD simulations investigated the

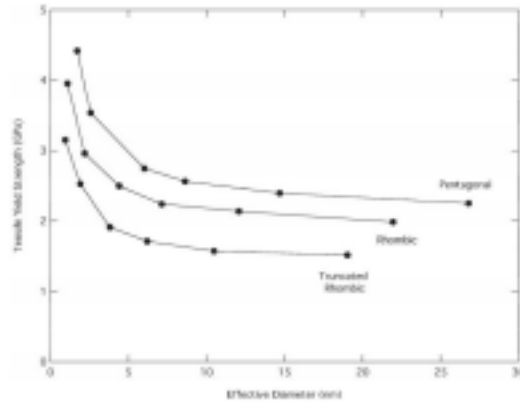


Figure 1.22: Size effect on the tensile yield strength of pentagonal, rhombic, cated-rhombic silver nanowires[73].

influence of cross-section area in determining the dominant deformation mechanisms in single crystalline $\langle 110 \rangle$ Ag nanowires. They have studied the influence of cross-section area by varying the aspect ratio, defined as the ratio of H and W (w is width, H is height of cross-section), and H_1 and H_2 , of truncated Ag nanowires as shown in Figures 1.23a. They have

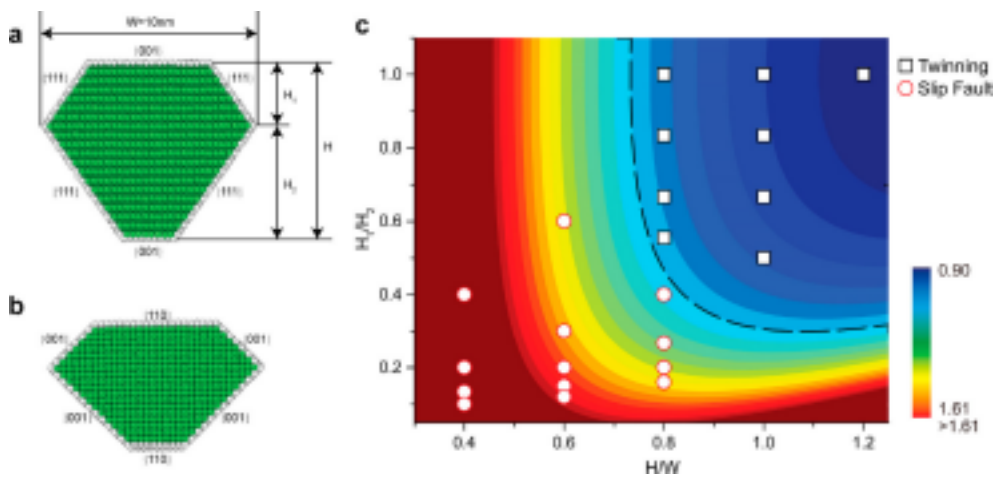


Figure 1.23: Influence of cross-sectional geometry on deformation behaviour of $\langle 110 \rangle$ Ag nanowires. a). Cross-sectional geometry of Ag nanowires. b) Reoriented $\langle 001 \rangle$ Ag nanowire with 110 and 001 Ag nanowires. c) Countour map explaining transition of deformation from twinning to dislocation slip for varying cross-sectional Open black squares refers to twinning-dominated mode, and open red circles indicates that deformation dominated by dislocation slip[74].

reported that by varying the cross-section area, dominant deformation mechanisms vary. In Ag nanowires with high H/W and high H_1/H_2 ratios, the deformation is dominated by deformation twinning. As a result, $\langle 110 \rangle$ Ag nanowires with 001 and 111 facets reorients to $\langle 001 \rangle$ Ag nanowires with 110 and 001 side surfaces. On the contrary, for nanowires with low H/W , the deformation is dominated by dislocation slip alone. This transition from twinning to dislocation

slip under the influence of cross-section geometry has been shown in Figure 1.23c.

1.4.3 Influence of twin boundaries on deformation behaviour

Grain boundaries play an important role in controlling the strength and deformation behaviour of polycrystalline materials. Existing literatures reveals the fact that twinned FCC nanopillars exhibit superior mechanical behaviour, when compared with that of their perfect counterparts. Twinned nanowires/nanopillars exhibit enhanced strength without loss of ductility [75, 76], improves crack resistance [77], and show high strain rate sensitivity [78]. The twin boundaries in nanowires can also acts as a source/sink and also as a glide plane for dislocations [79]. In nanowires, the presence of twin boundaries influences the plastic flow by way of strain hardening or strain softening or in some cases, without any hardening or softening, which depends on twin boundary orientation, twin boundary spacing, nanowire size and shape [80, 81, 82, 83]. For example, Zhang and Huang [81] reported that in Cu nanowires, the strengthening or softening due to twin boundaries depends on the cross-section shape of the nanowire as shown in Figure 1.24. It can be seen that the strength of circular twinned nanowires is higher than that of square shaped twinned nanowires. Further, in a square cross-section nanowire, the twin boundaries strengthen the nanowire, while in circular cross-section nanowire, the presence of twin boundaries leads to softening [81].

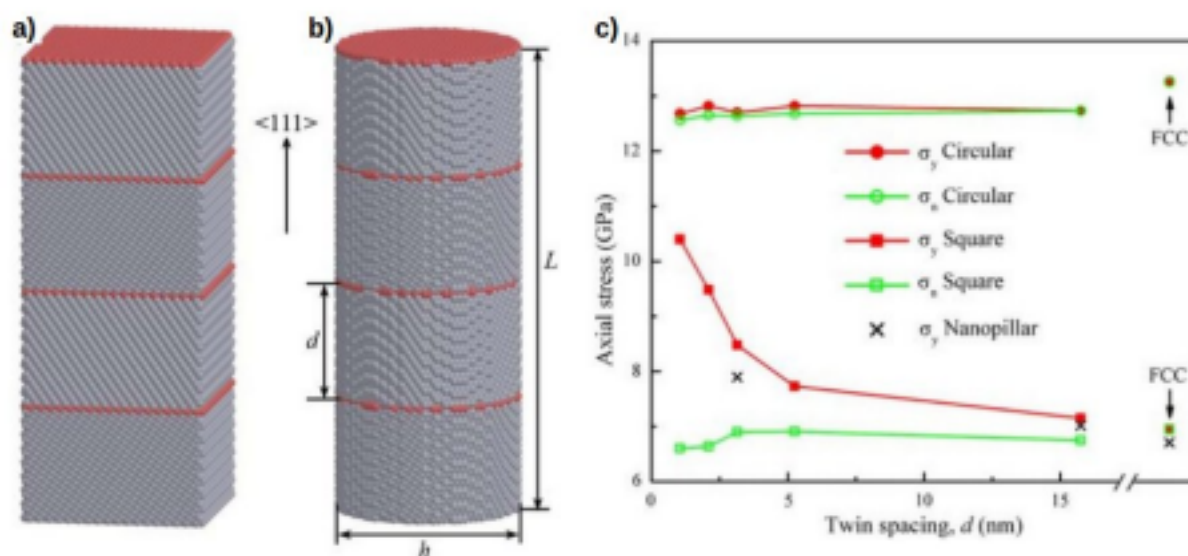


Figure 1.24: Shape dependent strengthening behaviour in twinned nanowires. Nanowires with a) square b) circular shaped nanowires. c) yield strength variation with twin boundary spacing for circular and square shaped nanowires [81].

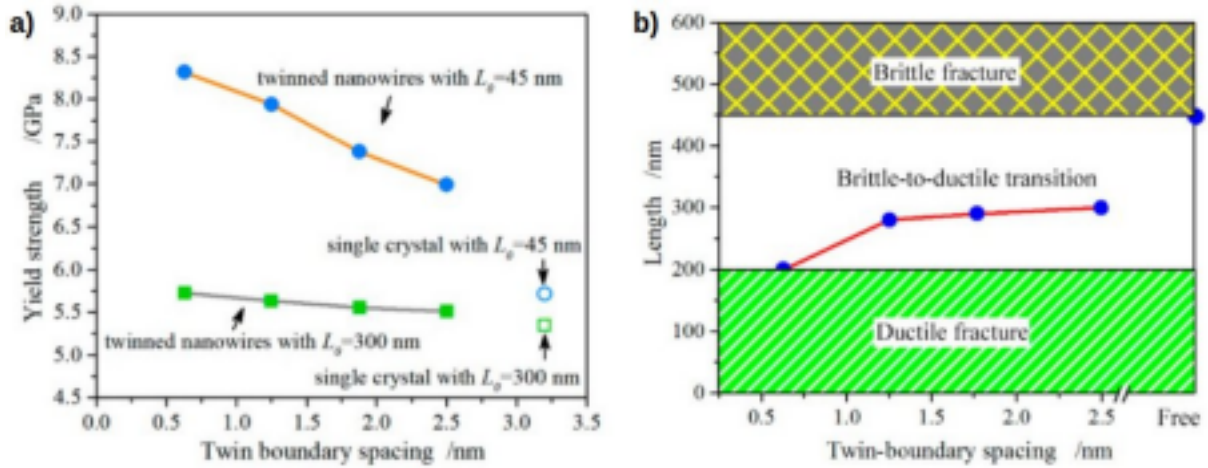


Figure 1.25: Mechanical behaviour of Cu nanowires. a) yield strength variation with twin boundary spacing for nanowires of different lengths. b) ductile to brittle transition with increasing twin boundary spacing [83].

Similarly, Sun et al. [83] investigated the combined influence of twin boundary spacing and nanowire length. They have confirmed that, for all nanowire lengths ($200 \text{ nm} < L < 450 \text{ nm}$) yield strength increases with decrease in twin boundary spacing, which is still higher than the perfect nanowires (Figure 1.25a). It has been explained that long nanowires with length ($L > 450 \text{ nm}$) always exhibit brittle failure, while short nanowires with $L < 200 \text{ nm}$ invariably fails in ductile manner, irrespective of twin boundary spacing as shown in Figure 1.25b. However, the nanowires with intermediate lengths ($200 \text{ nm} < L < 450 \text{ nm}$) have shown a ductile to brittle transition with increasing twin boundary spacing (high ductility for low twin boundary spacing) [83]. Similarly, using atomistic simulations and in-situ experiments, Jang et al. [84] shown a brittle to ductile transition in orthogonally twinned Cu nanopillars with decreasing twin-boundary spacing. Apart from influencing the strength and ductility, the twinned nanopillars have shown novel deformation mechanisms [79, 84, 85, 86]. Generally, dislocations in FCC materials such as Cu glide on $\{111\}$ planes. However, in twinned nanowires, the $1/2 \langle 110 \rangle$ dislocations glide on $\{100\}$ plane after penetrating the twin boundary [85]. In another study, Wang and Sui [86] have shown that the leading and trailing partials can exchange their order after passing through the twin boundary.

Further, the twin boundary orientation also affects the deformation mechanisms in FCC nanopillars. Due to special geometry, the twin boundaries orientated at different angles with respect to the loading direction possess distinct interactions with dislocations, which results in different deformation mechanisms [84, 87, 88, 89]. For example, Sun et al. [89] have investi-

gated the influence of twin boundary orientation on deformation mechanisms of Au nanowires. In nanopillars with orthogonal twin boundaries (twin boundaries perpendicular to the loading direction) and longitudinal twin boundaries (twin boundaries parallel to the loading direction), the twin boundary-dislocation interactions dominate the plastic flow and increases the flow stress, whereas de-twinning governs deformation in nanopillars with slanted twin boundaries (twin boundaries oriented other than 90° and 0° with respect to loading direction) [89]. The operating deformation mechanisms in longitudinal and slanted twinned nanowires has been shown in Figure 1.26. In nanopillars with slanted twin boundaries, the motion of Shockley partials along the twin boundary favors the twin boundary migration and de-twinning [89].

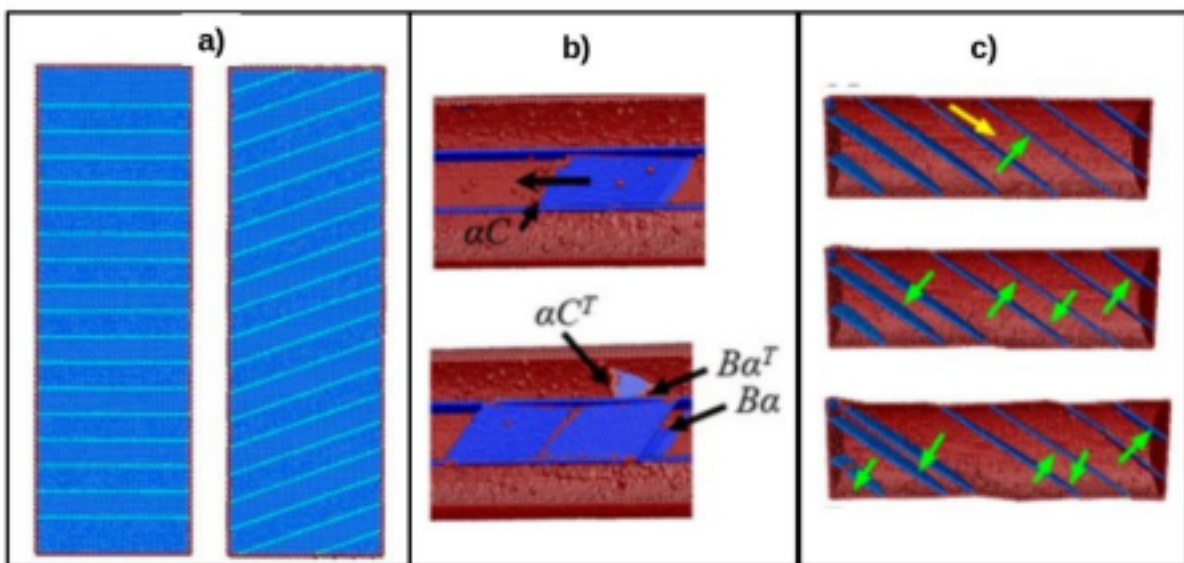


Figure 1.26: Operating deformation mechanisms in twinned Au nanowires [89]. a) Model twinned nanowires with orthogonal and slanted twin boundaries. deformation proceeded through b) discrete twin boundary -dislocation interactions in longitudinally twinned nanopillars, and c) de-twinning in slanted twin boundaries [89].

Along with twin boundaries, random grain boundaries also effects the strength and deformation behaviour of polycrystalline nanowires/nanopillars. It can be seen that both sample size and grain size influences the mechanical behaviour in polycrystalline nanowires. It has been well known that the coarse-grained/ bulk materials can be strengthened by introducing grain boundaries. It has become widely accepted that the plastic deformation is dominated by glide of full dislocation and their discrete interaction processes for the larger grain sizes (50 - 100 nm), which results in strengthening the coarse-grained/bulk materials. The variations in yield strength as a function of grain size follows the Hall-Petch (HP) relation [90, 91] as $\sigma_Y = \sigma_0 + Kd^{-1/2}$, where σ_0 is the friction stress in the absence of grain boundaries, k is a

constant, and d is the grain size. In other words, the yield stress increases with decreasing grain size. This is because the pile-ups in fine grain size materials contain fewer dislocations as a result, the stress at the tip of the pile-up is lower and thus, a larger applied stress is required to generate dislocations in the adjacent grain. Further in coarse-grained materials, the dislocations multiply by a well-known Frank-Read mechanism. However, theoretical models and MD simulations have suggested that at a sufficiently small d , such as nanometer grains with d in the range 15-50 nm, there exists a transition from full dislocations to partial dislocations, sometimes leading to deformation twin nucleation [92, 93, 94, 95]. Also, many reports have shown that as grain size decreases to few tens of nanometers, the HP relation will break down and also the Frank-Read mechanism no longer operates. A compilation of yield stress data taken by Meyers et al. [92] for Cu suggests that the critical grain size at which the HP relation breaks down is close to 20 nm. Below this grain size, the yield stress decreases with decrease in grain size. It has been observed that in this small grain size regime, the yield stress follows the inverse HP relation. This inverse HP relation has been first observed by Chokshi et al. [93] in Cu and Pd. The inverse HP relation has been explained based on the diffusional creep occurring through the transport of vacancies along the grain boundaries (GB), i.e., GB diffusional creep. However, Wolf et al. [94] reconciled GB diffusion creep and GB sliding as single deformation mechanism known as sliding accommodated grain boundary diffusion creep. In addition to sliding accommodating diffusional creep, grain rotation and coalescence of grains leading to grain growth has been observed as other dominant plastic deformation mechanisms [95].

Several MD simulation studies on the deformation of nanowires/ nanocrystalline materials under monotonic loading conditions have been performed [28, 87, 96, 97]. For instance, Schiotz et al. [96] performed MD simulations on nanocrystalline Cu with grain size varying from 3.3 to 6.6 nm at 300 K. The influence of grain size has been illustrated with the help of variations in true stress- strain for nanocrystalline Cu (Figure 1.27)a. The variation in yield strength and flow stress with grain size can be seen from Figure 1.27b-c. It can be seen that there exists an inverse HP relation with yield stress varying from 1 to 1.2 GPa for grain sizes of 3.3 - 6.6 nm (Figure 1.27).

Similarly, Rupert [97] performed MD simulations to understand the operating deformation mechanisms under uniaxial tensile loading for nanocrystalline Ni nanowire with mean grain sizes of 3 and 6 nm. They have shown that the deformation proceeds through slip of partial

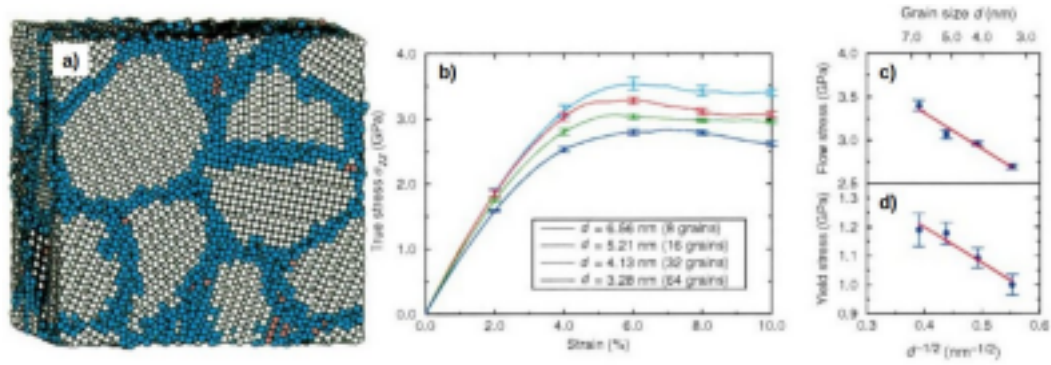


Figure 1.27: a) A model nanocrystalline copper with an average grain diameter of 5.2 nm. Grain boundary atoms are colored blue, while stacking fault atoms are colored red. b) true stress-strain behaviour of nanocrystalline Cu for different grain sizes/diameter. c) variations of flow stress and yield stress with grain size [96].

dislocations. The twin formation and propagation in a grain occurs initially through the glide of partial dislocation (Figure 1.28a). However, the twin formation is restricted by the glide of

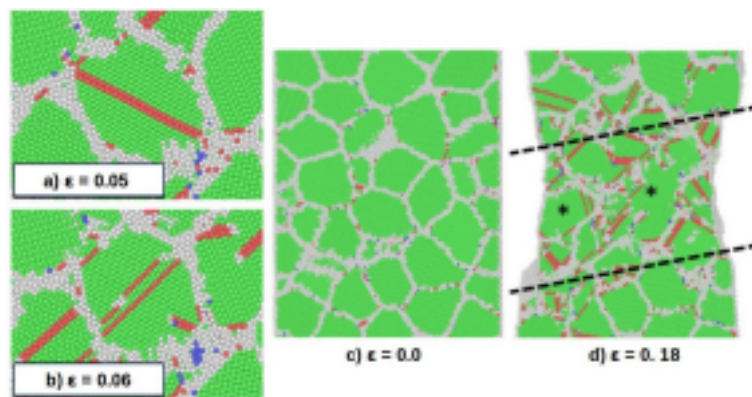


Figure 1.28: Operating deformation twinning process. a) Glide of partial dislocation enclosing stacking fault in the interior of grain. b) twin growth by a single lattice plane. c) before straining and d) after 18.1% applied strain. The plastic deformation induced extensive grain growth. The average grain size is 6 nm [97]. Two coarsened and elongated grains are marked with asterisks. All atoms are colored according to CNA. Green colored atoms represent pure FCC Ni, while red colored atoms represents stacking fault atoms and ash colored atoms represent grain boundary atoms.

another partial on a different plane. Eventually, with additional time and strain, the restricted partial dislocation is pushed all the way across the grain, resulting in the formation and growth of twin by a single lattice plane. This twin continues to grow with progressive straining on planes both above and below the original twin (Figure 1.28b). Further, they studied the extensive grain growth during the plastic deformation in nanocrystalline Ni [97]. As an example, the initial and deformed nanocrystalline Ni exhibiting the extensive grain growth has been shown

in Figure 1.28c-d. In another study, Li et al. [98] investigated the effect of grain size on deformation behaviour of nanocrystalline Pt. They have reported the size-dependent plastic deformation mechanisms of nanocrystalline Pt samples (Figure 1.29). A statistical distribution explains a clear transition from dominating plastic deformation mechanism with varying grain size, with decreasing d : the dislocations in action transits from full to partial inside the grains and eventually to those in the grain boundaries to mediate grain rotation (Figure 1.29).

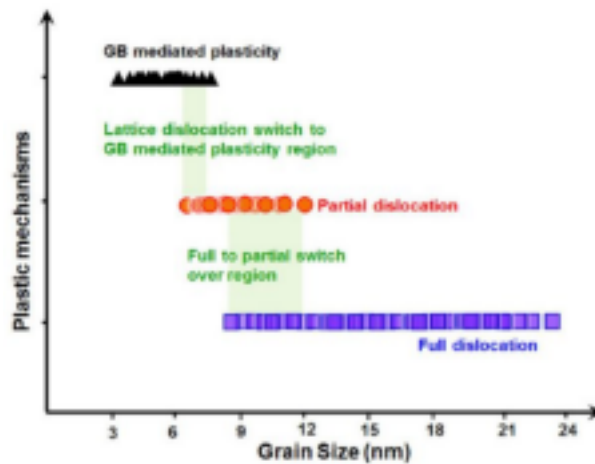


Figure 1.29: Statistical distribution explaining the operating deformation mechanism as a function of grain size d for nanocrystalline Pt [98]. At larger grains, deformation through full dislocations denoted by square symbol. For $6 < d < 10$ nm partial dislocations enclosing stacking faults denoted by dots were observed, and for $d < 6$ nm, the grain boundaries dominate the plasticity, indicated by black triangles.

It can be well understood from the previous studies that, most of the investigations have been focused the mechanical behaviour of nanocrystalline materials under monotonic loading. Only few studies exist in the literature pertaining to the MD simulations on cyclic deformation of metals. Further, due to time and length scale limitations involved in MD simulations, the cyclic deformation studies have been carried out only for few cycles. Rupert and Schuh [99] performed MD simulations to understand the cyclic deformation behaviour of polycrystalline Ni with grain sizes of 3, 4, 5, and 10 nm. The observed strengthening during cyclic deformation in Ni has been attributed to the grain boundary relaxation and the formation of low energy boundaries [99]. Recently, Panzarino et al. [100] characterized the grain structure evolution during the cyclic deformation of polycrystalline Al with grain size of 5 nm for 10 cycles. The cyclic strengthening was associated with the grain rotation, grain growth and the formation of many twin boundaries [100].

1.5 Objective and thesis outline

In view of the small size of nanowires, performing the accurate mechanical testing of nanowires is still challenging due to the difficulties in sample preparation, clamping and aligning the nanowire axial direction with loading direction [101]. On the other hand, atomistic simulations such as molecular dynamics (MD) simulations, coupled with reliable inter-atomic potentials, provides the mechanical behaviour of nanowires at atomic level in detail. In addition to mechanical behaviour, MD simulations also provides atomic trajectories in a great detail, which helps us in understanding discrete defect-defect interactions during plastic deformation. In the present thesis, we use molecular dynamics simulations to understand the deformation behaviour and dislocation mechanisms of Cu nanowires under the influence of various parameters such as crystallographic orientation, size, shape, strain rate and temperature. In addition, deformation behaviour has been studied for twinned nanopillars under tension and compression. For completeness, deformation in nanocrystalline Cu under monotonic and cyclic loading has been studied. The computational details such as inter-atomic potentials, boundary conditions, algorithms, and pre- and post processing techniques adapted during the present study has been provided in **Chapter 2**.

The simulation results, and detailed analysis has been provided in **Chapters 3-6**. The major research objectives of the present thesis has been listed in the following;

- It can be understood from the existing literature that the deformation mechanisms and tension-compression asymmetry have been investigated mainly in high symmetry $\langle 100 \rangle$, $\langle 110 \rangle$ and $\langle 111 \rangle$ crystallographic orientations, [28]. Further, the variations of yield strength and strength asymmetry with respect orientation have not been studied systematically. In view of this, we have performed MD simulations of Cu nanowires under tension and compression. Thirteen (13) different crystallographic orientations distributed uniformly on the standard stereographic triangle have been chosen for this study. Based on the obtained simulation results, we show that the tension-compression asymmetry in deformation mechanisms has been explained based on the parameter α_M , defined as the ratio of Schmid factors for leading and trailing partial dislocations. Similarly, the asymmetry in yield values has been attributed to the different Schmid factor values for leading

partial dislocations under tensile and compressive loading. The results of this findings have been presented in **Chapter 3**.

- With material size scaling down to nanolevel, nanowires possesses high surface area to volume ratio, as a result many size dependent properties can be observed. Detailed size dependent mechanical properties, deformation mechanisms have been outline in the previous section 1.4.2. Despite several studies in the literature, the influence of size on tensile deformation behaviour of $\langle 100 \rangle$ Cu nanowires needs further examination. For instance, the Schmid law predicts full dislocation slip during tensile deformation of $\langle 100 \rangle$ oriented FCC nanowires, while most of the reported results indicate slip of partial dislocations or twinning. Further, the variations in dislocation density and the average length of dislocations with respect to size, temperature and strain rate, and plastic strain are not fully established. Moreover, the relation between the ductility or failure strain as a function of nanowire size has not been explored. Generally, the size employed in these investigations appears to be reasonably low. In view of the above, large scale molecular dynamics (MD) simulations have been carried out on $\langle 100 \rangle$ Cu nanowires as a function of square cross-section width (d) ranging from 0.723 to 43.38 nm for constant length of 21.69 nm. The plastic deformation and fracture behaviour, variations in dislocation density, and average length of dislocations with respect to plastic strain for different nanowire size have been examined. The observed dislocation - dislocation, dislocation - stacking fault and dislocation - surface interactions, and the formation of various dislocation locks have been investigated. The size dependence of Young's modulus, yield strength and ductility has been studied. An attempt has been made to correlate the observed variations in yield strength with initial stress and dislocation nucleation, and failure strain with the operative deformation mechanisms. In addition, from the earlier studies, it can be understood that the cross-sectional geometry influences the yield strength and operating deformation behavior. Hence, the influence of cross-sections on deformation behavior needs to be investigated in detail. The results of these findings have been presented in **Chapter 4**.

- It is well established that the nanowires/nanopillars can be strengthened by introducing twin boundaries. However, most of studies have been focused on the variations in deformation mechanisms for nanopillars with orthogonal or slanted twin boundaries. Little has been investigated on nanopillars with longitudinal twin boundaries. Moreover, the cross-slip activity in FCC Cu nanowires under tension and compression have not been well established. Further, the influence of twin boundary spacing and its position from nanopillar surface has not been investigated. In view of this, the deformation behaviour of longitudinally twinned Cu nanopillars under compression and tension has been investigated using MD simulations. The simulation results indicate that under both compression and tension, yield strength increases with decreasing twin boundary spacing and is always higher than that of perfect nanopillars. Under compression, the deformation in perfect as well as twinned nanopillars proceeds by the slip of extended dislocations. On the other hand, under tensile loading, the deformation in perfect nanopillars occurs by partial slip/twinning, while in twinned nanopillars, it proceeds by the slip of extended dislocations. In addition, the influence of twin boundary position also has been investigated in Cu nanopillars. The results of this findings have been presented in **Chapter 5**.
- Pertaining to the deformation of nanocrystalline materials, several studies have been performed under monotonic loading conditions. However, only few studies exist on the cyclic deformation of nanocrystalline materials. In this backdrop, the effect of cyclic loading on the strength and deformation behaviour of polycrystalline Cu has been investigated for further insights. For comparison, the effect of grain size (1.54 - 5.42 nm) on the strength and deformation behaviour of polycrystalline Cu under monotonic (tensile) loading has also been presented in the **chapter 6**.

Finally, **Chapter 7** outlines the important observations, highlights and final conclusions on the deformation behaviour of FCC Cu nanowires/ nanopillars. Following this, few suggestions/ recommendations have been made for further understanding of the deformation behaviour in FCC nanowires.

Chapter 2

Atomistic simulation methods and pre- and post-processing techniques

Atomistic simulations are a collection of various numerical/computational approaches used to understand the processes of materials and systems. Atomistic simulations have been widely used to study the elementary mechanisms and other discrete defect interactions at atomic scale. In the present study, molecular dynamics (MD) simulations have been used to study the deformation behaviour of Cu nanowires/ nanopillars. MD simulation is a powerful technique to predict defect structures, dislocation-core structures, but can suffer from artifacts, due to its high sensitivity to the nature of inter-atomic potential. The present chapter provides the basics of molecular dynamics simulations and inter-atomic potentials. Further, the testing procedure involving the process of applying tensile/compressive load in MD simulations has been outlined. Also, the pre-processing tools adapted to create the required configurations of nanowire/nanopillars, and the post- processing techniques used for the visualizing different defect structures have been discussed in detail. Following this, a short note on LAMMPS package, which is used to carry out MD simulations has been presented. Finally, visualization softwares such as AtomEye and OVITO have been described. Detailed information on atomistic simulations can be found in Allen and Tildesley and Haile [103].

2.1 Molecular dynamics simulations

Molecular dynamics simulations is an atomistic simulation technique which adapts classical Newton's equation of motion for every atom of the system to track their positions with time. Molecular dynamics simulations assume that atoms/molecules are the building blocks of metals/materials and allows them to interact and change their position according to inter-atomic potentials [102, 104]. The trajectories of all such interacting particles can be determined by numerically solving classical laws of motion i.e., Newton's equation [102, 104]. The process of MD simulation is to advance the system by small time/time-step (Δt), and calculating the forces and velocities, and then repeat this process iteratively. If the time-step (Δt) is small enough, this produces an acceptable approximate solution to predict the trajectory of any system in continuous motion. The general MD simulation methodology has been shown in Figure 2.1. For a system of N atoms interacting through the potential U , the equation of motion for any atom i of mass m_i can be written as equation 2.1

$$F_i = m_i a_i = m_i \frac{d^2 r_i}{dt^2} = -\nabla U(r_1, r_2, \dots, r_N), i = 1, 2, \dots, N. \quad (2.1)$$

Where, \mathbf{a}_i is the acceleration, \mathbf{r}_i is the position of atom i , t is time, and \mathbf{F}_i is the force acting on this atom due to all other atoms in the system. Once the initial conditions (positions and velocities) and the inter-atomic potential are defined, the equations of motion can be solved numerically to get the phase space trajectory. Since, the position \mathbf{r}_i is a vector, its first and second derivatives, \mathbf{v}_i and \mathbf{a}_i , and corresponding \mathbf{F}_i , are also vectors. The total energy E is constant with time ($dE/dt = 0$), which is the case of an isolated system for MD simulations. F is related to the negative gradient of potential (U) with respect to position. Thus, force on atoms can be calculated for time evolution of the system.

Typical MD simulations are performed on systems with thousands to lakhs of atoms, which is comparatively smaller than the atoms in a single mole (i.e., Avogadro number of atoms in a single mole is $\sim 6.023 \times 10^{23}$ atoms). In general, the work flow involved in performing MD simulations has been outlined as:

i) Creating set of atoms with specified positions and velocities, and calculating the forces on each atom using the inter-atomic potential. These initial positions usually correspond to a

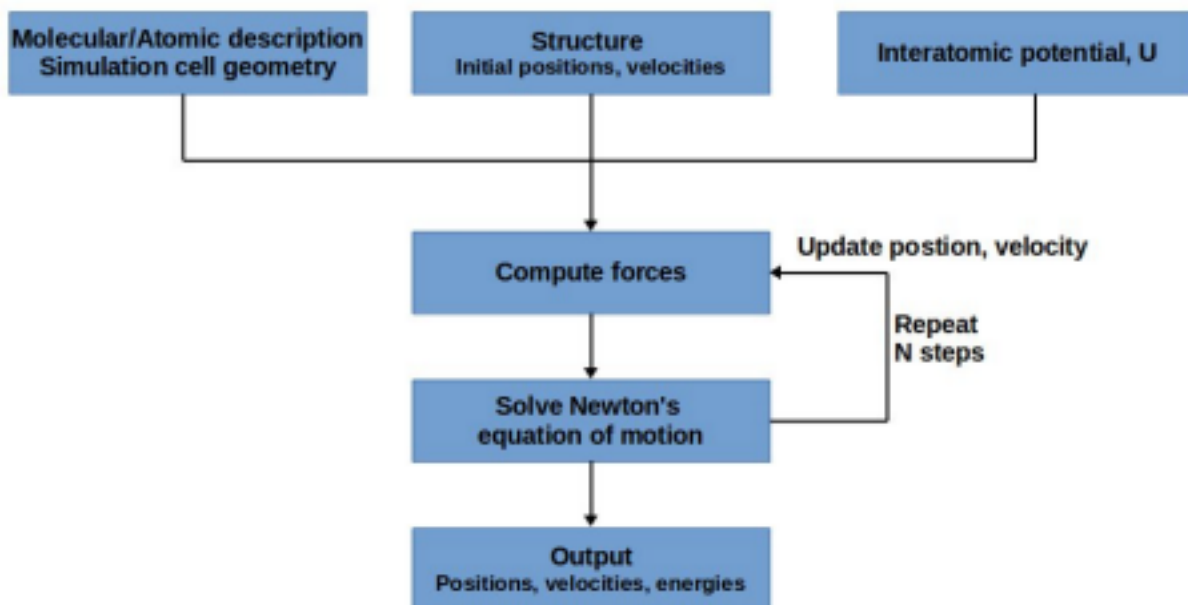


Figure 2.1: Flowchart explaining the molecular dynamics (MD) simulation methodology

known structure (from X-ray, or predicted models). Similarly, the initial velocities have been given according to the Maxwell-Boltzmann distribution at a certain temperature T .

ii) Using this information, the initial positions are advanced towards different energy states through a small time interval/timestep (Δt), resulting in new positions, and velocities.

iii) With this new data as input, the above steps are repeated iteratively, typically for more than thousands of such time interval/timesteps until an equilibrium is reached, where the energy of the system does not vary much with time.

As the simulation proceeds, thermodynamic properties of a system such as temperature, pressure, volume, total energy also change, which can be monitored/controlled by imposing external conditions such as ensembles, forces and other stimuli. In order to investigate the material properties from MD simulations accurately and efficiently, proper inter-atomic forces should be used.

2.1.1 Inter-atomic potentials

In order to perform MD simulations, we have to define some set of rules governing the interactions of atoms in the system. In classical and semi-classical simulations, these rules are often expressed in terms of potential functions [102, 104]. The potential function $U(r_1, r_2, \dots, r_N)$

describes how the potential energy of a system of N atoms depends on the coordinates of the atoms, r_1, r_2, \dots, r_N . At large inter-atomic distances, the interactions between the atoms are negligible and at the same time, the atoms cannot come too close to each other. Therefore, the inter-atomic potential contains an attractive term, so that the atoms bond together, and repulsive term giving rise to a state of equilibrium separation [102, 105]. The inter-atomic potential dictates the inter-atomic forces between atoms in simulation. As mentioned in the previous section, the forces between atoms in MD simulation are related to the potential by equation 2.1. In general, inter-atomic potentials can be written as a series expansion of functional terms that depend on the position of one, two and more atoms at a time [102, 104]. Then the total potential of the system can be written as

$$U(r_1, r_2, r_3, \dots, r_N) = \sum_i U_1(r_i) + \sum_i \sum_{j>i} U_2(r_i, r_j) + \sum_1 \sum_{j>k} \sum_{k>j} U_3(r_i, r_j, r_k) + \dots \quad (2.2)$$

Here, the summation notations indicate sums over all distinct pairs, triplets, and so forth without counting any of them twice.

- The first term, U_1 - one-body term and it may be due to an external field potential and depends on the each particles co-ordinates.
- The second term, U_2 - two-body term or a pair potential. Here, the interaction of any pair of atoms depends only on the distance between them..
- The third term, U_3 - three-body term and it arises when the interaction of a pair of atoms is modified by the presence of a third atom. The indices $i < j$ (for two body) and $i < j < k$ (for three body) is used to avoid the multiple counting of the bonds [102].

Based on the expansion, inter-atomic potentials can be classified into two classes: pair potentials, where only the second term, U_2 is present and many-body potentials, where, the third term U_3 and higher terms are included. Most of real potentials are often combinations of both U_2 and U_3 terms. To obtain accuracy in higher body interactions, some empirical terms are added for some of the potentials. The goal of the potential development is to obtain

the approximate functional form and the material specific set of parameters. Depending on the complexity of a material, the potential function may contain several parameters. Here, we briefly describe a simple pair potential and its modification for higher body interactions (embedded atom method potential).

Pair potentials for inert gases

For simple inert gases, intermolecular Van der Waals interactions in organic materials, pair potentials describe the precise interactions between atoms. In pair potentials, only the second term in equation 2.2 considers the two-atom interactions and neglects all other interactions [102]. Since many-atom effects of 3-atoms and so forth accounts for only 10% of total energy, pair potential seems a reasonable approximation for remaining part of energy. For example, Lennard-Jones potential is a mathematically simple pair potential that approximates the interaction between a pair of neutral atoms [102, 106]. $U_{LJ}(r)$ can be expressed in terms of inter-atomic distance, r , with two parameters:

$$U_{LJ}(r) = 4\epsilon\left[\left(\frac{\sigma}{r}\right)^{12} - \left(\frac{\sigma}{r}\right)^6\right], \quad (2.3)$$

and the corresponding force is as follows:

$$F_{LJ} = \frac{24\epsilon}{\sigma} \left[2\left(\frac{\sigma}{r}\right)^{13} - \left(\frac{\sigma}{r}\right)^7\right]. \quad (2.4)$$

Where parameter ϵ is the lowest energy of the potential curve (well depth), and the parameter σ is the finite distance at which the inter-atomic potential is zero, and r is the distance between the particles as shown in Figure 2.2. The magnitude of ϵ and σ vary from material to material and dictates many important properties of materials. For example, the materials having large ϵ have high melting point. Similarly, the elastic modulus depends strongly on the the shape of the curve, particularly around σ [105].

Several features are noted here when two Lennard-Jones atoms (for example Ar) approach each other from a long distance:

1. At $r = \infty$, both U_{LJ} and F_{LJ} are zero.
2. As they approach closer, the term r_{ij}^{-6} , dominating at large distance, constitute the attractive part and describes the cohesion to the system. This r_{ij}^{-6} attraction term describes van der

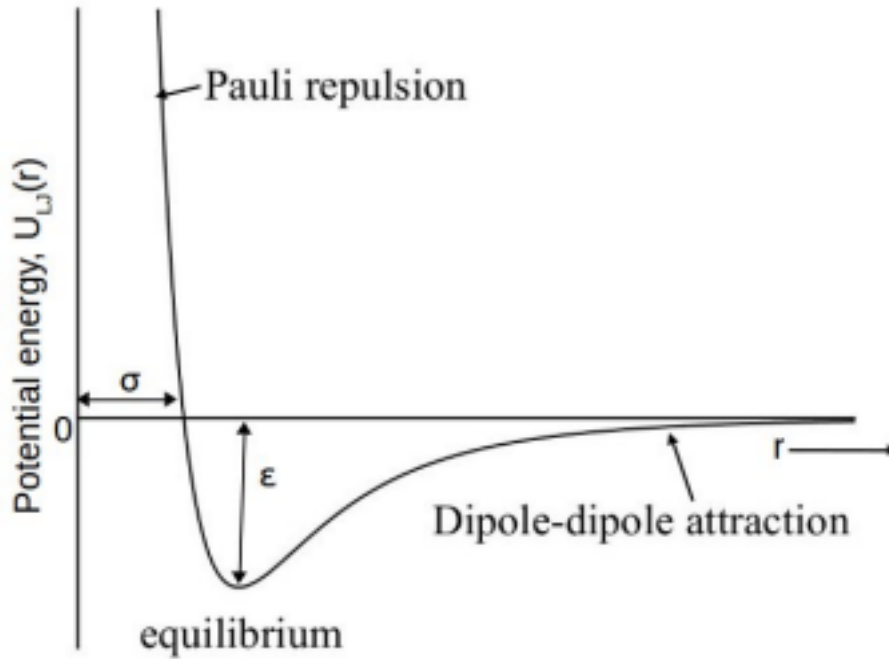


Figure 2.2: LJ potential illustrating the attractive and repulsive terms

Waals dispersion forces (dipole-dipole interactions due to fluctuating dipoles). These are rather weak interactions, which however are responsible for bonding in closed-shell systems, such as inert gases.

3. As they brought too close to each other, the repulsive term r_{ij}^{-12} dominates. Its physical origin is related to the Pauli principle: when the electronic clouds surrounding the atoms starts to overlap, the energy of the system increases abruptly. The exponent 12 was chosen on a practical basis: Lennard-Jones potential is particularly easy to compute [106]. In fact, on physical grounds an exponential behaviour would be more appropriate. Exponential term for repulsion is typically used in simulations where high-energy inter-atomic collisions are involved.

Simple pair potential can express the atomic interaction of noble gases (Ne, Ar, Kr etc.), spherical molecules and secondary bonds very well. However, this potential cannot be applied to metals, semiconductors and other solids due to following reasons:

- Pair potentials do not have **environmental dependence** (e.g. atom in the bulk is too similar to the atom on the surface or near a defect site). In reality, the strength of the individual bonds should decrease as the local environment becomes too crowded due to the Pauli's principle, but pair potentials do not depend on the environment and cannot account for this decrease.

- Pair potentials do not account for **directional nature of the bond**. Covalent contributions (d orbitals) of the transition metals can not be described. Pair potentials work better for metals in which cohesion is provided by s and p electrons.

Embedded-atom method potential for metallic systems

As discussed above, pair potentials, cannot provide an adequate description of metallic systems. An alternative simple but rather realistic approach to the description of bonding in metallic systems is based on the **concept of local density** [102]. This concept of local density accounts for the dependence of the strength of individual bonds on the local environment which is critical for simulation of surfaces and defects. In metallic systems, atoms are embedded in sea of electrons and are mostly coordinated by 8-12 other atoms. Columb interaction between atoms is long ranged and covers tens of atoms. Thus, modifications such as local electron density has been chosen to account for higher body interactions, while developing embedded atom method (EAM) potential. The embedded atom method (EAM) considers an attractive density dependent term and a repulsive pair potential [102, 107]. Here, the total potential of crystal lattice can be divided into two parts: one part is pair potential between the atoms in the crystal lattice and the other one is the embedded energy of atoms embedded in the electron cloud background, and it represents the higher body interactions. The total potential energy E_{tot} can be written as:

$$E_{tot} = \sum_i E_i, \quad E_i = F_i(\rho_i) + \frac{1}{2} \sum_{j \neq i} \phi(r_{ij}), \quad \rho_i = \sum_{j \neq i} f(r_{ij}). \quad (2.5)$$

Here, the energy of the atom i is determined by the local electron density at the position of the atom and the function f describes the contribution of electron density at the site of the atom i from all atoms j. The sum over function f is therefore a measure of local electron density ρ_i . The embedded energy F is the energy associated with placing an atom in electron environment described by the local electron density ρ_i . The pair-potential term ϕ describes electrostatic contributions [107]. Here, the embedded functional F is universal while the material dependency comes in through the local electron density ρ . The main advantage of this EAM methods over pair potentials is the ability to describe the variation of the bond strength with coordination [107]. Increase of coordination decreases the strength of each of the individual bonds and in-

creases the bond length. In this view, atoms near the defects such as a vacancies and surfaces are embedded into an electron gas of different density profile than atoms in the bulk. This allows one to account for the strength dependence of individual bonds on the local environment which is essential for simulation of surfaces and defects [102, 107]. Within these constraints, the EAM provides best and robust means of calculating energetics from which many properties can be calculated.

To be effective, an analytic inter-atomic potential must possess the following critical characteristics.

- **Flexibility:** A potential energy function must be sufficiently flexible that it can accommodate as wide a range of fitting data as possible. For solid systems, this data might include crystalline lattice constants, cohesive energies, elastic properties, vacancy formation energies, and surface energies.
- **Accuracy:** A potential should be able to accurately reproduce an appropriate fitting database. In other words, reproduce properties of interest as closely as possible.
- **Transferability:** A potential function should be able to describe at least qualitatively, if not with quantitative accuracy, structures not included in a fitting database.
- **Computational efficiency:** Evaluation of the function should be relatively efficient depending on quantities such as system sizes, and time scales of interest, as well as available computing resources.

The choice of the inter-atomic potential depends on the area of intended application. There are (almost) no good or bad potentials. There are potentials that are appropriate or inappropriate for a given problem. High accuracy is typically required in computational chemistry, while computational speed is often critical in materials science (processes have a collective character and big systems should be simulated for long times).

In order to obtain the potential function for a particular system, one can follow the following procedures:

1. Assuming a functional form for the potential function and then optimizing the parameters to reproduce a set of experimental data. This results in **empirical potential functions** (e.g. Lennard-Jones, Morse, Born-Mayer).

2. Calculating the electronic wavefunction for fixed atomic positions. This is difficult for a system of many atoms. Different approximations are used and analytic **semi-empirical potentials** are derived from quantum-mechanical arguments (e.g. Embedded Atom Method (EAM) by Foiles, Baskes, and Daw, bond-order potentials by Tersoff and Brenner, etc.).

3. One can perform direct electronic-structure (quantum-mechanics-based) calculations of forces using first principle calculations during so-called **Ab-initio** MD simulation (e.g., Car-Parrinello method using plane-wave pseudopotentials).

Among the above mentioned potentials, first principle calculations are computationally expensive and hence their utility is limited to a system with few hundred atoms or less [102]. As a result, most large-scale and long-time simulations are performed using empirical or semi-empirical potentials. In the present study, MD simulations have been performed employing an embedded atom method potential, a typical form of semi-empirical potential developed by **Mishin and co-workers** [108] has been chosen for deformation studies of pure Cu. This potential has been generated by using both experimental data and ab initio structural energies [108]. This EAM potential addresses the long-standing problem of the EAM potentials related to atomic interactions at shorter distances. Mishin and co-workers fitted the short-range parts of the potential functions to reproduce ab initio energies of the fcc phase and a diatomic molecule (dimer) of Cu at very short atomic separations, including repulsion energies in the keV range. This potential is expected to have an improved reliability in atomistic simulations involving short atomic separations, such as surface sputtering, shock waves, etc. The pair interaction function in the EAM potential had been parametrized as

$$V(r) = [E_1 M(r, r_0^{(1)}, \alpha_1) + E_2 M(r, r_0^{(2)}, \alpha_2) + \delta] \times \psi\left(\frac{r - r_c}{h}\right) - \sum_{n=1}^3 H(r_s^n - r) S_n (r_s^n - r)^4, \quad (2.6)$$

where,

$$M(r, r_0, \alpha) = \exp(-2\alpha(r - r_0)) - 2\exp(-\alpha(r - r_0)) \quad (2.7)$$

is a Morse function and $H(x)$ is a unit step function. Equation 2.8 includes a cutoff function $\psi(x)$ defined as $\psi(x) = 0$ if $x \geq 0$ and $\psi(x) = \frac{x^4}{(1+x^4)}$ if $x > 0$. The last term in equation 2.8 had been added to control the strength of pairwise repulsion between atoms at short distances. A total of 15 fitting parameters: $E_1, E_2, r_0^{(1)}, r_0^{(2)}, \alpha_1, \alpha_2, \delta, r_c, h,$ and $\{r_s(n), S_n\}_{n=1,2,3}$ can be observed in Equation 2.8. The electron density function had been considered as

$$\rho(r) = [a \exp(-\beta_1(r - r_0^{(3)})^2) + \exp(-\beta_2(r - r_0^{(4)}))] \times \psi\left(\frac{r - r_c}{h}\right), \quad (2.8)$$

with 5 more fitting parameters: $a, r_0^{(3)}, r_0^{(4)}, \beta_1,$ and β_2 . The cutoff function $\psi(x)$ guarantees that functions $V(r), \rho(r)$ and their derivatives up to the second one approach zero smoothly at the cutoff distance r_c . Then, Mishin and co-workers [108] had predicted elastic constants and phonon frequencies in the equilibrium fcc lattice of Cu in match with the experimental findings [108]. They have reported that material parameters are in agreement with that obtained from experiments as tabulated below:

Table 2.1: Material properties of Cu predicted by the Mishin and co-workers [108] EAM potential in comparison with experimental data.

	Mishin et al. EAM potential [108]	Experiment
lattice parameter(a_0), Å	3.615	3.615 [109]
cohesive energy(E_0), eV/atom	3.54	-3.54 [110]
vacancy formation energy(E_f), eV	1.272	1.27 [111]
vacancy formation volume(Ω_f/Ω_0)	0.701	0.78 [112]
$\gamma_{SF}, mJ/m^2$	44.4	45 [113]
$\gamma_S(111), mJ/m^2$	1239	1790 [114]
$\gamma_S(110), mJ/m^2$	1475	1790 [114]
$\gamma_S(100), mJ/m^2$	1345	1790 [114]
$\gamma_T, mJ/m^2$	22.2	24 [115]

As the stacking fault energy determines the width of dislocation dissociation in the fcc lattice, the accurate prediction of stacking fault energy is important for atomistic simulations of dislocations and fracture. As the calculated intrinsic stacking fault and $\{111\}$ twin energies from the present EAM potential are consistent with experimental data. Mishin et al. EAM potential [108] reproduces the mechanical properties of Cu with high reliability, and this potential has been widely used to study the mechanical properties and associated deformation mechanisms in Cu [25, 48].

2.1.2 Integration algorithms

The potential energy depends on the atomic positions of all the atoms in the system. Due to complicated potential energy dependence on atomic position, it is difficult to obtain a closed form for the Newton's equation of motion [102]. Usually, these equations of motion can be discretized in time, where finite difference method can be used effectively to integrate the equations of motion. Some of the finite difference methods used to integrate the Newton's equation of motion are Predictor-Corrector algorithm, Leap-frog algorithm, Verlet and velocity Verlet algorithms [102]. The choice of appropriate integrator depends on the following factors:

- The algorithm should conserve energy and momentum.
- It should be computationally efficient.
- It should permit a long time step for integration.

Among all the finite definite algorithms, Verlet algorithm has been commonly used finite difference method in molecular dynamics simulations. Using v (velocity) as first order derivative of the $r(t)$, and a (acceleration) as the second order derivative of the $r(t)$, and, two Taylor expansions for position $r(t)$, one at forward timestep ($t + \Delta t$) and the other at backward timestep ($t - \Delta t$);

$$r(t + \Delta t) = r(t) + v(t)\Delta t + \frac{1}{2}a(t)\Delta t^2 + \frac{1}{6}a'(t)\Delta t^3 + O(\Delta t^4), \quad (2.9)$$

$$r(t - \Delta t) = r(t) - v(t)\Delta t + \frac{1}{2}a(t)\Delta t^2 - \frac{1}{6}a'(t)\Delta t^3 + O(\Delta t^4), \quad (2.10)$$

Combining above two equations (2.9 and 2.10), we can obtain,

$$\implies r(t + \Delta t) = 2r(t) - r(t - \Delta t) + a(t)\Delta t^2 + O(\Delta t^4), \quad (2.11)$$

Using equation 2.1, equation 2.11 can be rewritten as

$$\implies r(t + \Delta t) = 2r(t) - r(t - \Delta t) + \frac{F}{m}(t)\Delta t^2 + O(\Delta t^4), \quad (2.12)$$

This relation predicts the position of atom at time $t + \Delta t$ using the position at current time t , and

previous time $t - \Delta t$ along with acceleration (force) at time t . This algorithm is known as Verlet algorithm [116]. This Verlet algorithm possesses high numerical stability, accuracy, and also conserves energy and momentum. Further, this algorithm is also time reversible because of the symmetric usage of $r(t + \Delta t)$ and $r(t - \Delta t)$. However, this algorithm performs calculations without using the velocities, which are necessary to calculate kinetic energy and temperature. To calculate velocities, we can perform mathematical operations to linear Taylor expansion. In other words, velocities can be calculated by subtracting linear Taylor expansion of $r(t + \Delta t)$ and $r(t - \Delta t)$ as,

$$r(t + \Delta t) - r(t - \Delta t) = 2v(t)\Delta t, \implies v(t) = \frac{r(t + \Delta t) - r(t - \Delta t)}{2\Delta t}. \quad (2.13)$$

Here, the velocity at present t can be calculated using positions at later time $t + \Delta t$. Further, the velocity in the Verlet algorithm has 2nd order accuracy, while the position in the Verlet algorithm has 4th order accuracy, and thus the accuracy of the Verlet algorithm is $O(\Delta t^2)$. In order to attend these issues, an improvised version of Verlet algorithm, known as velocity Verlet algorithm had been developed, which explicitly incorporates velocity of high accuracy. Velocity Verlet algorithm has been implemented to integrate the equations of motion and track the atomic trajectory of all atoms. This velocity Verlet algorithm takes the form

$$r(t + \Delta t) = r(t) + v(t)\Delta t + \frac{1}{2}a(t)\Delta t^2, \quad (2.14)$$

$$v(t + \Delta t) = v(t) + \frac{1}{2}\Delta t[a(t) + a(t + \Delta t)], \quad (2.15)$$

the standard implementation of velocity-Verlet integrator is as follows:

Step 1: Calculate velocities at mid step.

$$v(t + \frac{\Delta t}{2}) = v(t) + \frac{1}{2}a(t)\Delta t, \quad (2.16)$$

Step 2: Calculate positions at the next step.

$$r(t + \Delta t) = r(t) + v(t + \frac{\Delta t}{2})\Delta t, \quad (2.17)$$

Step 3: Calculate accelerations at next step from the potential.

Step 4: Update the velocities.

$$v(t + \Delta t) = v(t + \frac{\Delta t}{2}) + \frac{1}{2}(a + \Delta t)\Delta t, \quad (2.18)$$

Here, the new velocity is obtained based on previous velocity and current force or acceleration. Further, the accuracy of velocity is also improved to the order of $O(\Delta t^4)$ compared to that of Verlet algorithm ($O(\Delta t^2)$). Velocity Verlet algorithm have advantages such as long simulation time stability, time reversible and convergence [102, 117, 118]. Also, this algorithm is efficient as it only requires one force evaluation per time step.

While integrating the equations of motion, it can be noted that the accuracy of atomic positions and velocity is proportional to the order of $O(\Delta t^4)$. So choosing appropriate timestep (Δt) plays a vital role. In case of large time step, the truncated error($O(\Delta t^4)$) of atomic positions and velocity calculated through solving equations of motion leads to divergent unphysical trajectory and also violates conservation of energy and momentum. On the other hand, choosing too small timestep consumes high computational time and makes the calculations inefficient. However, there are no reliable methods to calculate the appropriate time step in molecular dynamics simulations. Timestep must be chosen by balancing both following accurate trajectory and spanning sufficient phase space. In general, the choice of time step is rate limited by the fastest process occurring during the simulations. Usually, the distance traveled by the atoms in one time step should not be larger than 1/20 of the inter-atomic distance and also it should be smaller than the 1/10 of the period of a bond oscillation [119]. At the same time, time step should be chosen to maintain energy conservation. In the present study, 2 fs has been chosen as the appropriate time step in all the simulations.

2.1.3 Boundary conditions

Due to limitations in computational speed and storage, molecular dynamics simulations cannot be performed for large number of atoms. At the same time, small number of atoms cannot represent the real systems, due to inherent surface effects, which influences material behaviour. So, simulation model should be prepared in such a way that it represents a larger system [102]. This issue can be addressed by the use of appropriate boundary conditions either periodic or non-periodic (free surface) boundary conditions as described below.

Periodic boundary conditions

The idea behind the periodic boundary conditions is that the one simulation cell of interest is infinitely duplicated in chosen orthogonal spatial dimensions; therefore, no free surfaces exist in these specified dimensions. For instance, Figure 2.3 represents a model system with periodic boundary conditions applied along three directions, which represents the bulk material. Here, the red colored box/cell represents the simulation cell of interest, the exact copies of this particular cell has been replicated in three orthogonal spatial dimensions and represented with blue color. As the simulation cell of particular interest has been duplicated, the cell information such as number of the atoms, and their velocities will be still conserved. Therefore, whenever N atoms leave the simulation cell, they are replaced by another N atom with exactly same velocity, entering from the opposite cell face. Thus, the atoms in original box and its periodic images behave in exactly the same manner. However, calculating the interaction of a particular atom with remaining atoms in a system with periodic boundary conditions may include its own images. This can be avoided using the *minimum image convention*. According to this convention, any atom interacts with surrounding atoms which fall within the virtual box centered at that particular atom. It is known that the largest contribution to potential comes from the nearest neighbors, the potential can be truncated above certain cut-off distance (r_{cut}). The cut-off distance must not be greater than $\frac{1}{2}L$ for consistency with minimum image convention [102].

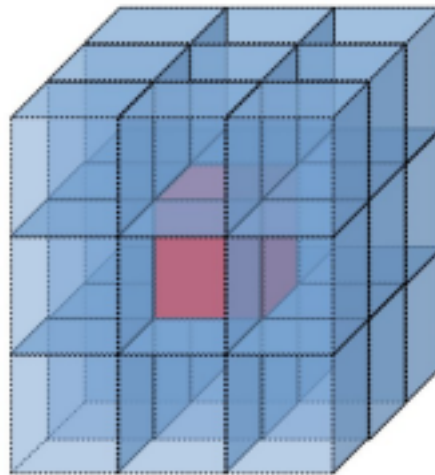


Figure 2.3: A model three dimensional system with periodic boundary conditions along three directions. Red colored region represents the original simulation cell and all blue colored cells are the exact replicas of red colored simulation cell.

Limitations of periodic boundary conditions:

- The size of simulation cell should be larger than the twice the R_{cut} , where R_{cut} is the double of cutoff distance (R_{cut}), cutoff distance of the interaction potential. In this case any atom i interacts with only one image of any atom j . And it does not interact with its own image (minimum image criterion).
- The characteristic size of any structural feature in the system of interest or the characteristic length-scale of any important effect should be smaller than the size of the simulation cell.

Free boundary conditions

In free boundary conditions, box/cell will be non-periodic in nature so that particles do not interact across the boundary and do not move from one side of the box to the other [102]. These boundary conditions should be used in model systems to create free surfaces. Free boundary condition can be also be appropriate for ultrafast processes such as sputtering, where the effect of boundaries is not of our concern due to the inherent short time-scale processes. However, using free boundary conditions may result in loss of atoms and this can be avoided by choosing the shrink-wrapped boundary conditions. In shrink-wrapped boundary conditions, the position of the face is set so as to hold the atoms within the computation cell in the same direction, no matter how far they move.

The choice of these boundary conditions whether periodic or shrink wrapped in any orthogonal spatial dimension depends the required model. For instance, application of periodic conditions in all three orthogonal spatial dimensions results in the replication and translation of model system in all three directions, resembling a bulk metal/material as shown in Figure 2.4a. For creating thin film model systems, periodic boundary conditions should be applied along two orthogonal directions, while the other direction were kept free as shown in Figure 2.4b. A nanofilm with negligible thickness compared to other two dimensions can be seen from Figure 2.4b. In order to simulate any infinitely long nanowire, periodic boundary conditions should be applied along one direction, while other two directions were kept free (Figure 2.4c). Similarly, choosing the free boundary conditions in all three directions simulates the conditions of a nanopillar which has $l \sim d$ as shown in Figure 2.4d.

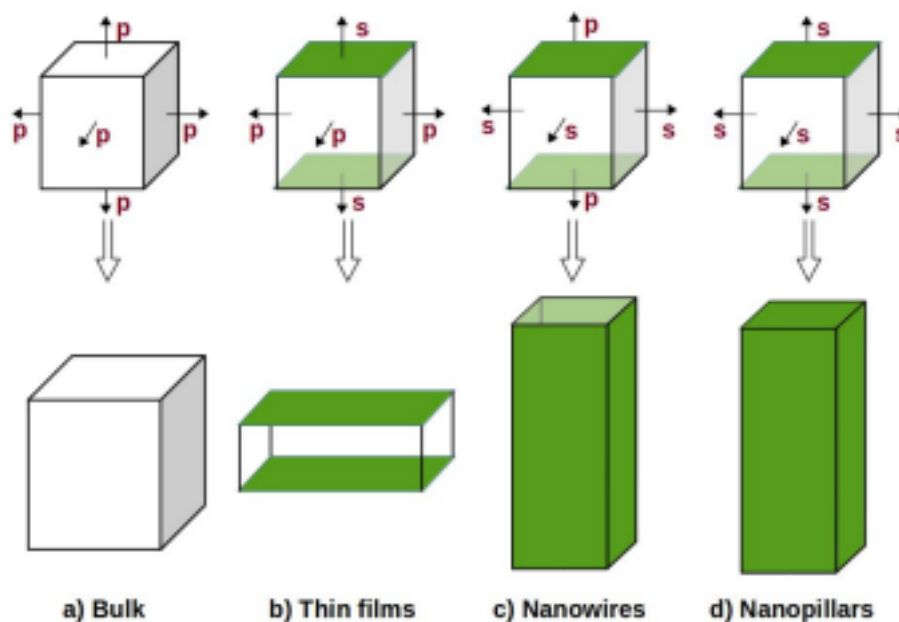


Figure 2.4: Boundary conditions applied for generating different models. a) Bulk material model, b) thin film model, c) nanowire model d) nanopillar model.

2.2 LAMMPS for molecular dynamics simulations

The concept of molecular dynamics was initially introduced by Alder and Wainwright in the late 1950's [120] to study the interactions of hard spheres. Following them, Rahman carried out the first computational simulation of molecular dynamics using a realistic potential for liquid argon in 1964 [121]. Similarly for simulation of liquid water, the first molecular dynamic simulations were performed in 1974 by Rahman and Stillinger [122]. Following Rahman and Stillinger, a number of codes for performing molecular dynamics have been developed over a period of time. Availability of open source codes with parallel processing increases the usage of existing codes than developing a new code. Some of widely used molecular dynamics codes are LAMMPS [123], CHARMM [124], AMBER [125], NAMD [126]. All these codes are primarily designed for modeling biological molecules, metals and materials. Among all these codes, LAMMPS has been chosen for this study as this code focusses on material modeling along with other advantages such as Open-source distribution, Spatial-decomposition of simulation domain for parallelism etc., In the present study, all the molecular dynamics simulations have been carried out in LAMMPS package installed in 134 Node HPC cluster at IGCAR. The maximum size of the system employed in the present thesis contains close to 3.5 million atoms.

2.3 Pre-processing

All simulation models with different sizes have been created using LAMMPS [123]. The size of nanowire models varies in the range 0.723-43.38 nm. Also the nanowire models with various crystallographic orientations distributed on a standard stereographic triangle has been created using LAMMPS package[123]. One of the objectives of the present study is to understand the shape/cross-section dependence of deformation behaviour. To study this shape effect, nanowires with different cross-sections such as triangular, square, pentagonal, hexagonal and circular has been chosen. These nanowire models with different cross-sections have been created with the help of Tinkercad [127]. Tinkercad is a free, online 3D modeling program that runs in a web browser, known for its simplicity and ease of use. Tinkercad allows users to add/remove/modify any set of shapes to create any intricate and detailed model to work with. Modeled shapes designed from Tinkercad can be imported in three formats: Standard Triangle Language (STL) and OBJ for 3D, and 2-dimensional Scalable Vector Graphics (SVG) shapes for extruding into 3D shapes. In the present study, we have used Tinkercad to create nanowires with different shapes as shown in Figure 2.5a, and export the nanowire models in STL formats and filled it with atoms with the help of software AtomsK [128].

In the present study, twinned nanopillars have been chosen to study the influence of twin boundary on mechanical behaviour. So to generate a twin boundary, the nanopillar has been divided into two regions. Following this, the twin boundary has been created by rotating one region of the crystal with respect to other by a required angle (180°) around a specific axis. This operation has been performed using AtomsK software [128]. AtomsK is a free, open source command-line program dedicated to the creation, manipulation, and conversion of data files for atomic-scale simulations. AtomsK proposes options for applying elementary transformations: duplicate, rotate, deform, insert dislocations, merge several systems, create bi-crystals and polycrystals, etc. It supports the file formats used by many programs such as LAMMPS [123], AtomEye [129], OVITO [130]. Similarly, the polycrystalline nanowire models in the present study has been prepared using Voronoi algorithm with random grain orientations using AtomEye utility [129, 131] as shown in Figure 2.5b.

Once the initial test nanowire/nanopillar models were generated using above mentioned techniques, the system may not be in a minimum energy configuration, i.e. the atoms may

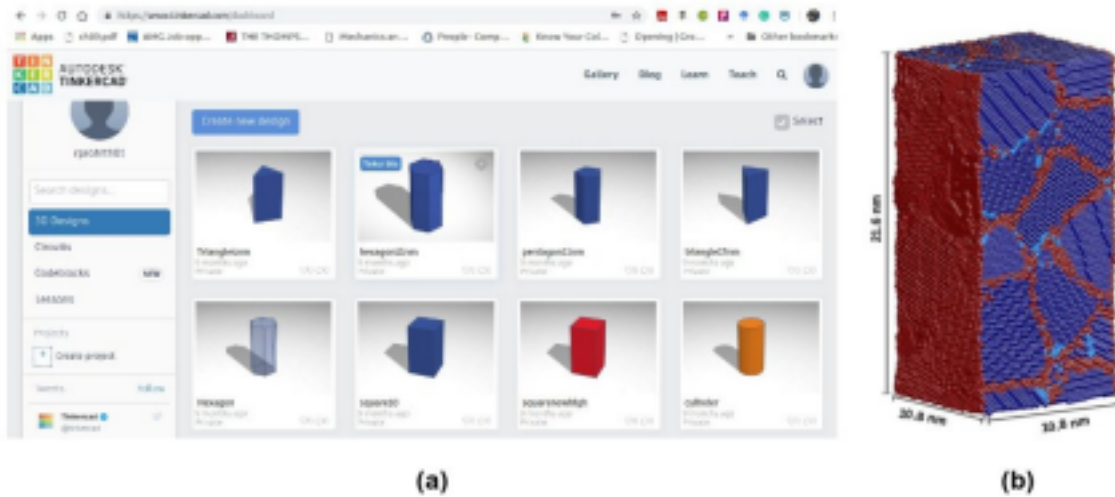


Figure 2.5: a) Tinkercad, an open source online platform for modeling nanowire shapes [127].
 b) A model polycrystal nanowire prepared using Voronoi algorithm from AtomEye software [129, 131]

be too close to each other. At this stage, if the equations of motions are integrated, the total energy of the system will not change, which may not be in equilibrium state, and the system is said to be in microcanonical ensemble (NVE). In this ensemble, the total number of particles N , system volume V , and total energy E are kept constant. As the state of the system does not represent the stable realistic experimental conditions, one has to use other ensembles such as canonical (NVT) and isobaric-isothermal (NPT), which allows to keep the system under a particular temperature and pressure. In the present thesis, canonical (NVT) ensemble has been maintained for all simulations, where, the total number of particles N , system volume V , and temperature T are kept constant. Then, the minimum energy configuration has been obtained by adjusting the atomic coordinates from their original position and then calculating the total energy of the system. This process has been repeated iteratively using conjugate gradient (CG) method to obtain a relaxed structure with equilibration atomic positions corresponding to the nanowire/nanopillar. The minimization has been carried out until the energy change between successive iterations divided by the energy magnitude is less than or equal to the specified energy tolerance i.e., 10^{-25} (stopping criterion). Following energy minimization, the equilibrated system has been thermally equilibrated by assigning initial velocities according to Gaussian distribution, to all atoms [102]. Following this, the system was thermally equilibrated by assigning the initial particle velocities from a Maxwell-Boltzmann distribution at the desired temperature and, then equilibrating for 100 ps.

To maintain constant temperature in canonical ensemble (NVT), velocity rescaling method

can be used, where the velocities of particles are scaled periodically to obtain the desired temperature. However, this method does not allow the fluctuations in temperature which is always present in canonical ensemble, and also violates the conservation of energy. This issue can be solved by attaching external thermostats such as Nose-Hoover thermostat [132, 133, 134] and Berendsen thermostat [135]. In the present thesis, Nose-Hoover thermostat has been used implemented by coupling additional degrees of freedom to the particle velocities, which modifies the equation of motions [132, 133, 134]. While attaching Nose-Hoover thermostat, a damping constant of 100 fs for all temperatures has been chosen. The choice of damping constant has been optimized due to the following constraints. If the temperature damping parameter is too small, then the temperature can fluctuate wildly. At the same time, if it is too large, the temperature will take a very long time to equilibrate. This specified value of damping constant has ensured that the temperature fluctuations are always lower than 1% during simulations irrespective of test temperature. With this step, the thermally equilibrated system is ready for loading step.

2.4 Loading procedure

The thermally equilibrated system has been loaded under tension and compression in two different types of loading procedures as follows:

2.4.1 Procedure I:

In this method, the simulation box (nanowire) height is varied uniformly along the loading/axial direction as shown in Figure 2.6. The initial nanowire dimensions along three mutually orthogonal directions is indicated by dotted lines as L_x , L_y , and L_z . During tensile loading, the nanowire has been pulled/elongated along L_z direction (Figure 2.6). Under tensile loading, the simulation cell dimensions varies with time and can be seen from Figure 2.6 as $L(t)_x$, $L(t)_y$, and $L(t)_z$. For maintaining the simulation cell volume constant, the simulation cell along transverse directions will shrink in line with Poisson's ratio. Further, to conserve the number of atoms and their trajectory, the coordinates of atomic positions have been remapped into the simulation box, whenever the box dimensions got changed. During MD simulations, the cell

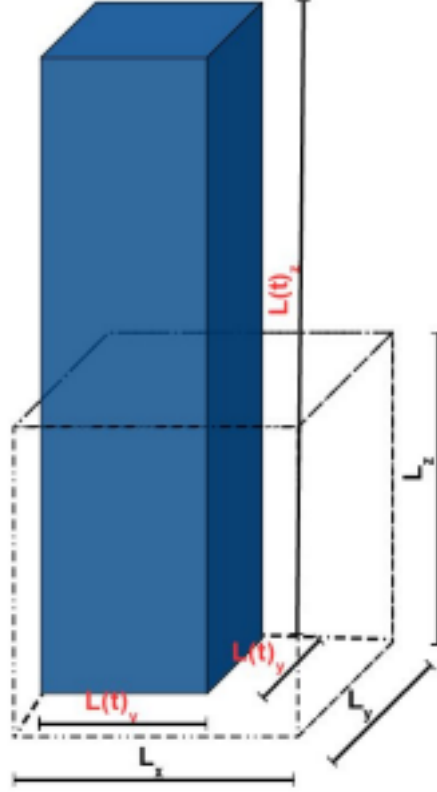


Figure 2.6: Testing procedure I: The original dimensions of simulation cell represented by dotted lines as L_x , L_y , and L_z . The instantaneous simulation cell dimensions during loading is shown by continuous line $L(t)_x$, $L(t)_y$, and $L(t)_z$.

height/length ($L(t)_z$) as a function of time is varied as

$$L(t)_z = (L)_z(1 + \dot{\epsilon}t). \quad (2.19)$$

Here, $\dot{\epsilon}$ is strain rate and t is the elapsed time. This equation (2.19) indicates that the simulation cell height/length changes linearly from initial value to a specified final value, which in-turn results in deformation of simulation cell at a constant engineering strain rate ($\dot{\epsilon}$). Similarly, under compressive loading too, MD simulations have been performed under constant strain rate ($\dot{\epsilon}$). All the nanowires deformed in the present study under either tension or compression have been loaded at uniform strain rate following this procedure.

2.4.2 Procedure II:

All nanopillars with free surfaces along three orthogonal directions, has been deformed under both tension and compression using this loading procedure. In this procedure, nanopillar model

is divided into three regions i.e., two fixed regions which acts as grips at the top and bottom of the nanopillar, and an active region as shown in Figure 2.7. This fixture in general resembles

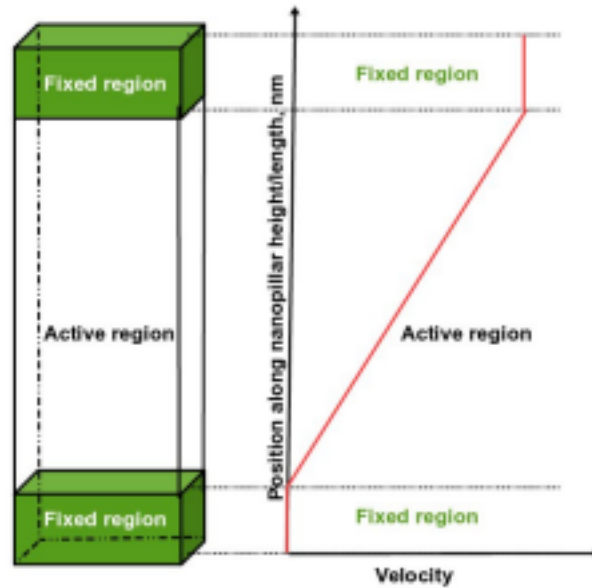


Figure 2.7: Procedure II: Bottom end of nanowires has been hold constant and the top end has been elongated at a constant velocity. Velocity profile vs position in correspondence to the simulation cell.

the experimental fixtures with grips at both ends of the specimen. In this method of loading, one end of the nanopillar, usually the bottom region has been held fixed and then the other end, i.e., the top region will be elongated/moved at a constant velocity under tension. The maximum constant velocity at the top region has been chosen in such a way that the atoms in atoms in the active region have been given a ramp velocity profile that varied linearly from zero at the bottom region to a maximum value at the top region as clearly shown in Figure 2.7. The ratio of maximum velocity at the top region to the original simulation cell/nanopillar length gives the magnitude of the applied strain rate ($\dot{\epsilon}$). Similar procedure has been applied during compression tests. This method is usually known as displacement controlled method of loading.

The important difference between the above two methods are, in procedure -I, only the atomic coordinates are remapped without altering their velocities, while in procedure -II, the moving boundaries can add a velocity component to the atoms. Irrespective of the method of loading, the strain rate considered in the the present MD simulations is significantly higher ($5 \times 10^7 s^{-1}$ to $1 \times 10^9 s^{-1}$) than the experimental strain rates (usually $1 \times 10^{-3} s^{-1}$), which is due to the inherent time scale limitations from molecular dynamics. As discussed earlier, the typical time-steps used in the present MD simulations is 2 fs. Despite high strain rates, many

results obtained using MD simulations are in good agreement with the experimental results qualitatively [29, 45, 46, 50, 136, 137]. During deformation, all nanowires/nanopillars were allowed to deform naturally at a constant strain rate without imposing any stress constraints in other two directions. The stress (σ) in the loading (z) direction has been calculated using the Virial expression [138] as implemented in LAMMPS's compute pressure command (Pzz) [123]. Stress calculated according to Virial definition [139, 140] takes the following form :

$$\sigma_{\alpha\beta} = \frac{1}{V} \left[\frac{1}{2} \sum_i^N \sum_{j \neq i}^N F_{ij}^\alpha r_{ij}^\beta - \sum_i^N m_i v_i^\alpha v_i^\beta \right]. \quad (2.20)$$

Here, N is the total number of atoms, V is the volume of the simulation cell, r_{ij}^β is the distance between atoms i and j along the direction β , F_{ij}^α is the force between atoms i and j along the direction α , m_i and v_i are the mass and velocity of particle i, and the indices α and β denote the Cartesian components and takes the values of x, y and z. The first term in the above equation is due to the inter-atomic force (potential energy) and the second term is due to thermal vibrations (kinetic energy). In general, the kinetic energy term is smaller than inter-atomic force term for solid materials [140]. This observation is especially true when stress calculations are performed at relatively low temperatures (10 K). This atomistic definition of stress is equivalent to the continuum Cauchy stress. Further, the strain (e) has been obtained as $e = (L_z - L_{z0})/L_{z0}$, where L_z is the instantaneous length and L_{z0} is the initial length after equilibration. These definition of stress and strain has been used in the present work to determine the stress-strain response of the nanowires/nanopillars under different loading conditions.

2.5 Post-Processing

As described earlier in previous section, MD simulations have been performed on the simulation cell models with atoms varied from a few thousands of atoms to a maximum of 3.5 million atoms. The space trajectory of all atoms, defect configurations and other such vast information which needs to be processed to draw reasonable conclusions. Various techniques have been developed and reported in the literature to distinguish the perfect atoms and defect structures. Different parameters such as coordination number, centro-symmetry parameter and common neighbor analysis have been utilized as post-processing techniques in the present study. These

parameters basically separate the defects such as vacancies, dislocations, stacking faults, surfaces and other structural features from the perfect regions. The basic principle behind each of these techniques is briefly described in the following;

2.5.1 Coordination number (CN)

The coordination number is defined as the number of nearest neighbor atoms in all directions. In face-centered cubic (FCC) lattice, each atom is surrounded by 12 nearest neighbors at a distance of $a/\sqrt{2}$ or $0.707a$, where a is the lattice parameter. Therefore, the coordination number of an atom in FCC lattice is 12, i.e., 6 atoms in the same plane ($\{111\}$) and 3 atoms located at above and below plane. This indicates that any atom with CN different from that of 12 denotes that the atom is not of FCC lattice, but of defect structures. These defects includes dislocation cores, stacking faults, surface orientations etc., Therefore, using color-coding the atoms based on their coordination number, the defects can be distinguished from the perfect lattice and also the FCC phase from BCC or any other phase. This can be done by removing the perfectly coordinated atoms, which leaves us only with defect configurations. Also, the coordination number can also be used to differentiate surfaces of various crystallographic orientations. However, the atoms in bulk HCP lattice have a coordination number of 12, similar to that of FCC, which cannot be differentiated based on coordination number. To differentiate HCP atoms from FCC atoms, another popular technique, common neighbor analysis (CNA) has been defined.

2.5.2 Common neighbor analysis (CNA)

Another popular structure analysis for defect visualization is the common neighbor analysis (CNA), which was proposed by Honeycutt and Anderson [141]. The common neighbor analysis (CNA) is useful parameter for obtaining local crystal structure around an atom. In CNA method, a characterized signature is computed from the detailed geometric analysis of a set of common neighbours of two atoms within a specific cut-off distance [141]. The detailed CNA methodology was described by Faken and Jonsson [142], and Tsuzuki and his co-workers [143]. In the original CNA method proposed by Honeycutt and Andersen [141], a structure is represented by diagrams. Starting with a pair of atoms, α and β , the diagram is classified by a set of four indexes [141, 143, 144]: i, j, k and l , where

- i with values 1 or 2 indicates that α and β are nearest-neighbors ($i = 1$) or not ($i = 2$);
- j indicates the number of nearest neighbors shared by the (α, β) pair (common neighbors);
- k indicates the number of bonds among the common neighbors;
- l differentiates diagrams with same $i, j,$ and k indexes and different bonding among common neighbors.

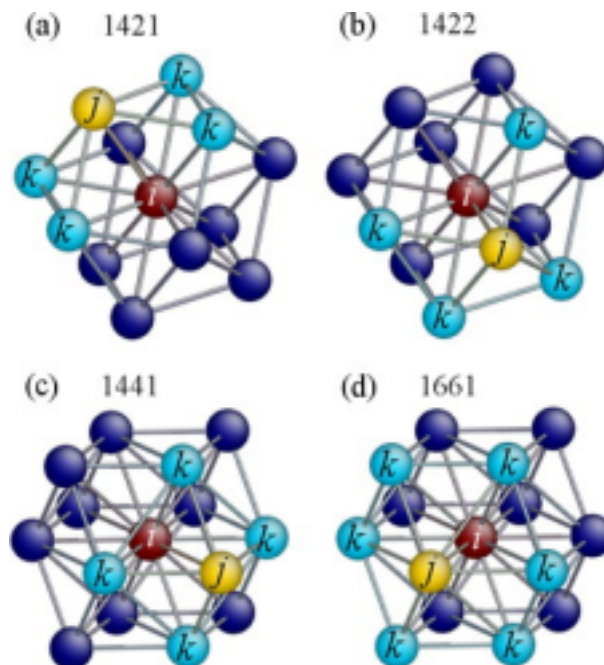


Figure 2.8: CNA for a) FCC b) HCP, and c-d) BCC systems with different indexes according to Honeycutt and Anderson [141].

For instance, the common neighbor analysis of bulk FCC, HCP and BCC has been shown in Figure 2.8. It can be seen that any atom in perfect FCC structure (for example brown atom in Figure 2.8a) has 12 nearest neighbors. Here, brown (α) and yellow (β) atoms indicate one pair of nearest neighbor atoms, which indicates $i = 1$. With each of nearest neighbors, the brown-yellow pair shares 4 common neighbors (the light-blue atoms, $j = 4$), i.e. the neighbors common to pair of atoms (brown and yellow) containing the original brown atom within this shell. Out of this four common neighbors, only two geometrical bonds are possible i.e. $k = 2$. This two bonds are the longest possible chains among the common neighbors and the number

of bonds in this chains is one, i.e. $l = 1$. Therefore, an atom in bulk FCC structure has a geometrical index of 1421. Since all 12 bonds of each atom are the same, a local environment with 12 nearest neighbors and an geometric index of 1421 can be identified as FCC structure [141, 143, 145]. Similarly, Figure 2.8b shows the diagram with index of 1422 which represents HCP structure. In the HCP structure half the pairs of nearest neighbor atoms form 1421 indexes, while the other half form 1422 indexes. Further, it can be seen from Figure 2.8c-d that both 1661 and 1441 indexes are found for BCC structure [141, 143]. The BCC structure has an unbalanced distribution of diagrams with 6/14 of the nearest neighbor atoms pairs forming 1441 indexes, while the rest 8/14 forming 1661 indexes. There is a slight difference between Honeycutt CNA indexes [141] and the CNA signatures proposed by Faken et al.[142] and Tsuzuki et al.[143]. The latter has only three indexes (jkl). The complete list of signatures for different structures and their surfaces can be found in the work of Cleveland et al.[146]. In the present thesis, LAMMPS [123] and OVITO [130] softwares, CNA methodology described by Faken et al.[142] and Tsuzuki et al.[143] ie., with only three indexes (jkl) has been used. At present, LAMMPS recognizes five different kinds of lattices with varied CNA signatures. Each crystal lattice has been assigned by a well defined value of 1, 2, 3, 4 and 5 for FCC, HCP, BCC, icosahedral and unknown (surfaces, dislocation cores) lattices respectively. This CNA parameter can be used to differentiate FCC phase from HCP, BCC or any other phases. For example, Figure 2.9 shows an atomic configuration of twinned Cu nanopillar visualized with the help of CNA. It can be seen that the blue color atoms represents the perfect FCC atoms, cyan color atoms represents HCP atoms (both stacking faults in FCC and twin boundaries), while the red color atoms indicate the free surfaces and dislocation core.

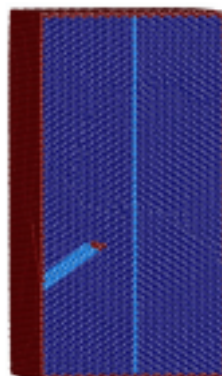


Figure 2.9: A model nanowires visualized using CNA parameter. The blue color atoms represents the perfect FCC atoms, cyan color atoms represents HCP atoms (both stacking faults in FCC and twin boundaries), while the red color atoms indicate the free surfaces and dislocation core.

2.5.3 Central symmetry parameter (CSP)

Central symmetry parameter is another powerful, robust method for analyzing the crystalline structures obtained from MD simulations with high precision. CSP is used to characterize the degree of inversion symmetry in each atom's local environment [147]. In other words, CSP method quantifies the local deviations from centrosymmetry in a given centrosymmetric structure such as FCC and BCC structures [147]. Based on these local deviations, defects are effectively identified and distinguished from elastically deformed regions. CSP calculations exploits the fact that a centrosymmetric material will remain centrosymmetric under a homogeneous elastic deformation [147, 143]. However, when a defect is present, this relation no longer holds good. In such materials each atom has a certain number of pairs of opposite bonds formed by the nearest neighbor atoms. Figure 2.10a-b shows the opposite pairs in the FCC, and BCC structures. In FCC structure (Figure 2.10a) each atom has 6 pairs of opposite nearest neighbor atoms (represented by same color), and therefore 6 pairs of opposite bonds. Similarly, in BCC structure, 7 pairs of opposite neighbors can be seen (both 1st and 2nd shell considered as single shell) in Figure 2.10b. Kelchner et al. [147] explained CSP for each atom as follows:

$$CSP = \sum_{i=1}^{N/2} |R_i - R_{1+N/2}|^2. \quad (2.21)$$

Where N is the nearest neighbor atoms (coordination number), R_i and $R_{i+N/2}$ are the vectors from the central atom to a particular pair of nearest neighbors. For an atom in a perfect lattice, the magnitude of CSP is zero and it still lies close to zero even for small thermal fluctuations [147]. However, in the presence of any defect structure, this symmetry is broken due to changes in either bonds length or direction, or both, which results in the positive magnitude of CSP. Depending on the crystal structure, the CSP has distinct values for dislocations, stacking faults, point defects and surfaces [147]. For example, any atom at a free surface or corner atoms exhibits a large positive CSP value i.e., 1 - 4.8. Similarly, CSP magnitude of 0.43 - 0.48 for stacking faults and twin boundaries, 0.37 - 0.38 for dislocation cores, and 0.06 - 0.36 for full dislocations and Shockley partials. Therefore, with the aid of an imaging software that colors the atoms according to their CSP values, different defect structures can be visualized more precisely, while hiding the atoms having the CSP values close to zero. Thus, the CSP can be used to identify a local lattice disorder around an atom. In the present work, CSP has been

used to detect point defects, partial/twinning dislocations, full dislocations, twin boundaries and other grain boundaries observed during the deformation of FCC Cu nanowires.

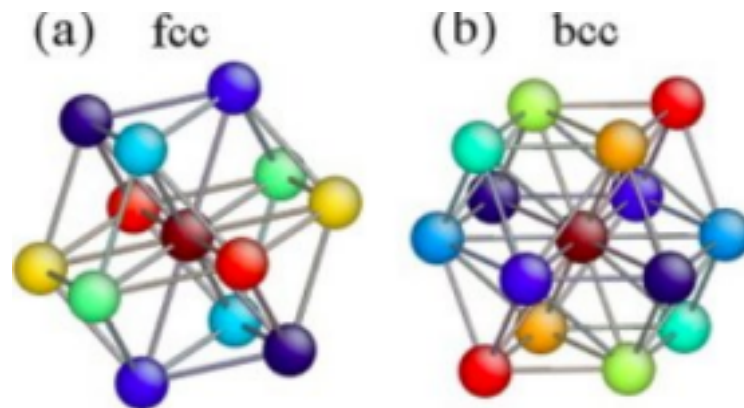


Figure 2.10: Colored opposite pairs in a) FCC, and b) BCC structures.

2.5.4 AtomEye

The various defect configurations generated during MD simulations have been visualized using AtomEye developed by Ju Li [129, 131]. It is a free atomistic three-dimensional visualization software and it shows the atoms as spheres and bonds as tubes/cylinders. The main functions of the AtomEye are as follows:

- 3D navigation with parallel and perspective projections
- coordination number calculations
- color-coding of atoms according to CNA/CSP parameters
- cutting of planes, and calculating the distance/angle between any two/three atoms
- produces high quality JPEG, PNG and EPS images and also supports animation scripting

AtomEye can handle more than one million atoms on a simple desktop computer. In the present work, the AtomEye package has been extensively used for the visualization of atomic

snapshots. However, the AtomEye is not capable of determining the type of defects i.e., dislocation, vacancy, grain boundary, etc. or any quantitative information such as dislocation density of defects or the Burgers vector of a dislocation. In this backdrop, Dislocation extraction algorithm (DXA)[148, 149] has been used

2.5.5 Dislocation extraction algorithm (DXA)

The Dislocation extraction algorithm (DXA) was proposed by Stukowski and Albe [148], which is a widely used powerful method for characterizing the topological structure of dislocations obtained from MD simulations. DXA identifies all dislocation line defects in an atomistic crystal, determines their Burgers vectors, and outputs in the form of line representation of dislocations. DXA determines the Burgers vectors of dislocations reliably, and the extracted dislocation network fulfills the Burgers vector conservation rule at each node [148]. All remaining crystal defects (grain boundaries, surfaces, etc), which cannot be represented by one-dimensional dislocation lines, are output as triangulated surfaces. This geometric representation is ideal for visualizing complex defect structures, even if they are not related to dislocation activity. DXA methodology involves the characterization of dislocation core atoms using standard CNA approach [141, 143, 144]. Then, an oriented, closed, two-dimensional interface mesh is built, which distinguishes crystalline atoms from the disordered ones. Finally, on this manifold for each dislocation segment, an initial Burgers circuit is constructed (Figure 2.11). While the closed Burgers circuit and its reverse copy are swept in both directions, a one-dimensional line representing of the dislocation segment is obtained by recording the current mass center of the Burgers circuit and the Burgers vector can be computed [148, 149]. DXA can identify and index dislocations including partial dislocations and secondary grain boundary dislocations and determine their Burgers vectors representing arbitrary dislocation networks by connected and fully indexed lines. It is a useful tool to analyze and visualize atomic simulations of material plasticity. In the present study, we have used DXA tool utility from an open source software Open Visualization Tool (Ovito) developed by Stukowski [130], to extract dislocation lines along with their Burgers vectors, and calculate dislocation density. In addition to dislocation analysis, the main functions of OVITO are calculation and visualization of displacement vectors obtained from the differences between two states of the system, slicing and cutting of atomic structures, selects atoms based on defined criteria, perform common neighbor analy-

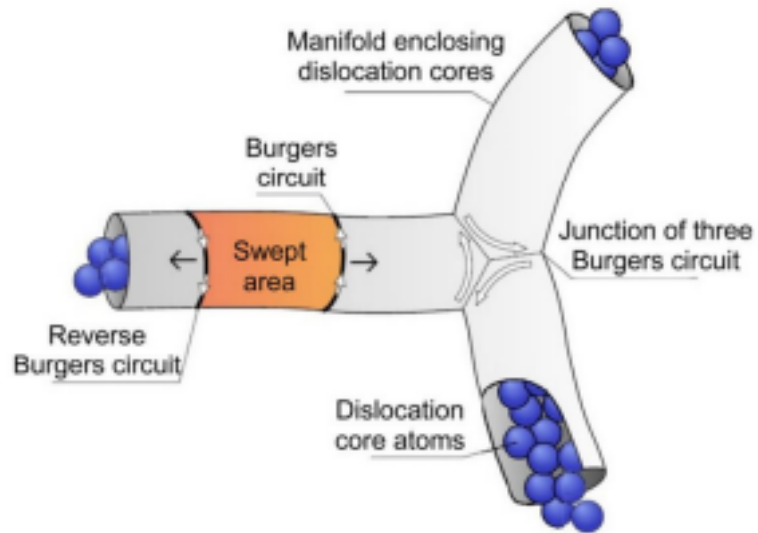


Figure 2.11: DXA methodology illustrating the interface mesh sweeping the dislocation line. While the Burgers circuit is being advanced in a step-wise fashion, triangle by triangle, a continuous line representation of the dislocation defect is produced.

sis, coordination number analysis, calculate radial distribution function and other atomic level strain tensors [130].

Chapter 3

Orientation dependent deformation behaviour of Cu nanowires under compression and tension

3.1 Introduction

It has been well established that, the important mechanisms of plastic deformation in single crystalline FCC nanowires like Au, Ag, Cu, Pt, Al, and Ni are slip through perfect and partial dislocations and deformation twinning [27, 37, 38, 39, 40, 41, 42, 43]. The competition between slip and twinning mechanisms depends mainly on the crystallographic orientation, size, shape and loading mode (tension/compression), temperature and strain rate [28, 29, 48]. However, among all these factors, crystallographic orientation has the strongest influence followed by mode of loading [27, 43, 28]. For example, Zheng et al. [37] studied the orientation dependent deformation behaviour of Au nanocrystals using in-situ high resolution transmission electron microscope (HRTEM) combined with MD simulations. It has been shown that under tensile loading of Au nanocrystal, the deformation by slip is favoured in $\langle 100 \rangle$ orientation, while twinning is observed in $\langle 110 \rangle$ orientation. Similar to $\langle 110 \rangle$ orientation, the deformation by partial slip/twinning is preferred under the tensile loading of $\langle 111 \rangle$ oriented FCC nanowires [27, 40]. Similarly to understand the influence of mode of loading (tension/compression), Lee et al. [38] carried out the experimental and atomistic simulation study

on the tensile and compressive deformation of $\langle 110 \rangle$ Au nanopillars. Under tensile loading, the deformation by twinning was observed, while dislocation slip has occurred under the compressive loading of $\langle 110 \rangle$ Au nanopillar [38]. Contrary to $\langle 110 \rangle$ orientation, the $\langle 100 \rangle$ oriented FCC nanowires deform by slip under tensile loading, while twinning is observed under compressive loading [27, 37, 28].

The above results strongly suggest that the deformation behaviour of FCC nanowires depends on the orientation and mode of loading. However in the literature, the deformation mechanisms and tension-compression asymmetry have been investigated mainly in high symmetry $\langle 100 \rangle$, $\langle 110 \rangle$ and $\langle 111 \rangle$ crystallographic orientations, which constitutes the corners of a standard stereographic triangle [28]. In view of this, understanding the deformation mechanisms over a wide range of orientations in FCC nanowires is important. Moreover, the variations of yield strength and its asymmetry with respect orientation have not been studied systematically. To fulfill these goals, MD simulations have been performed on Cu nanowires of different crystallographic orientations distributed uniformly on the standard stereographic triangle (Figure 3.1). The orientations falling on the corners, boundaries and in the interior of the standard stereographic triangle have been considered. In addition to above, the influence of loading mode (tension/compression) has been examined for all the orientations. The yielding behaviour, yield strength and deformation mechanisms of all the nanowires under tensile and compressive loadings have been presented and discussed. Finally an attempt has been made to understand the orientation dependent deformation mechanisms in terms of a single parameter α , defined as the ratio of leading partial Schmid factor to trailing partial Schmid factor.

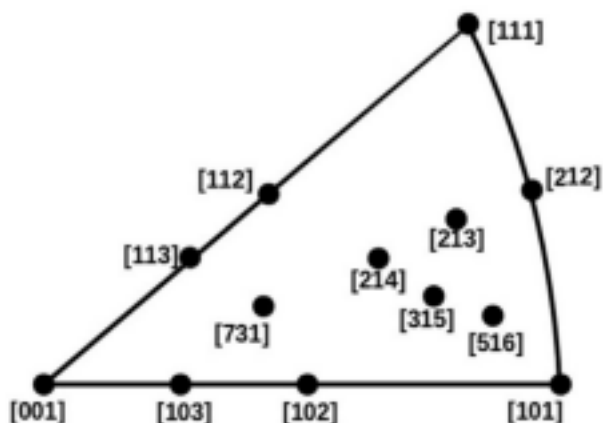


Figure 3.1: Standard stereographic triangle with various crystallographic orientations chosen in the present study. Cu nanowires with these orientations have been subjected to tensile and compressive loading.

3.2 MD simulation details

Molecular dynamics (MD) simulations have been performed using Large scale Atomic/Molecular Massively Parallel Simulator(LAMMPS) package [123] employing an embedded atom method(EAM) potential for FCC Cu given by Mishin and co-workers [108]. This potential has been chosen for being able to reproduce stacking fault and twinning fault energies for Cu [24], which are key variables for predicting the dislocation nucleation and deformation mechanisms in nanowires. For more details on potentials see 2.1.1.

In order to understand the orientation dependent deformation behaviour, the orientations falling on the corners ($\langle 100 \rangle$, $\langle 110 \rangle$ and $\langle 111 \rangle$), boundaries ($\langle 115 \rangle$, $\langle 113 \rangle$, $\langle 112 \rangle$, $\langle 212 \rangle$, $\langle 102 \rangle$ and $\langle 103 \rangle$) and interior ($\langle 213 \rangle$, $\langle 214 \rangle$, $\langle 315 \rangle$ and $\langle 516 \rangle$) of the standard stereographic triangle have been chosen in the present study. All these orientations are distributed uniformly over the standard stereographic triangle (Figure 3.1). The side surfaces of all the nanowires with different orientations have been presented in Table 3.1. All the nanowires

Table 3.1: The nanowire orientations along with their side surfaces.

Orientation	$\langle 100 \rangle$	$\langle 110 \rangle$	$\langle 102 \rangle$	$\langle 103 \rangle$	$\langle 111 \rangle$	$\langle 112 \rangle$	$\langle 113 \rangle$	$\langle 212 \rangle$	$\langle 213 \rangle$	$\langle 214 \rangle$	$\langle 315 \rangle$	$\langle 516 \rangle$
Side surface	{100}	{110}	{100}	{100}	{110}	{110}	{110}	{110}	{111}	{201}	{130}	{111}
Side surface	{100}	{110}	{120}	{130}	{112}	{111}	{233}	{114}	{145}	{1,2,10}	{123}	{4,7,11}

have a square cross-section width (d) of 10 nm and length(l) of 20 nm, providing an aspect ratio of 2:1. Periodic boundary conditions have been chosen along the nanowire length direction, while the other two directions were kept free in order to mimic an infinitely long nanowire. Following initial construction of the nanowire, energy minimization was performed by conjugate gradient method to obtain a relaxed structure. The relaxed nanowire is thermally equilibrated to a required temperature of 10 K in canonical ensemble (constant NVT) with a Nose-Hoover thermostat. Velocity Verlet algorithm has been used to integrate the equations of motion with a time step of 2 fs. Upon completion of the equilibration process, the nanowires were deformed under tensile and compressive loading at a constant engineering strain rate of $1 \times 10^8 \text{ s}^{-1}$ along the nanowire length direction. The stress has been obtained using the Virial expression [140], which is equivalent to a Cauchy's stress in an average sense as given in equation 2.20. Finally, AtomEye package [129, 131] and OVITO [130] have been used for the visualization of atomic snapshots with common neighbor analysis (CNA).

3.3 Results

3.3.1 Deformation behaviour under compression

The compressive loading has been performed on Cu nanowires of different crystallographic orientations up to a strain value of 0.4. The evolution of atomic configurations at various stages of deformation were analyzed for all the orientations using the common neighbor analysis. Based on this analysis, the deformation mechanisms under the compressive loading of Cu nanowires have been classified into twinning and dislocation slip as described in the following:

Deformation through twinning

Cu nanowires with $\langle 100 \rangle$, $\langle 103 \rangle$ and $\langle 113 \rangle$ orientations (Figure 3.1) deform by twinning mechanism under compressive loading. As a representative of twinning mechanism, Figure 3.2 shows the deformation behaviour of $\langle 100 \rangle$ Cu nanowire at different strain levels. It can be seen that the nanowire yields through the nucleation of a single $1/6\langle 112 \rangle$ Shockley partial dislocation on $\{111\}$ plane from the corner with a stacking fault in its wake (Figure 3.2a). On the contrary, nucleation of multiple Shockley partial dislocations has been observed during the compressive deformation of $\langle 103 \rangle$ and $\langle 113 \rangle$ Cu nanowires. Following yielding, another Shockley partial nucleates on the adjacent plane and creates nano-twin in the nanowire (Figure 3.2b). This shows that the presence of stacking faults are must for formation of twins in the nanowires [150, 151]. The stacking faults needed to form the twins were created by the glide of leading partials nucleated from the nanowire surface. With increasing strain, the continuous nucleation and glide of twinning partials along the twin boundaries leads to twin growth (Figure 3.2c-d). It can be seen that the twinning partials glide in mutually opposite directions on two twin boundaries and as a result the twin boundaries move away from each other leading to the twin growth (Figure 3.2c-d). The continuous propagation of twin boundaries along the nanowire length progressively reorients the twinned region. Due to periodic boundary conditions along the nanowire length, the twin boundaries across the length meet each other and annihilate leaving a defect free reoriented nanowire (Figure 3.2e). Thus, the deformation by twinning on a single twin system transforms the orientation of nanowire from $\langle 100 \rangle / \{100\}$ to $\langle 110 \rangle / \{111\}$. After the reorientation, the nanowire again undergoes an

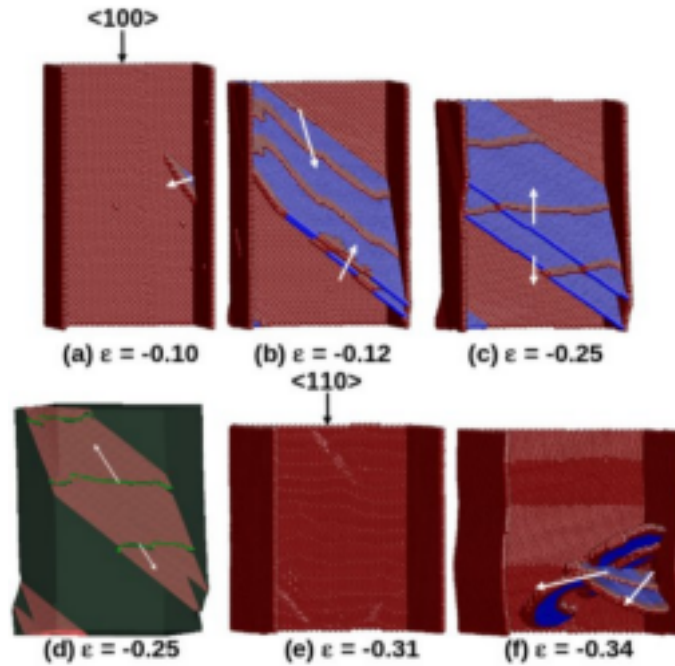


Figure 3.2: Atomic snapshots displaying (a) nucleation of a Shockley partial, (b) glide of twinning partial and nano-twin, (c-d) twin growth (e) reoriented nanowire, and (f) the slip of extended dislocation in the reoriented nanowire during the compressive deformation of $\langle 100 \rangle$ Cu nanowires. In Figure (d), the partial dislocations are shown as green lines as obtained in OVITO [130], while the remaining figures are obtained using AtomEye. The atoms are colored according to the common neighbor analysis (CNA). The blue color atoms represents the FCC and the red color atoms indicate the surfaces and dislocation core.

elastic deformation followed by yielding through the nucleation of a new $1/6\langle 112 \rangle$ Shockley partial on a different crystallographic plane. Following yielding, the deformation in the reoriented nanowire proceeds by the slip of extended dislocations (Figure 3.2f). Similar to $\langle 100 \rangle$ nanowire, deformation by partial slip and twinning has been observed under the compressive loading of $\langle 103 \rangle$ and $\langle 113 \rangle$ Cu nanowires. However, due to twin-twin interactions, the reorientation has not been observed in $\langle 103 \rangle$ and $\langle 113 \rangle$ nanowires.

Deformation through slip

The Cu nanowires with $\langle 101 \rangle$, $\langle 111 \rangle$, $\langle 102 \rangle$, $\langle 212 \rangle$, $\langle 213 \rangle$, $\langle 214 \rangle$, $\langle 315 \rangle$ and $\langle 516 \rangle$ orientations deform by full dislocation slip alone. As an example, the deformation behaviour in $\langle 111 \rangle$ (representing the orientations along the boundary of a triangle in Figure 3.1) and $\langle 214 \rangle$ (representing the orientations inside the triangle in Figure 3.1) Cu nanowires has been presented in Figures 3.3 and 3.4, respectively. It can be seen that the yielding in both the

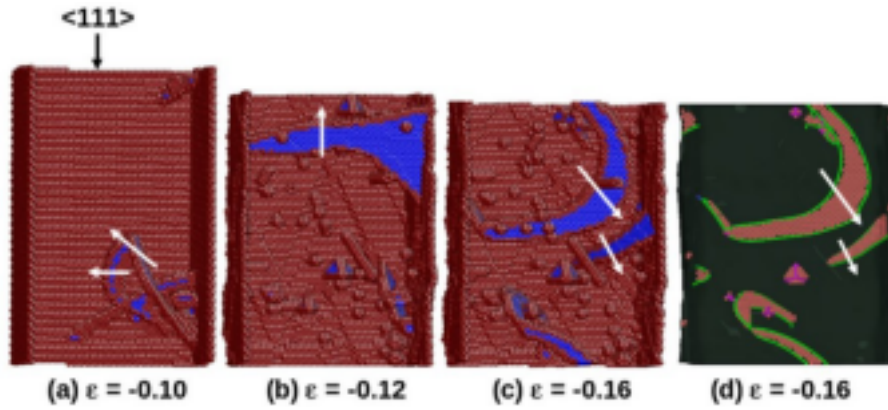


Figure 3.3: Atomic snapshots displaying the compressive deformation of $\langle 111 \rangle$ Cu nanowires as a function of strain. The deformation by the slip of extended dislocations along with stacking fault tetrahedron and many point defects can be seen in (b), (c) and (d). Figure (d) is the OVITO [130] output of Figure (c), where partial dislocations are shown as green lines, the stair-rod dislocations enclosing the stacking fault tetrahedron are shown in magenta lines. The atoms are colored according to the common neighbor analysis (CNA).

nanowires occurs through the nucleation of a leading partial immediately followed by trailing partial, thus constituting an extended dislocation (Figures 3.3a and 3.4a). However in $\langle 111 \rangle$ nanowire, the activation of many slip planes has been observed, while in $\langle 214 \rangle$ nanowire, the activation of only two slip systems has been observed. Following yielding, the nucleated dislocations glide from one corner of the nanowire to the opposite and gets annihilated by leaving a slip steps on the surface of the nanowire (Figures 3.3b and 3.4b). The activation of different slip systems in $\langle 111 \rangle$ nanowire facilitates dislocation-dislocation interactions, which results in the formation of many point defects and also the stacking fault tetrahedron as shown in Figure 3.3b-c. Due to the activation of limited slip system in $\langle 214 \rangle$ nanowire, the formation of point defects has not been observed in the strain range examined (Figure 3.4b-c). Generally, the stacking fault tetrahedron (SFT) in low stacking fault energy materials can form through vacancy condensation, or by an extension of Frank partial dislocation loop or through dislocation-dislocation interactions. However, the SFT formation through vacancy condensation requires longer time scales, which are difficult to access using MD simulations. In the present study, the SFTs have been formed through dislocation-dislocation interactions, similar to that observed by Wang et al. [152].

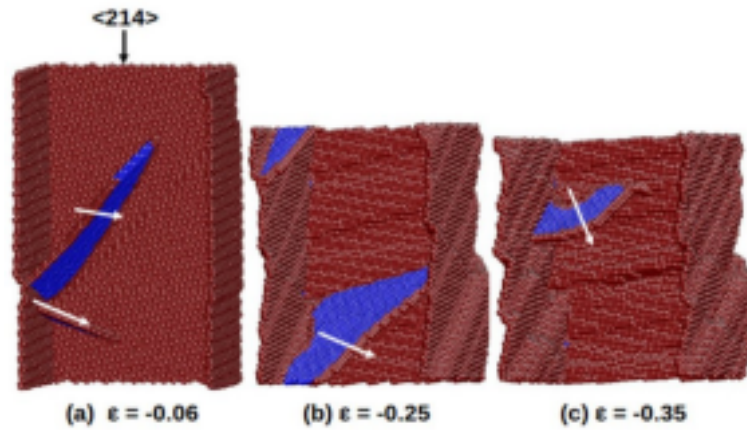


Figure 3.4: Atomic snapshots displaying the compressive deformation of $\langle 214 \rangle$ Cu nanowires as a function of strain. The deformation proceeds through the glide of extended dislocations. The atoms are colored according to the common neighbor analysis (CNA).

3.3.2 Deformation behaviour under tension

In order to investigate the influence of loading mode on the deformation behaviour, MD simulations have been performed on the tensile loading of Cu nanowires with different orientations shown in Figure 3.1. It has been observed that under tensile loading, the deformation in all the Cu nanowires is dominated by twinning mechanism irrespective of the orientations. Full dislocation slip has not been observed in any of the orientations examined. Further, it has been observed that the twinning in certain orientations leads to complete reorientation of the nanowires, while in remaining orientations, it leads to neck formation and early failure without any reorientation. Therefore, the tensile deformation of Cu nanowires has been classified into (i) twinning leading to full reorientation of the nanowire and (ii) twinning without full reorientation.

Twinning leading to full reorientation of the nanowire

Twinning under tensile loading of $\langle 101 \rangle$, $\langle 103 \rangle$, $\langle 212 \rangle$ and $\langle 214 \rangle$ orientations leads to complete reorientation of the nanowires. As an example, the deformation by twinning followed by reorientation in $\langle 101 \rangle$ and $\langle 214 \rangle$ nanowires has been presented in Figures 3.5 and 3.6, respectively. It can be seen that the yielding in both the orientations occurs by the nucleation of Shockley partial dislocations (Figures 3.5a and 3.6a). However in $\langle 101 \rangle$ nanowire, the activation of two different slip planes has been observed (Figure 3.5a), while in $\langle 214 \rangle$ nanowire,

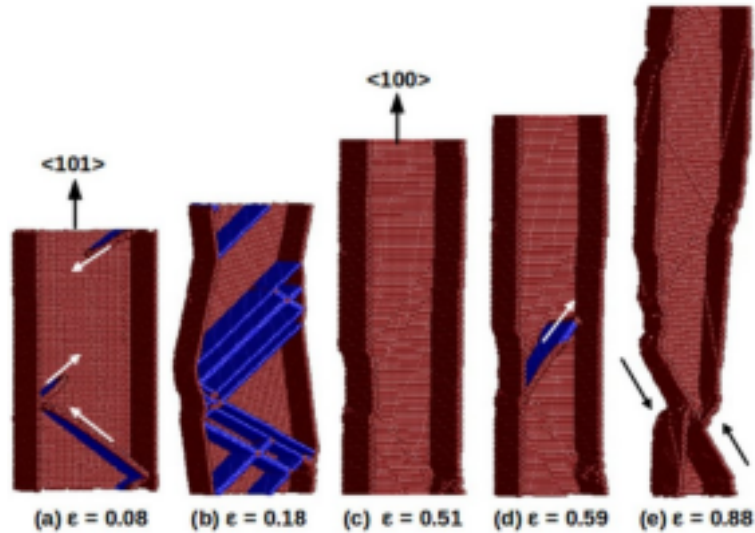


Figure 3.5: The atomic snapshots displaying the tensile deformation of $\langle 110 \rangle$ Cu nanowires as a function of strain. Deformation proceeds through twinning followed by reorientation to $\langle 100 \rangle$ axial direction.

the activation of only one slip system can be seen in Figure 3.6a. Following the nucleation of Shockley partials during yielding, the subsequent nucleation of twinning partial dislocations leads to the formation of twins on the corresponding $\{111\}$ planes (Figures 3.5b and 3.6b). With increasing strain, the twin grows along the nanowire axis leading to complete reorientation of nanowires (Figures 3.5c and 3.6c). Due to twinning, the $\langle 101 \rangle$ nanowire reorients to $\langle 100 \rangle$ nanowire, while $\langle 214 \rangle$ nanowire reorients to a high indexed $\langle hkl \rangle$ direction. Generally, the reorientation is not observed when the slip is activated on more than one twin system, due to twin-twin interactions. However, the $\langle 101 \rangle$ nanowire undergoes reorientation despite the activation of multiple twin systems (Figure 3.5a-c). Following the reorientation, the nanowires undergo a second elastic deformation followed by yielding through the nucleation of Shockley partial dislocations (Figures 3.5d and 3.6d). Following the second yielding in $\langle 101 \rangle$ nanowire, twin formation and the interaction of twin boundaries with Shockley partial dislocations results in neck formation and final failure as shown in Figure 3.5e. On the contrary, the sliding along the twin boundaries (Figure 3.6e) leading to shear failure (Figure 3.6f) accompanied with large strain to failure has been observed in $\langle 214 \rangle$ nanowire.

Twinning without full reorientation

Unlike the $\langle 101 \rangle$, $\langle 103 \rangle$, $\langle 212 \rangle$ and $\langle 214 \rangle$ orientations, the twinning in $\langle 100 \rangle$, $\langle 102 \rangle$, $\langle 111 \rangle$, $\langle 112 \rangle$ and $\langle 113 \rangle$ orientations does not lead to reorientation. Generally, when the

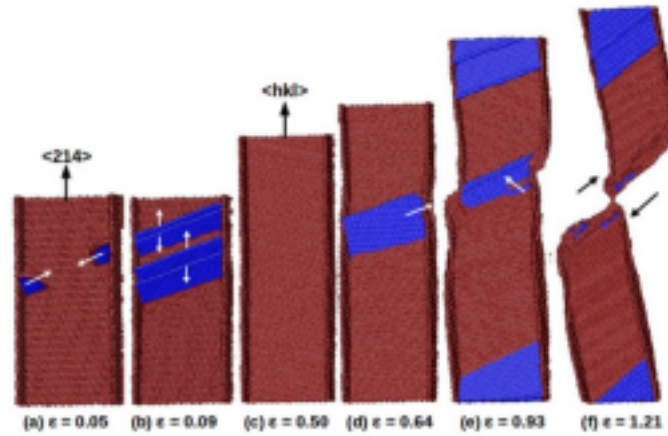


Figure 3.6: The atomic snapshots during the tensile deformation of $\langle 214 \rangle$ Cu nanowires as a function of strain. Deformation proceeds through twinning mechanism followed by reorientation to high index $\langle hkl \rangle$ direction. The final failure occurs by sliding along the twin boundaries.

slip is activated on more than one twin system, there is an increased probability of twin-twin interactions, which disrupts the twin growth process and reorientation [153]. Similarly, when the sliding along the twin boundaries is preferred over twin boundary migration (which is necessary for twin growth), the reorientation is not observed. As an example, the twin-twin interactions and the twin boundary sliding disrupting the reorientation process in $\langle 100 \rangle$ and $\langle 102 \rangle$ Cu nanowires has been demonstrated in Figure 3.7. In $\langle 100 \rangle$ nanowire, the twin boundary sliding dominates over twin growth (Fig 3.7a-b), thus making the nanowire to show shear failure without reorientation. On the other hand in $\langle 102 \rangle$ nanowire, the slip-twin interactions along with the sliding of twin boundaries were responsible for the absence of reorientation (Figure 3.7c-d).

3.3.3 Stress-strain behaviour

Figure 3.8 shows the stress-strain behaviour of Cu nanowires of different orientations under compressive loading. It can be seen that initially all the nanowires undergo elastic deformation up to a peak value followed by an abrupt drop in flow stress. Following the yield drop, the flow stress fluctuates about a constant mean value. In nanowires deforming by twinning mechanism, marginal fluctuations have been observed about a mean value of 1.3 GPa for $\langle 100 \rangle$ nanowire and 2.2 GPa for $\langle 103 \rangle$ nanowire (Figure 3.8a). Following this fluctuations about a mean value, $\langle 100 \rangle$ nanowire shows second large peak in the stress-strain curve, which is due to the

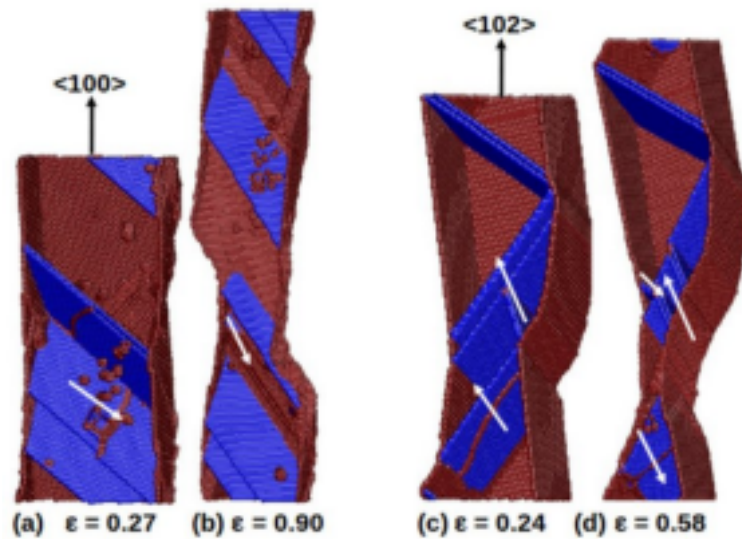


Figure 3.7: Atomic snapshots presenting the deformation and failure behaviour of $\langle 100 \rangle$ and $\langle 102 \rangle$ Cu nanowires under tensile loading. The twin-twin interactions and the twin boundary sliding disrupting the reorientation process can be seen in both the orientations.

twinning induced reorientation (Figure 3.8a). On the other hand in nanowires deforming by full dislocation slip, the flow stress shows large fluctuations about a constant mean value of 3 GPa irrespective of the nanowire orientation (Figure 3.8b)

Figure 3.9 shows the stress-strain behaviour of Cu nanowires with different orientations under tensile loading. It can be seen that the stress-strain behaviour of nanowires undergoing a twinning induced reorientation (Figure 3.9a) is different from that of the nanowires not showing the reorientation (Figure 3.9b). For nanowires, which does not undergoes the reorientation, the flow stress decreases continuously till failure (Figure 3.9b). On the other hand, for nanowires which undergoes reorientation, the flow stress shows a "U" shape behaviour (Figure 3.9a), where the second peak corresponds to the elastic deformation of the reoriented nanowires. Following the second peak, the flow stress decreases continuously till failure, similar to the nanowires not showing reorientation. Despite similar deformation mechanism by twinning, large variations in strain to failure can be seen in Cu nanowires of different orientations under tensile loading.

Following the yielding, the peak value in the stress-strain curve has been taken as the yield stress for Cu nanowires of different orientations and presented on the standard stereographic triangle under compressive and tensile loading as shown in Figure 3.10. Under compressive loading, it can be seen that the Cu nanowires with orientation close to $\langle 001 \rangle$ corner display

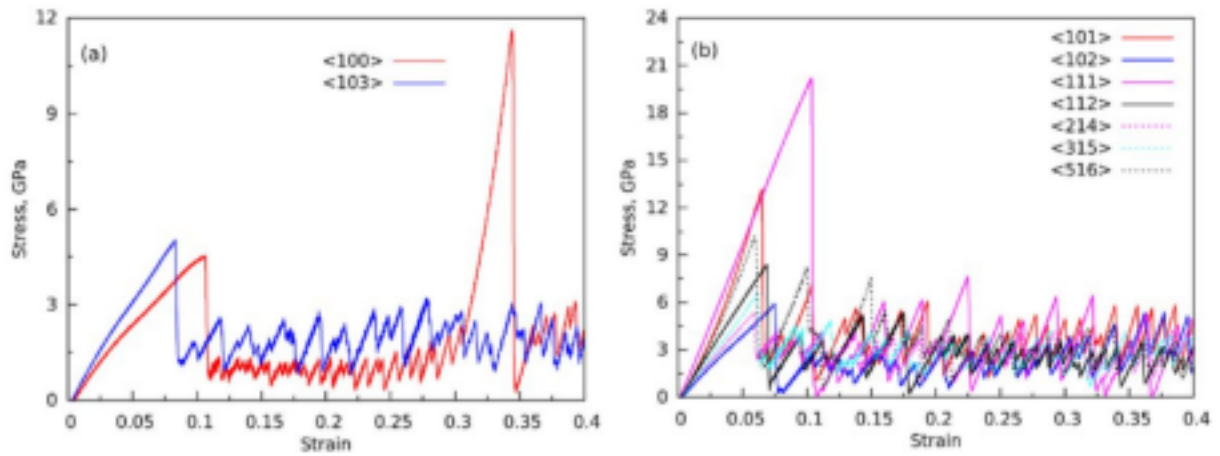


Figure 3.8: The stress-strain behaviour of Cu nanowires deforming by (a) twinning and (b) full dislocation slip under compressive loading of different orientations at 10 K.

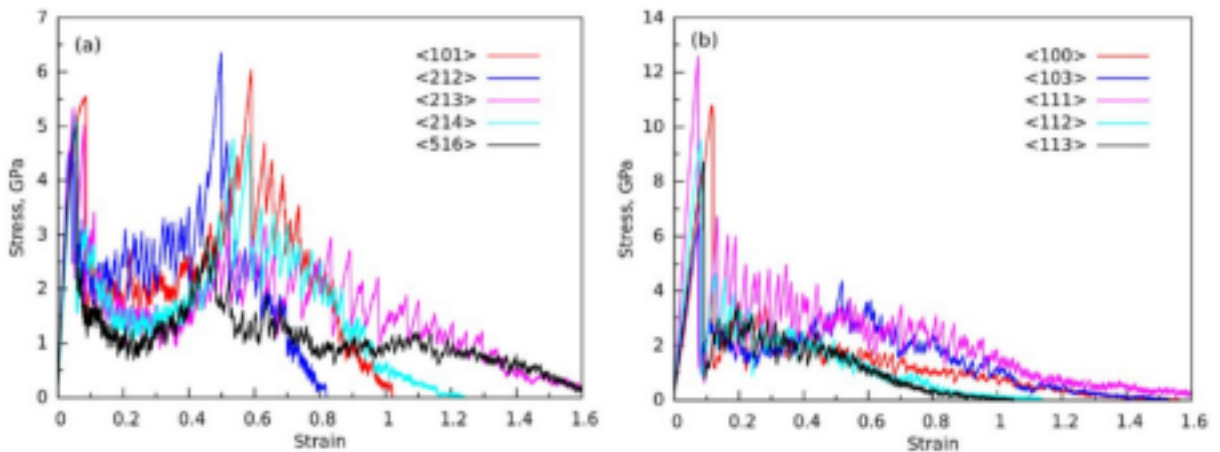


Figure 3.9: The stress-strain behaviour of Cu nanowires deforming by twinning (a) with reorientation and (b) without reorientation under tensile loading at 10 K.

the low values of yield stress (Figure 3.10a). As the orientations move away from the $\langle 001 \rangle$ corner, an increase in compressive yield stress can be seen. The $\langle 111 \rangle$ and $\langle 101 \rangle$ oriented nanowires display the highest compressive yield stress values of 20.2 GPa and 13.1 GPa, respectively (Figure 3.10a). Contrary to compressive loading, the orientations close to $\langle 101 \rangle$ corner display the low values of yield stress under tensile loading (Figure 3.10b). As the orientations move towards $\langle 111 \rangle$ and $\langle 001 \rangle$ corners, an increase in tensile yield stress can be seen in Figure 3.10b. Under tensile loading, the $\langle 111 \rangle$ and $\langle 001 \rangle$ oriented nanowires exhibit the highest values of yield stress. It is interesting to note that the $\langle 111 \rangle$ oriented Cu nanowires display the highest value of yield stress under both tensile and compressive loading.

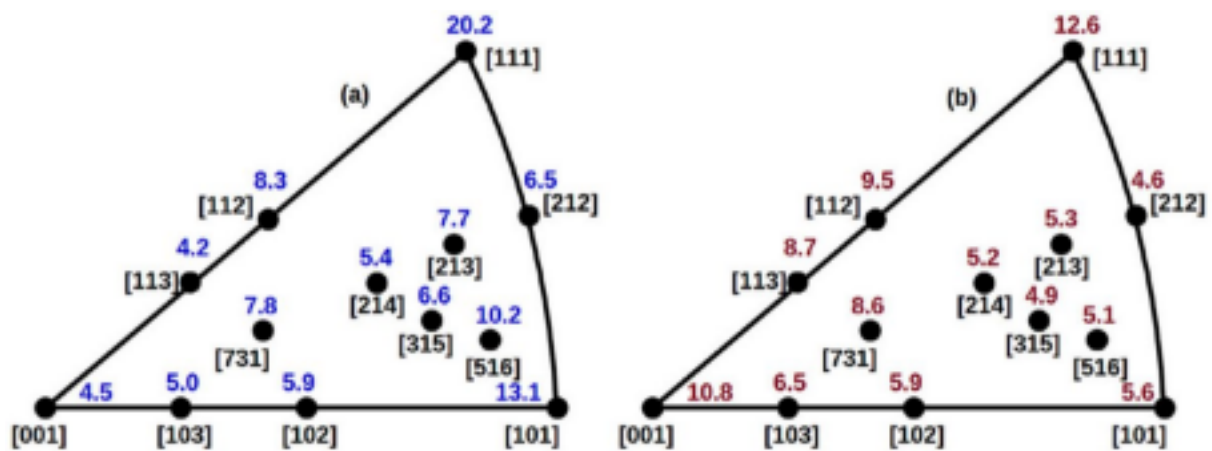


Figure 3.10: The variation of yield stress with respect to orientation presented on the standard stereographic triangle under (a) compressive loading, and (b) tensile loading of Cu nanowires. The yield stress values are in GPa.

3.4 Discussion

3.4.1 Orientation and loading mode dependent deformation mechanisms

MD simulation results indicate that under compressive loading, the $\langle 100 \rangle$, $\langle 103 \rangle$ and $\langle 113 \rangle$ oriented Cu nanowires deform by twinning mechanism, while the remaining orientations deform by dislocation slip. On the other hand all the nanowires deform by twinning mechanism under tensile loading. Full dislocation slip has not been observed in any of the orientations under tensile loading. The deformation by twinning in certain orientations has led to the complete reorientation of the nanowires. These results show that the $\langle 100 \rangle$, $\langle 103 \rangle$ and $\langle 113 \rangle$

Cu nanowires deform by twinning mechanism, irrespective of the loading modes of tension and compression. Cu nanowires with remaining orientations exhibit tension-compression asymmetry in deformation mechanisms in terms of full dislocation slip under compressive loading and twinning under tensile loading. In the past, the tension-compression asymmetry in deformation mechanisms has been revealed in BCC nanowires [153] and also in high symmetry $\langle 110 \rangle$ and $\langle 111 \rangle$ oriented FCC nanowires [27, 38]. However, the present study shows that the asymmetry in deformation mechanisms of FCC nanowires is not limited to $\langle 110 \rangle$ or $\langle 111 \rangle$ orientations, but it exists in many other orientations close to $\langle 110 \rangle$ and $\langle 111 \rangle$ corners of the standard stereographic triangle.

The orientation and mode of loading dependent deformation behaviour of FCC nanowires can be understood based on the Schmid factor (m) analysis [27, 28]. According to this analysis, if the Schmid factor of leading partial is higher than the trailing partial, then the deformation proceeds by the slip of partial dislocations or twinning [28]. On the other hand, if the Schmid factor of trailing partials is higher than the leading partials, nucleation of trailing partial immediately follows the already nucleated leading partial and this results in deformation dominated by the slip of full or extended dislocations [28]. The Schmid factor values for leading (m_L) and trailing (m_T) partials for some of the orientations of Cu nanowires along with the predicted and observed deformation mechanisms are presented in Table 3.2. It can be seen that for most of the orientations, the predicted mechanisms using the Schmid factor analysis are in good agreement with the observed mechanisms in the present study. The exception is being the $\langle 100 \rangle$, $\langle 103 \rangle$ and $\langle 113 \rangle$ orientations under tensile loading. This exception can arise from the effects associated with the orientation of the side surfaces and also the nanowire size, which are not considered in the Schmid factor calculations [27, 28]. When the nanowire is enclosed by high energy side surfaces, it tries to minimize the surface energy by reorienting the surfaces, which is possible only when the deformation proceeds by twinning mechanism. Therefore in nanowire with high energy side surfaces generally twinning is preferred over dislocation slip, even though Schmid factor predicts otherwise. Similarly in small size nanowires partial slip/twinning is preferred, while increasing the size above certain value changes the deformation mode from twinning to full dislocation slip as reported in the previous study on $\langle 100 \rangle$ Cu nanowires [50].

The above mentioned Schmid factor analysis can be generalized for all the orientations in

standard stereographic triangle by defining a parameter α_M , as the ratio of Schmid factors for leading and trailing partial dislocations (Table 3.2). The values of α_M for different orientations of Cu nanowires have been shown on standard stereographic triangle in Figure.3.11a and b under compressive and tensile loading, respectively. Based on the values of α_M , the orientations in the triangle can be divided into two regions, one with $\alpha_M > 1$ and the other with $\alpha_M < 1$, separated by a boundary line with $\alpha_M = 1$. It can be seen that for the region where $\alpha_M > 1$, the Schmid factor for leading partial is higher than the trailing partials irrespective of the loading mode and as a result, the deformation by twinning/partial dislocation slip is favored in orientations falling in this region. In contrast, for the region where $\alpha_M < 1$, the Schmid factor for trailing partial dislocations is higher than the leading partials. As a consequence, the deforma-

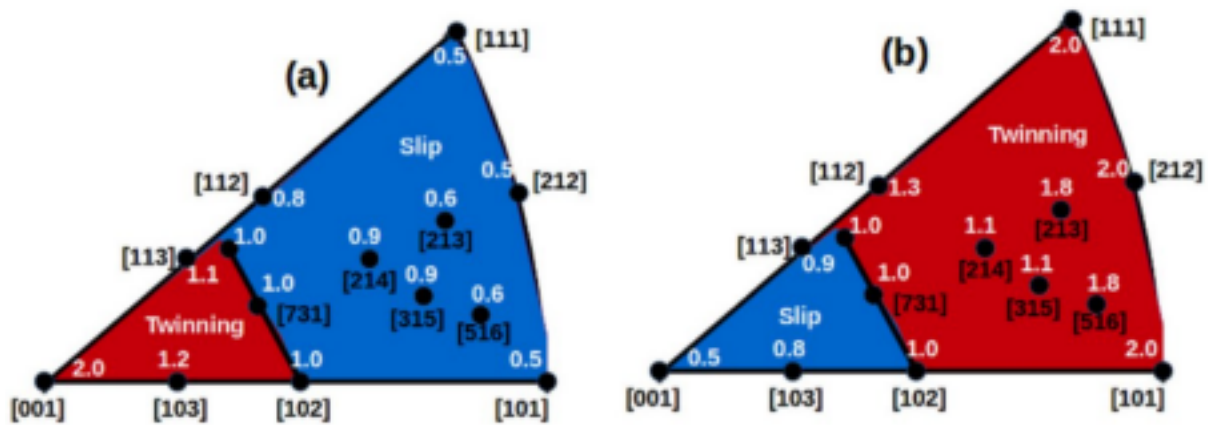


Figure 3.11: The standard stereographic triangle showing two different regions, one with $\alpha_M > 1$ (red color) and other with $\alpha_M < 1$ (light blue) under (a) compressive loading and (b) tensile loading. The black solid line between red and blue colors represent a boundary with $\alpha_M = 1$. The parameter, α_M is defined as the ratio of Schmid factors of leading and trailing partial dislocations.

tion by full/extended dislocations is favoured in this region. For the orientations falling on the boundary with $\alpha_M = 1$, both leading and trailing partials have equal Schmid factor values (e.g. $\langle 102 \rangle$ orientation in Table 3.2) and the deformation can proceed either through twinning or extended dislocations or by the combination of these two [154]. Therefore, if the nanowire orientation falls in the region with $\alpha_M > 1$, the deformation by twinning is preferred, while full dislocation slip is preferred if the orientation falls in the region with $\alpha_M < 1$. If it falls on the boundary line with $\alpha_M = 1$, both the mechanisms are equally probable [155]. The generalization of Schmid factor analysis based on the parameter α_M has an advantage as this method predicts the operative deformation mechanism in some arbitrary orientation simply based on its position on the triangle and loading mode.

Table 3.2: Schmid factor values for leading (m_L) and trailing (m_T) partial dislocations for some of the orientations of Cu nanowires along with the predicted and observed deformation mechanisms. The ratio of leading partial Schmid factor (m_L) to trailing partial Schmid factor (m_T) has been presented as α_M .

Nanowire orientation	Loading type	m_L	m_T	Predicted mechanism	Observed mechanism	$\alpha_M = m_L/m_T$
<100>	Tension	0.235	0.470	Full slip	Twinning	0.5
	Compression	0.470	0.235	Twinning/partial slip	Twinning	2.0
<102>	Tension	0.42	0.42	Full slip and Twinning	Twinning	1.0
	Compression	0.42	0.42	Full slip and Twinning	Full slip	1.0
<103>	Tension	0.38	0.47	Full slip	Twinning	0.8
	Compression	0.47	0.38	Twinning	Twinning	1.2
<110> & < 212 >	Tension	0.470	0.235	Twinning/partial slip	Twinning	0.2
	Compression	0.235	0.470	Full slip	Full slip	0.5
<111>	Tension	0.31	0.155	Twinning/partial slip	Twinning	2.0
	Compression	0.155	0.31	Full slip	Full slip	0.5
<112>	Tension	0.39	0.31	Twinning/partial slip	Twinning	1.3
	Compression	0.31	0.39	Full slip	Full slip	0.8
<113>	Tension	0.39	0.43	Full slip	Twinning	0.9
	Compression	0.43	0.39	Twinning	Twinning	1.1
<214>	Tension	0.44	0.39	Twinning/partial slip	Twinning	1.1
	Compression	0.39	0.44	Full slip	Full slip	0.9

3.4.2 Tension-compression asymmetry in yield stress

MD simulations results indicate that for most of the orientations, the values of yield stress were different under tensile and compressive loading i.e. the nanowires exhibit tension-compression asymmetry in yield stress. This asymmetry (r) can be better understood by considering the ratio of yield stress in tension to that in compression (T/C). Figure 3.12a shows the values of asymmetry factor 'r' for different orientations on the standard stereographic triangle. It can be seen that, the asymmetry values falls in the range 0.4-2.4 and for the orientations near <001> corner, the asymmetry values are higher than the values for the orientations close to <110> and <111> corners. This suggest that, the orientations close to <001> corner exhibit higher yield stress in tension than in compression, while the opposite behaviour (higher yield stress in compression than in tension) is observed in orientations close to <110> and <111> corners. Similar to the present study, the tension-compression asymmetry in yield strength has been observed in many FCC and BCC nanowires [27, 38, 153, 156, 157]. However, the present

results show that for the specific orientation of $\langle 102 \rangle$, the values of yield stress under tensile and compressive loadings have been observed to be the same, thus indicating the absence of asymmetry. In order to understand this asymmetry in yield strength, different explanations have been given in literature [156]. Weinberger et al. [156] have pointed out that the presence of tensile surface stresses is responsible for the asymmetry in yield stress of FCC nanowires. The surface stress, which is generally tensile in nature, induces a compressive stress in the nanowires and makes them stronger in tension and weaker in compression [156]. However, the

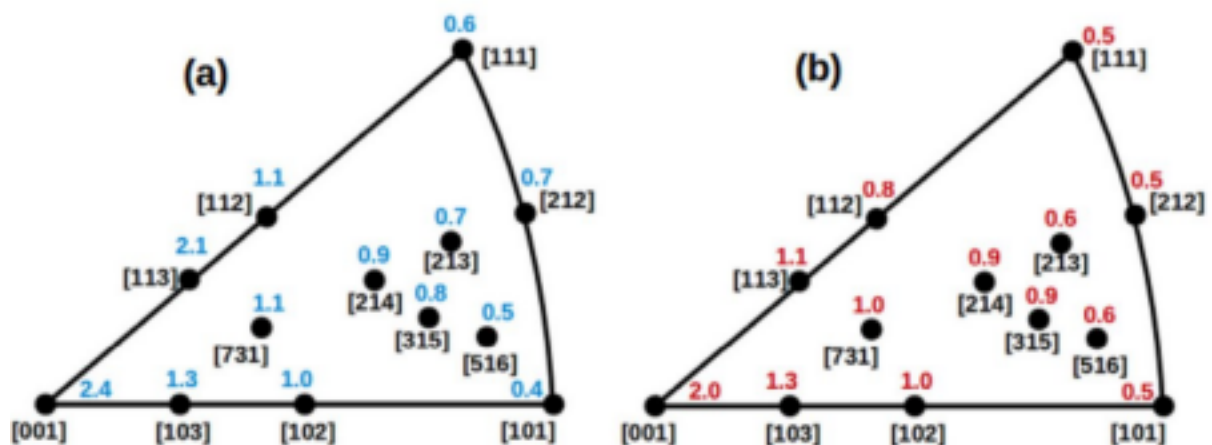


Figure 3.12: The values of (a) yield stress asymmetry (b) Schmid factor asymmetry shown on the standard stereographic graphic triangle for different orientations of Cu nanowires. Yield stress asymmetry is defined as the ratio of yield stress in tension to that in compression (T/C), while the Schmid factor asymmetry is defined as the ratio of leading partial Schmid factor in compression to that in tension (C/T).

present results show that this explanation may not be valid for the orientations close to $\langle 110 \rangle$ and $\langle 111 \rangle$ corners. Further, the tension-compression asymmetry has been reported in FCC bulk single crystals, where there is no presence of surface stresses [158, 159, 160]. In the absence of surface stresses, it has been proposed that the stress normal to the slip direction and also the atomic stacking of the $\{111\}$ slip planes, which is not symmetrical about the $\langle 110 \rangle$ slip direction were responsible for the tension-compression asymmetry in FCC single crystals [158, 159, 160]. Different from the previous studies, the tension-compression asymmetry in FCC nanowires can be explained based on the Schmid factors of leading partial dislocations, which are different under tensile and compressive loading. Here, the Schmid factors of only leading partials is necessary because irrespective of the deformation mechanism (full slip/partial slip/twinning), the first pop-in event during yielding is the nucleation of leading partial dislocation. Therefore, the yield stress is controlled mainly by the Schmid factor of leading partial dislocations. In order to relate the observed yield stress asymmetry (r) to Schmid factors

of leading partials, the ratio of leading partial Schmid factor in compression to that in tension (C/T) has been taken as the Schmid factor asymmetry (s). Figure 3.12b shows the values of Schmid factor asymmetry (s) for different orientations on the standard stereographic triangle. It can be seen that for most of the orientations, the values of Schmid factor asymmetry (s) were approximately close to the values of yield stress asymmetry i.e. there is one to one correlation between yield stress asymmetry and Schmid factor asymmetry (Figure 3.12a and b). This correlation suggest that the asymmetry in yield stress of nanowires is arising mainly due to the different Schmid factors for leading partial dislocation under tensile and compressive loading.

3.5 Conclusions

Molecular dynamics simulation results have shown that the deformation mechanisms in Cu nanowires vary significantly with crystallographic orientation and mode of loading. Under compressive loading, the orientations close to $\langle 100 \rangle$ corner of a standard stereographic triangle i.e. $\langle 100 \rangle$, $\langle 103 \rangle$ and $\langle 113 \rangle$ orientations deformed by twinning mechanism, while the remaining orientations deformed by full dislocation slip. On the other hand, all the orientations irrespective of their position on the stereographic triangle deformed by twinning mechanism under tensile loading. Further, the orientations close to $\langle 110 \rangle$ and $\langle 111 \rangle$ corners exhibited asymmetry in deformation mechanisms in terms of full dislocation slip under compressive loading and twinning under tensile loading. Irrespective of twinning or full dislocations, the orientations falling in the interior of the standard stereographic triangle deformed on a single slip/twin system, while the orientations falling on the border deformed on multiple slip/twin systems. In addition to deformation mechanisms, it has been observed that the Cu nanowires display tension-compression asymmetry in yield stress. The orientations close to $\langle 001 \rangle$ corner exhibit higher yield stress in tension than in compression, while higher yield stress in compression than in tension has been observed in orientations close to $\langle 110 \rangle$ and $\langle 111 \rangle$ corners. Interestingly, for the specific orientation of $\langle 102 \rangle$, the values of yield stress under tensile and compressive loading were found to be same, thus indicating the absence of yield stress asymmetry in $\langle 102 \rangle$ Cu nanowire. Irrespective of loading mode, the $\langle 111 \rangle$ oriented Cu nanowires displayed the highest yield stress among all the orientations investigated. The tension-compression asymmetry in deformation mechanisms has been explained based on the parameter α_M , defined as the ratio of Schmid factors for leading and trailing partial disloca-

tions. For the nanowire orientations falling in the region with $\alpha_M > 1$, the deformation by twinning is preferred, while full dislocation slip is observed for the orientations falling in the region with $\alpha_M < 1$. For the orientations falling on the boundary line with $\alpha_M = 1$, both the mechanisms are equally probable. However, the exception is being the $\langle 100 \rangle$, $\langle 103 \rangle$ and $\langle 113 \rangle$ orientations under tensile loading, where twinning has been observed under tensile and compressive loading. Similarly, the asymmetry in yield values has been attributed to the different Schmid factor values for leading partial dislocations under tensile and compressive loading.

Chapter 4

Effect of shape and size on the deformation behaviour of Cu nanowires

4.1 Introduction

The application of low dimensional systems such as nanopillars/nanowires is mainly driven by superior physical and mechanical properties compared to their bulk counterparts. The superior properties of nanowires arise from their finite size resulting in high surface area and low defect density. Size effects on deformation behaviour of FCC nanowires have been documented as a part of literature review in Section 1.4.2, where it has been shown that the size influences various material properties such as nucleation and character of dislocations [45, 50], deformation mechanisms [45, 50], defect interactions [57, 58], failure behaviour [57, 58] and strength [54]. Apart from these, it has been demonstrated that the Young's modulus also exhibit the size dependence in FCC nanowires [63]. These results suggests that, the reported size effects are unique to nanoscale materials.

Despite several studies in the literature, the influence of size on tensile deformation behaviour of Cu nanowires needs further examination. For example, the Schmid's law predicts full dislocation slip during tensile deformation of $\langle 100 \rangle$ oriented FCC nanowires, while most of the reported results indicate slip of partial dislocations or twinning. Many atomistic simulations and experimental studies have shown that the $\langle 110 \rangle$ FCC nanowires also deform by twinning mechanism and undergo reorientation from $\langle 110 \rangle$ to $\langle 100 \rangle$ [27, 46, 87, 161].

However along with $\langle 1100 \rangle$ nanowires, the atomistic simulations have shown that the $\langle 100 \rangle$ FCC nanowires such as Cu deform by twinning mechanism and reorients to $\langle 110 \rangle$ orientation [23, 25]. Therefore, the separate observations of reorientation from $\langle 100 \rangle$ to $\langle 110 \rangle$ and $\langle 110 \rangle$ to $\langle 100 \rangle$ under the tensile loading of FCC nanowires invite the question of double or sequential reorientation in a single test. Further, the variations in dislocation density and the average length of dislocations with respect to size, plastic strain, strain rate and temperature are not fully explored. Moreover, the relation between the ductility or failure strain as a function of nanowire size has not been studied. Also, the size employed in the previous investigations appears to be reasonably low. In view of these, large scale molecular dynamics (MD) simulations have been carried out on $\langle 100 \rangle$ Cu nanowires as a function of square cross-section width (d) ranging from 0.723 to 43.38 nm for constant length of 21.69 nm. The plastic deformation and fracture behaviour and the variations in dislocation density and average length of dislocations with respect to plastic strain for different nanowire size, strain rate, and temperature have been examined in the present study. The observed dislocation-dislocation, dislocation-stacking fault and dislocation-surface interactions, and the formation of various dislocation locks have been described. The size dependence of Young's modulus, yield strength and ductility has been reported. An attempt has been made to correlate the observed variations in yield strength with initial stress and dislocation nucleation, and failure strain with the operative deformation mechanisms.

Also, a sequential twinning-induced double reorientation observed in $\langle 110 \rangle$ oriented Cu nanowires had been discussed as a special case. Further, most of the previous studies have focused on either square or circular cross-sectional nanowires. However, few studies have shown that cross-section geometry influences the yield strength and dominant deformation behavior [73, 74]. Still, the influence of shape has not been studied in detail for Cu nanowires. In view of this, a systematic study of shape dependent mechanical behaviour and the associated deformation mechanisms have been studied and presented in this chapter.

4.2 MD simulation details

MD simulations have been carried out in LAMMPS package [123] employing an EAM potential given by Mishin and co-workers [108]. The visualization of atomic structure is ac-

completed using AtomEye [129, 131] with centro-symmetry parameter [147] and common neighbour analysis (CNA) [141, 143, 145]. Periodic boundary conditions were chosen along the nanowire length direction, while the other two directions were kept free in order to mimic an infinitely long nanowire.

In the present chapter, single crystal Cu oriented in [001] axial or length direction with {100} as side surfaces were considered. In order to examine the effect of size on the deformation behaviour, MD simulations have been performed on $\langle 100 \rangle$ Cu nanowires of fixed length of 21.69 nm with varying square cross-sections width (d) in the range 0.723-43.38 nm (Figure 4.1). The chosen dimensions provide an aspect ratio ranging from 0.5 to 30. In the present study, the Cu nanowires of fixed length have been chosen to examine the sole effect of cross-section width (d) on the deformation behaviour. In the present study, the square shape cross-section is chosen due to its geometrical simplicity and based on previous atomistic simulations. In order to study the dislocation mechanisms at various temperatures and strain rates, MD simulations have been performed at various temperatures in the range 10-500 K and strain rates varying from 5×10^7 to 1×10^9 s⁻¹.

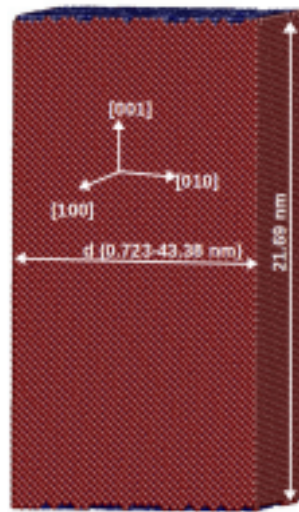


Figure 4.1: Square shaped nanowires of fixed length of 21.69 nm with varying square cross-sections width (d) of 10.48 nm. The cross-sections width (d) of nanowires has been varied in the range 0.723-43.38 nm.

To investigate the possibility of double/sequential reorientation, the deformation behaviour of Cu nanowires oriented in $\langle 110 \rangle$ axial orientation with {111} and {112} as side surfaces, denoted as $\langle 110 \rangle / \{112\}\{111\}$ has been investigated as a special scenario. The nanowire with square cross-section width (d) of 7.15 nm and length (l) varying from 3.57 to 214.5 nm

has been considered.

The choice of cross-section shape is important as it influences the strength values [73] and deformation mechanisms [74]. In order to study the influence of shape of the nanowires, five different cross-sectional geometries i.e., triangle, square, pentagon, hexagon and circle have been chosen in the present study (Figure 4.2). All the nanowires in the present study were oriented in $\langle 100 \rangle$ along axial direction enclosed by different surfaces. The equilibrated side surfaces for all nanowires with different cross-sections has been shown in Figure 4.2. It can be seen that the triangular and hexagonal shaped nanowires have enclosed by $\{470\}$ and $\{100\}$ type side surfaces, while square nanowire is enclosed by all $\{100\}$ type surfaces (Figure 4.2). Similarly, the pentagonal shaped nanowire has $\{130\}$, $\{1070\}$ and $\{100\}$ as side surfaces, while the circular nanowire is surrounded by $\{100\}$, $\{110\}$ and $\{212\}$ type side surfaces (Figure 4.2).

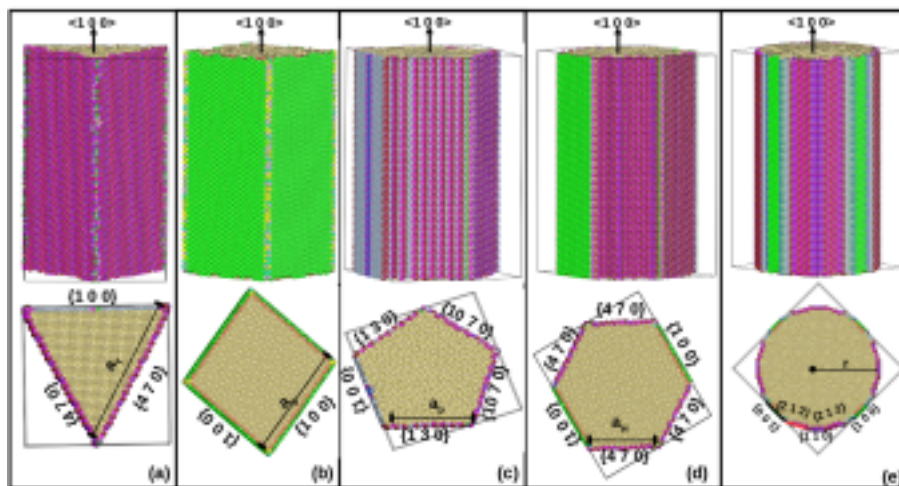


Figure 4.2: The nanowires cross-section shapes considered in the present study. (a) Triangular, (b) square, (c) pentagonal, (d) hexagonal, and (e) circular, with their corresponding side surfaces.

Following the creation of the model nanowires with different shapes, the energy minimization was performed by a conjugate gradient method to obtain a relaxed structure. To retain the sample at the required temperature, all the atoms have been assigned initial velocities according to the Gaussian distribution. Following this, the nanowires were thermally equilibrated to a required temperature of 10 K in canonical ensemble (constant NVT) with a Nose-Hoover thermostat. The velocity verlet algorithm has been used to integrate the equations of motion with a time step of 2 fs. Following thermal equilibration, the tensile deformation was carried out by maintaining a constant strain rate of $1 \times 10^8 \text{ s}^{-1}$ along the axial direction. The stress has

been obtained using the Virial expression [140], which is equivalent to a Cauchy's stress in an average sense.

4.3 Size effects in $\langle 100 \rangle$ Cu nanowires

4.3.1 Stress-strain behaviour

The stress-strain behaviour of $\langle 100 \rangle / \{100\}$ Cu nanowires of fixed length 21.69 nm with square cross-section width (d) ranging from 0.723 to 43.38 nm is shown in Figure 4.3. It can be seen that, initially all the nanowires undergo elastic deformation with a linear increase in stress up to a peak value followed by an abrupt drop in flow stress. Following abrupt drop, the flow stress either remains constant or increases marginally up to certain strain followed by a continuous decrease till failure. The rate of continuous decrease in flow stress with plastic strain has been observed to be the lowest in large size nanowires. A systematic increase in the rate of decrease in flow stress with decrease in nanowire size can be seen in Figure 4.3. As a result, the small size nanowires exhibit a negligibly small plastic deformation and lower strain to failure/ductility. In general, flow stress oscillations without significant strain hardening for all the nanowires can also be seen in Figure 4.3. From the stress-strain curves, the Young's modulus values have been calculated from the linear elastic deformation region and the variations in Young's modulus with nanowire size is shown in Figure 4.4. It can be seen that with increasing size, the Young's modulus decreases rapidly in small size nanowires followed by a gradual decrease to saturation at larger sizes. This is in agreement with those reported for $\langle 100 \rangle$ and $\langle 111 \rangle$ oriented Cu nanowires [63]. It has been suggested that the observed size dependence of Young's modulus originates from the surface induced elasticity and non-linear elasticity of the nanowire core in Cu nanowires [63].

Based on the stress-strain behaviour as a function of size observed in the present investigation, there appears a possibility to predict the operative deformation mechanism in Cu nanowires. Several MD simulation studies on nanowires have shown that the shape of the stress-strain curve depends sensitively on the operating deformation mechanisms [24, 162, 163]. As observed in the present study, stress-strain behaviour of nanowires deforming by dislocation slip mode is characterized by initial elastic loading up to a peak stress followed

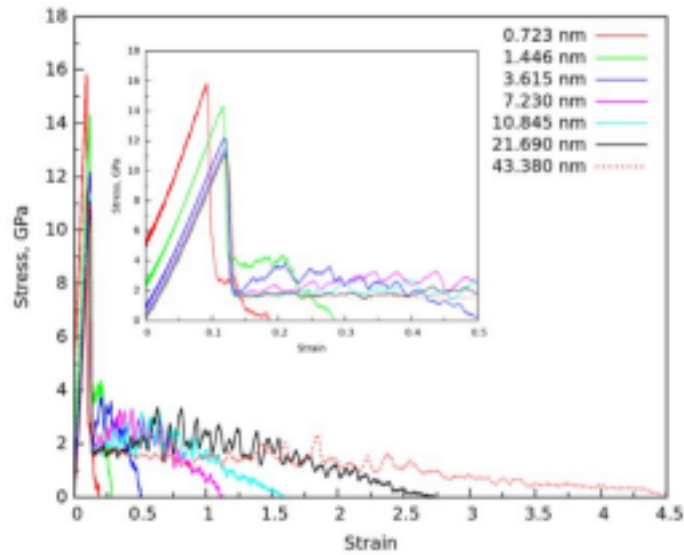


Figure 4.3: Stress-strain curves for $\langle 100 \rangle$ Cu nanowires with constant length of 21.69 nm at different cross section width (d) in the range 0.723-43.38 nm at 10 K. For clarity of elastic deformation, the magnified figure at small strains is shown in inset.

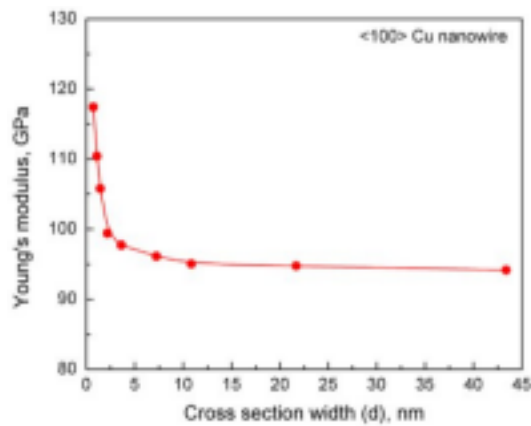


Figure 4.4: The variation of Young's modulus as a function of cross section width (d) for $\langle 100 \rangle$ Cu nanowires at 10 K.

by significant drop due to yielding and a decrease in flow stress with plastic deformation till failure [24, 162, 163]. On the other hand, when nanowires deform only by twinning that leads to reorientation, the stress-strain response consists of linear elastic regime followed by yielding and plastic deformation governed by either a plateau in flow stress (in BCC nanowires) or a marginal increase in flow stress (in FCC nanowires) over a wide range of plastic strains [24, 162, 163]. The absence of flow stress plateaus and second elastic peak obtained in the present study necessarily indicates that the deformation remains dominated mainly by slip of dislocations.

4.3.2 Yield stress and dislocation nucleation

Following elastic deformation, the peak stress in the stress-strain curve has been considered as the yield stress (σ_Y) of defect free nanowire. The variations in yield stress with nanowire size are shown in Figure 4.5. The reported results on the yield stress variation with size on $\langle 100 \rangle$ Cu nanowires [164, 165] are also superimposed. Like Young's modulus, the yield stress also exhibited a rapid decrease in small size nanowires followed by gradual decrease to saturation at larger size. The decrease in yield strength has been correlated with nanowire cross-section width (d) as $\sigma_Y = 11.06 + 3.9d^{-1}$ (Figure 4.5). A good agreement between yield strength values obtained in the present investigation with those reported for $\langle 100 \rangle$ Cu nanowires [164, 165] can be seen in Figure 4.5. Further, the yield stress value at saturation has been observed to be reasonably close to the reported theoretical/ideal strength of perfect $\langle 100 \rangle$ Cu without any defects [166]. The observed decrease in yield strength at small size nanowires approaching towards ideal strength at larger size is in agreement with that reported for Au nanowires by Gall et al. [167].

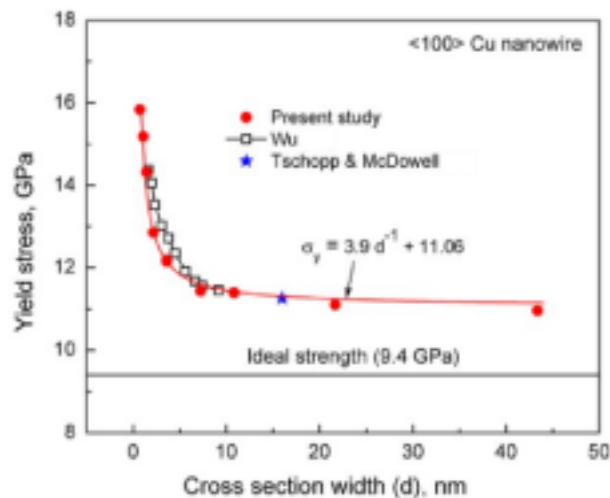


Figure 4.5: Variation of yield strength as a function of cross section width (d) for $\langle 100 \rangle$ Cu nanowires at 10 K. For comparison, the results from other MD simulations on $\langle 100 \rangle$ Cu nanowires [164, 165] are superimposed.

The size dependence of yield stress in metallic nanowires can be described based on the effects associated with surface stress and defect nucleation [168, 169, 170]. The surface stress arising due to the broken bonds on the surface results in the presence of residual stress in the nanowire core or interior and at equilibrium, they balance each other. In the present study, the presence of intrinsic residual stresses has been observed and this has been shown as the

variation in initial stress with nanowire size in Figure 4.6. The initial stress has been taken as the stress in the nanowire at zero strain or before the application of any load. The magnitude of the initial stresses has been obtained in the order of GPa. The initial stress exhibits a rapid decrease in small size nanowires followed by a gradual decrease approaching towards close to zero at larger size. Presence of initial/residual stress has been observed in other FCC and BCC metallic nanowires [65, 67, 171]. In order to initiate the deformation, the applied stress must

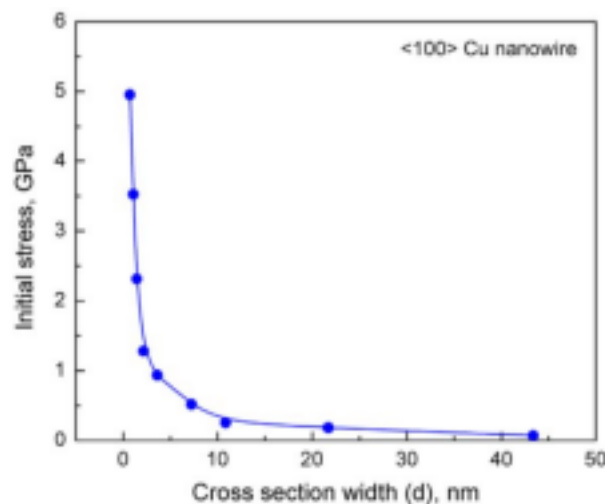


Figure 4.6: The variation of initial stress as a function of cross section width (d) for < 100 > Cu nanowires at 10 K.

overcome the residual stresses present in the nanowires. High residual stresses contribute significantly towards higher yield stress in small size nanowires. However, in large size nanowires, such a contribution appears to be either small or negligible. The other important factor, which influences the yield strength, arises from the number of potential nucleation sites for defects in nanowires [169, 170]. Figure 4.7 shows nucleation of dislocations in Cu nanowires for different sizes. Irrespective of size, all the dislocations nucleating from the corners of the nanowires have been observed to be $1/6\langle 112 \rangle$ Shockley partials with stacking faults behind. A general increase in dislocation nucleation with increase in nanowire size can be seen in Figure 4.7. Yielding in small size nanowires has been associated with dislocations nucleating only from a few sites (Figures 4.7a-d), while in large size nanowires yielding results from the nucleation of many partial dislocations (Figure 4.7e-f). In small size nanowires, the limited activation volume restricts the number of probable sites for defect nucleation and this results in high yield stress [67, 169]. Contrary to this, the large size nanowires provide higher number of nucleation sites for Shockley partials leading to lower yield strength values. The strength reduction due to higher number of nucleation sites arises from the effects associated with higher nucleation

attempts and decrease in activation energy for the nucleation process with increase in nanowire size [67, 169].

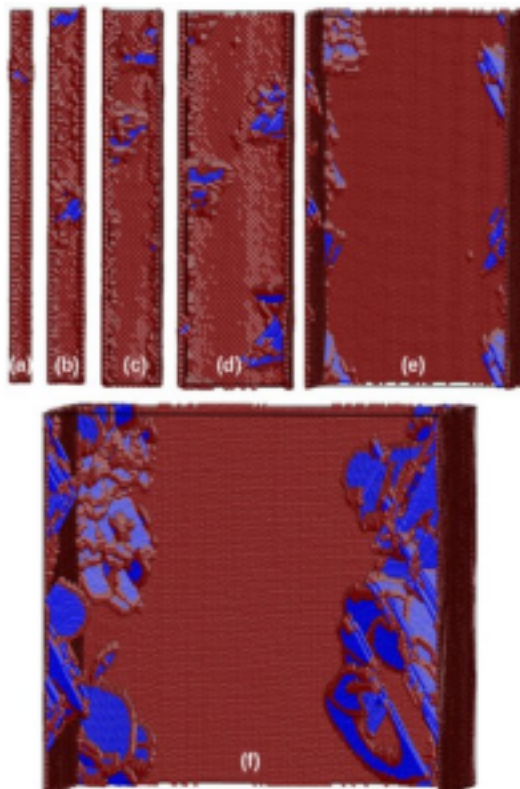


Figure 4.7: Yielding by the nucleation of $1/6\langle 112 \rangle$ Shockley partial dislocations in $\langle 100 \rangle$ Cu nanowires of different cross section width (d) in the range 0.723-43.38 nm at 10 K. (a) $d = 0.723$ nm (b) $d = 1.446$ nm (c) $d = 2.169$ nm (d) $d = 3.615$ nm (e) $d = 10.845$ nm (f) $d = 43.380$ nm. With increasing size, the increase in defect nucleation sites can be seen. The blue color atoms represent the stacking faults and the red color atoms indicate the surfaces and dislocation core. The perfect FCC atoms were removed for clarity.

4.3.3 Deformation mechanisms

In order to understand the influence of nanowire size on deformation behaviour, the atomic configurations have been analyzed using the CNA in AtomEye. Following yielding, the plastic deformation of $\langle 100 \rangle$ Cu nanowires under tensile loading occurred mainly by the slip of $1/6\langle 112 \rangle$ Shockley partial dislocations irrespective of nanowire size (Figure 4.8a-c). In addition to stacking faults, deformation twins randomly distributed on multiple twin systems have also been observed in all the nanowires (Figure 4.8). During plastic deformation of $\langle 100 \rangle$ Cu nanowires, a few important differences with respect to size have been observed particularly at



Figure 4.8: Deformation behaviour in small size $\langle 100 \rangle$ Cu nanowires with cross section width $(d) = 3.615$ nm under tensile loading. The deformation occurring by slip of partial dislocations can be seen at all strains. The blue color atoms represent the stacking faults and the red color atoms indicate the surfaces and dislocation core. The perfect FCC atoms were removed for clarity.

high strains. In small size nanowires, the nucleation of trailing partial dislocations has been rarely observed and as a result, glide of leading partial dislocations leaves many stacking faults (Figure 4.8). Contrary to this, in nanowires with $d > 20.69$ nm, the plastic deformation has been dominated by slip of partial dislocations at small strains (Figure 4.9a) and slip of extended dislocations at high strains (Figure 4.9b-d). Additionally, in large size nanowires, the glide of extended dislocations resulted in the formation of many point defects as shown in Figure 4.9b-d. In single crystal nanowires or bulk specimens, the deformation by the dominance of partial (twinning) or full dislocation slip can be understood by the Schmid factor analysis [27, 28]. For $\langle 100 \rangle$ tensile axis, the Schmid factors for leading and trailing partial dislocations are 0.235 and 0.471, respectively. Since, the Schmid factor for trailing partials is higher than that of leading partials, the nucleation of trailing partials becomes easier than leading partials. As a result, the trailing partials immediately follow the nucleation of leading partials and the deformation remains dominated by slip of extended dislocations. However, in small size nanowires, only slip of partial dislocations has been observed at all strains (Figure 4.8), while in large size

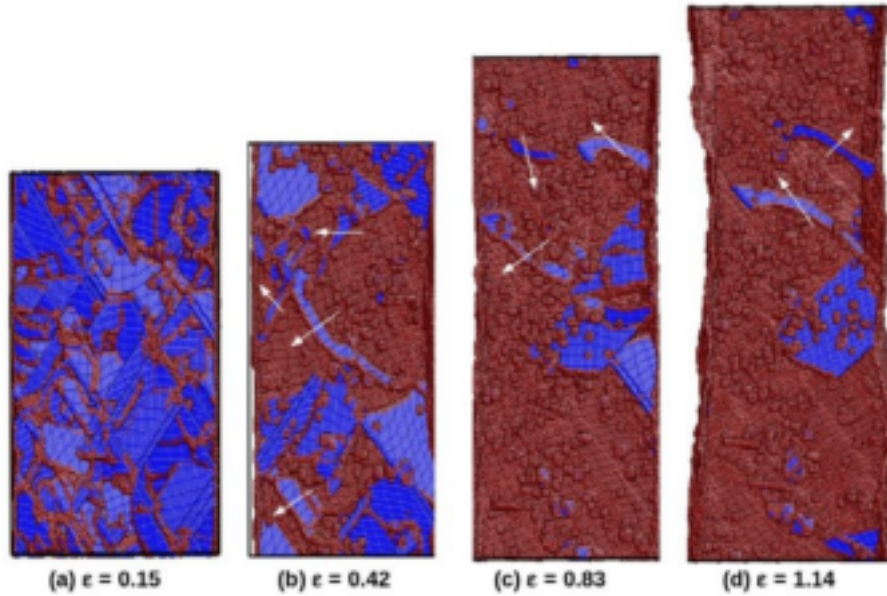


Figure 4.9: Deformation behaviour in large size $\langle 100 \rangle$ Cu nanowires with cross section width $(d) = 20.69$ nm under tensile loading. In addition to partial dislocation slip at small strains, deformation dominated by slip of extended dislocations can be seen at high strains. The white arrow indicates the extended dislocations. The blue color atoms represent the stacking faults and the red color atoms indicate the surfaces and dislocation core. The perfect FCC atoms were removed for clarity.

nanowires, the slip of extended dislocations occurs mainly at high strains. These observations indicate that the deformation in small size $\langle 100 \rangle$ Cu nanowires violates the Schmid law. In earlier studies, this violation of Schmid law has been attributed to the effects associated with the surface stresses and the orientation of the side surfaces [27, 28], which are not considered in the Schmid factor calculations. Further, the difference in dislocation travel distance in large and small size nanowires may also change the deformation mechanisms. Since the influence of these surface factors decreases significantly with increasing size (Figure 4.6), deformation by slip of extended dislocations can be expected in large size nanowires (Figure 4.9). Thus, the deformation in large size nanowires is in agreement with the Schmid law predictions.

4.3.4 Variations in dislocation density

In FCC nanowires, it has been shown that various mechanisms such as source truncation, source exhaustion and dislocation starvation occur during plastic deformation [59, 60, 61]. In order to reveal the influence of size and applied strain on these mechanisms, the dislocation density has been calculated as a function of strain for various cross-section width of $\langle 100 \rangle$ Cu nanowires.

Figure 4.10 shows the variations in dislocation density along with dislocation microstructure and flow stress as a function of strain for nanowire with $d = 21.69$ nm. Dislocation density in nanowires has been observed in the order of $1 \times 10^{17} m^{-2}$, which is a few orders of magnitude higher than those observed in experimental investigations. However, such high dislocation densities have been observed in MD simulations [61, 174], which can arise from high applied strain rates ($1 \times 10^9 s^{-1}$). Following yielding, the dislocation density reaches its maximum

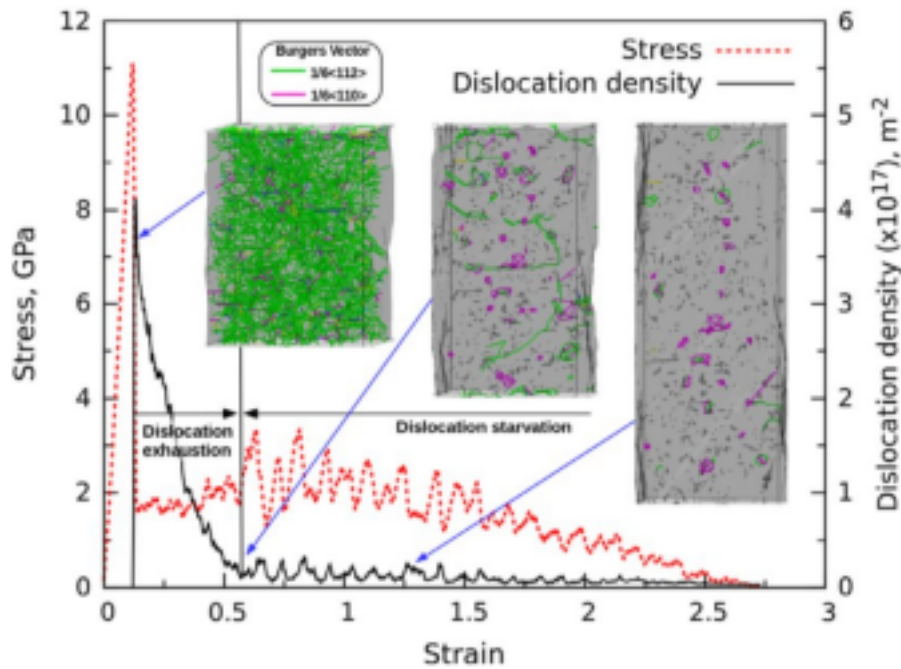


Figure 4.10: Variation of dislocation density, dislocation microstructure and flow stress as a function of strain for Cu nanowire with $d = 21.69$ nm under tensile loading at 10 K. In the inset snapshots, the green color lines show the $1/6\langle 112 \rangle$ Shockley partial dislocations and the magenta lines represent the L-C dislocations having Burgers vector $1/6\langle 110 \rangle$. The thick black dots represent the point defects. The snapshots of the nanowire shown in inset figures were obtained in OVITO [130].

value followed by a rapid decrease up to a strain value of 0.53, and a low and steady state value till failure. The rapid decrease in dislocation density associated with marginal increase in flow stress suggests that this hardening results from dislocation exhaustion from the nanowire. The steady state nature of dislocation density at strains higher than 0.53 indicates that the nanowire is depleted of dislocations and the deformation is dominated by discrete events of dislocation nucleation and exhaustion known as dislocation starvation [175]. This unique variation of dislocation density indicates that the deformation of nanowires can be divided into two stages as a function of strain: (i) dislocation exhaustion phase at small strains followed by (ii) dislocation starvation at higher strains. The dislocation microstructure shown in Figure 4.10 at

different stages also confirms these observations. In agreement with the present study, dislocation exhaustion at small strains followed by source limited activation or dislocation starvation at higher strains has been reported in Cu nanopillars under compressive loading [59]. In dislocation exhaustion phase, the rapid decrease in dislocation density indicates that the rate of dislocation exhaustion is higher than the rate of dislocation nucleation. With this assumption, the dislocation starvation can be considered as a special case of dislocation exhaustion with equal rate of dislocation nucleation and exhaustion. The dislocation microstructure shown in Figure 4.10 also indicates many stable stacking fault tetrahedrons (SFTs) with corners containing $1/6\langle 110 \rangle$ Lomer-Cottrell (L-C) dislocations at higher strains. Further, the number of SFTs has been found to decrease with decrease in nanowire size. In the small size nanowire ($d < 3.615$ nm), SFTs have not been observed. In general, the formation of SFTs in nanowires indicates the activation of all four $\{111\}$ slip planes. The absence of SFTs in the small size nanowires suggests that not all four planes are active. The formation of SFTs can be ascribed mainly to dislocation-dislocation and dislocation-stacking fault interactions during plastic deformation in large size nanowires. In order to investigate the influence of size, temperature and strain rate on the variations in dislocation exhaustion and starvation stages, the dislocation density as a function of strain (or time) has been calculated for all the cases. Figure 4.11a shows the variations in dislocation density as a function of strain (or time) for Cu nanowires of different cross section width in the range 1.446-43.38 nm and strain rate of 1×10^9 s⁻¹ at 10 K. Dislocation density is shown only up to a strain level of 1 as it remains almost constant above this level. It can be seen that for all sizes except the smallest, dislocation density exhibits two stages; dislocation exhaustion stage followed by dislocation starvation stage (Figure 4.11a). In the smallest nanowire, large fluctuations around low value of dislocation density suggest that there is no dislocation exhaustion stage and dislocation starvation alone dominates the deformation at all strains. Further, the transition strain at which the dislocation mechanism changes from exhaustion stage to starvation stage increases with increasing size. This indicates that the rate of dislocation exhaustion is higher in small size nanowires. The rate of dislocation exhaustion is calculated as a slope of dislocation density vs. time plot as typically shown in Figure 4.11a for nanowire of size 43.38 nm. Figure 4.11b shows the variation of dislocation exhaustion rate as a function of nanowire size. It can be clearly seen that, the rate of dislocation exhaustion ($\dot{\rho}$) decreases with increasing size (d) (Figure 4.11b) and follows the relation $\dot{\rho} = \rho_{d0} + ae^{-bd}$, where ρ_{d0} , a , and b are constants. The high exhaustion rates or low resident

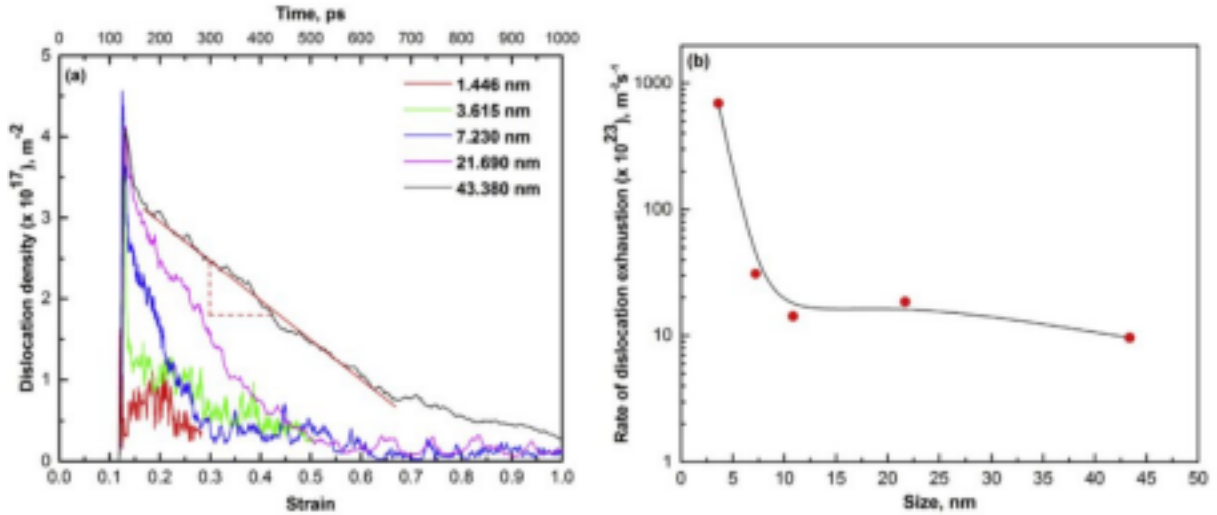


Figure 4.11: (a) Variations in dislocation density as a function of strain (or time) for nanowires of different size deformed at a constant strain rate of $1 \times 10^9 \text{ s}^{-1}$ and temperature of 10 K. (b) The variations in rate of dislocation exhaustion with respect to nanowire size.

time of dislocations in small size nanowires is due to many factors like lower probability of dislocation-defect interactions and high image stresses. On the contrary, the high probability of dislocation-defect interactions and low image stress results in low rate of dislocation exhaustion in large nanowires (Figure 4.11b).

The variations in dislocation density for a nanowire of size (d) = 10.85 nm as a function of strain (or time) at different temperatures (10-500 K) are shown in Figure 4.12a at a constant strain rate of $1 \times 10^9 \text{ s}^{-1}$. At all temperatures, dislocation density in nanowires clearly display dislocation exhaustion and starvation stages. Further, with increasing temperature, the maximum in dislocation density, which is observed at yielding, decreases (Figure 4.12a), while the rate of dislocation exhaustion increases (Figure 4.12b). The rate of dislocation exhaustion ($\dot{\rho}$) with temperature (T) follows the relation $\dot{\rho} = \rho_{T0} - ae^{-bT}$, where ρ_{T0} , a , and b are constants. The high dislocation exhaustion rates at high temperatures results in low values of transition strain for change in deformation mechanisms from exhaustion to starvation. The low exhaustion rates at low temperatures are due to high dislocation density at yielding (Figure 4.12a) and low velocity of dislocations [176], which increases the probability of dislocation interactions. The high probability of dislocation interactions restricts the ease of dislocation annihilation to surfaces resulting in low exhaustion rates at low temperatures.

Figure 4.13a shows the variations in different dislocation mechanisms (dislocation exhaus-

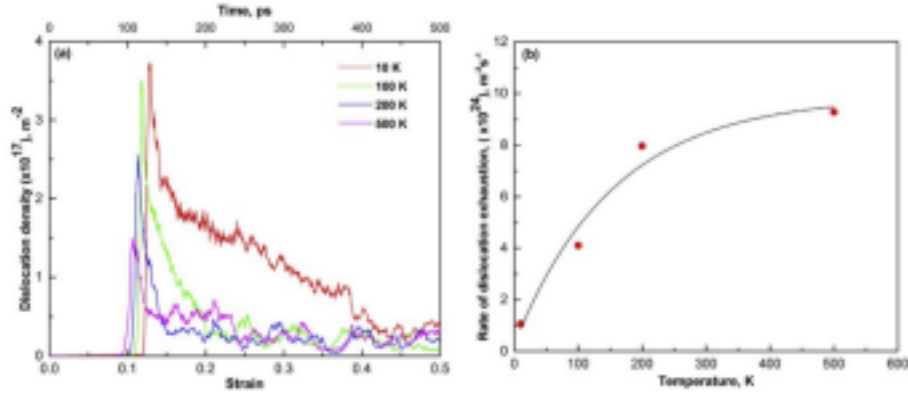


Figure 4.12: (a) Variations in dislocation density as a function of strain (or time) at different temperatures for a nanowire of size (d) = 10.85 nm deformed at a constant strain rate of $1 \times 10^9 \text{ s}^{-1}$. (b) The variations in dislocation exhaustion rates as a function of temperature.

tion and starvation stages) as a function of strain at different strain rates (5×10^7 to $1 \times 10^9 \text{ s}^{-1}$) for a nanowire of size (d) = 10.85 nm at 10 K. Due to different applied strain rates, which results in different time scales, the time axis has not shown in Figure 4.13a. Similar to size and temperature, it shows that the strain rate also influences the dislocation mechanisms in Cu nanowires. It can be seen that, with increasing strain rates, both maximum dislocation density at yielding and transition strain (exhaustion to starvation) increases (Figure 4.13a). However, unlike size and temperature cases, the variations in dislocation density show different behaviour with respect to strain and time. With respect to strain (Figure 4.13a), it appears that the dislocations exhaust at low rates under high strain rate conditions. However, this is not actually true when the calculations are obtained from dislocation density vs. time. This difference with respect to strain and time is due to different time scales involved at different strain rates. For example, under high strain rate condition, it takes very short time to reach the strain value of 0.5, while it takes longer time to reach the same strain value under low strain rate case. Interestingly, the results obtained from dislocation density vs. time graph show that the dislocation exhaustion rate increases with increasing strain rate as shown in Figure 4.13b and follows the relation $\dot{\rho} = \rho_{\dot{\epsilon}} - a e^{b\dot{\epsilon}}$, where $\rho_{\dot{\epsilon}}$, a , and b are constants. Since the dislocation velocity is directly proportional to strain rate [33], high exhaustion rates are expected under high strain rate conditions. The dislocation density influences the different properties of materials, out of which the most prominent being the mechanical properties. In bulk materials increasing the dislocation density increases the yield strength, which results in work hardening [33]. Similarly, the variations in dislocation density in the nanowires has many consequences on strength, ductility and

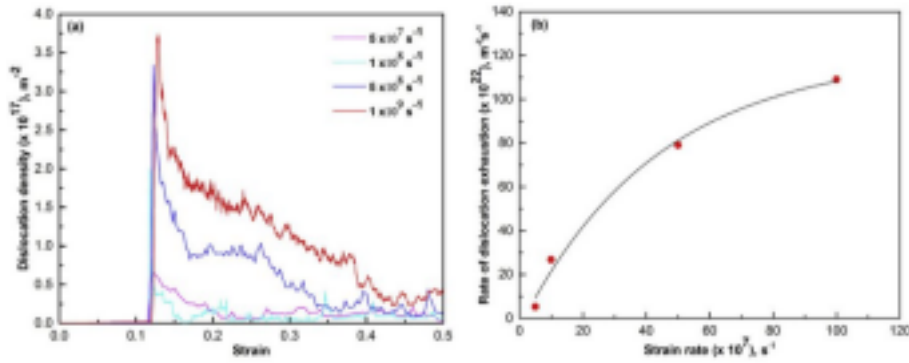


Figure 4.13: (a) Variations in dislocation density as a function of strain at different strain rates for a nanowire of size (d) = 10.85 nm deformed at 10 K. (b) The variations in dislocation exhaustion rate as a function of strain rates.

deformation mechanisms [177]. For example, it has been shown that the yield stress is very sensitive to initial dislocation density [177]. In a crystal with low initial dislocation density, the nucleation and growth of twins along with strain hardening has been reported, whereas in crystal with high initial dislocation density, the deformation proceeds by dislocation multiplication and motion without any twins and exhibit no strain hardening [177].

4.3.5 Average length of dislocations

The average length of dislocations as function of strain for different cross section width in $\langle 100 \rangle$ Cu nanowires has been shown in Figure 4.14. The average length of dislocations has been obtained by dividing the total length of dislocations in the nanowires with the number of dislocation segments. It can be seen that the average length of dislocations remains nearly constant with strain (varying between 2 and 2.5 nm) with minimum oscillations during the course of deformation in the largest nanowire with $d = 43.38$ nm. All other nanowires display large fluctuations in the average length of dislocations. It can be seen that in dislocation exhaustion phase, the average length of dislocations displayed comparatively lower fluctuations than that in dislocation starvation phase. The large fluctuations in the dislocation starvation phase at high strains can be ascribed to discrete nature of dislocation nucleation and exhaustion. In spite of these fluctuations, the average length of dislocations still lies between 2 and 2.5 nm for all the nanowires, except in the smallest size with $d = 1.446$ nm. In the smallest size nanowire, since the dislocation length cannot exceed the nanowire diameter, low average length of dislocations between 0.8 and 1.3 nm has been observed. These results clearly indicate that the average

length of dislocations remain independent of nanowire size with $d > 1.446$ nm. The average length of dislocations of 2-2.5 nm obtained in the present investigation is in agreement with the value of 2.5 nm reported for Cu nanowires with $d = 90$ and 130 nm recently [61].

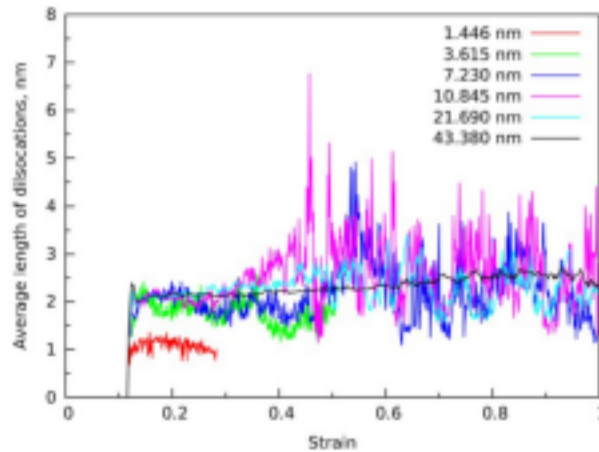


Figure 4.14: The variation of average length of dislocations as a function of strain in $\langle 100 \rangle$ Cu nanowires with different cross section width.

4.3.6 Dislocation-defect interactions

During plastic deformation of nanowires many dislocation-surface, dislocation-dislocation and dislocation-stacking fault interactions have been observed. Kolluri et al. [174] reported various dislocation-stacking faults interactions in Cu thin film and suggested that the dislocation-stacking fault interactions eventually result in the annihilation of stacking faults [174]. Similar dislocation-stacking fault interactions leading to the annihilation of the stacking faults have been observed for the range of nanowire sizes examined in the present study. For example, a significant decrease in stacking faults with increasing strain in the dislocation exhaustion regime can be clearly seen in Figure 4.9. Dislocation-stacking fault interactions facilitating annihilation of the stacking faults is explicitly shown for nanowire size with $d = 20.69$ nm in Figure 4.15. An extended dislocation with Burgers vector $1/2[\bar{1}01]$ glides on $\{111\}$ plane and approaches towards an obstacle stacking fault (Figure 4.15a). With increasing strain, the leading partial penetrates through this obstacle stacking fault (Figure 4.15b), while the trailing partial dissociates into a stair rod dislocation and Shockley partial dislocation on the plane of

obstacle stacking fault (Figure 4.15c). The corresponding reactions can be written as

$$\frac{1}{6}[\bar{2}\bar{1}1](1\bar{1}1)\{Leading\} + \frac{1}{6}[\bar{1}12](1\bar{1}1)\{Trailing\} \longrightarrow \frac{1}{2}[\bar{1}01](1\bar{1}1) + SF(1\bar{1}1). \quad (4.1)$$

$$\frac{1}{6}[\bar{1}12](1\bar{1}1)\{Trailing\} \longrightarrow \frac{1}{3}[\bar{1}10] + \frac{1}{6}[\bar{1}1\bar{2}](1\bar{1}\bar{1}). \quad (4.2)$$

The resultant partial dislocation $1/6[\bar{1}\bar{1}2]$ unzips the obstacle stacking fault in one direction (Figure 4.15c). The stair-rod dislocation $1/3[\bar{1}10]$ again dissociates into two Shockley partials lying on two different planes (Figure 4.15d) according to following reaction,

$$\frac{1}{3}[\bar{1}10] \longrightarrow \frac{1}{6}[\bar{1}12](1\bar{1}1) + \frac{1}{6}[\bar{1}1\bar{2}](1\bar{1}\bar{1}). \quad (4.3)$$

One of the partial dislocations follows the leading partial and constitutes an extended disloca-

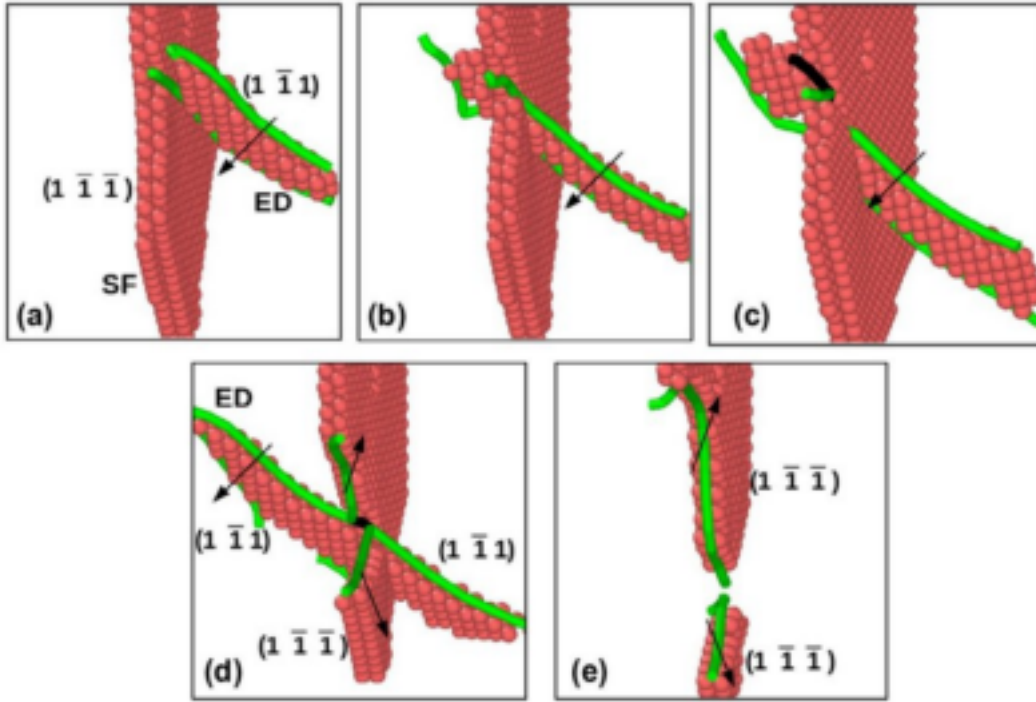


Figure 4.15: Dislocation-stacking fault interactions leading to annihilation of stacking faults in Cu nanowire with $d = 20.69$ nm. The green color lines show $1/6 \langle 112 \rangle$ Shockley partial dislocations and black lines display $1/3 \langle 110 \rangle$ stair-rod dislocations.

tion, and the other unzips the obstacle stacking fault (Figures. 4.15d-e). Here, it is important to mention that the intermediate stair-rod dislocation $1/3[\bar{1}10]$ observed in the present study is slightly different than $1/6[\bar{3}10]$ observed by Kolluri et al. [174]. Like dislocation-stacking fault interactions, dislocation-surface interactions have been observed in all the nanowires. In

addition to dislocation-stacking fault interactions, the dislocation surface interactions also contribute annihilation of stacking faults.

Figure 4.16 shows the interaction of dislocation with the surface in large size nanowire. It is well known that once the dislocation reaches the nanowire surface, it gets annihilated by leaving a slip step on the surface. However, Figure 4.16 displays a different scenario in terms of nucleation of a new partial dislocation. Once the leading partial nucleate from one surface (Figure 4.16a), it glides further and reaches the opposite surface as shown in Figure 4.16b-c. At this juncture, the dislocation simply does not gets annihilated but gives rise to nucleation of new trailing partial dislocation which annihilates the stacking fault produced by original leading partial dislocation (Figures 4.16c-f). Recently, it has been shown that a trailing partial annihilation

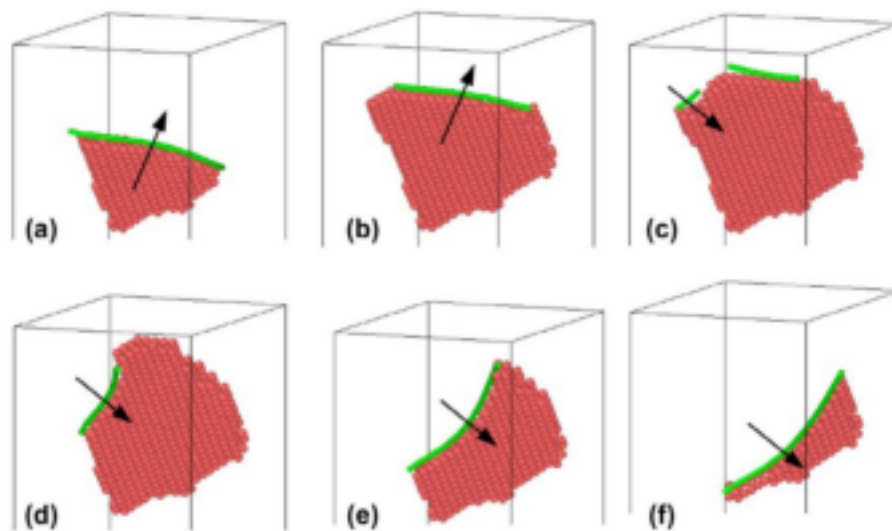


Figure 4.16: The interaction of a leading partial dislocation with the surface in large size nanowires. The annihilation of leading partial at the surface gives rise to the nucleation of a new trailing partial dislocation.

at the surface gives rise to the nucleation of a leading partial dislocation [178]. This process of annihilation immediately followed by regeneration of a dislocation is termed as surface rebound process [178]. Using atomistic simulations, it has been clearly shown that when the velocity of incident dislocation is sufficiently high, it can bounce back from the free surfaces with single or multiple rebounds [178]. Since the strain rates imposed in MD simulations are very high, the dislocation velocities reaches high values and therefore, the surface rebound process is expected to occur during deformation of nanowires. Other important dislocation-surface interaction observed in the present study is shown in Figure 4.17, where dislocation rebounds multiple times. However, this interaction has been observed only in small size nanowires with

$d < 2.17$ nm. In this case, once the leading partial dislocation reaches the nanowire surface, it gets annihilated followed by reflection of a new leading partial dislocation gliding on a different plane (Figure 4.17a-b). The reflected leading partial dislocation again reaches the opposite surface of nanowire and triggers nucleation of a new leading partial dislocation (Figure 4.17c) with same Burgers vector as that of the original dislocation shown in Figure 4.17a. The continuous repetition of this process along the length of nanowire results in the formation of stacking faults with triangular wave shape particularly in small size nanowires (Figure 4.17d). A similar

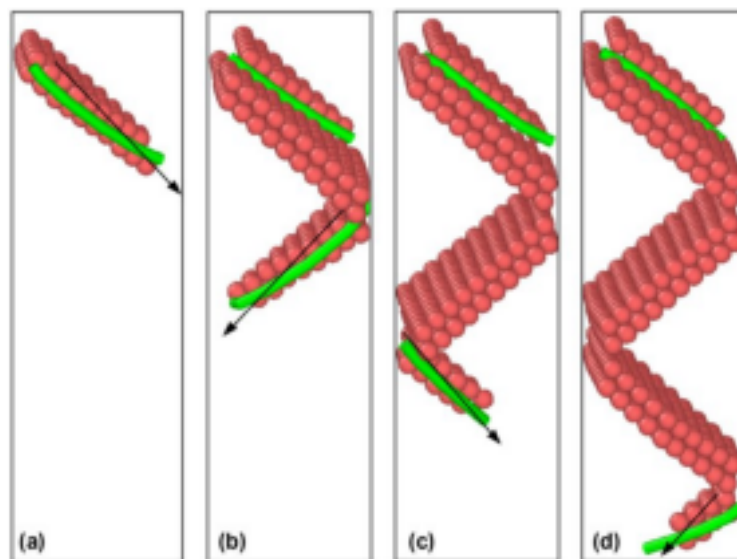


Figure 4.17: Interaction of a leading partial dislocation with surface in small size nanowires. The partial dislocation reflects multiple times from the nanowire surface.

multiple reflections of perfect dislocations from the interface have been proposed by Dregia and Hirth [179] in layered structures.

It well known that, when two mobile dislocations approach each other, they interact and form various dislocation locks, which act as a barriers for the glide of dislocations. Dislocation-dislocation interactions leading to the formation of different dislocation locks in Cu nanowires are shown in Figure 4.18. Figure 4.18a shows glide of two leading partials with Burgers vectors $1/6[1\bar{2}\bar{1}]$ and $1/6[\bar{2}1\bar{1}]$ on parallel $\{111\}$ planes and stopped by the stacking fault. With increasing strain, one more twinning partial nucleates on the stacking fault barrier and interacts with the two existing partial dislocations leading to the formation of L-C lock at the acute junction and Hirth lock at obtuse junction (Figure 4.18b). As this twinning partial glides further on the stacking fault barrier, the length of these dislocation locks increases and gives rise to the formation of well defined nano-twin in between these locks (Figure 4.18c). These two reactions

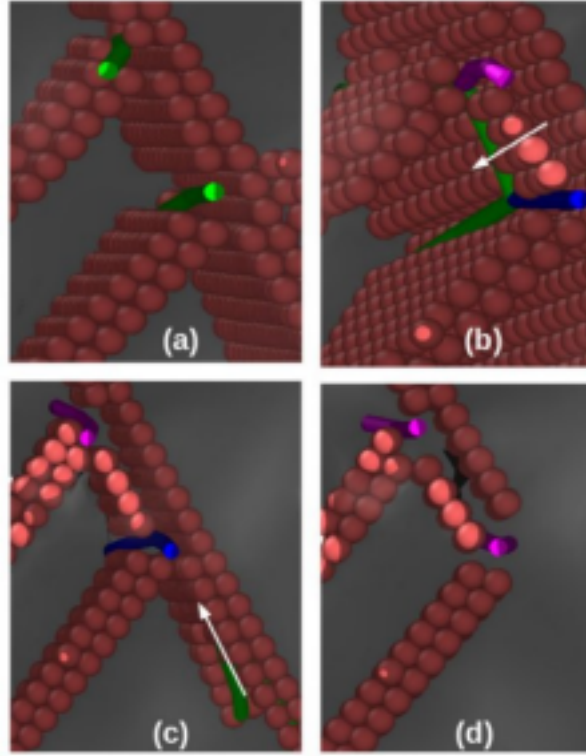


Figure 4.18: Dislocation-dislocation interactions leading to the formation of L-C lock at acute junction and Hirth lock at obtuse junction of $\{111\}$ planes in $\langle 100 \rangle$ Cu nanowires. The green lines indicate Shockley partials, magenta color lines represent L-C dislocations and blue color lines show Hirth dislocation.

can be expressed as

$$\frac{1}{6}[1\bar{2}\bar{1}] + \frac{1}{6}[\bar{2}1\bar{1}] \longrightarrow \frac{1}{6}[\bar{1}\bar{1}0] \{\text{L-C lock}\}. \quad (4.4)$$

$$\frac{1}{6}[\bar{2}1\bar{1}] + \frac{1}{6}[2\bar{1}\bar{1}] \longrightarrow \frac{1}{3}[00\bar{1}] \{\text{Hirth lock}\}. \quad (4.5)$$

Following the formation of these locks, one more trailing partial dislocation nucleates on the stacking fault barrier and approaches towards the Hirth lock as shown in Figure 4.18c. With further glide, this trailing partial dislocation interacts with the existing Hirth lock and forms L-C lock. As a result of these interactions, two L-C locks enclosing a nano-twin can be seen in Figure 4.18(d).

Similar to the interaction of Shockley partial with Hirth lock, the interaction of Shockley partial with L-C lock is shown in Figure 4.19. It can be seen that a Shockley partial dislocation interacts with L-C dislocation and forms a Frank partial. The reactions leading to the conversion of Hirth lock into L-C lock, and L-C lock into Frank partial can be expressed as

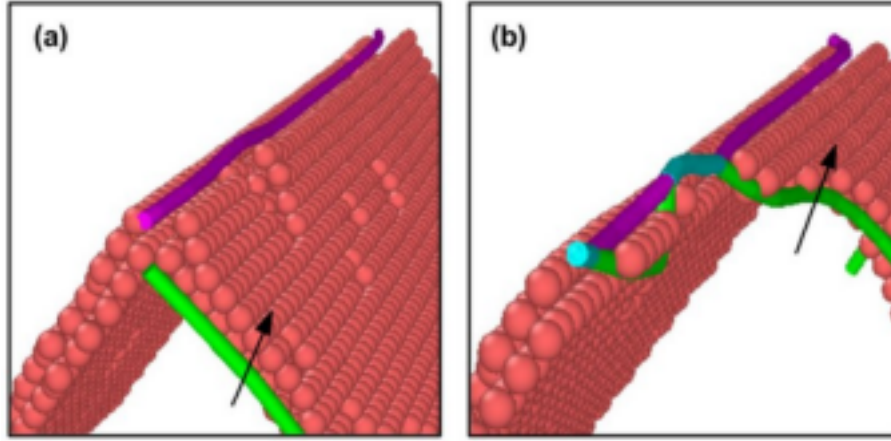
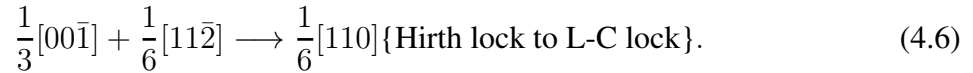


Figure 4.19: The interaction of Shockley partial dislocation with L-C dislocation leading to the formation of Frank partial. The green lines indicate Shockley partials, magenta color lines represent L-C dislocations and cyan color lines show Frank partials.



The L-C and Hirth locks and also the conversion of Hirth lock into L-C lock have been observed frequently in all the Cu nanowires irrespective of size. However, the Frank partials have been observed occasionally.

4.3.7 Ductility and failure behaviour

Following the deformation through the slip of partial or extended dislocations, all the nanowires undergo necking and finally fail by ductile manner. Figure 4.20 shows the variation of strain to failure or ductility as function of size in $\langle 100 \rangle$ Cu nanowires. It can be seen that the ductility of Cu nanowires increases linearly with increase in size and is correlated with cross-section width (d) as $\epsilon_f = 0.11d + 0.16$. This observation clearly indicates that the thick nanowires exhibit high strain to failure, while thin nanowires fail with insignificant plastic deformation. The correlation of ductility with nanowire size observed in the present investigation appears to be significant as there is no such correlation exists in the literature. In large size nanowires, the partial dislocations nucleated on multiple slip planes (Figure 4.7) interacts over large strains and the plastic deformation spreads uniformly across the nanowire (Figure 4.9(a)). These interactions over large plastic strains delay flow localization and contribute higher pre-necking

deformation in large size nanowires. In addition to above, the post-necking deformation also occurs over large strains due to higher cross-section width in large size nanowires and contributes significantly towards enhanced ductility. Therefore, both the higher pre- and post-necking deformation results in higher ductility in the large size nanowires. On the other hand, in small size nanowires, the nucleated Shockley partials are small in number (Figure 4.7), the interactions between these partial dislocations are either negligible or limited (Figure 4.8). As a result, localized deformation at low strains leads to early failure in absence of significant plastic deformation and this result in low values of ductility in small size nanowires.

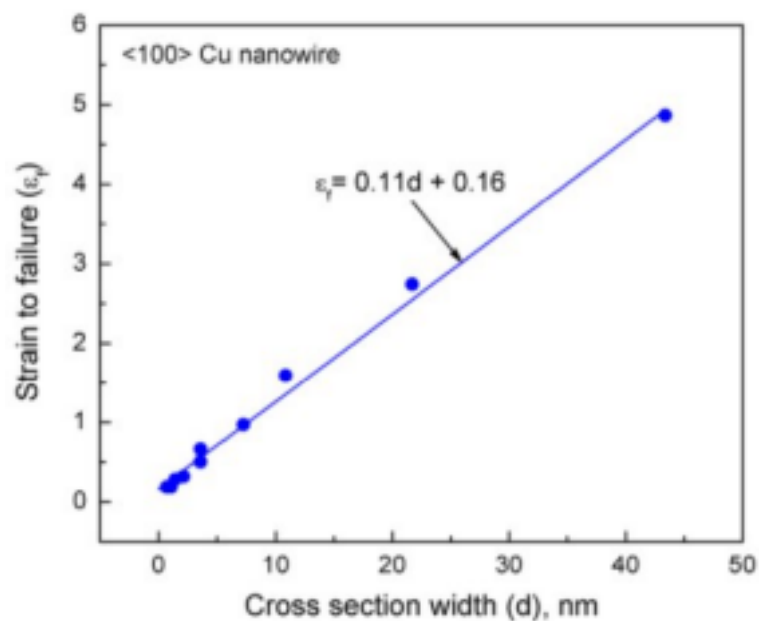


Figure 4.20: Variation of strain to failure or ductility as a function of cross section width (d) for <100> Cu nanowires at 10 K.

Interestingly, since the cross-section width is close to a few atomic spacings in small size nanowires, some of the disordered atoms in neck region rearrange themselves and forms pentagonal atomic chain as shown in Figure 4.21a. These atomic chains consist of a central atom having a coordination of 10 atoms enclosed by two pentagonal rings (each pentagonal ring consists of 5 atoms) as shown in the inset in Figure 4.21a. The pentagonal atomic chains have not been observed in nanowires with $d \geq 3.615$ nm (Figure 4.21b-c). Formation of pentagonal atomic chains has been reported in Cu nanowires with $d < 1.5$ nm [65, 180]. A detailed study on the size-dependent deformation at reasonably higher temperatures also demonstrated formation of long and stable pentagonal atomic chains in ultra thin BCC Fe nanowires [181]. The transformation of perfectly crystalline FCC lattice into pentagonal structure can be understood

in terms of energy minimization [70, 182]. As the cross-section width decreases to few atomic spacings in the neck region, internal atomic rearrangements of FCC atoms results in change in local coordination number leading to increase in cohesive energy. This increase in energy is compensated by the nucleation of pentagonal structure.

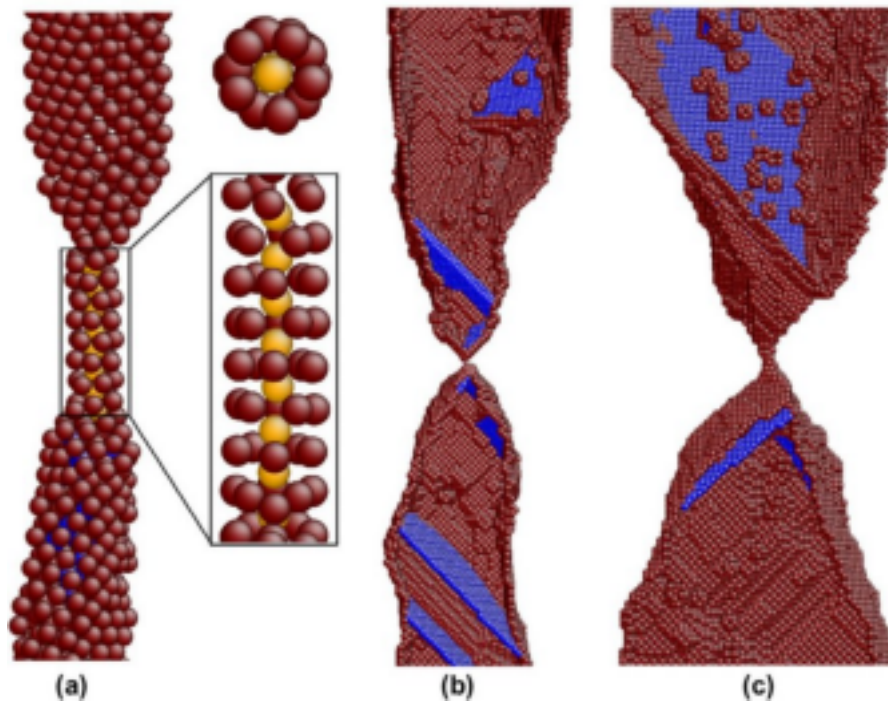


Figure 4.21: Failure behaviour in (a) the smallest size ($d = 0.723$ nm) (b) intermediate size ($d = 10.845$ nm) (c) large size ($d = 21.69$ nm) $\langle 100 \rangle$ Cu nanowire during tensile deformation at 10 K. The formation of pentagonal atomic chain in the necking region of the smallest size nanowire can be seen in a.

4.4 Size effects in $\langle 110 \rangle$ Cu nanowires and double reorientation

4.4.1 Size effects

Along with varying nanowire size by only varying cross section width, the nanowire dimensions can be changed by varying length, while maintaining nanowire cross section width constant. During such scenario, previous studies had suggested that the variations in length does not vary the material properties such as Young's modulus and yield strength of $\langle 100 \rangle$ Cu nanowires [172]. Interestingly, along with consistent results of maintaining constant Young's

modulus and yield strength, $\langle 110 \rangle$ Cu nanowires displays a sequential double reorientation for nanowires of small lengths. In general, as deformation proceeds by twinning and the twin boundaries sweep across the nanowire length, the orientation of the nanowire changes and this phenomenon is known as reorientation. The reorientation mechanism has been observed in many FCC and BCC metallic nanowires [23, 24, 66, 67], and also in inter-metallic alloy nanowires [68]. However, a sequential double reorientation in FCC nanowires is uncommon. However, the double reorientation has been observed recently in HCP Mg nanowire as a result of primary and sequential secondary twinning processes [173].

4.4.2 Double reorientation

The double or sequential reorientation observed during tensile deformation of $\langle 110 \rangle$ Cu nanowire of cross-section width (d) and length (l) = 7.15 nm is typically shown in Figure 4.22. It can be seen that under tensile loading, the original $\langle 110 \rangle$ nanowire with $\{111\}$ and $\{112\}$ side surfaces (Figure 4.22a) undergoes a primary reorientation to $\langle 100 \rangle$ nanowire having $\{100\}$ and $\{310\}$ lateral surfaces (Figure. 4.22b). With further deformation, the reoriented $\langle 100 \rangle$ nanowire undergoes second reorientation to $\langle 112 \rangle$ as axial direction and $\{111\}$ and $\{641\}$ as side surfaces (Figure 4.22c). The sequential reorientation in $\langle 110 \rangle$ Cu nanowire changes the cross section shape from square to rhombus (Figure 4.22a-b) and then rhombus to parallelogram (Figure 4.22b and c). The measured angles between the sides of rhombic cross section have been obtained as 70° and 110° , and these are in agreement with the angles between $\{100\}$ and $\{310\}$ surfaces. Similarly, the angle between the sides of the parallelogram are 78° and 102° , same as the angles between $\{111\}$ and $\{641\}$ surfaces. Based on atomistic simulation studies, the primary reorientation from $\langle 110 \rangle$ to $\langle 100 \rangle$ has been reported in FCC nanowires [22, 27], but the successive second reorientation from $\langle 100 \rangle$ to $\langle 112 \rangle$ has been reported for the first time in Cu nanowire.

In order to understand operating deformation mechanisms responsible for the observed sequential or double reorientation, the atomic configurations have been analyzed at various strain levels using common neighbor analysis and the results are presented in Figure 4.23. It can be seen that the original $\langle 110 \rangle$ Cu nanowire yields through the nucleation of single $1/6\langle 112 \rangle$ Shockley partial dislocation on $\{111\}$ plane from the corner (Figure 4.23a). Following yielding, another $1/6\langle 112 \rangle$ Shockley partial nucleates on the adjacent plane and creates a one layer

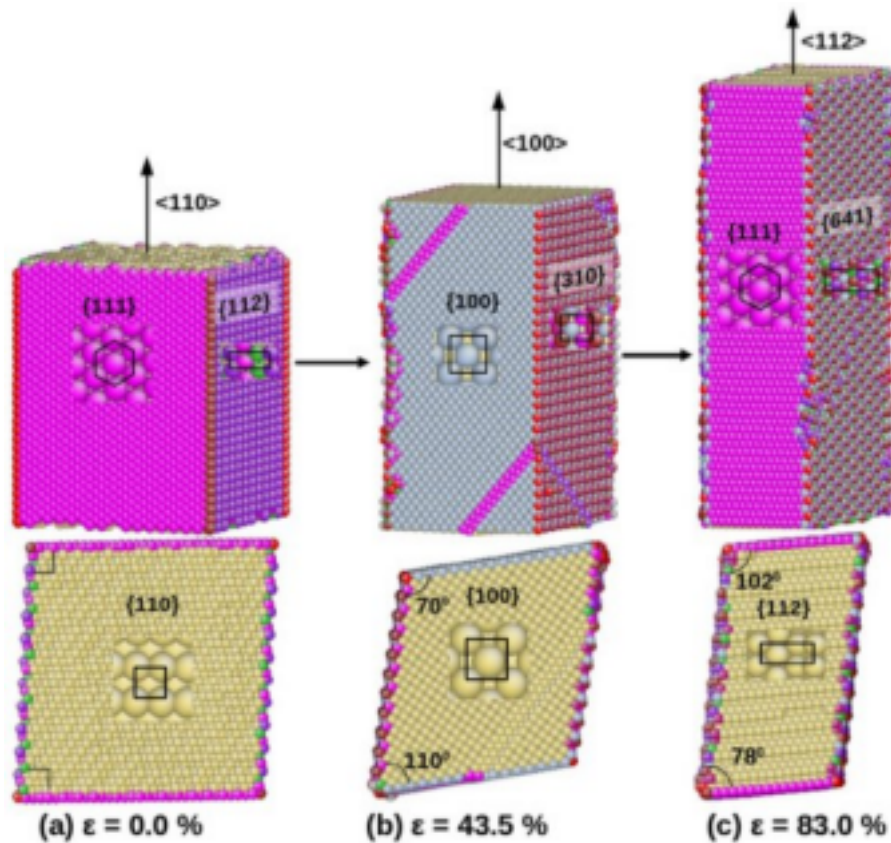


Figure 4.22: The double or sequential reorientation of $\langle 110 \rangle$ Cu nanowire of cross section width (d) and length (l) = 7.15 nm (aspect ratio 1) under tensile loading. The double reorientation changes the cross section shape from square to rhombus and then rhombus to parallelogram. The atoms are colored according to their coordination number.

nano-twin as shown in Figure 4.23a. With increasing deformation, the continuous nucleation and glide of twinning partials along the twin boundaries transform the nano-twin into a full twin enclosed by two twin boundaries (Figure 4.23b). In addition to the nucleation of twinning partials and twin growth, the nucleation of Shockley partials leading to the formation of stable stacking faults have also been observed in untwinned region of the nanowire (Figure 4.23b-c). The twinning partials glide in mutually opposite directions on the twin boundaries, and as a result the twin boundaries move away from each other leading to layer by layer growth of twin (Figure 4.23b-d). The continuous propagation of twin boundaries along the nanowire length progressively reorients the twinned region. In the absence of obstacles, the twin boundaries easily sweep across the nanowire length, and due to periodic boundary conditions along the length, they meet each other and leaves a stacking fault in the reoriented nanowire (Figure 4.23e). Therefore, the deformation by twinning on a single twin system transforms the orientation of the nanowire from $\langle 110 \rangle / \{112\}\{111\}$ to $\langle 100 \rangle / \{100\}\{310\}$. Following the

primary reorientation, the nanowire again undergoes an elastic deformation followed by yield-

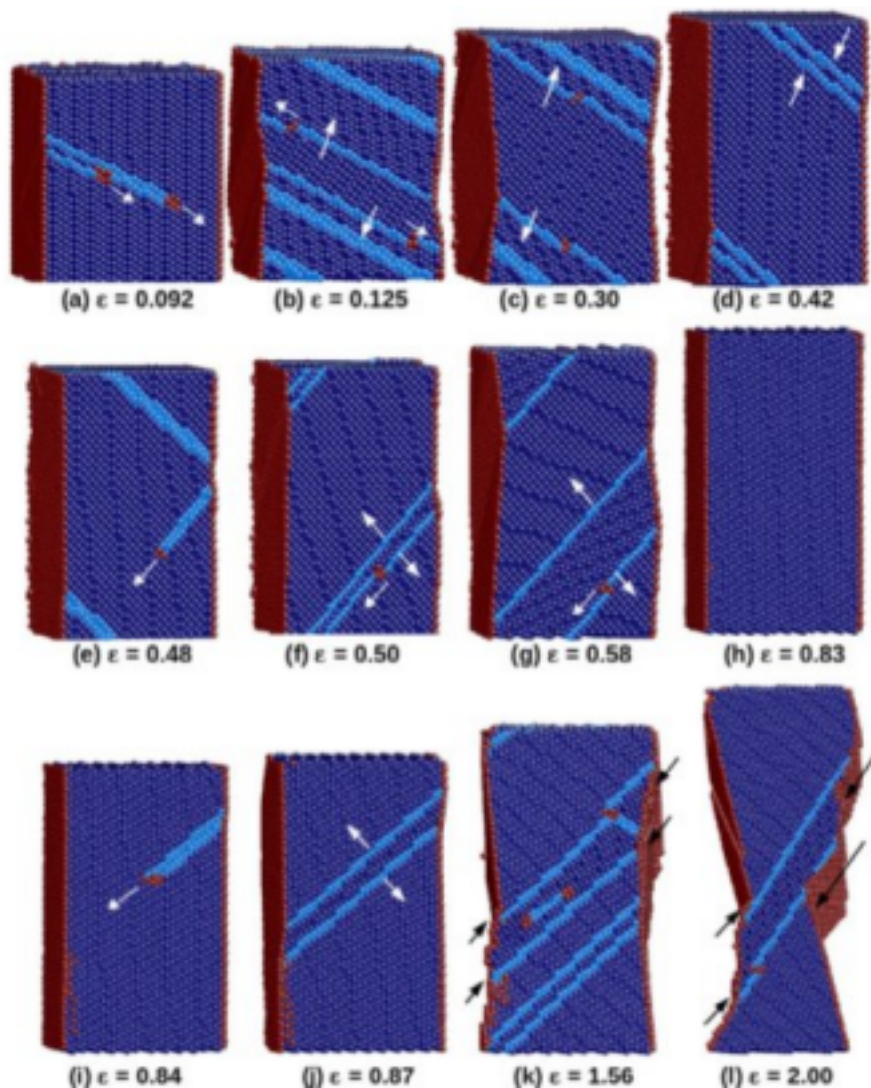


Figure 4.23: Detailed deformation mechanisms responsible for double reorientation from $\langle 110 \rangle$ tensile axis to $\langle 100 \rangle$ axis and then $\langle 100 \rangle$ axis to $\langle 112 \rangle$ axis in Cu nanowire. The blue color represents the FCC atoms, cyan color atoms represent the stacking faults and twin boundaries and the red color atoms indicate the surfaces and dislocation core. The atoms color has been assigned according to the common neighbor analysis (CNA).

ing by the nucleation $1/6\langle 112 \rangle$ Shockley partial dislocation on a different slip system (Figure 4.23e). With increasing deformation, the full twin forms from the Shockley partial (by a similar process shown in Figure 4.23a-b) and grows by the repeated nucleation and glide of twinning partials on the twin boundaries (Figure 4.23f-g). Following the annihilation of twin boundaries due to periodic boundary conditions, the nanowire becomes completely defect free even at the strain value as high as 0.83 (Figure 4.23h) and the nanowire undergoes a second reorientation from $\langle 100 \rangle / \{100\}\{310\}$ orientation to $\langle 112 \rangle / \{110\}\{641\}$ orientation. After second

reorientation, the nanowire again undergoes elastic deformation and yields through the nucleation of a $1/6\langle 112 \rangle$ Shockley partial dislocation (Figure 4.23i). Following yielding, the twin forms and grows similar to those observed during successive first and second reorientations (Figure 4.23j). However, the twin boundaries were not able to sweep across the nanowire and as a result, the nanowire does not undergo full reorientation and fails by shearing along the twin boundary plane (Figure 4.23k-l). This arises mainly from the activation of multiple slip systems and also the glide of extended dislocations within the twinned region disrupting the twin growth and the reorientation process (Figure 4.23k). The activation of multiple slip systems and twin-twin interactions leads to the formation of different dislocation locks, which hinders the motion of twin boundaries. As a result, the additional strain is accommodated by shear along the twin boundaries and this contributes to large plastic strain leading to superplastic like behaviour in the nanowire (Figure 4.23i-l).

It is well-known that the nanowire size plays an important role on the reorientation process. In order to examine the influence of size on the reorientation process, MD simulations have been performed on $\langle 110 \rangle$ Cu nanowires of different lengths (l) ranging from 3.57 nm to 214.5 nm with constant cross-section width (d) of 7.15 nm and thereby giving rise to different aspect ratios in the range 0.5-30. It has been observed that the double reorientation occurs for nanowire length below or equal to 7.15 nm with aspect ratio ≤ 1 . Above this length, the reorientation process has not been observed and the nanowires fail at much lower strains. Typical deformation behaviour of $\langle 110 \rangle$ Cu nanowire of length 14.3 nm with aspect ratio 2 is shown in Figure 4.24. It can be seen that, the yielding in the nanowire is associated with the nucleation of multiple $1/6\langle 112 \rangle$ Shockley partials on different $\{111\}$ planes (Figure 4.24a). Following yielding, the deformation in the nanowire proceeds by twinning on two different twin systems (Figure. 4.24b-c). As a result, the twin boundaries of two different twin systems interact with each other thus making them immobile (Figure 4.24c). With increasing strain, the glide of Shockley/twinning partials along the twin boundaries leads to the shear failure at significantly low strain values without any reorientation (Figure 4.24d).

It has been observed that double or sequential reorientation of $\langle 110 \rangle$ Cu nanowire results from the occurrence of twinning mode of deformation in both the original $\langle 110 \rangle$ as well as the reoriented $\langle 100 \rangle$ nanowire (Figure 4.23). In FCC nanowires, the deformation by twinning or slip of full dislocations can be understood based on the Schmid factor (m) analysis as shown

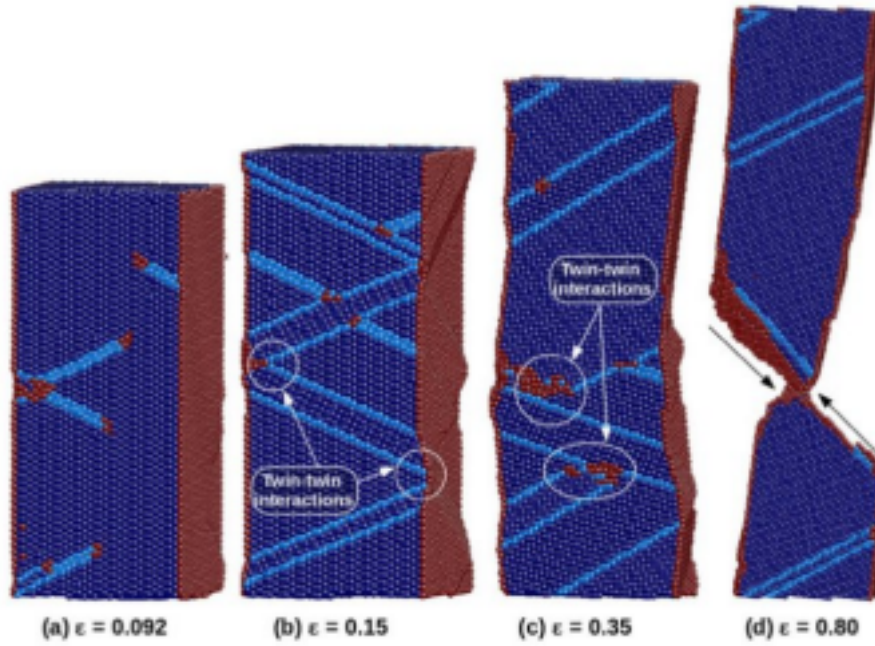


Figure 4.24: Absence of reorientation during the tensile deformation of $\langle 110 \rangle$ Cu nanowire of cross section width (d) = 7.15 nm and length (l) = 14.3 nm (aspect ratio 2). The blue color represents the FCC atoms, cyan color atoms represent the stacking faults and twin boundaries and the red color atoms indicate the surfaces and dislocation core. The atoms color has been assigned according the common neighbor analysis (CNA).

in Table 4.1 [27, 28, 42]. Under tensile loading of $\langle 110 \rangle$ nanowire, the Schmid factor for trailing partial is lower than the leading partial (Table 4.1) and as a result, the nucleation of trailing partial requires relatively higher stresses compared to leading partial. In other words, the nucleation of leading partials becomes easier than the trailing partials in $\langle 110 \rangle$ nanowire and this leads to the nucleation of leading partial alone during yielding of the nanowire. With increasing strain, the continuous nucleation of leading partials on adjacent planes leads to the dominance of deformation twinning in $\langle 110 \rangle$ Cu nanowire (Figure 4.23a-d). Due to activation of single twin system, the twin boundaries are able to sweep across the nanowire leading to the reorientation from $\langle 110 \rangle$ tensile axis to $\langle 100 \rangle$ tensile axis (Figure 4.22a-b). During tensile loading of the reoriented $\langle 100 \rangle$ nanowire, the Schmid factor for trailing partial is higher than the leading partial (Table 4.1) and as a result, the trailing partials should immediately follow the nucleation of leading partial and the deformation should be dominated by slip of full or extended dislocations. However, the results indicate that the reoriented $\langle 100 \rangle$ nanowire also deform by twinning mechanism (Figure 4.23e-h). This is mainly because the $\langle 100 \rangle$ nanowire, which is enclosed by the high energy (widely packed) $\{100\}$ and $\{310\}$

Table 4.1: The Schmid factors (m) for leading and trailing partial dislocations under the tensile loading of $\langle 110 \rangle$, $\langle 100 \rangle$ and $\langle 112 \rangle$ orientations.

Orientations	Schmid factors (m)		Mechanism	
	Leading	Trailing	Predicted	Observed
$\langle 110 \rangle$ -Tension	0.470	0.235	Twinning/partial slip	Twinning
$\langle 100 \rangle$ -Tension	0.235	0.470	Full dislocations	Twinning
$\langle 112 \rangle$ -Tension	0.390	0.310	Twinning/partial slip	Twinning

surfaces (Figure 4.22b), tends minimize its surface energy by reorienting the surfaces to low energy (closely packed) configurations such as $\{111\}$ and $\{641\}$ (Figure 4.22c). This reorientation of surfaces is possible only when the deformation proceeds by twinning mechanism. Therefore, in order to minimize its surface energy, $\langle 100 \rangle / \{100\} \{310\}$ nanowire also deform by twinning on a single twin system leading to second reorientation from $\langle 100 \rangle$ to $\langle 112 \rangle$ nanowire (Figure 4.22b and c). Interestingly in $\langle 112 \rangle$ nanowire also, the Schmid factor for leading partial is higher than the trailing partial (Table 4.22) and this leads to deformation by twinning mechanism (Figure 4.23i-k). However, due to the activation of multiple twin systems which facilitates twin-twin interactions, the twin boundaries are not able to sweep across the nanowire leading to shear failure without reorientation (Figure 4.23l).

4.4.3 Stress-strain behaviour

The stress-strain behaviour of $\langle 110 \rangle$ Cu nanowires for two different aspect ratios of 1 (representing nanowires undergoing double reorientation) and 2 (representing nanowires without reorientation) is shown in Figure 4.25. It can be seen that irrespective of aspect ratio, both nanowires exhibit identical elastic deformation, yield stress and drop in flow stress following yielding. The Young's modulus of $\langle 110 \rangle$ Cu nanowire is obtained as 95 GPa. Following elastic deformation and yielding, the flow stress of two nanowires differs significantly during plastic deformation. The nanowire with aspect ratio 1 exhibits large and uniform oscillations in the strain range 0.1-0.44 followed by second elastic deformation. Following second yielding, the flow stress again shows an abrupt drop and random fluctuations leading towards the third elastic peak. The second and third peaks correspond to the elastic deformation of reoriented $\langle 100 \rangle$ and $\langle 112 \rangle$ nanowires, respectively. Following the third elastic peak, the nanowire displayed a jerky flow with gradual decrease in flow stress over a large strain range till fail-

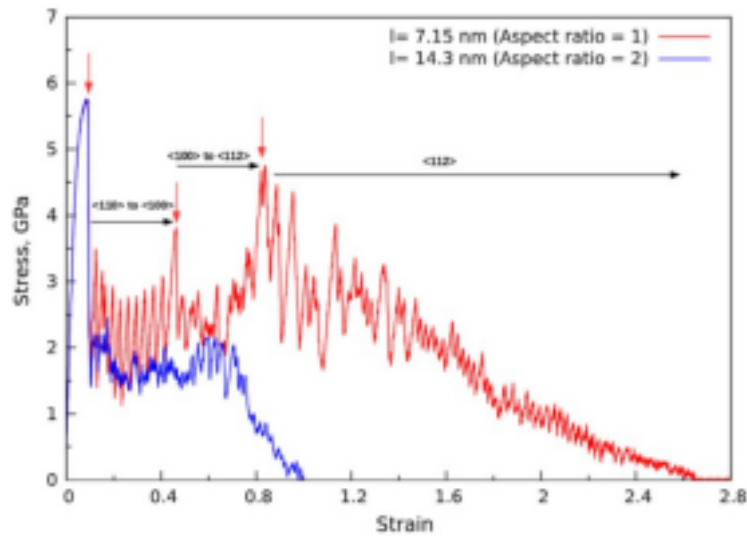


Figure 4.25: Stress-strain behaviour of $\langle 110 \rangle$ Cu nanowire with constant cross section width (d) = 7.15 nm and different length (l) of 7.15 nm (aspect ratio = 1) and 14.31 nm (aspect ratio = 2). Nanowire undergoing double reorientation (aspect ratio = 1) show three elastic peaks (shown by arrows) separated by twin growth regimes.

ure. Successive reorientations and shearing along the twin boundary lead to strain to failure as high as 2.6. On the other hand, $\langle 110 \rangle$ nanowire with high aspect ratio of 2 exhibited nearly constant flow stress up to strain level of 0.6 followed by rapid decrease till failure. Further, no secondary peaks in stress-strain behaviour of $\langle 110 \rangle$ nanowire with aspect ratio 2 have been observed in the absence of reorientation (Figure 4.24). In general, $\langle 110 \rangle$ nanowires with aspect ratio higher than 1 have displayed low tensile ductility as shown for nanowire with high aspect ratio 2 in Figure 4.25.

4.5 Influence of nanowire cross section/shape

The size of nanowires of different shapes has been chosen in two different ways. In the first scenario, the size of the nanowires of different shapes is chosen in such a way that it can be inscribed in a nanowire with circular cross-section as shown in Figure 4.26. As a consequence, all shapes have different surface area to volume ratio as shown in Table 4.2. In the second scenario, the size of the nanowires has been chosen in such a way that the surface area to volume ratio of all the shapes remains constant (Table 4.2). The corresponding size of nanowires of different shapes is shown in Table 4.2 for these two different cases of varying and constant surface area to volume ratios. For both cases, the length of all the nanowires has been chosen

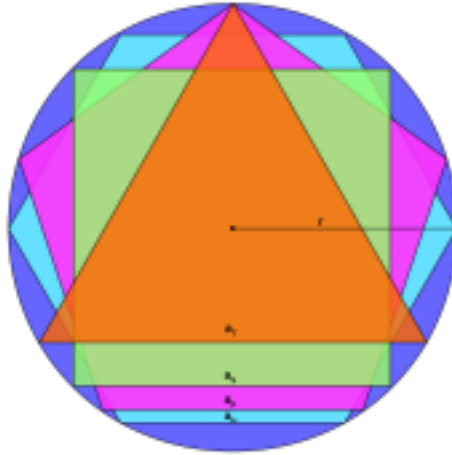


Figure 4.26: A method showing the inscription all the shapes within the circular shape. In the first scenario, the size for different shapes is chosen in such a way that all shapes can be inscribed in circular nanowire of radius 'r'. a_T , a_S , a_P , and a_H represents the side length of triangular, square, pentagonal and hexagonal shaped nanowires.

as two times that of the cross-section width i.e., an aspect ratio of 2:1.

Table 4.2: The nanowire size and surface area to volume ratio of different shapes in Scenario-I and Scenario-II. In scenario-I, the nanowire size has been chosen in such a way that all shapes can be inscribed in circular shape as shown in Figure 4.26. In scenario-II, nanowire size has been chosen in such a way that all the shapes have same surface area to volume ratio.

Nanowire shape	Scenario-I		Scenario-II	
	Side length (a), nm	Surface area to volume ratio	Side length (a), nm	Surface area to volume ratio
Triangle	8.66	0.8	17.32	0.4
Square	7.07	0.565	10	0.4
Pentagon	5.88	0.496	7.26	0.4
Hexagon	5	0.46	5.77	0.4
Circle	10	0.4	10	0.4

4.5.1 Nanowires of different shape having different surface area to volume ratio

In this scenario, the size of the nanowires of different shapes has been chosen in such a way that all the shapes can be inscribed in nanowire of circular cross-section shape having diameter of 10 nm (Figure 4.26). Accordingly, all nanowires have different surface area to volume ratio (Table 4.2). The circular nanowire has a lowest surface area to volume ratio of 0.4, while

the triangular nanowire has the highest and twice the value of circular nanowire. Figure 4.27 shows the stress-strain behaviour of nanowires of different shape having different surface area to volume ratio. For better clarity, inset figure shows the stress-strain curve till a strain value of 20%. Initially, all the nanowires show linear elastic behaviour up to a peak value followed by an abrupt drop in flow stress (except triangular nanowire). In triangular nanowire, the abrupt drop in flow stress is absent and flow stress increases marginally after yielding to a peak value of 5.16 GPa. Following the yielding in all the nanowires, the flow stress decreases continuously with increase in strain till failure. During this decrease, the flow stress exhibits a rapid fluctuations (Figure 4.27). Further, the flow stress of the triangular nanowires is always lower than the flow stress of the other nanowires. Finally, the square shaped nanowire exhibits the highest failure strain of around 180%, while the failure strain is lowest for triangular shaped nanowire. Figure

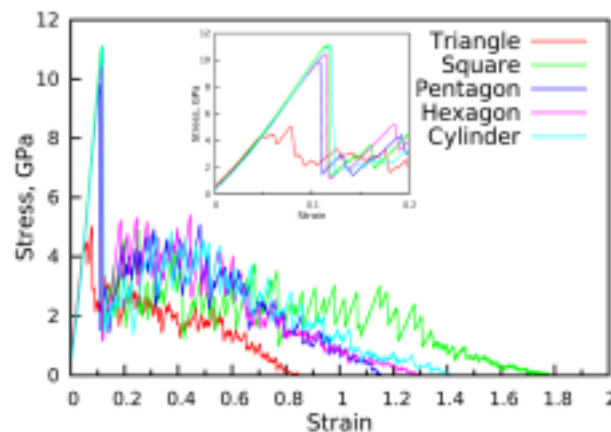


Figure 4.27: Stress-strain behaviour of $\langle 100 \rangle$ Cu nanowires of different shape in Scenario-1, where each shape has a different surface area to volume ratio. The stress-strain behaviour till strain of 20 % has been shown in inset for better clarity.

4.27 also shows that the slope of linear elastic regime is almost same for all the nanowires, which indicates that the Young's modulus is insensitive to the nanowire shape. The value of Young's modulus is obtained as 92 GPa, which is in good agreement with previous reported value [22]. Further, in the atomistic simulation study of Cao and Ma [40], it was observed that both circular and square shaped nanowires possess the same value of Young's modulus, which affirm the present observation that the Young's modulus is insensitive to nanowire shape. Here, it is interesting to see that despite the different surface area to volume ratio, Young's modulus remains same for different shapes. However, it must be noted that Young's modulus can be influenced by surface area to volume ratio when it is varied by nanowire size [22, 172]. The variations in yield strength for nanowires of different shapes has been presented in Figure 4.28.

It can be seen that the triangular nanowires exhibit a minimum yield strength value of 5.16

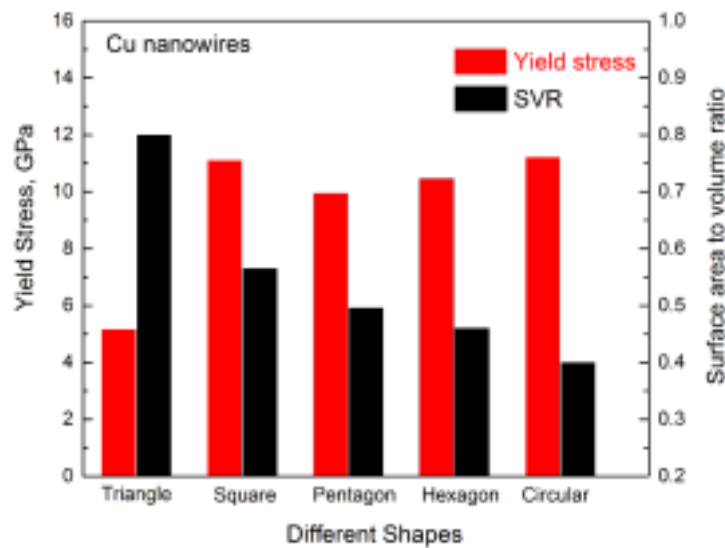


Figure 4.28: Variation of yield strength along with surface area to volume ratio for different nanowire shapes in Scenario-1.

GPa. The magnitude of yield strength increases with increasing the number of the side surfaces and attains a maximum for circular shaped nanowire (Figure 4.28). The variations in yield stress values for different shapes can be attributed to the variations in surface area to volume ratio. The surface area to volume ratio for different shapes has been calculated (Table 4.2) and plotted by superimposing in Figure 4.28. It can be seen that the surface area to volume ratio decreases in the order of triangular, pentagonal, hexagonal, and circular nanowires. These variations clearly indicates that yield stress is inversely proportional to surface area to volume ratio, i.e., the yield strength of nanowires is high for nanowires with low surface area to volume ratios (Figure 4.28).

4.5.2 Nanowires of different shapes having same surface area to volume ratio

In previous section, the effect of shape has been studied by considering different nanowire shapes having different surface area to volume ratio. In order to study the sole effect of shape, here the surface area to volume ratio has been kept same for all shapes. Accordingly, the size of the nanowires has been varied as shown in Table 4.2. Figure 4.29 shows the stress-strain behaviour of nanowires of different shapes with same surface area to volume ratio under tensile

loading. For clarity, the magnified version of stress-strain behaviour till a strain value of 20 % has been shown in inset figure. Similar to scenario-1, all the nanowires exhibit linear elastic deformation up to a peak value of stress. After elastic deformation, all the nanowires including the triangular one show drastic yield drop followed by decrease in flow stress with increasing strain until failure. Further, as in the previous case, the flow stress of the triangular nanowires is considerably lower than the flow stress of the other nanowires (Figure 4.29). Finally, the square shaped nanowire exhibits the highest failure strain, while it is lowest for hexagon and triangular shaped nanowires (Figure 4.29). Similar to previous scenario, the Young's modulus

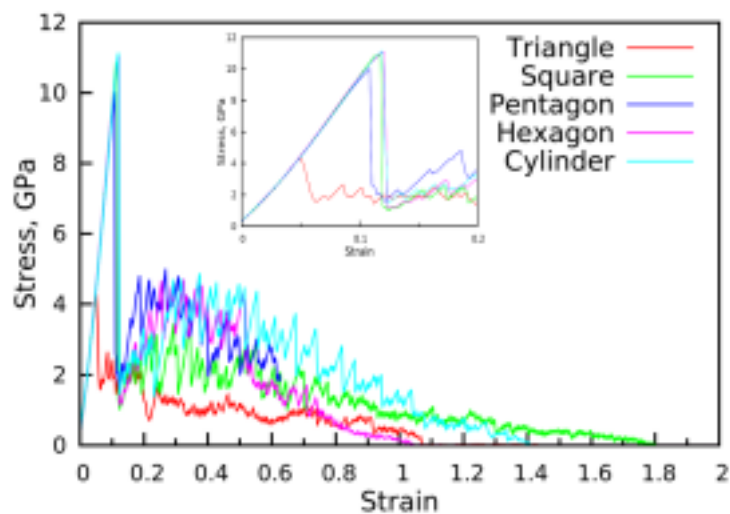


Figure 4.29: Stress-strain behaviour of $\langle 100 \rangle$ Cu nanowires of different shape in Scenario-2, where all the shapes have same surface area to volume ratio. The stress-strain behaviour till strain of 20 % has been shown in inset for better clarity.

has been calculated as the slope of the linear elastic regime and found to be around 92 GPa for all nanowires. This indicate that the Young's modulus is insensitive to the nanowire shape, irrespective of whether the surface area to volume ratio is varied or kept constant. The variations in yield stress for different shaped nanowires with same surface area to volume ratio is shown in Figure 4.30. Here, it is interesting to observe that despite the same surface area to volume ratio, the yield strength still varies for different shapes. Like the previous scenario, the triangular nanowire exhibits the lowest yield stress and it increases with increasing number of side surfaces before attaining the maximum for circular nanowire. However, unlike the previous case, this variation in yield stress cannot be explained by the surface area to volume ratio as it is constant. To understand this variations in the present scenario, the potential energy for different shapes has been calculated and shown in Figure 4.30. Interestingly, both the potential energy and yield stress varies in a similar fashion. Like yield stress, the potential energy

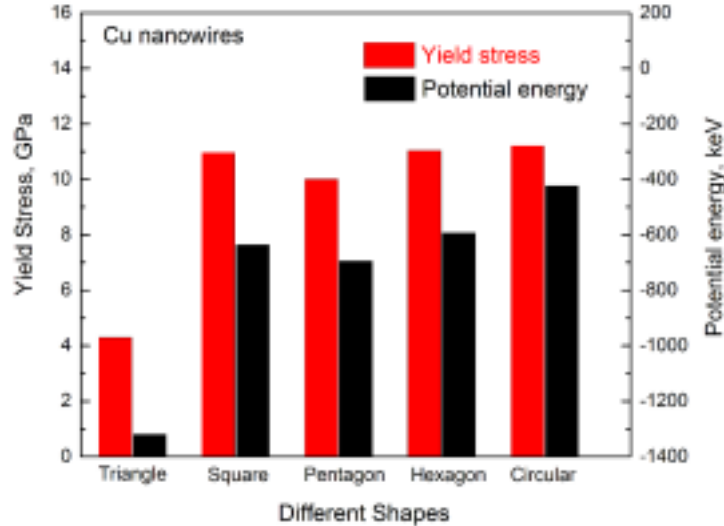


Figure 4.30: Variation of yield strength and potential energy for different nanowire shapes in Scenario-2.

also increases with increase in number of side surfaces exhibiting the highest value for circular nanowire and the lowest for triangular nanowire. These variations indicates that there exists a one to one correlation between potential energy and yield stress. Hence, the variations in yield strength can be attributed to the variations in potential energy of the nanowires (Figure 4.30). Here, it must be noted that in the previous case (nanowires with different shape and different surface area to volume ratio), there were no significant variations in potential energy and no correlation has been found between yield stress and potential energy.

4.5.3 Deformation mechanisms in different shapes

In order to understand the effect of shape on the dislocation nucleation and deformation mechanisms, the atomic configurations have been analyzed for two different scenarios using the CNA parameter and visualized using AtomEye. The results indicate that the defect nucleation and deformation mechanisms were same for both the scenarios. Following yielding, the sudden drop in flow stress corresponds to the defect nucleation in the nanowires and this can also be considered as the initiation of plastic deformation. The initial defect nucleation corresponding to the yielding in the nanowires of different shapes is shown in Figure 4.31. It can be seen that in all the nanowires including the circular one, the yielding occurs through the nucleation of $1/6\langle 112 \rangle$ Shockley partial dislocations from the corners (or intersection of two different side surfaces) of the nanowires. In circular nanowire, the defect nucleation has been observed

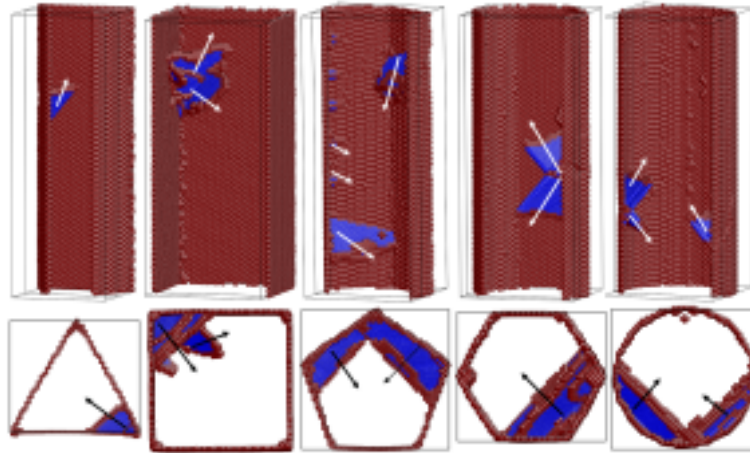


Figure 4.31: The dislocation nucleation during the yielding/beginning of plastic deformation in nanowires of different shapes. This nucleation mechanism remains the same for both scenarios. The white arrows indicates the direction of dislocation motion. The nucleation occurs from the intersection of two different side surfaces.

from the intersection of $\{212\}$ and $\{110\}$ type side surfaces (Figure 4.26). It is well known that the atoms at the corners (or intersection of two different side surfaces) of nanowires have low coordination resulting in high stress concentration. As a result, the corners act as a favorable sites for defect nucleation (Figure 4.31).

Following the nucleation of Shockley partials from the corners, the deformation behaviour in nanowires of different shapes is dominated by the slip through partial dislocations along with deformation twinning (Figure 4.32). However, occasionally the extended dislocations were also

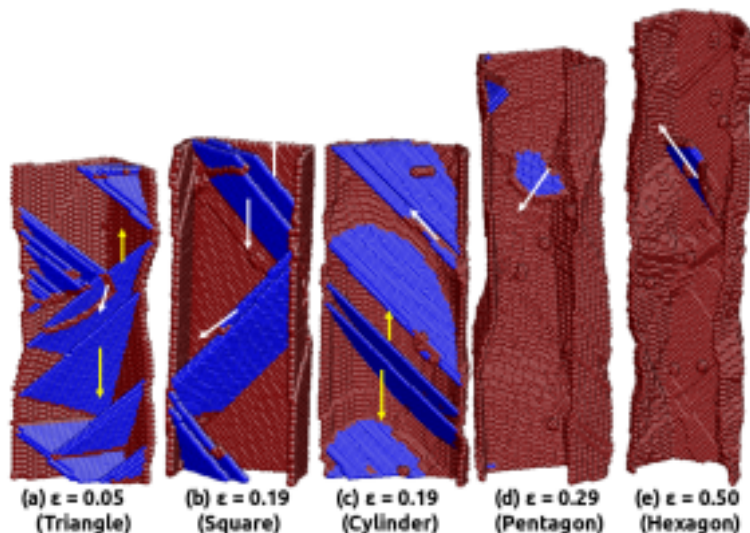


Figure 4.32: The deformation mechanisms observed in nanowires of different shapes, each shown at different strain value. The yellow arrows indicate the direction of twin boundaries movement. The white arrows indicate the direction of glide of Shockley partial dislocations on $\{111\}$ planes.

observed, but only at high strains ($> 50\%$). As shown in Figure 4.32, the twinning has been observed on multiple $\{111\}$ planes. It has been well known that the deformation twinning alters the surface orientation of the nanowires at the twinned region [27, 28]. In the present study, the deformation twinning changed the initial $\{100\}$ side surface of square shaped nanowires to $\{111\}$ type surface (Figure. 4.33b). Similarly, in triangular and hexagonal shaped nanowires, the twinning changes the initial $\{470\}$ surface to $\{315\}$ type surface and $\{100\}$ surface to $\{111\}$ surface (Figure 4.33a & c). In pentagonal and circular nanowires, even though the deformation twinning has been observed, but we are not able to identify the new surface orientations due to high roughness.

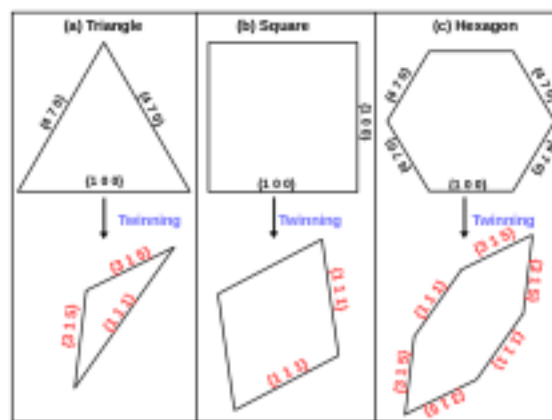


Figure 4.33: The schematic showing the orientation of initial (top row) and twinned side surfaces for (a) triangular, (b) square and, (c) hexagonal shaped nanowires. In pentagonal and circular nanowires, even though the deformation twinning has been observed, but we are not able to identify the new surface orientations due to high roughness.

Figure 4.34 shows the necking and final failure behaviour in nanowires with different cross-section shapes. As shown in Figure. 4.32, the plastic deformation spreads across the nanowire length. Following uniform deformation, the discrete dislocation interactions among different partials leads to the formation of a localized necking (Figure 4.34). In all nanowires, like dislocation nucleation, the necking starts from the corners or the intersection of different side surfaces of the nanowires (Figure 4.34). The formation of necking localizes the plastic deformation and also minimize the effect of corners for any further dislocation nucleation. The localized plastic deformation results in final failure of the nanowires in a ductile manner (Figure 4.34).

In single crystal nanowires, the deformation by partial or full dislocation slip can be under-

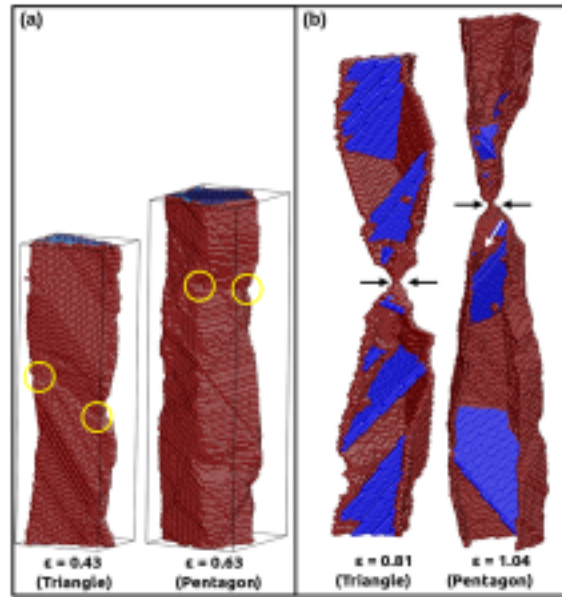


Figure 4.34: The final failure behaviour of nanowires of different shapes. The encircled regions indicate the initiation of necking and black arrows shows failed region.

stood based on the parameter α_M , defined as the ratio of Schmid factors for leading and trailing partial dislocations as described in the section 3.4.1. For a given orientation of a nanowire, if $\alpha_M > 1$, the deformation by twinning/partial dislocation slip is favored. On the other hand, if $\alpha_M < 1$, the deformation by full/extended dislocations is favored. Similarly, if $\alpha_M = 1$, the deformation can proceed either through twinning or extended dislocations or by the combination of these two. It has been shown that for $\langle 100 \rangle$ orientation, the value of α_M is 0.5 under tensile loading. Accordingly, the deformation by full/extended dislocation should be observed. However, in the present study the deformation through slip of Shockley partials has been observed (Figure 4.32). This discrepancy between the predicted and observed deformation mechanism can be attributed to the effects associated with side surfaces [27, 28], whose contribution is absent in the analysis based on α_M . Similar to the present study, many previous studies [27, 28] have shown that the nanowires oriented $\langle 100 \rangle$ tensile axis deform by partial dislocation slip under tensile loading.

4.6 Conclusions

Based on detailed investigation on the size-dependent deformation behaviour of Cu nanowires, following conclusions have been drawn;

The yielding in all $\langle 100 \rangle$ Cu nanowires occurred by the nucleation of $1/6\langle 112 \rangle$ Shockley partial dislocations and the number of dislocations nucleated during yielding increased with increasing nanowire size. The plastic deformation in small size nanowires occurred mainly by slip of partial dislocations at all strains, while in large size nanowires, slip of partial dislocations at low strains followed by slip of extended dislocation at high strains were observed. Young's modulus and yield strength values decreased rapidly in small size nanowires followed by gradual decrease approaching towards saturation at larger size. The size dependence of yield strength has been explained in terms of initial stress and the number of dislocations nucleated during yielding. During plastic deformation, $\langle 100 \rangle$ nanowires with $d \geq 3.615$ nm exhibited initial dislocation exhaustion at small strains followed by dislocation starvation at high strains. Further, the rate of dislocation exhaustion increases with decrease in nanowire size. On the other hand, the nanowires with $d < 3.615$ nm show mainly dislocation starvation at all strains. The large size nanowires show lower exhaustion rates as compared to smaller ones, i.e., resident time of dislocations within the nanowire increases with increasing size. In a nanowire of particular size, the dislocation exhaustion rates increases with increasing temperature and strain rate. Correspondingly, the transition strain decreases with increasing temperature and decreasing strain rate. The lower exhaustion rates at low temperatures and low strain rates are mainly due to low dislocation velocities, which increases the probability of dislocation interactions with existing defects or dislocations and thus restricting the ease of dislocation annihilation to surfaces. Also, the average length of dislocations remained nearly constant between 2 and 2.5 nm during deformation in all the $\langle 100 \rangle$ Cu nanowires, except in the small size nanowire with $d \leq 1.446$ nm. Finally, the failure strain has been found to increase linearly with increase in nanowire size and this has been correlated with higher pre- and post-necking deformation in large size nanowires. Further, formation of pentagonal atomic chains has been observed in small size nanowires with $d \leq 1.446$ nm. Dislocation-stacking fault interactions resulting in the formation of intermediate stair-rod dislocations and their dissociation lead to annihilation of stacking faults in all the nanowires. Dislocation-dislocation interactions on intersecting $\{111\}$ planes lead to the formation of L-C lock at the acute junction and Hirth lock at obtuse junction. The partial dislocation interaction with Hirth lock results in L-C lock and partial dislocation interaction with L-C lock gives rise to Frank partial.

Interestingly, $\langle 110 \rangle$ Cu nanowires with aspect ratio ≤ 1 display double reorientation during tensile deformation. It has been observed that the original $\langle 110 \rangle$ as well as reoriented

$\langle 100 \rangle$ and $\langle 112 \rangle$ Cu nanowires deform by twinning mechanism facilitating double reorientation from $\langle 110 \rangle$ to $\langle 100 \rangle$ and from $\langle 100 \rangle$ to $\langle 112 \rangle$ orientations. The deformation by twinning in $\langle 110 \rangle$ and $\langle 112 \rangle$ orientations has been explained using the Schmid factor analysis, while twinning in $\langle 100 \rangle$ orientation has been ascribed to the minimization of surface energy.

Surprisingly, Young's modulus is insensitive to the nanowire shape. The yield strength increases with increasing number of side surfaces. The triangular nanowire shows the lowest strength and ductility (failure strain), while the circular nanowire display highest strength combined with good ductility. All nanowires irrespective of their shape and surface area to volume ratio, the deformation is dominated by the slip through Shockley partial dislocations and deformation twinning. The deformation twinning changed the orientation of side surfaces at the twinned region, whose orientation is different for different shapes. Finally nanowires of all shapes fail in a ductile manner.

Chapter 5

Role of axial twin boundaries on the deformation mechanisms in Cu nanopillars

5.1 Introduction

It is well established that the nanowires/nanopillars can be strengthened by introducing twin boundaries (TBs). Twin boundaries can be introduced at different angles with respect to loading axis. Depending on the angles, the operating deformation mechanisms in twinned nanowires/nanopillars varies. As discussed in section [1.4.3](#), many studies were carried out on nanopillars with orthogonal and slanted twin boundaries. Little has been investigated on twinned nanowires when the twin boundaries are parallel to the loading direction (axial or longitudinal twin boundaries). In longitudinally twinned nanowires, the loading direction can be either $\langle 110 \rangle$ or $\langle 112 \rangle$. However, previous reports had focused on $\langle 110 \rangle$ nanopillars. Further, the influence of TB spacing and its position from nanopillar surface have not been investigated. In view of this, the deformation behaviour of longitudinally twinned Cu nanopillars under compression and tension has been investigated and presented in this chapter. In addition, influence of TB position also has been presented.

5.2 Computational details

Molecular dynamics (MD) simulations have been performed using LAMMPS package [123] employing an Mishin's EAM potential for FCC Cu [108]. AtomEye [129, 131] and OVITO [130] packages have been used for the visualization and analysis of deformation mechanisms. Common neighbour analysis (CNA) as implemented in AtomEye and OVITO and dislocation extraction algorithm as implemented in OVITO have been used to identify the stacking faults and various type of dislocations based on the Burgers vector.

In order to create a longitudinal twin boundary, the procedure followed in Ref. [183] has been adapted. First, a defect free Cu nanopillar of square cross section width (d) = 10 nm, oriented in $\langle 112 \rangle$ axial direction with $\{110\}$ and $\{111\}$ as side surfaces has been chosen. The nanopillar length (l) was twice the cross section width (d) and no periodic boundary conditions were used in any direction. Then, the nanowire has been divided into two equal parts along the $\langle 111 \rangle$ direction and, one part of the crystal is rotated with respect to the other by 180° . Following the rotation, a twin boundary forms at the interface, which lies on $\{111\}$ plane. Similar procedure has been adapted to create more number of twin boundaries. The nanopillars containing one, two, three, four and five twin boundaries resulted in twin boundary spacings of 5.0, 3.3, 2.5, 2.0 and 1.6 nm, respectively. The typical nanopillars with different twin boundary spacings considered in this study along with perfect nanopillar are shown in Figure 5.1. The double Thompson tetrahedron showing the slip planes and directions in parent and twinned lattice is shown in Figure 5.1d. In the present study, this notation has been used to describe the various dislocation-twin boundary interactions.

In order to understand the influence of twin boundary position on yield strength of Cu nanopillars, the twin boundary position has been altered by positioning single twin at various distances (x) from the free surface of nanopillar as shown in Figure 5.2. Following the creation of the model nanowires, the energy minimization was performed by a conjugate gradient method to obtain a relaxed structure. To put the sample at the required temperature, all the atoms have been assigned initial velocities according to the Gaussian distribution. Following this, the nanopillar system was thermally equilibrated to a required temperature of 10 K in canonical ensemble (constant NVT) with a Nose-Hoover thermostat. The velocity verlet algorithm has been used to integrate the equations of motion with a time step of 2 fs. Following

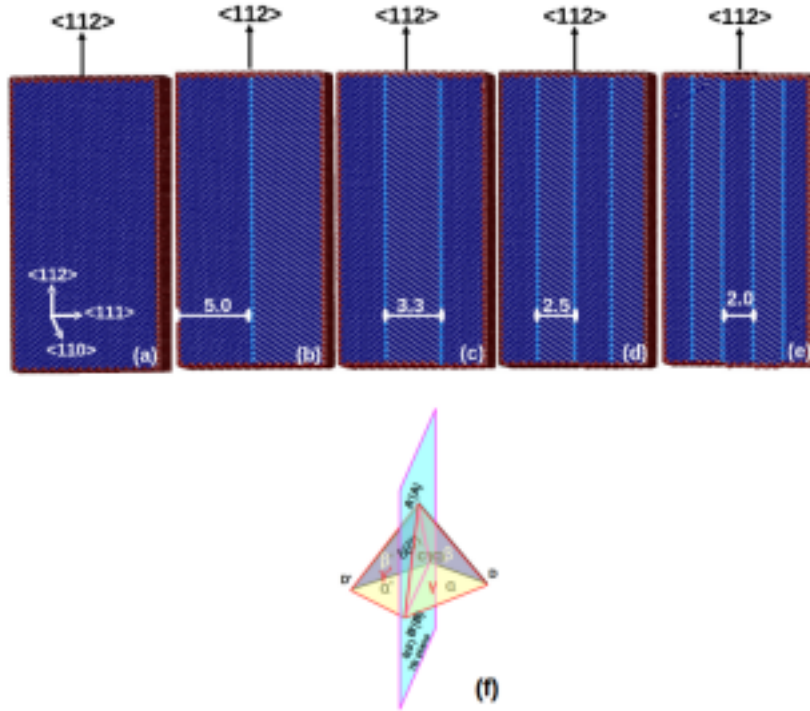


Figure 5.1: The model system of (a) perfect Cu nanopillar and twinned Cu nanopillars with (b) one (c) two (d) three and, (e) four, equidistant twins. The double Thompson tetrahedron illustrating the slip planes and directions is shown in (f). The crystallographic orientation and twin boundary spacing has been shown for clarity. The cross-section width (d) of all the nanowires is 10 nm. In (a)-(e), The front surfaces are removed and the atoms are colored according to the common neighbor analysis (CNA).

thermal equilibration, the tensile or compressive deformation was carried out in a displacement controlled mode at a constant strain rate of $1 \times 10^8 \text{ s}^{-1}$ by imposing displacements to atoms along the axial direction (i.e., $\langle 112 \rangle$ axis) that varied linearly from zero at the bottom to a maximum value at the top layer. Finally, the stress has been obtained using the Virial expression [140], which is equivalent to a Cauchy's stress in an average sense.

5.3 Effect of twin boundary spacing

5.3.1 Stress-strain behaviour

Figure 5.3 shows the stress-strain behaviour of perfect as well as twinned $\langle 112 \rangle$ Cu nanopillars subjected to tensile and compressive loading. The tensile loading has been performed until a nanopillar attains a strain of 50%, while in compression, the loading has been applied until

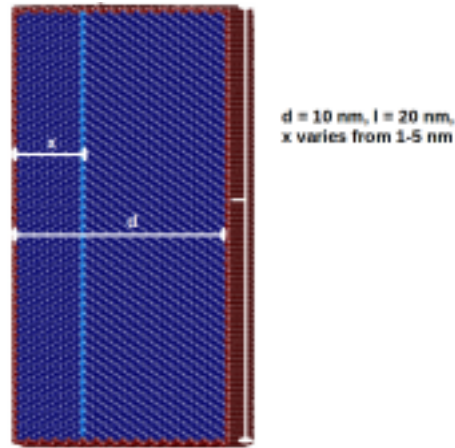


Figure 5.2: The atomic configuration of twinned nanopillar with varied twin boundary position. Twin boundary position has been modified by changing twin distance (x) from surface in the range 1 nm to 5 nm (For instance, $x = 3$ nm as shown in the present Figure). The atoms are colored according to the common neighbor analysis (CNA). The blue color atoms indicate the pure FCC Cu atoms, while cyan color atoms indicate the twin boundary atoms and the red color atoms represent surface atoms.

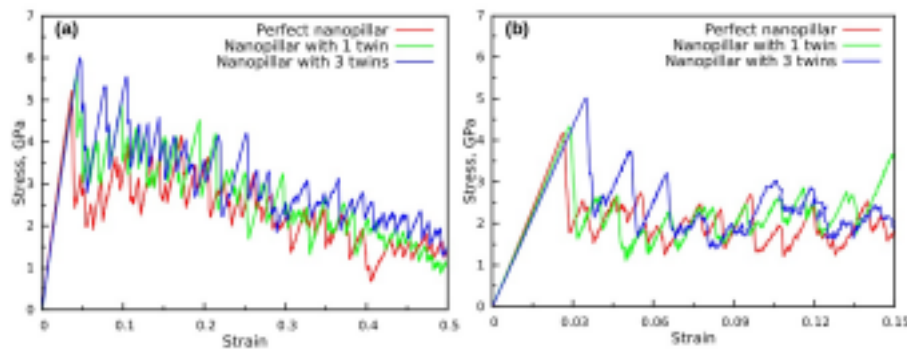


Figure 5.3: The stress-strain curves of $\langle 112 \rangle$ Cu nanopillars with and without axial twin boundaries under (a) tension (b) compression.

a strain of 15%. It can be seen that, all the nanopillars exhibit a linear elastic deformation up to a maximum value of stress (designated as yield stress) followed by a precipitous drop of around 2-3 GPa. Following the drop, the flow stress under tensile loading show an overall decreasing behaviour with large fluctuations (Figure 5.3a). On the other hand, the flow stress under compressive loading display large fluctuations around a constant mean stress of 2 GPa (Figure 5.3b). The peak value of the stress-strain curve has been taken as the yield stress of the nanopillar. It can be seen that, under both tensile and compressive loading, the introduction of twin boundaries increases the strength of the nanopillar as compared to the perfect nanopillar (Figure 5.3). Further, higher the number of twin boundaries, higher the strength.

To quantify the effect of twin boundaries, the twin boundary spacing has been chosen as the

variable parameter. Figure 5.4 shows the variation of yield stress as a function of twin boundary spacing under tensile and compressive loading. For comparison, the yield stress of perfect $\langle 112 \rangle$ nanopillar has been shown as a horizontal line under respective loading conditions. It can be seen that the yield stress of all the twinned nanopillars falls above the horizontal line (Figure 5.4), indicating that the strength of twinned nanopillars is higher than the perfect twin free nanopillars. Further, the yield stress values under tensile and compressive loading decrease with increasing twin boundary spacing (Figure 5.4), which is similar to that observed in orthogonally twinned FCC nanopillars [75, 81, 84, 88, 184]. It can also be seen that, for perfect as well as twinned nanopillars, the yield stress values under tensile loading are higher than that in compressive loading i.e., all the nanopillars display tension-compression asymmetry in yield stress. Figure 5.5 shows the values of yield stress asymmetry measured as the ratio of yield

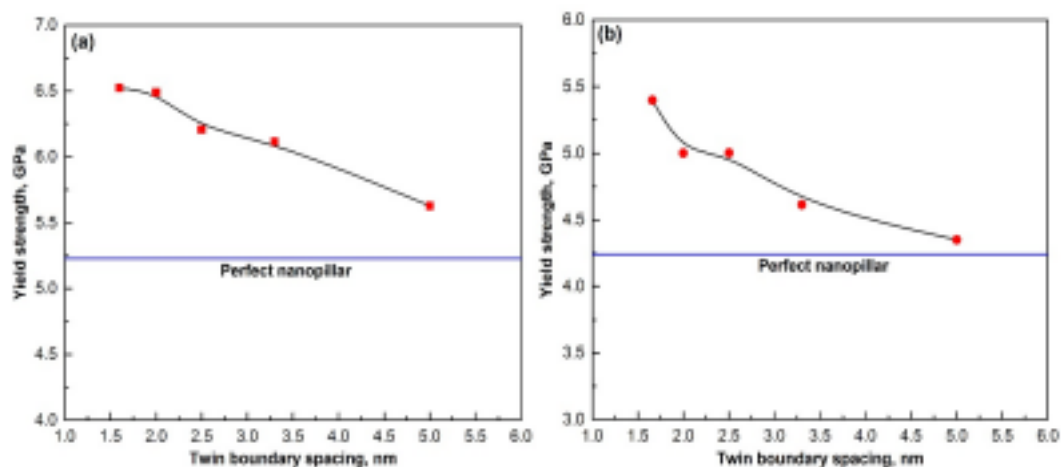


Figure 5.4: The variation of yield strength as a function of twin boundary spacing (TBS) under (a) tensile (b) compressive loading. For reference, the yield strength of perfect nanopillar has been represented as a horizontal line.

stress in tension to that in compression, as a function of twin boundary spacing. The yield stress asymmetry of perfect nanopillar is obtained as 1.2, which is shown as horizontal line in Figure 5.5. It can be seen that the yield stress asymmetry for twinned nanopillars is different from that of the perfect nanopillars (higher the number of twin boundaries, lower the asymmetry), which indicates that the twin boundaries can also influence the tension-compression asymmetry. In section 3.4.2, it has been shown that the asymmetry in yield stress arises due to different values of Schmid factor for leading partials under tensile and compressive loading. Further, Salehinia and Bahr [185] have shown that the asymmetry in the strength of nanowires decreases with increasing defect density, which is in agreement with the present findings.

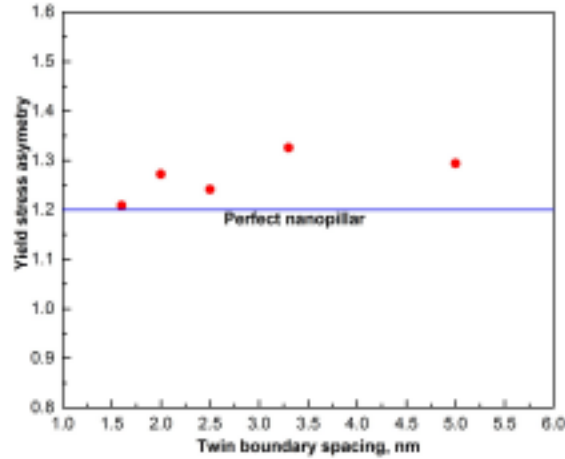


Figure 5.5: Variation of yield strength asymmetry in twinned nanopillar of different twin boundary spacings. For comparison, the yield strength asymmetry of perfect nanopillar has been shown as a horizontal line. Here, the yield strength asymmetry is defined as the ratio of yield stress in tension (σ_{yt}) to that in compression (σ_{yc}).

5.3.2 Deformation mechanisms in perfect $\langle 112 \rangle$ Cu nanopillars

In order to understand the clear role of twin boundaries on deformation mechanisms, first, the deformation mechanisms in perfect $\langle 112 \rangle$ Cu nanopillars has been investigated. Under compressive loading, the deformation is governed by the slip of extended dislocations. An extended dislocation consist of a leading and trailing partial dislocations separated by a stacking fault. Different from compressive loading, the deformation under tensile loading of perfect $\langle 112 \rangle$ Cu nanopillars occurs through the slip of Shockley partial dislocations along with deformation twinning. These results are in agreement with that predicted using Schmid factor analysis for Cu nanowires in section 3.4.1.

5.3.3 Deformation mechanisms in twinned $\langle 112 \rangle$ Cu nanopillars under compressive loading

The deformation of Cu nanopillar with single and multiple twin boundaries has been investigated under compressive loading. As a representative one, the deformation behaviour of Cu nanopillar with two twin boundaries has been shown in Figure 5.6. It can be seen that the yielding in twinned nanopillars occurs through the nucleation of extended dislocation consisting of leading ($1/6[\bar{1}12]$) and trailing ($1/6[121]$) partials. Following yielding, the extended dislocation glides towards a nearby twin boundary as shown in Figure 5.6a. Since the presence of

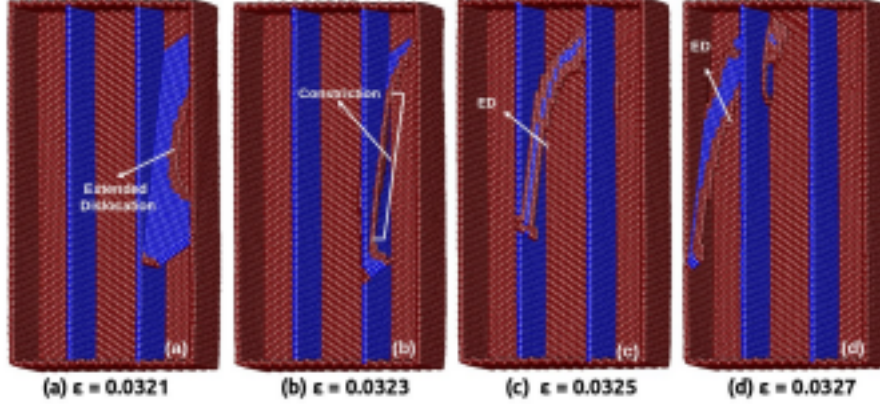
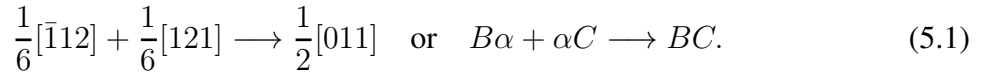
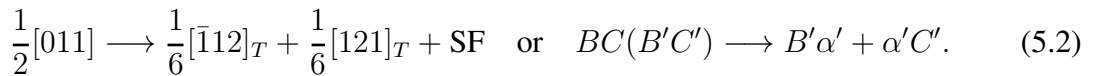


Figure 5.6: The deformation behaviour under the compressive loading of twinned Cu nanopillars at different strains. The glide of an extended dislocation (ED) undergoing slip transmission through multiple twin boundaries can be seen. This process involves the constriction of an extended dislocation followed by cross-slip. The atoms are colored according to the common neighbor analysis (CNA). The blue color atoms represents the FCC and the red color atoms indicate the surfaces and dislocation core.

twin boundary restricts the free glide, the extended dislocation gets constricted and forms full dislocation at the twin boundary (Figure 5.6b) according to the following reaction:



This constricted full dislocation, which has high energy, cross-slips to neighboring twinned grain on a plane symmetric to the original (symmetric slip transmission) by dissociating into an extended dislocation (Figure 5.6c). This dissociation can be written as



Here, the subscript "T" for the leading and trailing partial indicates Burger's vector in twinned grain. The extended dislocation again undergoes similar constriction and transmission upon facing the subsequent twin boundaries before annihilating at the free surface (Figure 5.6d).

In addition to symmetric slip transmission aided by the formation of constriction and dissociation, it has been observed that the extended dislocation can also cross-slip to twin boundary plane without forming any intermediate constriction (Figure 5.7). Initially, the glide of leading partial (part of an extended dislocation) is restricted at the twin boundary with trailing partial far behind (Figure 5.7a). This leading partial with Burger vector of $1/6[12\bar{1}]$ dissociates into a

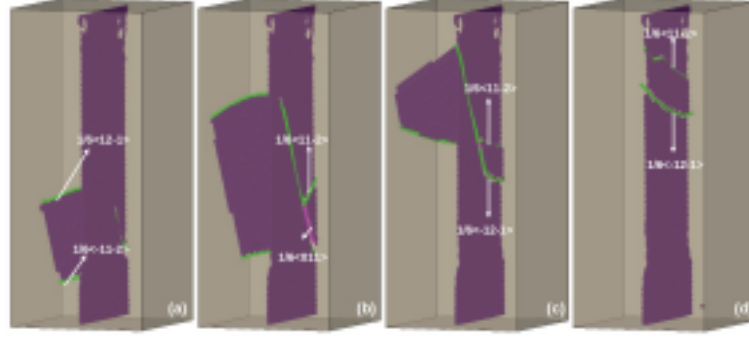


Figure 5.7: The deformation behaviour under the compressive loading of twinned Cu nanopillars (a-d). Here, the extended dislocation cross-slips to the twin boundary plane by forming an intermediate stair-rod dislocation. The purple color surface represents the stacking fault and twin boundary. The green color lines indicate the Shockley partial dislocations and the magenta color line represents stair-rod dislocation.

stair-rod dislocation ($1/6[011]$) and a Shockley partial dislocation $1/6[11\bar{2}]$ on the plane of the twin boundary (Figure 5.7b). In Burger vector terms, this dissociation can be written as

$$\frac{1}{6}[12\bar{1}] \longrightarrow \frac{1}{6}[11\bar{2}] + \frac{1}{6}[011] \quad \text{or} \quad C\beta \longrightarrow C\delta + \delta\beta. \quad (5.3)$$

With increasing deformation, the trailing partial comes to the twin boundary and its interaction with existing stair-rod dislocation leads to the formation of Shockley partial lying on the twin boundary (Figure 5.7c). This reaction can be written as

$$\frac{1}{6}[011] + \frac{1}{6}[\bar{1}1\bar{2}] \longrightarrow \frac{1}{6}[\bar{1}2\bar{1}] \quad \text{or} \quad \delta\beta + \beta A \longrightarrow \delta A. \quad (5.4)$$

Now, the two Shockley partials lying on the twin boundary ($C\delta$ and δA), which are separated by a finite distance, constitutes an extended dislocation with a Burgers vector of $1/2[01\bar{1}]$ or CA , which also lies on twin boundary (Figure 5.7c). With increasing deformation, the incident extended dislocation completely cross-slips to the twin boundary plane and glides further on the same plane as shown in Figure 5.7d.

Thus, under the compressive loading of twinned nanopillars, the extended dislocations show symmetric slip transmission (Figure 5.6) and also the cross-slip to the twin boundary plane (Figure 5.7).

5.3.4 Deformation mechanisms in twinned $\langle 112 \rangle$ Cu nanopillars under tensile loading

Like compressive loading, tensile deformation of nanopillars with single and multiple twin boundaries has been investigated. Figure 5.8 shows the atomic snapshots of twinned $\langle 112 \rangle$ Cu nanopillar containing a single twin boundary under tensile loading. The yielding in twinned nanopillar occurs through the nucleation of leading partial dislocations from two different corners of the nanopillar (Figure 5.8a). The two nucleated leading partials glide towards each other and interact at twin boundary resulting in the formation of a stair-rod dislocation (Figure 5.8b), which again lies on twin boundary plane. With increasing deformation, the stair-rod dislocation again dissociates into two trailing partials gliding on the same planes as that of the original leading partials (Figure 5.8c). The dissociation of stair-rod into two trailing partials annihilate the stacking faults produced by leading partials (Figure 5.8c). This novel mechanism of stair-rod formation and dissociation results in deformation proceeding through extended dislocations (leading followed by trailing) in twinned nanopillars as shown in Figure 5.8d. Similar formation of stair-rod and its dissociation at the twin boundary has been reported in earlier studies [87, 186].

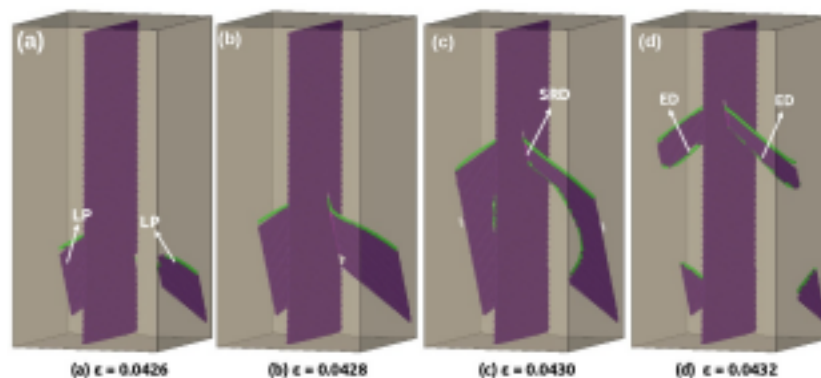
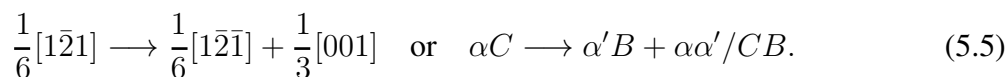
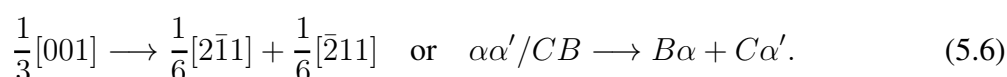


Figure 5.8: The atomic configurations displaying the deformation behaviour of twinned Cu nanopillars under tensile loading. The two leading partials (LP) (a-b) interact at the twin boundary and result in the formation of a stair-rod dislocation (b). The stair-rod dislocation (SRD) again dissociates into two trailing partials (c), which glide on the same plane as that of the leading partials but in opposite direction. The sequential glide of leading and trailing partials enclosing the stacking fault makes the deformation to proceed by extended dislocations (ED) (d). The purple color surface represents the stacking fault and twin boundary. The green color lines indicate the Shockley partial dislocations and the magenta color line represents a stair-rod dislocation.

In addition to stair-rod formation through two leading partials at the twin boundary, the stair-rod formation due to a single leading partial dislocation has also been observed as shown in Figure 5.9. Here, once the leading partial encounters the twin boundary (Figure 5.9a), it cross-slips to the next grain leaving behind a Hirth stair-rod dislocation at the twin boundary (Figure 5.9b) according to the following reaction,



With increasing stain, the Hirth dislocation on the twin boundary dissociates into two Shockley partial dislocations, one gliding back into the original grain and the other gliding behind the leading partial on the cross-slip plane (Figure 5.9b). This dissociation of Hirth dislocation can be written as



Here, it can be seen that these dissociated partials act as trailing dislocations making the deformation in nanopillars proceed through extended dislocations (Figure 5.9b-c). The Burgers vector of these extended dislocations is the summation of leading and trailing partials as shown below

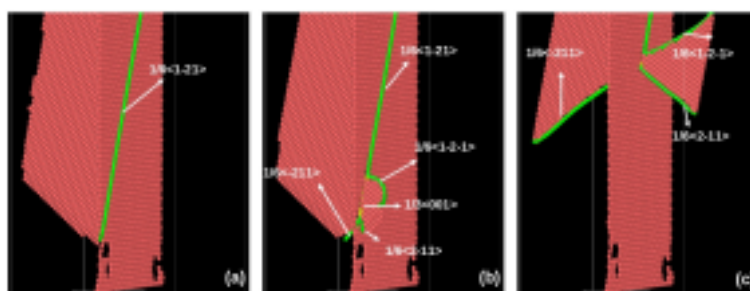


Figure 5.9: The deformation mechanism under the tensile loading of twinned Cu nanopillars. The leading partial impeded by the twin boundary can be seen in (a). This partial dislocation cross-slips to the next grain leaving behind a Hirth stair-rod dislocation at the twin boundary (b). The Hirth dislocation again dissociates into two partials, which results the deformation in the nanopillar to proceed by extended dislocations (c). The perfect and surface atoms are removed for clarity. The red color atoms represents the HCP atoms (stacking fault and twin boundaries). The green color lines indicate Shockley partials and yellow color line shows Hirth stair-rod.

Similar to the cross-slip mechanism seen in compressive loading, it has been observed that under tensile loading also the extended dislocation can cross-slip to twin boundary plane. However, this cross-slip onto the twin boundary plane has been mediated by forming a constriction. Following the cross-slip, the extended dislocation lying on the twin boundary can be seen in Figure 5.10a. Interestingly, one partial of this extended dislocation gets dissociated into a stair-

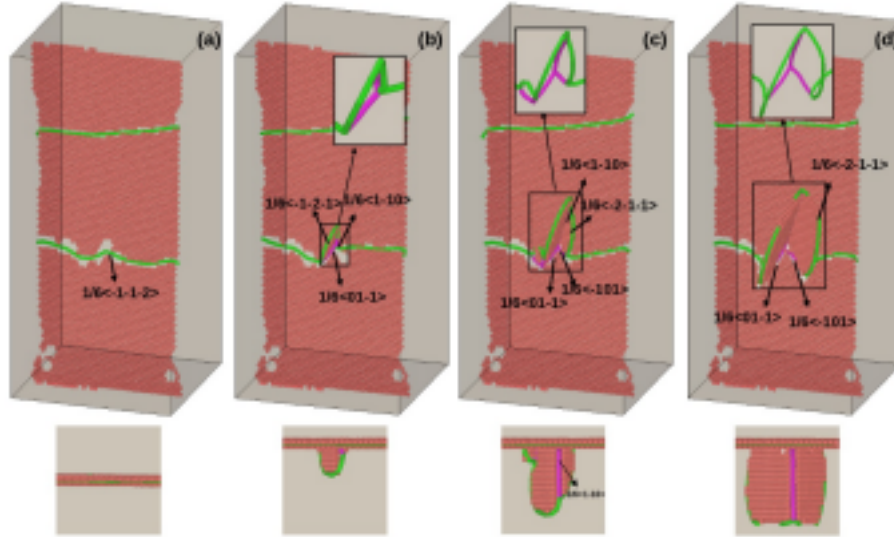


Figure 5.10: The dislocation activity at the twin boundary resulting in the formation of well organized dislocation network. The bottom line figure shows the top view of the nanopylar. For clarity, the dislocation network without the stacking fault atoms are shown in inset figures.

rod dislocation (which lies on the twin boundary) and a Shockley partial dislocation (which protruded out of the twin boundary) as shown in Figure 5.10b. This dissociation can be written as

$$\frac{1}{6}[\bar{1}\bar{1}\bar{2}] \longrightarrow \frac{1}{6}[01\bar{1}] + \frac{1}{6}[\bar{1}\bar{2}\bar{1}] \quad \text{or} \quad \delta C \longrightarrow \delta\alpha' + \alpha' C. \quad (5.8)$$

Following this dissociation, the small segment of protruded Shockley partial dislocation again dissociates into a stair-rod dislocation and a Shockley partial dislocation as shown in Figure 5.10c. This dissociation in Burger's vector terms can be written as

$$\frac{1}{6}[\bar{1}\bar{2}\bar{1}] \longrightarrow \frac{1}{6}[1\bar{1}0] + \frac{1}{6}[\bar{2}\bar{1}\bar{1}] \quad \text{or} \quad \alpha' C \longrightarrow \alpha'\beta' + \beta' C. \quad (5.9)$$

As the deformation proceeds, the length of both stair-rod dislocation and Shockley partial dislocation increases (Figure 5.10c). Then, a new stair-rod dislocation (which lies on the twin boundary) forms upon the interaction of dissociated Shockley partial and a Shockley partial

lying on the twin boundary (Figure 5.10c). The formation of stair-rod occurs according to the following reaction:



Upon new stair-rod formation on the twin boundary, all dislocations (stair-rods and Shockley partials) lying on the twin boundary plane glide towards the surface (Figure 5.10d). Similarly, the protruded stair-rod and Shockley partial dislocations also move away from the twin boundary (Figure 5.10d).

Thus, the stair-rod formation due to two or one leading partials makes the deformation to proceed by extended dislocations under tensile loading. Likewise, Figure 5.11 shows the plastic deformation in nanopillar with multiple twin boundaries, which is also dominated by extended dislocations formed through similar mechanism of stair-rod formation and dissociation. Here,

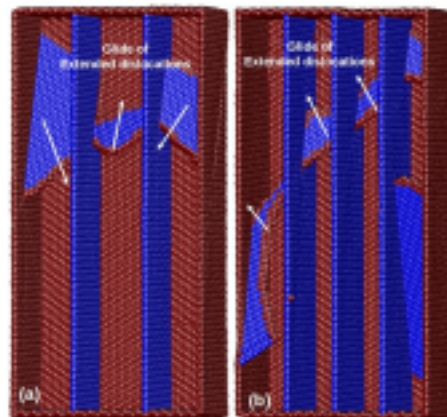


Figure 5.11: The atomic snapshots displaying the deformation behaviour of twinned $\langle 112 \rangle$ Cu nanopillars under tensile loading. The deformation behaviour in nanopillar with (a) two twins and, (b) three twins. The atoms are colored according to the common neighbor analysis (CNA). The blue color atoms represents the FCC and the red color atoms indicate the surfaces and dislocation core.

it is interesting to note that the plastic deformation in twinned nanopillars (which occurred through extended dislocations) is quite different from partial dislocation slip in perfect $\langle 112 \rangle$ nanopillars.

5.3.5 Yield stress in twinned nanopillars

The results with respect to the strength of axially twinned Cu nanopillars indicate that, irrespective of twin boundary spacing, all the twinned nanopillars possess higher strength as compared to their perfect counterparts (Figure 5.4). Further, the yield strength decreases with increasing the twin boundary spacing. In orthogonally twinned nanopillars, the higher strength of twinned nanopillars has been attributed to different factors like redistribution of interior stress within the nanopillar [75] and strong repulsive force offered by twin boundaries on dislocations [187, 188, 189]. In axially twinned nanopillars also similar factors influence the yield strength.

In order to understand the role of stress redistribution in individual twinned regions, the strength of single crystal nanopillars with cross-section width (d) equal to the twin boundary spacing has been investigated. Figure 5.12a shows the variation of yield strength in perfect nanopillars as a function of cross-section width (d) (here d is equivalent to twin boundary spacing). For comparison, the strength of original perfect nanopillar ($d = 10$ nm) and twinned nanopillars of different twin boundary spacing has also been shown in Figure 5.12a. It can be seen that, the perfect nanopillars (of size equivalent to twin boundary spacing) exhibit an expected size effect i.e., strength decreases with increasing size [164]. Further, the yield strength of the twinned nanopillar is much lower than the yield strength of corresponding perfect nanopillar with size equal to twin boundary spacing. With this comparison, it can be concluded that the strength of individual twinned regions has some contribution in dictating the overall strength of the twinned nanopillars. However, it is not directly additive i.e., the sum of the yield strength of individual perfect nanopillars (of size equal to twin boundary spacing), is not equal to the strength of twinned nanopillar of same spacing. This may be attributed to the surface modification introduced due to the incorporation of twin boundaries from individual perfect nanopillars.

The other factor is the repulsive force acting on the dislocations due to twin boundaries [183, 187, 188, 189]. Deng and Sansoz [188] have shown that the repulsive force acting on the dislocations is proportional to the Burgers vector and inversely proportional to twin boundary spacing. Generally, the critical resolved shear stress (CRSS) for dislocation nucleation in twinned nanopillars (τ_c) can be written as [190] $\tau_c = \tau_o + \tau_{tb}$, where τ_c is the CRSS in pure twin free nanopillar and τ_{tb} is the additional contribution to CRSS due to the presence of twin

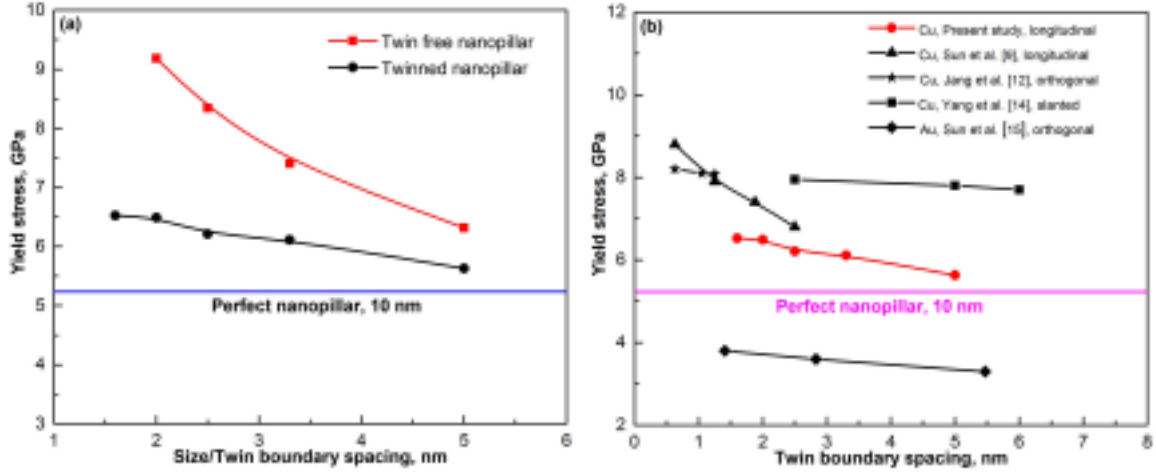


Figure 5.12: (a) Comparison of yield stress in twinned and twin free nanopillars with size equal to twin boundary spacing. (b) Comparison of yield stress in twinned nanopillars with that reported in other studies from the literature [83, 84, 88, 89]. For comparison, the yield stress of perfect nanopillar of size 10 nm has also been shown.

boundaries. Here, τ_o is simply the product of yield stress and maximum value of Schmid factor in perfect nanopillars and the τ_{tb} is given by Deng and Sansoz [188] as follows;

$$\tau_{tb} = \lambda \frac{\mu b \sin \theta}{4\pi x(1-\nu)} \left(1 + \frac{b}{2r} \ln \frac{8r}{b} \right). \quad (5.11)$$

Here for Cu, λ is approximately 0.3 [188], the shear modulus (μ) is 53.31 GPa, θ is the angle between the twin boundary and the $\{111\}$ slip plane, ν is the Poisson's ratio, b is the Burgers vector of partial dislocations, x is the twin boundary spacing, $r = \sqrt{bD \cos \theta}$ and D is the size of the nanopillars. Based on this formulation and given parameters, the values of τ_c have been calculated for nanopillars with different twin boundary spacing in the range 1.6 - 5 nm. It has been observed that τ_c varies in the range 2.28 GPa (for nanopillar with $x = 1.6$ nm) to 2.11 GPa (for nanopillar with $x = 5$ nm). In other words, higher is the twin boundary spacing lower is the repulsive force and this leads to lower yield stress values. In nanopillars with smaller twin boundary spacing, the high repulsive force makes the dislocation nucleation and glide difficult, thus giving rise to increase in yield strength.

Figure 5.12b compares the yield stress values of twinned nanopillars in the present study with that reported in other studies in literature [83, 84, 88, 89]. Similar to the present study, many studies in the literature have reported that the yield stress decreases with increasing twin boundary spacing. However, the absolute values of yield stress are different in different studies. This difference in yield stress values may arise due to many factors like nanowire size, cross

section shape and twin boundary orientation.

5.3.6 Deformation mechanisms and cross-slip

The results also indicate that the axial twin boundaries significantly influence the deformation mechanisms of Cu nanopillars. The deformation in perfect $\langle 112 \rangle$ nanopillars occurs by partial dislocation slip/twinning under tensile loading. Generally, in $\langle 112 \rangle$ oriented nanopillars, the deformation by partial dislocation slip is predicted according to Schmid factor analysis. However, the introduction of twin boundaries changed the deformation mode from partial dislocation slip/twinning to extended dislocation slip. The extended dislocations in twinned nanopillars are facilitated by the stair-rod formation and its dissociation on the twin boundary. On the other hand, the deformation is dominated by the slip of extended dislocations under the compressive loading of perfect as well as twinned nanopillars, which is in agreement with Schmid factor based predictions as discussed in section 3.4.1. This indicates that under compression, the deformation mechanisms are not influenced by the presence of twin boundaries.

Irrespective of loading conditions, the presence of twin boundaries has introduced an extensive cross-slip of dislocations from one grain to the neighboring grain and also the cross-slip onto the twin boundary plane. This indicates that the presence of twin boundaries significantly influences the deformation in FCC Cu nanopillars by the cross-slip activity. Since the deformation under compressive loading is dominated by extended dislocations, these extended dislocations get constricted at the twin boundary and result in the formation of full dislocation (Figure 5.6). This constricted full dislocation, which has high energy, cross-slips to the neighboring grain on a plane symmetric to the original by dissociating into an extended dislocation (Figure 5.6). This mechanism is similar to the Friedel-Escaig (FE) [191, 192, 193] cross-slip mechanism as shown schematically in Figure 5.13a. The FE cross-slip mechanism involves the constriction of two partials in the initial glide plane followed by re-dissociation into the cross-slip plane (Figure 5.13a). In addition to the FE mechanism, it has also been observed that the extended dislocation can also cross-slip to the twin boundary plane without forming any constriction. As shown in Figure 5.7, the cross-slip of an extended dislocation is also facilitated by forming an intermediate stair-rod dislocation, which is similar to the Fleischer mechanism of cross-slip in FCC metals [194] as shown schematically in Figure 5.13b. In the Fleischer mechanism of cross-slip, the leading partial dissociates into a stair-rod and another Shockley partial on the cross-slip plane

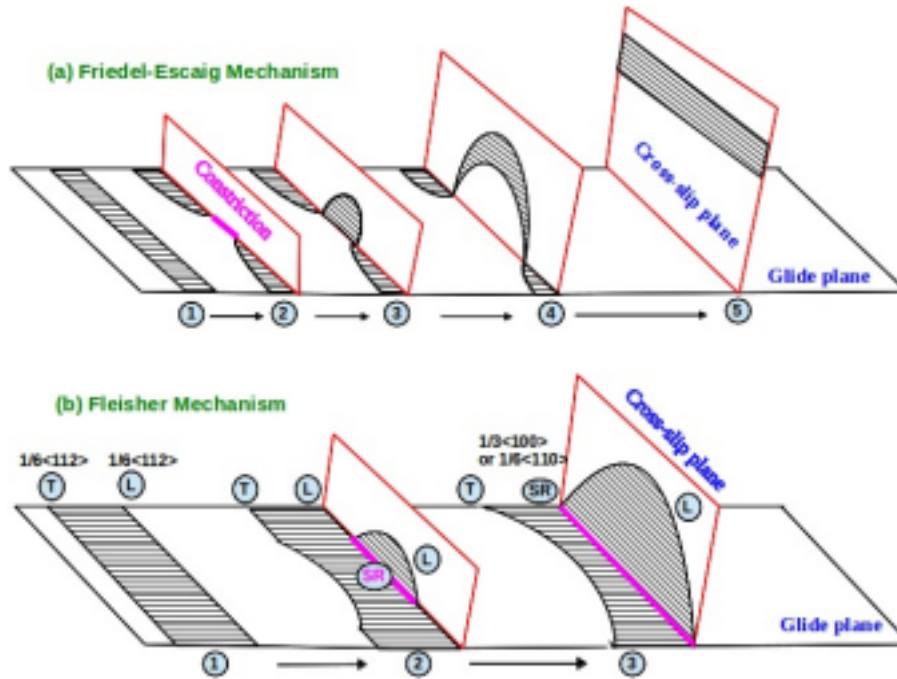


Figure 5.13: The schematic view showing a sequence of events in (a) Friedel-Escaig (FE) [191, 192, 193], and (b) Fleischer mechanism [194] of cross-slip. In FE mechanism, the constriction of two partials in the initial glide plane followed by re-dissociation into the cross-slip plane can be seen. In Fleischer mechanism, the leading partial and stacking fault fold over from initial glide plane to cross-slip plane, by leaving a stair-rod dislocation at the intersection.

without the concept of constriction. In other words, the leading partial and stacking fault fold over from initial glide plane to cross-slip plane, by leaving a stair-rod dislocation at the intersection (Figure 5.13b). If the the glide plane and crosss-slip plane are at an acute angle, then the low energy stair-rod ($1/6\langle 110 \rangle$) forms at the intersection (Figure 5.7), while high energy Hirth stair-rod ($1/3\langle 100 \rangle$) forms at obtuse intersection (Figure 5.9).

Similar to compressive loading, cross-slip through Fleischer mechanism has also been observed under tensile loading (Figure 5.9). However, the Friedel-Escaig mechanism of cross-slip has not been observed. This is mainly because the trailing partials under tensile loading are generated from the dissociation of stair-rod dislocation lying on the twin boundary. This restricts the probability of constriction of leading and trailing partials. Similar to that observed in the present study, Zhu et al. [195] have modeled the slip transfer reactions of $1/2\langle 110 \rangle$ screw dislocations in nanotwinned Cu bi-crystals and predicted the two different cross-slip mechanisms in accordance with Friedel-Escaig and Fleischer. Further, Fleischer mechanism was also observed in atomistic simulations of stress driven cross-slip in FCC Al [196].

The other interesting observation in the present study is the glide of partial/extended dislocation along the plane of twin boundary. Since the twin boundary is parallel to the loading direction, the shear stress acting on dislocations lying on this plane is zero. Therefore, the glide of any dislocations on the axial twin boundary is not expected. However, under both tensile and compressive loading, the frequent glide of partial/extended dislocations has been observed along this plane. An example of such glide can be seen from Figures 5.7c-d. Similar glide of partial dislocations migrating on the twin boundary has been reported by Jeon and Dehm [197]. This unusual glide may be due to the rotation of the sample under tensile/compressive loading or stress localization in the vicinity of twin boundaries.

Finally, it is important to mention that the twin boundary spacing considered in the present study is in the range 1.5 - 5 nm, which has been compared with that of equilibrium spacing of the partial dislocations in Cu. The equilibrium spacing of the partial dislocations in Cu has been obtained by introducing and equilibrating an edge dislocation with Burgers vector $1/2\langle 110 \rangle$ on YZ plane with length along Z-axis in a thin films. The thin film is oriented along in [1-11], [110] and [1-1-2] along X, Y and Z axis respectively with thickness (t) varied from 1.25 to 13.77 nm along X axis (Figure 5.14). Depending on thinfilm thickness, the equilibrium spacing of the partial dislocations in Cu varies in the range 1.5-3 nm (Figure 5.14). Similar values of equilibrium spacing of the partial dislocations i.e., 2-5 nm has been reported earlier based on the variations in dislocation orientation [199]. These equilibrium spacing of the partial dislocations values (i.e., 1.5-3 nm) are in the same order of magnitude as that of the twin boundary spacing considered in the present study (i.e., 1.5 - 5 nm). For a perfect nanowire of size 10 nm, the equilibrium spacing will be around 3 nm (Figure 5.14). However, in the presence of twin boundaries, it may get reduced due to the repulsive force from twin boundaries. In this context, it is interesting to understand the relevance of this length scale to the observed deformation mechanisms, particularly the cross-slip. It is well known that the cross-slip mechanism strongly depends on the stacking fault energy (SFE) of the materials, which in turn is related to the equilibrium separation of partials. The dislocations easily cross-slips in materials with high SFE, while the cross-slip is difficult in low SFE materials. As the SFE is inversely proportional to equilibrium separation of partials, the extended dislocations having a wider partial separation finds it difficult to cross-slip, while cross-slip is easy for dislocations with smaller partial separation. Thus, it can be concluded that the length scale of the equilibrium separation of partial dislocations has some effect on the observed deformation mechanisms in the present

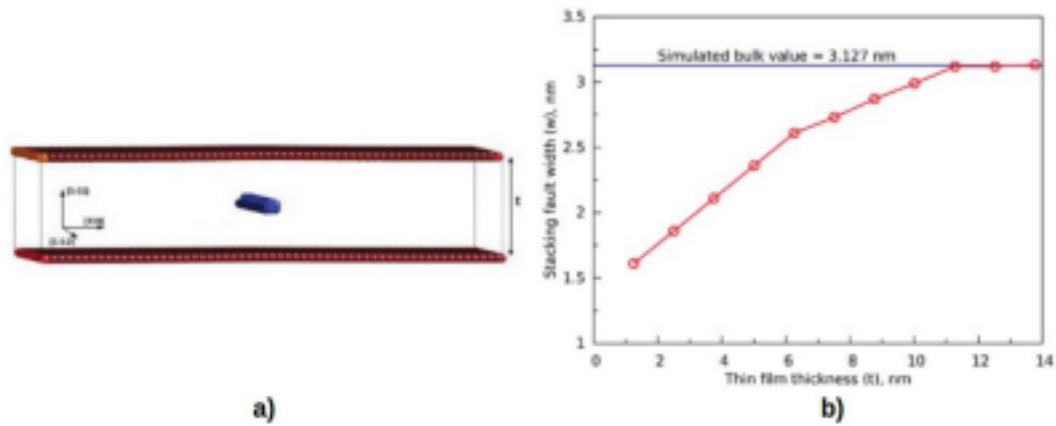


Figure 5.14: (a) Cu thin film of thickness "t" oriented in [1-11], [110] and [1-1-2] axial directions containing a $1/2\langle 110 \rangle$ edge dislocation on [1-11] plane. (b) Variation of stacking fault width as a function of thin film thickness in Cu. The horizontal line shows the stacking fault width in thin film of infinite thickness.

study, particularly the cross-slip mechanism.

5.4 Influence of twin boundary position

The above results suggest that the twin boundary spacing significantly influences the yield strength and deformation behaviour of twinned nanopillars. Also, the previous reports suggests that twin boundary orientation dictates the operating deformation mechanisms [84, 87, 88, 89]. However, along with twin boundary spacing and orientation, twin boundary position (distance of twin boundary from the surface) also influences the yield strength. In twinned nanopillars, both the twin boundary and surface influences the dislocation nucleation from the surface. In other words, the dislocation nucleation from the surface is influenced by repulsive force offered by twin boundary in addition to the force exerted by surface. However, the influence of twin boundary position on the yield strength has not been reported so far. In view of this, the influence of twin boundary position on the yield strength of twinned nanopillars has been investigated and reported in the following sections

5.4.1 Stress-strain behaviour

The tensile stress-strain behaviour of nanopillar of single twin with varying distance (x) from the surface has been shown in Figure 5.15a. It can be seen that, all the nanopillars exhibit the

linear elastic deformation till the peak stress, followed by the sudden drop in flow stress. With further plastic deformation, the flow stress gradually decreases in an oscillating fashion. The slope of linear elastic region had been calculated as Young's modulus and found to remain constant (~ 138 GPa) for nanopillars with different twin distance (Figure 5.15a).

The peak stress corresponding to the nucleation of Shockley partials, following the elastic deformation in twinned nanopillars had been considered as yield strength. As the twin boundary position varies with respect to free surface, the variations in yield stress can be observed (Figure 5.15a). The variations in yield strength with twin boundary position (x) has been presented in Figure 5.15b. It can be seen that, the yield strength of twinned nanopillars increases with increasing twin distance from the free surface. Further, it can be seen that, for all nanowires with different sizes (i.e., for 10 nm and 15 nm), and crystallographic orientations (i.e., $\langle 112 \rangle$ and $\langle 110 \rangle$), similar variations in yield strength with twin boundary position can be observed (Figure 5.15b). In other words, irrespective of size and orientation, the yield strength of twinned nanopillars increases with increasing the twin boundary distance (x) from the surface. Further, the yield strength of twinned nanopillars with small sizes is always higher than the twinned nanopillar of larger size, at all equivalent twin distances (y) from free surfaces. In addition, the yield strength of twinned nanopillars irrespective of twin boundary position and size, is always higher than the perfect nanopillars of same size.

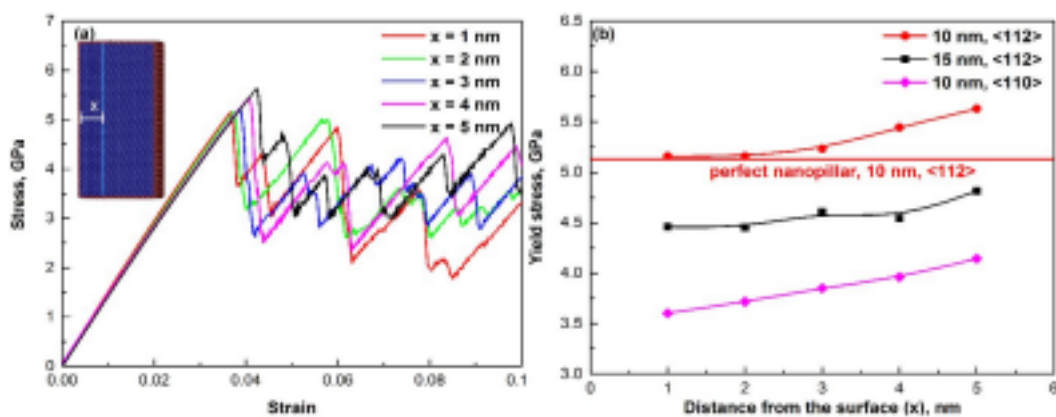


Figure 5.15: (a) The stress-strain behaviour of $\langle 112 \rangle$ longitudinally twinned Cu nanopillars of single twin, with twin boundary located at with different distances (x) from the surface. (b) The variations of yield strength of twinned nanopillar of single twin as a function of twin boundary distance at various nanopillar sizes and orientation. For comparison, the yield strength of perfect nanopillar has been represented as a straight line.

5.4.2 Yield strength dependence on twin boundary position

In order to understand the yield strength dependence on the distance of the twin boundary from the surface, the atomic configuration of nanopillars during yielding has been captured and analyzed. The atomic snapshots corresponding to yielding of nanopillars with different distances from the surface has been shown in Figure 5.16. In all twinned nanopillars, the yielding occurs through the nucleation of Shockley partials (Figure 5.16a-b). Interestingly, we had observed that, the nucleation occurs from the corners far away from the twin boundary (Figures 5.16a-b). This clearly suggests that the repulsive force exerted by the twin boundaries influences the nucleation of Shockley partials thereby, influencing the yield strength of the nanopillars. As the Shockley partials nucleate far away from the twin boundary, the distance between twin boundary and free surface (where nucleation of Shockley partial occurs) has been considered during repulsive force calculations. For nanopillar with single twin boundary at a distance of x nm from the surface, it can be visualized that, the same twin boundary is " $l-x$ " nm away from the opposite surface. Then the repulsive force (f_{tb}) of the twin boundary as a function of distance ($l-x$) can be calculated according to equation 5.12.

$$f_{tb} = \frac{\lambda\mu b^2}{4\pi(l-x)}. \quad (5.12)$$

Here for Cu, λ is dimensionless measure of the interaction strength due to the elasticity mismatch between the twin and perfect Cu and is approximately 0.3 [188], the shear modulus (μ) is 53.31 GPa, and b is the Burgers vector of partial dislocations. The variations in repulsive force as a function of distance ($l-x$) from free surface has been shown in Figure 5.16c. It can be seen that repulsive force decreases with increasing distance ($l-x$) of twin boundary from the free surface. In other words, the repulsive force due to the twin boundary is inversely proportional to the distance. Further, the variations in yield strength as a function of distance ($l-x$) has also been presented in Figure 5.16c. The yield strength as function of distance ($l-x$) decreases with increase in twin distance ($l-x$) (Figure 5.16c). The decrease in yield strength can be directly correlated with the decrease in repulsive force exerted by the twin boundary, with increasing the twin distance from the free surface. Studies related to the influence of twin boundary on dislocations has been reported earlier. For instance, Chen et al. [187] had reported the variation of interaction force between screw dislocation and the twin boundary. They had shown that

repulsive forces due to the twin boundary attributes to the major part of the interaction energy in twinned grains.

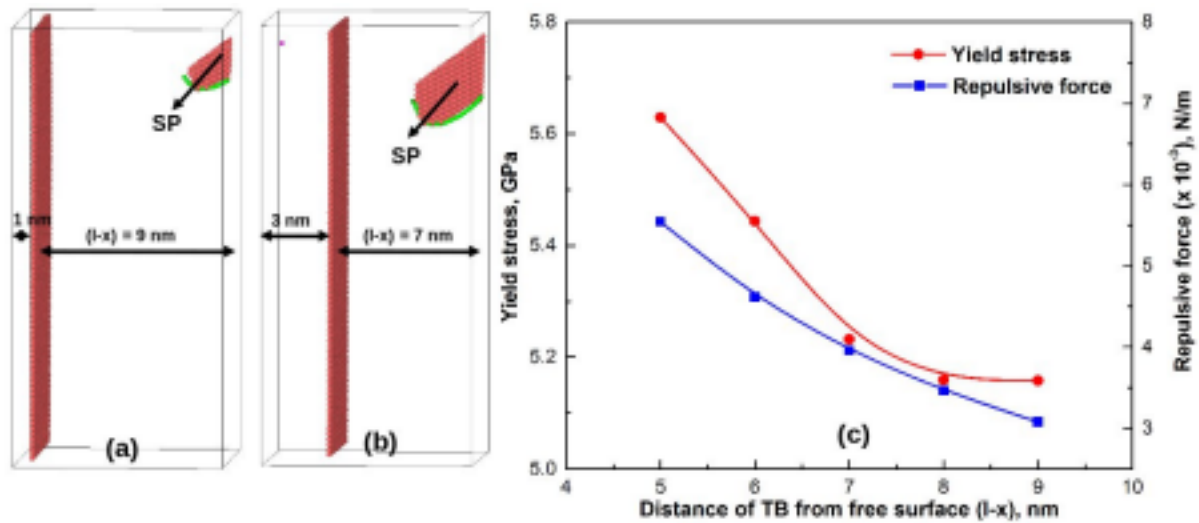


Figure 5.16: (a,b) The atomic configurations displaying the nucleation of $1/6\langle 112 \rangle$ Shockley partial (SP) dislocations in twinned Cu nanopillars with single twin under tensile loading. The nucleation in all twinned nanopillars occurs at free surface which is far away from the twin boundary. (c) The variations of repulsive force and the yield strength of twinned nanopillars with single twin, as a function of twin boundary distance ($l-x$). The perfect and surface atoms were removed for better clarity. The red color atoms represents the HCP atoms (stacking fault and twin boundaries). The green color lines indicate $1/6\langle 112 \rangle$ Shockley partial (SP) dislocations.

5.5 Conclusions

The role of twin boundaries on the strength and deformation mechanisms of perfect and $\langle 112 \rangle$ twinned Cu nanopillars has been investigated under tensile and compressive loading by means of atomistic simulations. The simulation results indicated that the presence of twin boundaries strengthens the nanopillars. The yield strength in longitudinally or axial twinned nanopillars increases with decreasing twin boundary spacing, which is similar to that observed in orthogonally twinned nanopillars. This strengthening in twinned nanopillars may be attributed to repulsive force offered by twin boundaries on dislocations and stress redistribution in individual twinned regions. Further, the yield strength of twinned nanopillars show tension-compression asymmetry, which is higher than that exhibited by perfect nanopillars.

In addition to strength, the presence of twin boundaries also changes the operative defor-

mation mechanisms as compared to perfect nanopillars. Under compressive loading, the deformation in $\langle 112 \rangle$ perfect as well as twinned nanopillars is dominated by the slip of extended dislocations. Further, the presence of twin boundaries under compressive loading introduces extensive cross-slip activity from one grain the other and also onto the twin boundary plane. This cross-slip activity under compressive loading occurs through two different mechanisms namely Friedel-Escaig mechanism and Fleischer mechanism. However, no cross-slip activity has been noticed in perfect nanopillars.

On the other hand, under tensile loading, the deformation in perfect nanopillars occurs by partial dislocation slip/twinning, which changes to extended dislocation activity following the introduction of twin boundaries. This change in twinned nanopillars is due to the formation and dissociation of a stair-rod dislocation on the twin boundary. This stair-rod dislocation, which forms through the interaction of two leading partials at the twin boundary, dissociates into two trailing partials gliding on the same plane as that of the leading partials, thus constituting an extended dislocation slip. This extended dislocations under tensile loading also exhibit cross-slip activity in twinned nanopillars. However, this cross-slip occurs only through Fleischer mechanism and no Friedel-Escaig mechanism of cross-slip has been observed under tensile loading. Further, the dislocation glide along the twin boundary has also been observed under tensile and compressive loading, despite zero resolved shear stress on the twin boundary plane.

Further, with increasing the distance (x) of twin boundary from the free surface, the yield strength of twinned nanopillars increases. This increase in yield strength is attributed to the variations in the repulsive force which in-turn varies with twin boundary position (x). Interestingly, the variations in yield strength of twinned nanopillars as function of twin boundary positions can be seen in all nanowires irrespective of the nanopillar size and crystallographic orientation.

Chapter 6

Deformation behaviour of polycrystalline Cu under monotonic and cyclic loading

6.1 Introduction

It has been well established that bulk materials/coarse grained materials can be strengthened/controlled by manipulating the grain boundaries through Hall-Petch (HP) relation [90, 91]. Also, many reports have shown that as grain size decreases below certain value HP relation will break down. For instance, Meyers et al. [92] had suggested that the critical grain size at which the HP relation breaks down for Cu is close to 20 nm. Below this grain size, the yield stress decreases with decrease in grain size. It has been observed that in this small grain size regime, the yield stress follows the inverse Hall-Petch relation (equation 6.1).

$$\sigma_Y = \sigma - \frac{k}{d^{0.5}} \quad (6.1)$$

Here σ_Y is yield stress expressed in GPa, k is material constant and d is the grain size in nm. Pertaining to the deformation of polycrystalline materials, several studies have been performed under monotonic loading conditions. Detailed literature related to deformation of polycrystalline materials under monotonic loading has been discussed in previous section 1.4.3. However, only few studies exist on the cyclic deformation of polycrystalline materials. In this backdrop, the effect of cyclic loading on the strength and deformation behaviour of polycrystalline Cu has been investigated. For comparison, effect of grain size (1.54-5.42 nm) on strength and defor-

mation behaviour of polycrystalline Cu under monotonic loading has also been investigated in this chapter.

6.2 Computational details

Similar to previous chapters, MD simulations have been performed using LAMMPS [123] employing Mishin's EAM potential for FCC Cu [108]. The stress has been obtained using the Virial expression [140], which is equivalent to a Cauchy's stress in an average sense. The visualization of atomic configurations is accomplished in AtomEye [129] with common neighbor analysis (CNA) parameter [142].

The polycrystalline Cu nanowires have been prepared using the Voronoi algorithm with random grain orientation [129, 131]. All the nanowires used in the present study have a square cross section width (d) of 10.8 nm and length of 21.6 nm providing an aspect ratio of 2:1. In order to understand the effect of grain size on the deformation and failure behaviour, the grain size has been varied from 1.54 to 5.42 nm. As a model system, a nanocrystalline Cu with a mean grain size of 5.4 nm has been shown in Figure 6.1a. Since the surfaces play an important role under cyclic loading, periodic boundary conditions were chosen along length direction, while the other directions were kept free in order to mimic an infinitely long nanowire. Use of periodic boundary conditions removes the artificial effects associated with end grips, which acts as localized sites for defect nucleation and failure [200]. To relax the internal stress present in the nanowire particularly at grain boundaries, the model system was first heated to 300 K and then cooled back to 10 K, where the actual tensile loading has been carried out. Velocity Verlet algorithm has been used to integrate the equations of motion with a time step of 2 fs. Upon equilibration at 10 K, the nanowires were deformed under tensile (monotonic) loading at a constant strain rate of $1 \times 10^9 \text{ s}^{-1}$ along the axial direction.

To understand the deformation behaviour of polycrystalline Cu under fatigue loading, a model system of average grain size of 5.4 nm has been chosen as shown in Figure 6.1a. Then, the fatigue simulations were carried out at strain amplitude of $\pm 4\%$ for 10 cycles under total strain controlled cyclic loading and by employing fully reversed sinusoidal waveform with a time period of 100 ps (Figure 6.1b). This provided a constant strain rate of $1.6 \times 10^9 \text{ s}^{-1}$. The strain rates considered in MD simulations during both monotonic and cyclic loading's are

significantly higher than the experimental strain rates, which is due to the inherent time scale limitations from MD.

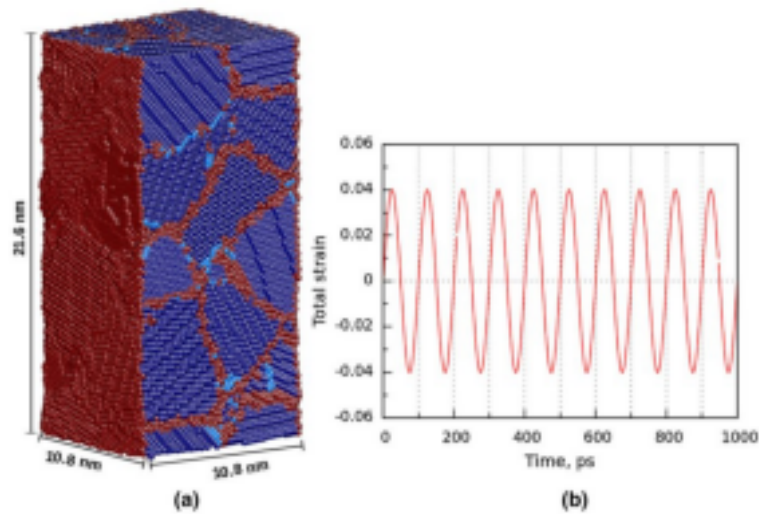


Figure 6.1: The model polycrystalline Cu with a average grain size of 5.4 nm after the equilibration. The front surfaces of model system has been removed and the atoms are colored according to the common neighbor analysis (CNA)

6.3 Results

6.3.1 Deformation behaviour under monotonic loading

The tensile stress-strain behaviour of polycrystalline Cu nanowires of grain size in the range of 1.54-5.42 nm has been presented in Figure 6.2. It can be seen that all the nanowires undergo elastic deformation up to a peak stress followed by a marginal stress reduction. For clarity, the initial elastic regime has been shown in the inset. The values of the Young's modulus have been calculated from the elastic regime of stress-strain curve and they were found to be in the range of 45-60 GPa. The observed Young's modulus values are in agreement with the experimental results of Nieman et al. [201]. Following the elastic deformation, the flow stress decreases gradually along with marginal oscillations until failure. Interestingly, all the nanowire fails at approximately the same values of strain, irrespective of their grain size.

The peak stress values at the end of elastic regime have been considered as yield stress in all the nanowires. Figure 6.3a shows the variation of yield stress and flow stress at 10% as a function of grain size. It can be seen that both the yield stress and flow stress increases

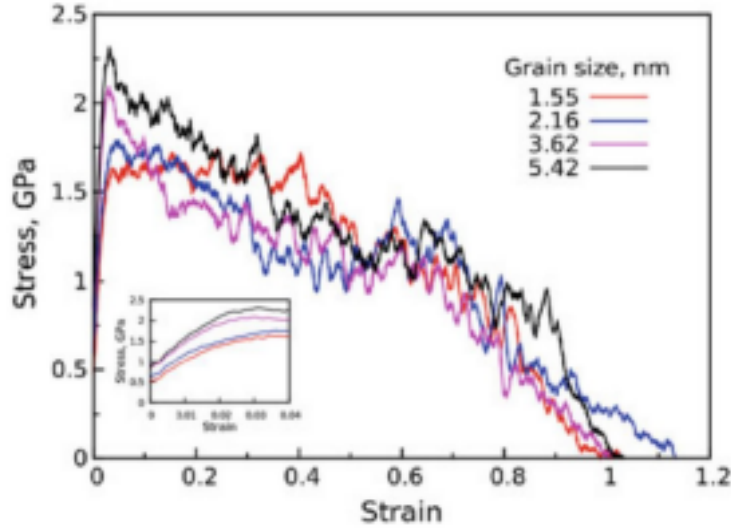


Figure 6.2: Stress-strain curves for polycrystalline Cu nanowires ($10.84 \times 10.84 \times 21.69$ nm) with different average grain size in the range of 1.54-5.42 nm at 10 K.

linearly with an increase in grain size. The obtained yield stress values in polycrystalline Cu nanowires (1.6-2.3 GPa) are much lower than the single crystalline nanowires (11.5 GPa) [172]. This is due to the heterogeneous behaviour of grain boundaries, which results in high stress concentration and thus reduces the yield strength significantly [202]. Figure 6.3b shows the yield stress variation with the inverse square root of the grain size. By linear fitting of data, the slope is found to be negative. This negative slope (-1.80) indicates that the polycrystalline Cu nanowires with grain sizes in the range of 1.54-5.42 nm follows inverse Hall-Petch behaviour. This inverse Hall-Petch behaviour at nanoscale has been reported for many polycrystalline materials [93, 94, 95, 96, 172]. Saha et al. [203] have observed the similar slope exhibiting the inverse Hall-Petch relationship in polycrystalline W nanowires. The inverse Hall-Petch relation for polycrystalline Cu nanowire has been shown as follows:

$$\sigma_Y = 3.05832 - \frac{1.80192}{d^{0.5}}. \quad (6.2)$$

Here σ_Y is yield stress expressed in GPa and d is the grain size in nm. Many mechanisms have been proposed for this inverse Hall-Petch behaviour such as suppression of dislocation pile-ups [204], dislocation motion through multiple grains [205], sliding in the grain boundaries [206, 207], grain rotation [207], and enhanced diffusional creep in the grain boundaries [93]. The increase in strength with an increase in grain size (inverse Hall-Petch) in the present study can be attributed to the grain boundary sliding mechanism [94, 208]. However, the observed

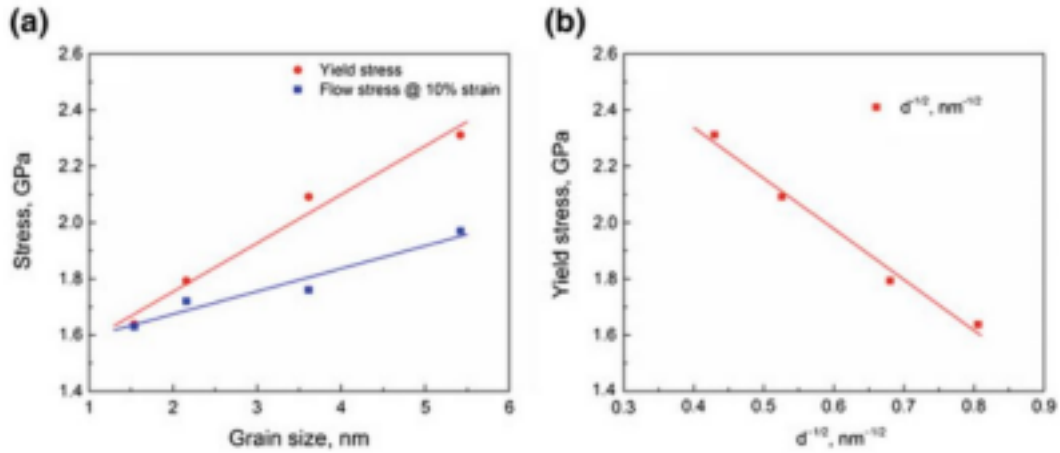


Figure 6.3: a The variation of yield stress and flow stress at 10% strain as a function of grain size for polycrystalline Cu nanowire at 10 K. b Yield stress variation with the inverse square root of grain size ($d^{-1/2}$) in $nm^{-1/2}$ exhibiting inverse Hall-Petch (IHP) relation.

yield stress variation with grain size can be explained based on dislocation nucleation from grain boundaries. Due to higher fraction of grain boundary atoms in small grain size sample, the dislocation nucleation is easier leading to lower yield strength, while lower fraction of grain boundary atoms increases the stress required for dislocation nucleation at large grain sizes.

The atomic configurations during the tensile deformation of polycrystalline Cu nanowire with a grain size of 3.61 nm have been presented in Figure 6.4. The stress reduction following the elastic deformation of polycrystalline Cu nanowires is associated with nucleation of Shockley partial dislocation from the grain boundaries (Figure 6.4a). Due to large number of the disordered atoms, the grain boundaries possess high energy as compared to the grain interior. The high energy of the grain boundaries makes them favorable sites for dislocation nucleation. The dislocation nucleation from grain boundaries rather than free surfaces is the reason for much lower yield stress of polycrystalline nanowires as compared to their single crystal counterparts [172]. The plastic deformation in Cu nanowires is dominated by the glide of $1/6 \langle 112 \rangle$ partial dislocations nucleated from the grain boundaries. The $1/6 \langle 112 \rangle$ Shockley partial enclosing the stacking faults have been found. The cyan colored atoms which represent the stacking fault atoms confirms the dislocation-mediated plasticity in polycrystalline copper. However, along with dislocation-mediated plasticity, deformation twinning is also observed. The observed twinning mechanism along with dislocation-mediated plasticity in polycrystalline nanowires is in agreement with that observed in polycrystalline Cu under tensile and torsion loading [202].

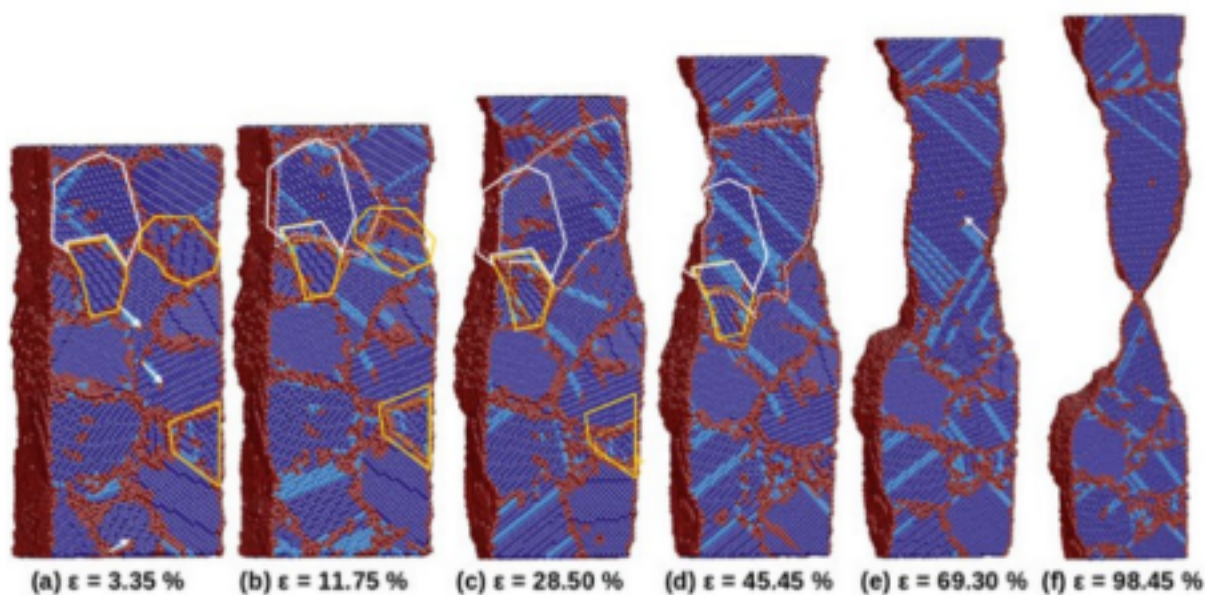


Figure 6.4: Deformation behaviour of polycrystalline Cu nanowire with grain size of 3.61 nm under tensile loading. The deformation through the slip of partial dislocations can be seen at all strains. The blue color atoms represent FCC atoms, cyan color atoms represent the stacking faults and the red color atoms indicate the surfaces, grain boundaries and dislocation cores. The solid (green, white, yellow and ash) curves represent the trace of initial grain boundaries, while the dashed curves represent the traces of instantaneous grain boundaries.

With increase in strain, the deformation induced grain growth has been observed (Figure 6.4-c). The traces of initial grain boundaries have been indicated by solid lines as shown in Figure 6.4a. Following the grain growth with increasing strain, the trace line for each grain boundary has been shown as a dotted line. The grains with white colored trace line expands (Figure 6.4a-d), while the grain with yellow colored trace line shrinks (Figure 6.4, b) and completely disappears in Figure 6.4c. This indicates that the large grains expand at the expense of smaller grains. This grain coarsening/growth has been observed for all nanowires irrespective of their grain size. The grain growth in our MD simulations occurs through grain boundary sliding. Usually, at high temperature, the thermal energy acts as a driving force for grain growth[31, 32, 33]. However, at low temperatures, the applied stress, which is in the order of few GPa, acts as a driving force [210]. Under external stress, the rotation of neighboring grains coupled with atomic shuffling from grain interior to grain boundary (order to disorder) or grain boundary to grain interior (disorder to order) results in grain growth . Similar grain growth mechanism has been reported in earlier studies [209, 210]. The continuous grain coarsening results in the formation of a single large grain (yellow colored dotted trace line in Figure 6.4d), where the deformation localizes and nanowire fails through shear intra-granular failure.

An interesting phenomenon observed during the tensile deformation of polycrystalline Cu nanowires is the formation of fivefold deformation twins near the grain boundaries as shown in Figure 6.5. Successive emission of partial dislocations along the same glide plane from the grain boundaries results in the twin formation. This twin formation mechanism in polycrystalline Cu nanowires is similar to that in single crystalline Cu nanowires as discussed in section 3.3.2. Formation of twin from grain boundaries relieves the strain in the grain interior. Intersection of deformation twins with different Burgers vector leads to the formation of fivefold twin symmetry. Similar fivefold twin formation has been reported earlier through experimental investigations and MD simulations [202, 211, 212, 213].

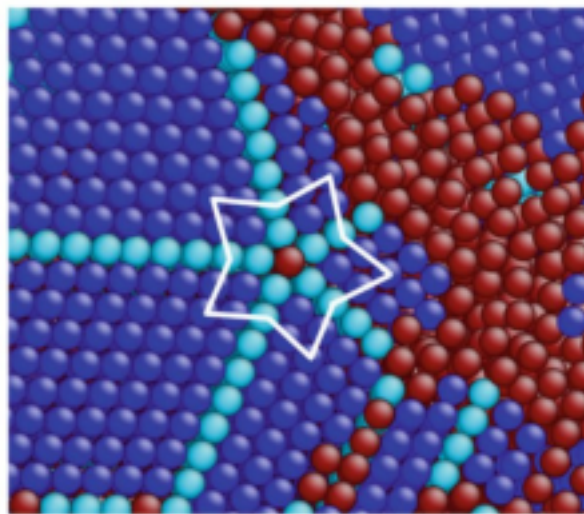


Figure 6.5: The fivefold deformation twin observed during tensile deformation of polycrystalline Cu nanowire with a grain size of 2.16 nm. The blue color atoms represent the perfect FCC atoms, the cyan color atoms represent the twin boundaries and the red color atoms represent the grain boundary.

As shown in Figure 6.4, the plastic deformation is dominated by dislocation-mediated plasticity and deformation twinning irrespective of the grain size. However, it has been observed that the failure mechanism is different in nanowires of different grain size. In nanowires with a grain size up to 3.61 nm, the failure occurs by the shear along the slip plane of single grain, i.e., intra-granular failure (Figure 6.6a-c). However in nanowire with a grain size of 5.42 nm, the failure has been observed along the grain boundary, i.e., intergranular failure (Figure 6.6d). Finally, all the nanowires irrespective of grain size, exhibit the same ductility (failure strain), which indicates that ductility is insensitive to grain size.

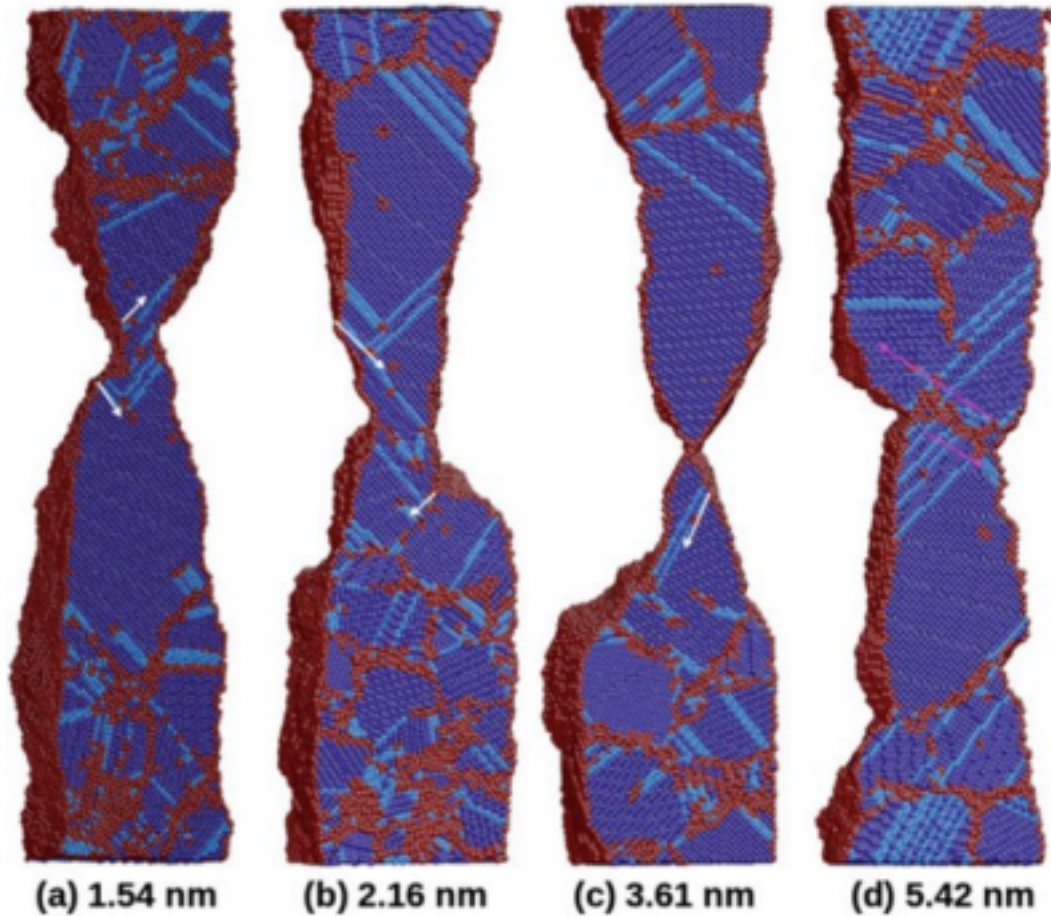


Figure 6.6: The fivefold deformation twin observed during tensile deformation of polycrystalline Cu nanowire with a grain size of 2.16 nm. The blue color atoms represent the perfect FCC atoms, the cyan color atoms represent the twin boundaries and the red color atoms represent the grain boundary.

6.3.2 Deformation behaviour under cyclic loading

Figure 6.3, It has been observed that the polycrystalline Cu in nanoscale undergoes an elastic deformation up to a strain level of 0.03 followed by the irreversible plastic deformation. Based on this, the strain amplitude of 4% has been chosen for fatigue simulations. Typical stress-strain hysteresis loops corresponding to 1st, 5th and 10th cycles are shown in Figure 6.7a. Similar to monotonic loading, the stress increases linearly during elastic deformation followed by yielding and plastic deformation up to 4% strain. Upon reversal at 4% strain the stress-strain varies linearly followed by yielding at relatively lower stress and plastic deformation up to -4% strain in compression. A well defined hysteresis loop develops due to irreversible plastic deformation and subsequent cyclic loading resulted in cyclic hardening. Figure 6.7b shows the variations in peak cyclic stress response (CSR) in tension and compression as a function of

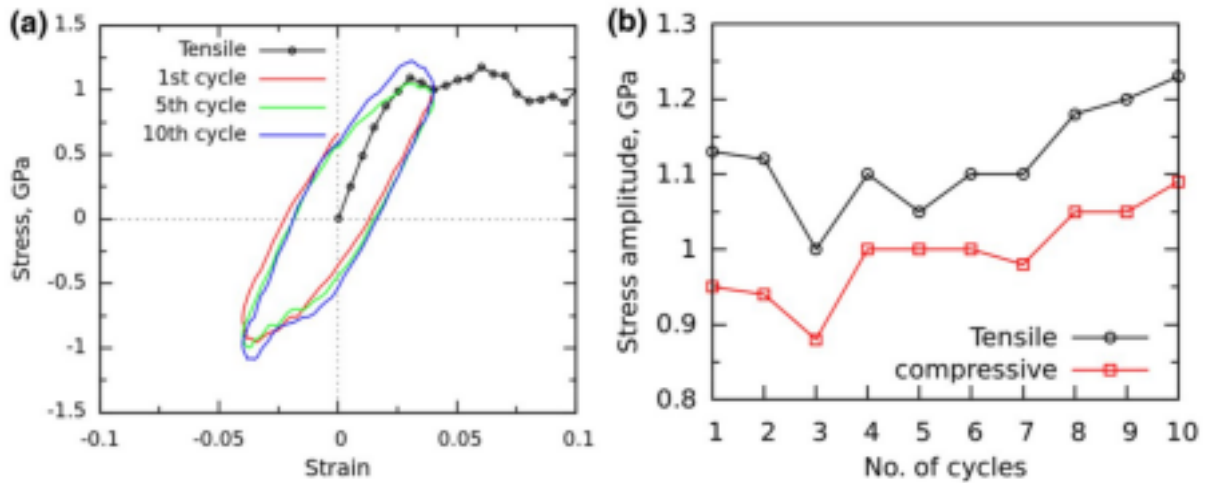


Figure 6.7: a The monotonic and the cyclic stress-strain behaviour of polycrystalline Cu. The peak cyclic stress response in tension and compression with number of cycles is shown in (b)

number of cycles. Cyclic softening up to 3 cycles followed by continuous hardening till the end of 10th cycle can be seen in Figure 6.7b. MD simulation results for the grain size 7.2 and 9.4 nm also exhibited similar cyclic stress response. The observed cyclic stress response is in agreement with those reported for nanocrystalline Ni [99, 214] and Al [100] examined using experiments [214] and MD simulations [99, 100].

The progressive plastic deformation with number of cycles at 3% total strain in tension for 1st, 5th and 10th cycles is shown in Figure 6.8. The plastic deformation is mainly dominated by the glide of $1/6\langle 112 \rangle$ partial dislocations nucleating from the grain boundaries. The $1/6\langle 112 \rangle$ partial dislocations have been found by enclosing the stacking faults. It can be seen that, during the first cycle, the plastic deformation is activated only in few grains (Figure 6.8a), and with increase in the number of cycles, more grains participate in the deformation process (Figure 6.8b, c). The partial dislocations nucleating from one grain boundary (Figure 6.8a) moves towards the opposite grain boundary and gets annihilated. This suggests that the grain boundaries acts as a source as well as sink for dislocations. The nucleation, glide and annihilation of partial dislocations leave a stacking fault ribbons within the grain. Many such stacking fault ribbons produced by the movement of partials dislocations are shown with white arrows in Figure 6.8. The continuous nucleation of partial dislocations from the incoherent twin boundary (ICTB) (Figure 6.8a) and their reverse motion upon strain reversals converts the ICTB into a coherent twin boundary (Figure 6.8b). The coherent twin boundary formed during

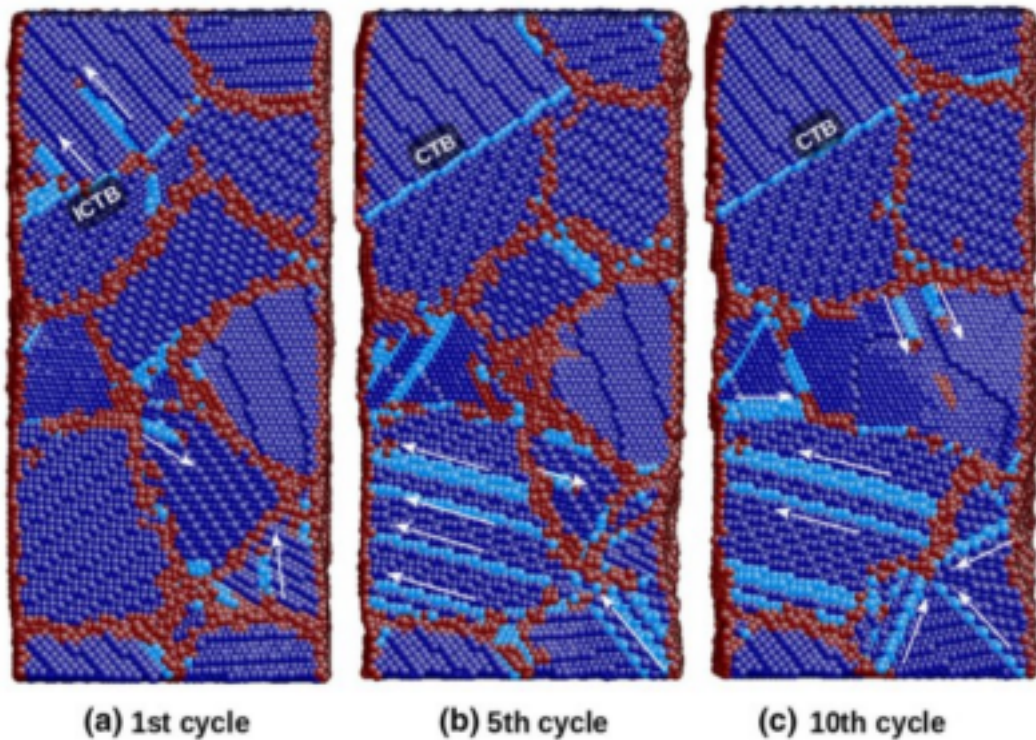


Figure 6.8: The atomic snapshots showing plastic deformation at a strain level of 3 % for a 1st, b 5th and c 10th cycles. The front surface was removed for clarity. The atoms were colored according to the CNA. The red atoms represent the grain boundaries, dislocation cores and surface atoms. Blue atoms represent perfect FCC atoms and cyan atoms represent HCP atoms.

first few cycles remains highly stable during further cyclic deformation (Figure 6.8c). Contrary to this, the high angle grain boundaries have been found to be highly unstable under the cyclic deformation. It has been observed that the heavily deformed grains coarsen at the expense of undeformed grains associated with grain boundary migration. This grain coarsening results in the appearance of large but lower number of grains at the end of 10th cycle (Figure 6.8c). Our preliminary analysis indicates that the grain growth is due to continuous impingement of partial dislocations on the grain boundary. In order to get more understanding of grain growth phenomena, further analysis is in progress. The observed cyclic deformation induced grain growth is in agreement with those reported by Panzarino et al. [100] in Al and Schiotz [215] in Cu. This is also consistent with the deformation-induced grain growth in polycrystalline materials. In order to further confirm and quantify the grain coarsening, the number of disordered atoms have been calculated and presented as a function of cyclic deformation in Figure 6.9. The disordered atoms include the atoms in the surface, partial dislocation core and grain boundaries. By assuming the surface atoms to be constant and the dislocation core atoms to be low during

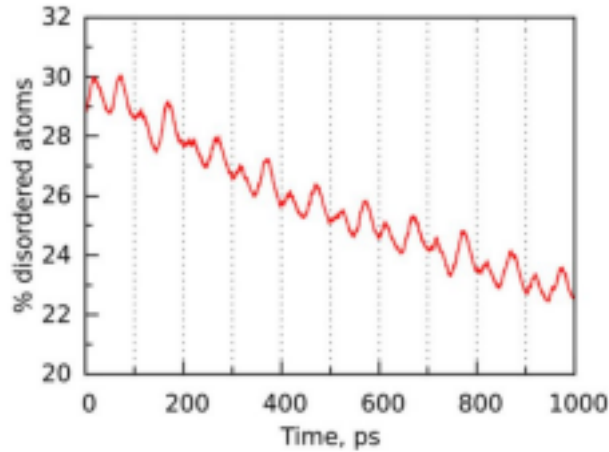


Figure 6.9: The percentage of disordered atoms as a function of time during cyclic deformation. The disordered atoms include the grain boundary atoms, surfaces and the dislocation core atoms. Each 100 ps is equivalent to one cycle as shown by vertical grids.

the deformation, the observed overall decreases in % disordered atoms indicates that the total grain boundary area decreases with increase in cyclic deformation. The fluctuations observed in Figure 6.9 are due to fluctuations in dislocation core atoms during the deformation. The plastic deformation dominated by the glide of $1/6\langle 112 \rangle$ partial dislocations nucleating from the grain boundaries has been also observed at relatively larger grain sizes of 7.2 and 9.4 nm. Further, similar coarsening of heavily deformed grains at the expense of undeformed grains associated with grain boundary migration has been found for the grain size 7.2 and 9.4 nm.

In polycrystalline materials, it is well known that the grain size and strength are related by the inverse Hall-Petch equation. Based on this, the observed increase in strength from 3rd to 10th cycles can be attributed to the increase in grain size [100]. In order to understand the initial softening followed by hardening, the variations of dislocation density and % stacking fault atoms have been calculated as a function of cyclic deformation (Figure 6.10). The dislocation density is calculated by using dislocation extraction algorithm [148]. The average dislocation density exhibited an increase up to 300 ps, i.e., 3 cycles followed by a continuous decrease up to 1000 ps or, 10th cycle (Figure 6.10a). The initial increase in dislocation density has been associated with a similar increase in the % stacking fault atoms in the first 3 cycles followed by nearly constant % stacking fault atoms at higher number of cycles (Figure 6.10b). Since the deformation in all the grains is not activated in the first cycle, the increase dislocation density and stacking fault atoms up to 3-4 cycles is mainly due to the continuous activation

of dislocation sources in the undeformed grains. Contrary to this, the decrease in dislocation

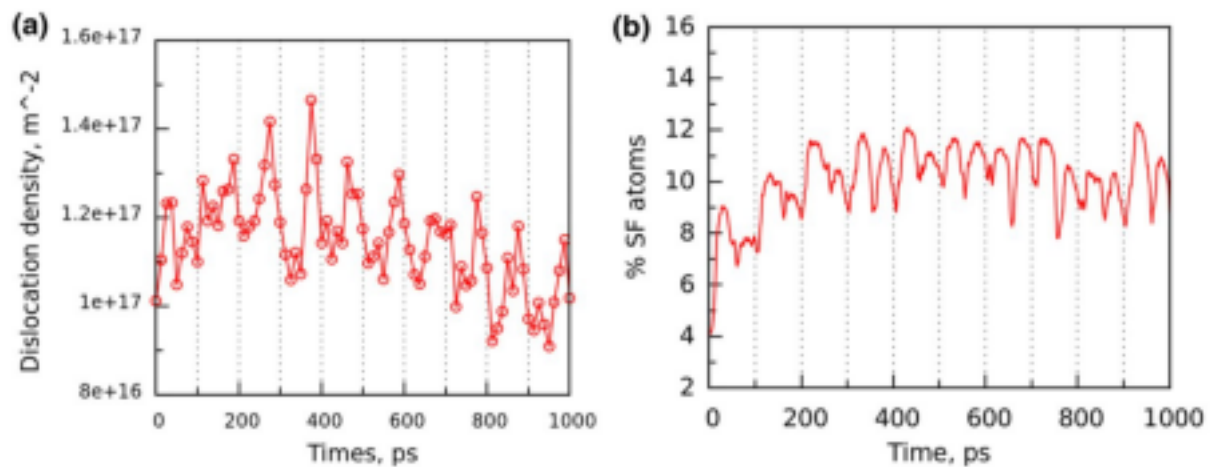


Figure 6.10: The variations of a dislocation density and b the percentage of stacking fault atoms as a function of time during cyclic deformation. Each 100 ps is equivalent to one cycle shown by vertical grids

density from 4th to 10th cycle arises mainly from the decreases in dislocation sources (grain boundaries) resulting from the grain growth. This decrease in dislocation sources leads to the hardening as observed from 3rd to the end of 10th cycle.

6.4 Conclusions

MD simulations have been performed to investigate the tensile (monotonic) and fatigue deformation behaviour of polycrystalline Cu nanowires. The conclusion drawn are as follows:

- The tensile stress-strain behaviour is characterized by the initial elastic deformation up to peak stress followed by a gradual decrease in flow stress until failure.
- The variation of yield stress and flow stress follows the inverse Hall-Petch relation as a function of grain size.
- The deformation behaviour under the tensile deformation is dominated by the glide of partial dislocations which nucleated mainly from the grain boundaries. Along with partial

dislocation mediated plasticity, deformation by twinning has also been observed. Due to twinning on multiple and interacting twin systems, the formation of fivefold twin has been observed.

- Under both monotonic and cyclic loading, extensive grain growth resulting in the formation of large grains has been observed during the plastic deformation.
- For nanowires of grain size up to 3.61 nm, the failure has been observed by the shear along the slip planes, while, grain boundary failure has been observed in nanowire with a grain size of 5.42 nm. Irrespective of the grain size, all nanowires exhibit similar ductility (failure strain) indicating that ductility is insensitive to grain size.
- The cyclic stress-strain behaviour is characterized by initial softening up to 3rd cycle followed by hardening till the end of 10th cycle.
- Deformation behaviour under cyclic loading is dominated by the glide of partial dislocations enclosing the stacking faults. During the cyclic deformation, the twin boundaries were found to be stable boundaries, while the remaining high angle grain boundaries were highly unstable. As a result, an extensive grain growth is observed during the cyclic deformation.



Role of axial twin boundaries on deformation mechanisms in Cu nanopillars

P. Rohith ^{a,b}, G. Sainath ^b, Sunil Goyal^{a,b}, A. Nagesha^{a,b} and V. S. Srinivasan^{a,c}

^aHomi Bhabha National Institute (HBNI), Indira Gandhi Centre for Atomic Research, Kalpakkam, India; ^bMaterials Development and Technology Division, Indira Gandhi Centre for Atomic Research, Kalpakkam, India; ^cScientific Information Resource Division, Resource Management & Public Awareness Group, Indira Gandhi Centre for Atomic Research, Kalpakkam, India

ABSTRACT

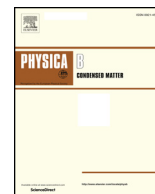
In recent years, twinned nanopillars have attracted tremendous attention for research due to their superior mechanical properties. However, most of the studies were focused on nanopillars with twin boundaries (TBs) perpendicular to loading direction. Nanopillars with TBs parallel to loading direction have received minimal interest. In this backdrop, the present study is aimed at understanding the role of axial TBs on strength and deformation behaviour of Cu nanopillars using atomistic simulations. Tensile and compression tests have been performed on $\langle 112 \rangle$ nanopillars with and without TBs. Twinned nanopillars with twin boundary spacing in the range 1.6–5 nm were considered. The results indicate that, under both tension and compression, yield strength increases with decreasing twin boundary spacing and is always higher than that of perfect nanopillars. Under compression, the deformation in $\langle 112 \rangle$ perfect as well as twinned nanopillars proceeds by the slip of extended dislocations. In twinned nanopillars, an extensive cross-slip by way of Friedel-Escaig and Fleischer mechanisms has been observed in compression. On the other hand, under tensile loading, the deformation in perfect nanopillars occurs by partial slip/twinning, while in twinned nanopillars, it proceeds by the slip of extended dislocations. This extended dislocation activity is facilitated by stair-rod formation and its dissociation on the twin boundary. Similar to compressive loading, the extended dislocations under tensile loading also exhibit cross-slip activity in twinned nanopillars. However, this cross-slip activity occurs only through Fleischer mechanism and no Friedel-Escaig mechanism of cross-slip has been observed under tensile loading.

ARTICLE HISTORY

Received 20 May 2019
Accepted 31 October 2019

KEYWORDS

Atomistic simulations;
nanopillars; twin boundaries;
dislocations; cross-slip



Effect of size, temperature and strain rate on dislocation density and deformation mechanisms in Cu nanowires



P. Rohith^{a,b}, G. Sainath^{b,*}, V.S. Srinivasan^{a,c}

^a Homi Bhabha National Institute (HBNI), Indira Gandhi Centre for Atomic Research, Kalpakkam, Tamilnadu 603102, India

^b Materials Development and Technology Division, Metallurgy and Materials Group, Indira Gandhi Centre for Atomic Research, Kalpakkam, Tamilnadu 603102, India

^c Scientific Information Resource Division, Resource Management & Public Awareness Group, Indira Gandhi Centre for Atomic Research, Kalpakkam, Tamilnadu 603102, India

ARTICLE INFO

Keywords:

Molecular dynamics simulations
Cu nanowire
Dislocation density
Dislocation exhaustion
Dislocations starvation

ABSTRACT

In the present study, molecular dynamics (MD) simulations have been performed to understand the effect of nanowire size, temperature and strain rate on the variations in dislocation density and deformation mechanisms in $< 100 >$ Cu nanowires. The nanowire size has been varied in the range 1.446 – 43.38 nm with a constant length of 21.69 nm. Different temperatures varying from 10 K to 700 K and strain rates in the range of $5 \times 10^7 - 1 \times 10^9 \text{ s}^{-1}$ have been considered. For all the conditions, the variations in dislocation density (ρ) has been calculated as a function of strain. The results indicate that the variations in dislocation density exhibits two stages irrespective of the conditions: (i) dislocation exhaustion at small strains followed by (ii) dislocation starvation at high strains. However, with decreasing size and increasing temperature, the rate of dislocation exhaustion increases, which results in early transition from dislocation exhaustion stage to dislocation starvation stage. Similarly, with increasing strain rate, the rate of dislocation exhaustion and also the transition strain increases.

1. Introduction

Technological advancements have paved the way towards the development of nanocomponents in nanoelectro mechanical systems (NEMS). Nano components used in NEMS are required to withstand the complex stress state with minimal probability of failure. Hence, it is important to understand the mechanical properties such as strength and associated deformation mechanisms like dislocation density. Generally, the mechanical properties of nanowires are determined using nanoindentation tests, while tensile tests are most common in bulk materials. However, performing experiments at nanoscale involves many complications. Alternatively, molecular dynamics (MD) simulations provide great insights in determining mechanical properties and understanding the deformation behaviour of nanowires with atomic-scale resolution.

Plastic deformation in bulk materials is characterized by dislocation multiplication, dislocation pile-up, dislocation cross-slip and similar processes, which leads to strain hardening/softening before final failure. However, in nanomaterials, dislocations can travel limited distances before annihilating at free surfaces/grain boundaries, thereby reducing the probability of dislocation multiplication [1,2]. The

strengthening behaviour in the bulk materials with respect to grain size can be described by the well known Hall-Petch relation. A physical basis for this behaviour is associated with the difficulty of dislocation movement across grain boundaries and the stress concentration arising due to dislocation pile-up [3,4]. However, as the grain size decreases to nanoscale regime, the grain boundary volume fraction increases significantly and as a result, the grain boundary mediated processes such as GB sliding and GB rotation becomes more important [3,4]. In particular, when the grain size is reduced to below certain critical size, the strength of materials decreases with decreasing grain size, i.e., it follows inverse Hall-Petch relation. In the absence of grain boundaries in single crystalline nanowires, the surface alone influences the strength and deformation mechanisms [5]. In nanowires, the strength increases with decreasing size, which is mainly attributed to surface effects. Contrary to nanowires, the surface effects are absent in bulk single crystals. These differences suggests that the deformation mechanisms governing the plastic deformation in nanomaterials/nanowires are quite different from their bulk counterparts. Since then, many researchers have proposed different mechanisms such as source exhaustion and source truncation, dislocation exhaustion, dislocation starvation, and weakest link theory to understand the deformation behaviour

* Corresponding author.

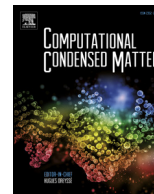
E-mail address: sg@igcar.gov.in (G. Sainath).

<https://doi.org/10.1016/j.physb.2019.03.003>

Received 2 January 2019; Received in revised form 22 February 2019; Accepted 5 March 2019

Available online 08 March 2019

0921-4526/ © 2019 Elsevier B.V. All rights reserved.



Effect of orientation and mode of loading on deformation behaviour of Cu nanowires

P. Rohith, G. Sainath^{*}, B.K. Choudhary

Materials Development and Technology Division, Indira Gandhi Centre for Atomic Research, HBNI, Kalpakkam, Tamilnadu, 603102, India

ARTICLE INFO

Article history:

Received 26 April 2018

Received in revised form

3 July 2018

Accepted 27 August 2018

Keywords:

Molecular dynamics simulations

Cu nanowire

Orientation

Dislocations and twinning

ABSTRACT

Molecular dynamics simulations have been performed to understand the variations in deformation mechanisms of Cu nanowires as a function of orientation and loading mode (tension or compression). Cu nanowires of different crystallographic orientations distributed uniformly on the standard stereographic triangle have been considered under tensile and compressive loading. The simulation results indicate that under compressive loading, the orientations close to $\langle 100 \rangle$ corner deform by twinning mechanism, while the remaining orientations deform by dislocation slip. On the other hand, all the nanowires deform by twinning mechanism under tensile loading. Further, the orientations close to $\langle 110 \rangle$ and $\langle 111 \rangle$ corner exhibit tension-compression asymmetry in deformation mechanisms. In addition to deformation mechanisms, Cu nanowires also display tension-compression asymmetry in yield stress. The orientations close to $\langle 001 \rangle$ corner exhibits higher yield stress in tension than in compression, while the opposite behaviour (higher yield stress in compression than in tension) has been observed in orientations close to $\langle 110 \rangle$ and $\langle 111 \rangle$ corners. For the specific orientation of $\langle 102 \rangle$, the yield stress asymmetry has not been observed. The tension-compression asymmetry in deformation mechanisms has been explained based on the parameter α_M , defined as the ratio of Schmid factors for leading and trailing partial dislocations. Similarly, the asymmetry in yield stress values has been attributed to the different Schmid factor values for leading partial dislocations under tensile and compressive loading.

© 2018 Elsevier B.V. All rights reserved.

1. Introduction

In recent years, the metallic nanowires have attracted a significant interest for research due to their superior electrical, optical, thermal and mechanical properties. In particular the Cu nanowires/nanopillars, nanobelts, nanosprings and nanofilms have emerged as the next-generation materials in nano/micro electromechanical systems (NEMS/MEMS) due to their excellent performance with conductivity, transmittance, mechanical flexibility, low cost, easy and inexpensive synthesis [1,2]. In view of this, understanding the deformation behaviour of Cu nanowires becomes essential for their effective practical applications. The knowledge of deformation mechanisms also becomes important for fine-tuning the physical properties of nanowires such as reorientation, shape-memory and pseudo-elasticity [3], which have practical implications in the design of novel and flexible NEMS/MEMS devices.

In view of the small size of nanowires, performing the accurate

mechanical testing of nanowires is still challenging due to the difficulties in sample preparation, clamping and aligning the nanowire axial direction with loading direction [4]. This complexities in experimental techniques preclude the conventional methods and lend towards theoretical/computational tools. With the rapid progress of computational capability and the availability of reliable inter-atomic potentials, molecular dynamics (MD) simulations have become a major tool to probe the mechanical properties of nanoscale materials. In addition to the usual mechanical properties, MD simulations provide the real-time deformation process of nanowire at the atomic scale. In the present study, MD simulations have been used to understand the deformation mechanisms in Cu nanowires.

In the past, many experimental/atomistic simulations have been performed on FCC nanowires/nanopillars such as Au [5–7], Ag [8], Cu [5,9], Pt [10], Al [11] and Ni [5,12]. All these studies have shown that the important mechanisms of plastic deformation in FCC nanowires are slip through perfect and partial dislocations and deformation twinning. The competition between slip and twinning mechanisms depends mainly on the crystallographic orientation,

^{*} Corresponding author.

E-mail address: sg@igcar.gov.in (G. Sainath).



Double reorientation in $\langle 110 \rangle$ Cu nanowires

P. Rohith, G. Sainath  and B. K. Choudhary

Deformation and Damage Modeling Section, Mechanical Metallurgy Division, Indira Gandhi Centre for Atomic Research, HBNI, Kalpakkam, India

ABSTRACT

Molecular dynamics simulations performed on tensile deformation of $\langle 110 \rangle$ Cu nanowire indicated that the nanowire undergoes double reorientation from $\langle 110 \rangle$ to $\langle 100 \rangle$ tensile axis followed by $\langle 100 \rangle$ to $\langle 112 \rangle$ tensile axis. It has been observed that the double reorientation results from the occurrence of twinning mode of deformation in both the original $\langle 110 \rangle$ and reoriented $\langle 100 \rangle$ Cu nanowires. The double reorientation in $\langle 110 \rangle$ Cu nanowire leads to tensile ductility as high as 260% thereby displaying superplastic like behaviour. The occurrence of double reorientation and the associated high tensile ductility have been restricted to low nanowire length below or equal to 7.15 nm with aspect ratio ≤ 1 . Above this length (higher aspect ratio), the reorientation process has not been observed and the nanowire fails at significantly lower strains due to activation of multiple twin systems facilitating twin–twin interactions.

ARTICLE HISTORY

Received 31 May 2017
Accepted 29 September 2017

KEYWORDS

Molecular dynamics simulation; $\langle 110 \rangle$ Cu nanowire; tensile deformation; twinning; double reorientation

1. Introduction

In recent years, there is an increasing interest in understanding the deformation behaviour and the associated mechanical properties of metallic nanowires/nanopillars due to their potential applications in future nano/micro electromechanical systems (NEMS/MEMS) [1,2]. Due to extremely small lateral dimensions, the nanowires possess an intrinsic surface stresses as high as tens of GPa. The high surface stresses make the nanowires to display unique structural transformations and thermo-mechanical behaviour such as phase transformation, reorientation, shape memory effect, pseudo-elasticity and superplasticity [3–6]. This unique phenomenon enables the design of novel and flexible NEMS/MEMS having potential applications in self-healing materials, nano-manipulators, energy storage, sensors, switches, etc. [1]. Moreover, Cu nanowires can be used as smart sensors, resonators, inter-connectors, transparent electrodes, organic solar cells and other components of electronic circuits of NEMS/MEMS [7,8]. In view of these, understanding deformation behaviour of nanowires and the conditions in which these structural transformations and thermo-mechanical behaviour can be realised become necessary for effective practical applications.

CONTACT B. K. Choudhary  bkc@igcar.gov.in

© 2017 Informa UK Limited, trading as Taylor & Francis Group



Size dependent deformation behaviour and dislocation mechanisms in $\langle 1\ 0\ 0 \rangle$ Cu nanowires

G. Sainath , P. Rohith and B. K. Choudhary

Deformation and Damage Modeling Section, Mechanical Metallurgy Division, Indira Gandhi Centre for Atomic Research, HBNI, Kalpakkam, India

ABSTRACT

Molecular dynamics simulations have been performed to understand the size-dependent tensile deformation behaviour of $\langle 1\ 0\ 0 \rangle$ Cu nanowires at 10 K. The influence of nanowire size has been examined by varying square cross-section width (d) from 0.723 to 43.38 nm using constant length of 21.69 nm. The results indicated that the yielding in all the nanowires occurs through nucleation of partial dislocations. Following yielding, the plastic deformation in small size nanowires occurs mainly by slip of partial dislocations at all strains, while in large size nanowires, slip of extended dislocations has been observed at high strains in addition to slip of partial dislocations. Further, the variations in dislocation density indicated that the nanowires with $d > 3.615$ nm exhibit dislocation exhaustion at small strains followed by dislocation starvation at high strains. On the other hand, small size nanowires with $d < 3.615$ nm displayed mainly dislocation starvation at all strains. The average length of dislocations has been found to be same and nearly constant in all the nanowires. Both the Young's modulus and yield strength exhibited a rapid decrease at small size nanowires followed by gradual decrease to saturation at larger size. The observed linear increase in ductility with size has been correlated with the pre- and post-necking deformation. Finally, dislocation–dislocation interactions leading to the formation of various dislocation locks, the dislocation–stacking fault interactions resulting in the annihilation of stacking faults and the size dependence of dislocation–surface interactions have been discussed.

ARTICLE HISTORY

Received 6 April 2017
Accepted 22 June 2017

KEYWORDS

Molecular dynamics simulations; $\langle 1\ 0\ 0 \rangle$ Cu nanowire; plastic deformation; partial dislocations and dislocation density

1. Introduction

Understanding the deformation behaviour and the associated mechanical properties of metallic nanopillars/nanowires has attracted huge interest from material scientists due to large potential applications as key components in nano/micro

Fatigue Deformation of Polycrystalline Cu Using Molecular Dynamics Simulations

G. Sainath¹ · P. Rohith¹ · B. K. Choudhary¹

Received: 6 October 2015 / Accepted: 13 December 2015
© The Indian Institute of Metals - IIM 2016

Abstract Molecular dynamics (MD) simulations have been performed to investigate the fatigue deformation behaviour of polycrystalline Cu with grain size of 5.4 nm. The samples were prepared using Voronoi algorithm with random grain orientations. Fatigue simulations were carried out by employing fully reversed, total strain controlled cyclic loading at strain amplitude of $\pm 4\%$ for 10 cycles. The MD simulation results indicated that the deformation behaviour under cyclic loading is dominated by the slip of partial dislocations enclosing the stacking faults. At higher number of cycles, the grain boundary migration leading to coarsening of larger grains at the expense of the smaller grains has been observed. The cyclic stress–strain behaviour, the deformation mechanisms and the variation of dislocation density as a function of cyclic deformation have been discussed.

Keywords Molecular dynamics simulation · Polycrystalline Cu · Fatigue · Partial dislocations · Grain growth

1 Introduction

Fatigue deformation in polycrystalline materials is a multi-scale problem involving the crack nucleation at the atomic scale to the final failure at the engineering scale [1]. Therefore, understanding the fatigue deformation at

multiple length scales becomes important in order to design the optimum microstructure against the fatigue failure. Due to difficulties in performing experiments at the atomic scale, most of the studies in the past have concentrated on the damage at the micro and/or macro scales. With the rapid advancement of computational capability and the availability of reliable inter-atomic potentials, molecular dynamics (MD) simulations have become a major tool to examine the mechanical behaviour of materials at the atomic scale. However, the grain sizes accessible by the MD simulations are in the order of nanometers (nm). Therefore, the nanocrystalline materials with a grain size in the order of few tens of nm can only be studied using MD simulations.

Several MD simulation studies on the deformation of nanowires/nanocrystalline materials under monotonic loading conditions have been performed [2–4]. Only few studies exist in the literature pertaining to the MD simulations on cyclic deformation of metals. Further, due to time and length scale limitations involved in MD simulations, the cyclic deformation studies have been carried out only for few cycles. Rupert and Schuh [5] performed MD simulations to understand the cyclic deformation behaviour of polycrystalline Ni with grain sizes of 3, 4, 5, and 10 nm. The observed strengthening during cyclic deformation in Ni has been attributed to the grain boundary relaxation and the formation of low energy boundaries [5]. Recently, Panzarino et al. [6] characterized the grain structure evolution during the cyclic deformation of polycrystalline Al having grain size of 5 nm for 10 cycles. The cyclic strengthening was associated with the grain rotation, grain growth and the formation of many twin boundaries [6]. Like polycrystalline Al and Ni in nanoscale, MD simulations on the polycrystalline Cu with 5.5 nm grain size revealed the occurrence of grain coarsening during the

✉ B. K. Choudhary
bkc@igcar.gov.in

¹ Deformation and Damage Modeling Section, Mechanical Metallurgy Division, Indira Gandhi Centre for Atomic Research, Kalpakkam, Tamil Nadu 603102, India

Molecular Dynamics Simulations Study on the Grain Size Dependence of Deformation and Failure Behavior of Polycrystalline Cu



P. Rohith, G. Sainath and B. K. Choudhary

Abstract The tensile deformation and failure behavior of polycrystalline Cu nanowires have been examined using molecular dynamics (MD) simulations at 10 K. MD simulations have been performed on polycrystalline Cu nanowires with grain size ranging from 1.54 to 5.42 nm. The simulation results indicate that the yielding as well plastic deformation in all the Cu nanowires proceeds by the slip of Shockley partial dislocations irrespective of grain size. Interestingly, the formation of fivefold twin and deformation induced grain growth has been observed during the plastic deformation. The polycrystalline Cu with the grain size of 5.42 nm fails through shear along the grain boundary (intergranular failure), while the shear along the slip planes within the grain (intra-granular failure) has been observed for grain size less than 5.42 nm. The variations of yield strength and flow stress at 10% strain as a function of grain size follows inverse Hall–Petch relation.

Keywords Molecular dynamics simulations · Nanocrystalline Cu · Partial dislocations · Grain growth

1 Introduction

Nanocrystalline materials are promising materials for a large number of applications in nano/micromechanical (NEMS/MEMS) systems such as transparent electrodes, sensors, and flexible electronics [1, 2]. The optimal utilization and reliability of these materials critically depend on a thorough understanding of their mechanical properties and associated deformation mechanisms. Many experimental investigations and computer simulations have confirmed the superior mechanical properties of nanocrystalline materials and also their dependence on size, shape, strain rate and temperature [3–12]. These superior properties arise from their finite

P. Rohith (✉) · G. Sainath · B. K. Choudhary
Materials Development and Technology Division, Metallurgy and Materials Group Indira Gandhi Centre for Atomic Research, HBNI, Kalpakkam 603 102, Tamil Nadu, India
e-mail: rohith@igcar.gov.in

Dependence of Equilibrium Stacking Fault Width on Thickness of Cu Thin Films : A Molecular Dynamics Study

P. Rohith*, G. Sainath and B. K. Choudhary

*Deformation and Damage Modeling Section, Metallurgy and Materials Group
Indira Gandhi Centre for Atomic Research, Kalpakkam – 603102, Tamil Nadu, India
(*Email : rohith@igcar.gov.in)*

Abstract. In face centered cubic systems, due to decrease in energy all perfect dislocations dissociates into two Shockley partials separated by stacking fault width. The stacking fault width, which influences the deformation behavior depends on many factors such as composition, stacking fault energy, temperature, surface energy and applied stress. Additionally in thin films, thickness also influences the stacking fault width of dissociated dislocations. In this paper, we investigate the effect of thin film thickness on stacking fault width in Cu using molecular dynamics simulations. The results indicate that with increase in film thickness from 1.25 nm to 11 nm, the stacking fault width increases from 1.6 nm to 3.12 nm. A bi-linear behavior has been observed. Above 11 nm thickness, the width of stacking fault has attained a saturation at higher thickness. This thickness dependent dissociation has been explained using the concept of image dislocations and associated image forces.

Keywords: Molecular Dynamics Simulations, Thin films, Dislocations, Stacking fault.

PACS: 83.10.Rs, 43.35.Ns, 68.60.Bs, 61.72.Ff, 61.72.Nn

INTRODUCTION

It is widely accepted that the motion of dislocations plays a vital role in the plastic deformation of crystalline materials. In face centered cubic (FCC) materials, due to decrease in energy all perfect dislocations dissociates into two Shockley partials separated by stacking fault width [1]. This stacking fault width is inversely proportional to the stacking fault energy of the material. The width of stacking fault is determined by a balance of repulsive force between two Shockley partials and the attractive force due to surface tension of the stacking fault. The partial dislocations will settle at an equilibrium distance determined mainly by stacking fault energy [2]. The stacking fault energy depends on various factors such as composition, temperature and applied stress [3]. At nano scale the stacking fault width and grain size have similar dimensions, as a result the stacking fault width changes with grain diameter in addition to stacking fault energy [4]. Recent molecular dynamics (MD) simulations have reported that the stacking fault width significantly influences the deformation processes such as cross slip and dislocation climb [5]. However, due to difficulties in experiments, determining the equilibrium stacking fault width is not straightforward. Using high-resolution transmission electron

microscopy, Liao et al [6]. have found an average stacking fault width of 3.5 nm for polycrystalline Al, while for single crystal it has been found to be 0.55 nm. In this context, MD simulations with appropriate inter-atomic potentials can be useful tool to accurately determine the stacking fault width and the factors associated with it. In this paper using MD simulations, the effect of thickness on stacking fault width of Cu thin films has been investigated.

SIMULATION DETAILS

All MD simulations have been carried out using LAMMPS package [7] with embedded atom method potential developed by Mishin and co-workers [8]. Cu thin films were oriented in [1-11], [110] and [1-1-2] along X, Y and Z axis respectively with thickness (t) varied from 1.25 to 13.77 nm along X axis (Fig. 1). In order to mimic a thin film, periodic boundary conditions were imposed along Y and Z axis while thickness direction has been kept free. Following the creation of a thin film, an edge dislocation with Burgers vector $1/2\langle 110 \rangle$ has been introduced at on YZ plane with length along Z-axis as shown in Fig. 1. Once the dislocation is introduced, the system is allowed to equilibrate using conjugate gradient method. This stabilized system is then thermally

Thesis Highlight

Name of the Student: P. Rohith

Name of the CI: IGCAR

Enrolment No.: ENGG02201405016

Thesis Title: A Study on Deformation Mechanisms in Perfect and Twinned Cu Nanowires by Atomistic Simulations

Discipline: Engineering Sciences

Sub-Area of Discipline: Metallurgy

Date of viva voce: 02-03-2021

Metallic nanowires exhibit mechanical properties different from their bulk counterparts due to high surface area to volume ratio and low defect density. Hence, it is necessary to characterize and understand the deformation of nanowires. With rapid progress of computational capability and availability of reliable inter-atomic potentials, molecular dynamics (MD) approach has become an important simulation tool to examine the deformation behaviour. In the present thesis, deformation and dislocation mechanisms of single crystalline, and twinned nanopillars has been studied using MD simulations. The simulation results indicated that:

- In single-crystalline Cu nanowires with different orientations, the yield stress exhibits tension-compression asymmetry. Also, deformation behaviour varies significantly with compression and tension. Under compression, orientations close to $\langle 100 \rangle$ corner of a standard stereographic triangle orientations deformed by twin, while remaining orientations deformed by full dislocation slip. On the other hand, all orientations deformed by twinning mechanism under tension.
- For $\langle 100 \rangle$ Cu nanowires, Young's modulus and yield strength values decreased rapidly in small size nanowires followed by gradual decrease approaching towards saturation at larger size. Yielding in all nanowires occurs through the nucleation of $1/6\langle 112 \rangle$ Shockley partial dislocations. The plastic deformation in small size nanowires occurred mainly by slip of partial dislocations at all strains, while in large size nanowires, slip of partial dislocations at low strains followed by slip of extended dislocation at high strains were observed.
- In large size nanowires, the leading partial annihilation at the surface gives rise to the nucleation of a new trailing partial dislocation, while in small size nanowires, it gives rises to multiple reflections from the nanowire surface.
- Failure strain increases linearly with increase in size and formation of pentagonal atomic chains has been observed in small size nanowires with $d \leq 1.446$ nm.
- Dislocation exhaustion rates increases with increase in temperature and strain rate, and decrease in size.
- Double reorientation has been observed in $\langle 110 \rangle$ nanowires with aspect ratio ≤ 1 .
- Yield stress increases with decreasing twin boundary spacing in twinned nanopillars.
- Under compression, deformation in $\langle 112 \rangle$ perfect and twinned nanopillars is dominated by extended dislocations. Further, extensive cross-slip activity occurs through Friedel-Escaig (FE) mechanism and Fleischer (FL) mechanism. On the other hand, under tension, deformation in perfect nanopillars occurs by partial dislocation slip/twinning, which changes to extended dislocation slip in twinned nanopillars. Also, cross-slip occurs only through Fleischer mechanism in tension.
- In polycrystalline Cu, yield stress follows inverse Hall-Petch relation with grain size. Deformation proceeds through partial dislocation slip under monotonic and cyclic loading. Also, deformation induced grain growth under both monotonic and cyclic loading has been observed. Under cyclic loading, Softening up to 3rd cycle followed by hardening till 10th cycle in polycrystalline Cu under cyclic loading.